*Nano Sm$_2$O$_3$ dispersed in Y-211, Chapter IV, page 109*



Y-211

Nano Sm$_2$O$_3$

200 nm



*Nano twinning and Core formation in YNSG-Ba Chapter VI, page 190*



**Ph.D. Thesis**
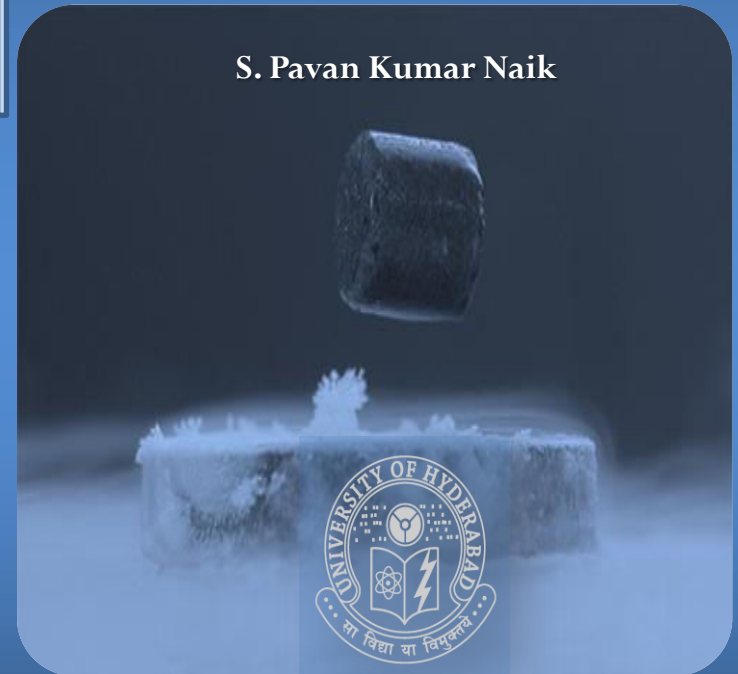
**S. Pavan Kumar Naik**

**2015**

# EFFECT OF RE-DOPING AT NANOSCALE ON THE MICROSTRUCTURES AND FLUX PINNING IN INFILTRATION GROWTH PROCESSED (Y, LRE)BCO SUPERCONDUCTORS

**S. Pavan Kumar Naik**



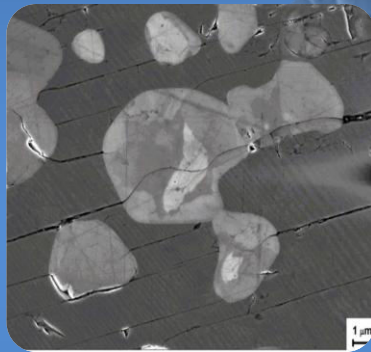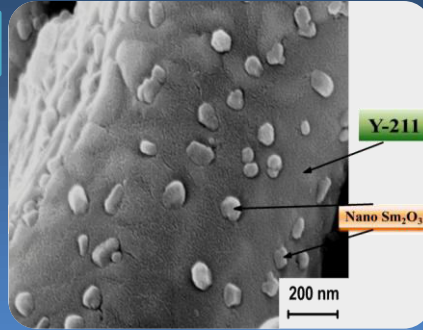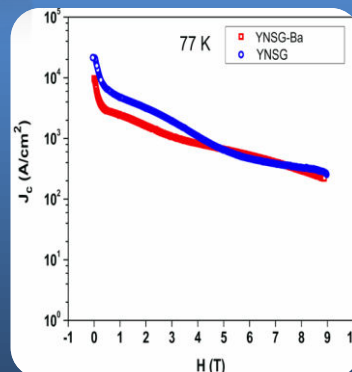School of Physics
University of Hyderabad

2015

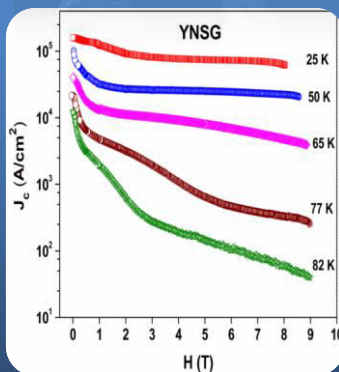# Effect of RE-doping at Nanoscale on the Microstructures and Flux Pinning in Infiltration Growth Processed (Y, LRE)BCO Superconductors

A Thesis submitted for the degree of

**Doctor of Philosophy in Physics**

by

**S. Pavan Kumar Naik**

School of Physics
University of Hyderabad – Hyderabad
(August 2015)

"I do not know what I may appear to the world, but to myself I seem to have been only like a boy playing on the sea-shore, and diverting myself in now and then finding a smoother pebble or a prettier shell than ordinary, while the great ocean of undiscovered truth lay all undiscovered before me"

*Sir Isaac Newton*

DEDICATED

TO

MY PARENTS AND TEACHERS

# DECLARATION

This thesis is a presentation of my original research work has been carried out by me under the supervision of *Professor V. Seshubai*, School of Physics, University of Hyderabad, and Hyderabad, India. I hereby declare that wherever contributions of others are involved, every effort is made to indicate this clearly, with due reference to the literature and acknowledgement of collaborative research and discussions. I also declare that it has not been previously, and is not concurrently, submitted for any other degree at University of Hyderabad, India or at any other institution. I hereby agree that my thesis can be deposited in shodhganga/INFLIBNET.

**A report on plagiarism statistics from the university librarian is enclosed.**

Date: 10<sup>th</sup>August 2015                                    (**S. Pavan Kumar**

**Naik**)Place: Hyderabad

# CERTIFICATE

This is to certify that the research work compiled in this thesis entitled "*Effect of RE-doping at nanoscale on the microstructures and flux pinning in Infiltration Growth processed (Y, LRE)BCO Superconductors*" has been carried out by *Mr. S. Pavan Kumar Naik, (Regd. No. 10PHPH15)* under my supervision and the same has not been submitted for the award of any degree of any University.

A report on plagiarism statistics from the University Librarian is enclosed

**Dr. V. SESHUBAI**

RESEARCH SUPERVISOR

Date: 10<sup>th</sup>August 2015          PROFESSOR, School of Physics

Place: Hyderabad                              University of Hyderabad

**DEAN**
**SCHOOL OF PHYSICS**

# ACKNOWLEDGEMENTS

*Thanks my Lord for everything I've got*

Since this thesis marks the conclusion of my five years of research life here at School of Physics, University of Hyderabad, I take this opportunity to express my sincere gratitude for all those who have guided and encouraged me through my stay here.

There are no words to express my gratitude towards my parents ***S. Bojja Naik (late) and S. Lakshmakka*** who have borne patience and continuously supported me to make my desire a reality.

There are many people who contributed to the work in this thesis. First of all, I would like to express my gratitude to my advisor ***Professor V. Seshubai*** for her supervision, enthusiasm, ideas through my research work and her tireless efforts to help me improve my level of achievement.

I thank the Dean ***Prof. Rajender Singh***, School of Physics for enabling me to use all the central facilities of the school required for the work reported in the thesis. I also thank former Deans of the school ***Prof. C. Bansal, Prof. N. Tiwary, Prof. S. Chaturvedi*** and all other faculty of the School for their constant support and encouragement.

I thank my doctoral committee members, ***Prof. M. Ghanashyam Krishna*** and ***Prof. S. Srinath*** for their sage counsel and suggestions throughout my research work.

structural analysis and for finalizing the results. I also wish to acknowledge all my friends in School of Physics, School of Engineering Science and Technology, ACRHEM, Chemistry and School of Life Sciences for their cooperation during my research work and for making my stay in the University a pleasant and beneficial experience.

I wish to extend my thanks to my brother *S. Kishore Kumar* and convey my love to my niece *R. Lakshmi Prasanna*. I have been extremely fortunate to have the supports from friends to whom I am truly grateful: I would like to thank my friends who supported and encouraged to me *G. Gangadhar, R. Ramesh, Ramu, M. Devaraju, B. Chandra Babu, K. Ramya, P. Sandhya Rani, R. Parvathi* and all friends.

PLACE: Hyderabad
DATE: 10<sup>th</sup>August 2015

**(S. Pavan Kumar Naik)**

# INDEX

# CONTENTS

# Chapter I

# Introduction

# Chapter II

# Experimental Techniques

# Chapter III

# Study of growth mechanism and the effect of infiltration temperature on the properties of Preform Optimized Infiltration Growth processed YBCO superconductors

# Chapter IV

# Structural and microstructural studies of POIG processed (Y, Sm)BCO superconductors

# Chapter V


# Structural, microstructural and magnetic investigations of POIG processed (Y, NSG)BCO superconductor

# Chapter VI

## Study of key factors that control microstructures and flux pinning in (Y, LRE)-BCO superconductors

# Chapter VII

# Summary and Conclusions

# CHAPTER I

# INTRODUCTION

The importance of the area of superconductivity can be clearly seen from the number of Nobel Prizes won in this field. The potential applications of superconducting materials are transmission line cables, generators, magnetic energy storage systems, magnetic levitation, the medical imaging etc., *Superconductivity is a phenomenon characterized by two properties: zero resistance below a critical temperature ($T_c$) and expulsion of magnetic flux below a critical field ($H_c$).* Superconductivity is a phenomenon of strongly correlated behavior in a many-body system, which is important and is still an unsolved mystery in physics. The discovery of surprising properties in the field drives experimentalists and theorists to understand and complete the puzzles [1].

After successfully liquefying helium (He) at the boiling point of 4.2 K, which was accomplished in July 1908, Dutch physicist Kamerlingh Onnes measured temperature dependence of resistance of mercury (Hg) and found that at approximately 4.2 K the resistance of Hg dropped suddenly to zero. This suggested that the metal had undergone transition to a new state, which he called the superconductive state [2-3]. From studies on several elements, many other elements have been found to be superconducting with different transition temperatures ($T_c$) [4-8]. Onnes was awarded Nobel Prize for Physics in 1913.

Meissner and Ochsenfeld in November 1933 found that superconductors are normal metals above their critical temperature and allow all magnetic field lines from an external field to penetrate into the samples. After entering into superconducting state, superconductors expel the external magnetic field lines by

generating equal and opposite fields on their own, thus exhibiting perfect diamagnetism below its critical temperature. This property is known as Meissner effect and it determines whether a compound is in its normal state or in superconducting state [9]. Meissner and Ochsenfeld also found that there is a limit to the magnetic field value ($H_c$) below which the superconductivity is sustained. If the magnetic field becomes stronger than $H_c$, then superconductivity will be destroyed. $H_c$ is temperature dependent.

Over the years superconductivity has been discovered in many metals and metallic compounds with increasing critical temperatures. In most of the applications before 1986 the superconductors used were alloys like NbTi, $Nb_3Sn$, $V_3Sn$, and NbN and were used to construct the first superconducting high field magnets. Even though the field and current carrying properties were satisfactory, the fact that the highest critical temperature is around 25 K had limited their applications, since liquid helium was preferred to utilize these superconductors. The alternative coolant liquid hydrogen (boiling point is 20 K), required special safety considerations, and cryo-refrigerators, which made their operation complex and hence was not attractive. However, the cost of liquid helium being high made any application costly to maintain or operate.

However in 1986, Alex Muller and Georg Bednorz [10] discovered a whole new class of superconductors in $La_{2-x}Ba_xCuO_4$, with the highest known critical temperature, at that time, of 35 K, now known to belong to a family of cuprate superconductors. For this invention they were awarded Nobel prize in 1987. After this great discovery, the search for high temperature superconductors was amplified. Since 1986, the number of researchers working in the field of superconductivity increased tremendously.

With variations introduced to the crystal structure, the critical temperature of these materials quickly increased to 90 K and above. Because of this jump in $T_c$, these superconductors are often referred to as high temperature superconductors (HTSC or HTS). In 1987, a joint group of Wu and Chu had discovered a superconductor of composition $YBa_2Cu_3O_{7-\delta}$ (referred to as YBCO or Y-123) with a transition temperature of 93 K [11]. Subsequently Bi and Tl containing compounds were discovered with transition temperatures of 110 K and 125 K respectively in 1988 [12-13]. The highest known critical temperature is 135 K, to date, which is a thallium-doped mercuric-cuprate ($HgBa_2Ca_2Cu_3O_8$) discovered in 1993 [14-15].

Many cuprate superconductors have transition temperatures above 77 K, and this unlocks the practical applications which were not economically viable with conventional low temperature superconductors. Since these superconductors can be easily cooled in liquid nitrogen ($LN_2$, boiling point is 77 K), which is significantly cheaper than liquid helium, the opportunity for research as well as the ability to use them in industries has drastically increased.

## 1.1. Types of Superconductors:

Based on their response to the applied magnetic properties, superconductors can be divided into two types (Type I and Type II). Type I superconductors are pure metals and they display perfect diamagnetism and zero electrical resistance below their critical temperatures. They expel the external magnetic field completely and are able to levitate over a magnet, but the levitation is unstable because they can move about on the magnetic field lines. Type II superconductors are alloys or intermetallic compounds which also display zero electrical resistance below their critical temperatures but are able to trap some external magnetic fields in certain magnetic field range. Type II superconductors can stably levitate over a magnet.

They can also suspend underneath the magnets which is because they possess a property known as flux pinning, discussed in further sections.
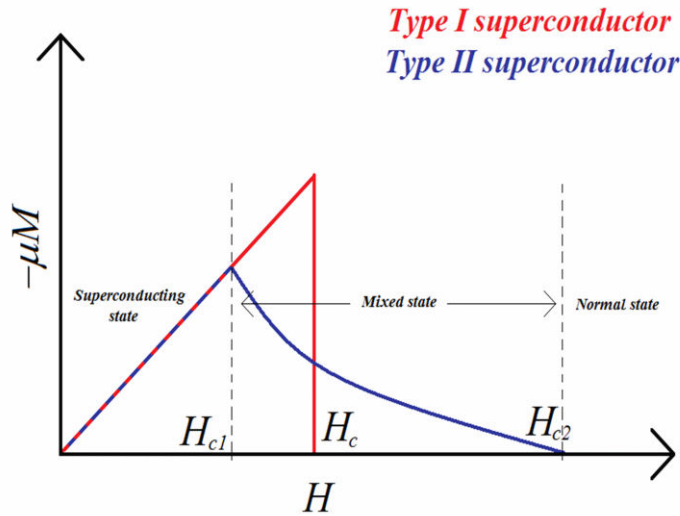


**Fig. 1.1.** Typical H vs T phase diagram for a Type-I and Type-II superconductors. Note there is only one critical field in Type-I superconductor and type-II superconductor displaying the existence of two critical fields ($Hc_1$ and $Hc_2$).

Type I superconductors exist in two phases (i) non-superconducting phase which is above their $T_c$ (normal state) and (ii) superconducting phase below $T_c$ where it shows complete Meissner effect. On the other hand, Type II superconductors also have a non-superconducting (normal phase) and a Meissner phase. Along with these two phases they consist of a mixed phase between them. This phase contains regions of normal state within the volume of the Meissner state. These superconductors have two critical magnetic fields, namely the lower critical field ($H_{c1}(T)$) and the upper critical field ($H_{c2}(T)$), which are the limits for the Meissner state and the mixed state respectively. When the external magnetic field is equal to $H_{c1}$, the magnetic flux abruptly enters the sample. The penetration of the magnetic field increases parabolically until $H_{c2}$ into the superconductor, where it

reaches normal state [16-17]. H-T phase diagram of both the superconductors (Type-I and Type-II) is shown in fig. 1.1.

As the applied magnetic field or the average flux density increases, the distance between vortices decreases, and when the applied field reaches the value of $H_{c2}$ of the superconductor then the vortices begin to overlap causing the order parameter to decrease until it vanishes. If the superconductor contains impurities or defect i.e. if it is not a perfect single crystal, magnetic field lines may pass through such defects in the superconductor. These vortices (and their normal cores) may be stationary or mobile depending on the specific superconductor.

In the mixed phase, the magnetic flux enters the superconductor in the form of a series of magnetic flux lines called the flux line lattice. Each flux line (called a vortex) carries a quantized flux, $\Phi_o = h/2e = 2.07 \times 10^{-15}$ Tm$^2$, generated due to the supercurrents circulating around the flux [16, 18]. The center of the vortex is in the normal state, which is non-superconducting, and the vortex is surrounded by the material in superconducting state; hence the name "mixed state".
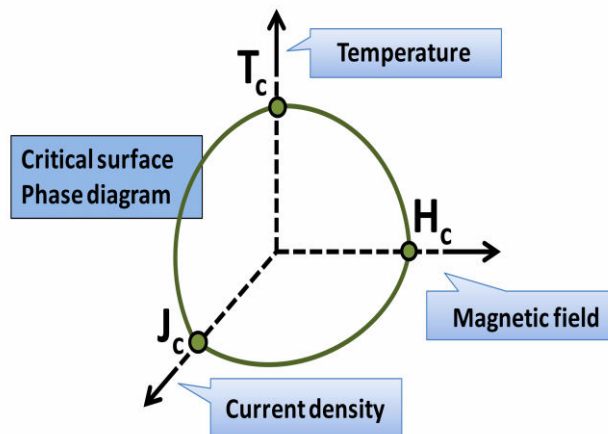


**Fig. 1.2.** Phase diagram of a superconductor.

Further research revealed that the current, applied magnetic field, and temperature are coupled together to define the superconducting limits of a material as a phase diagram for a superconductor as is shown in fig. 1.2. It is these upper limits of $T_c$, $H_c$ and $J_c$ that material scientists and engineers make attempts to improve in order to realize applications.

The critical temperature is unique to each element or material. The evolution in the $T_c$ of the superconducting materials, over years, from elementary mercury to various high $T_c$ superconductors, is shown in fig. 1.3. Recent discoveries in this field are also included.
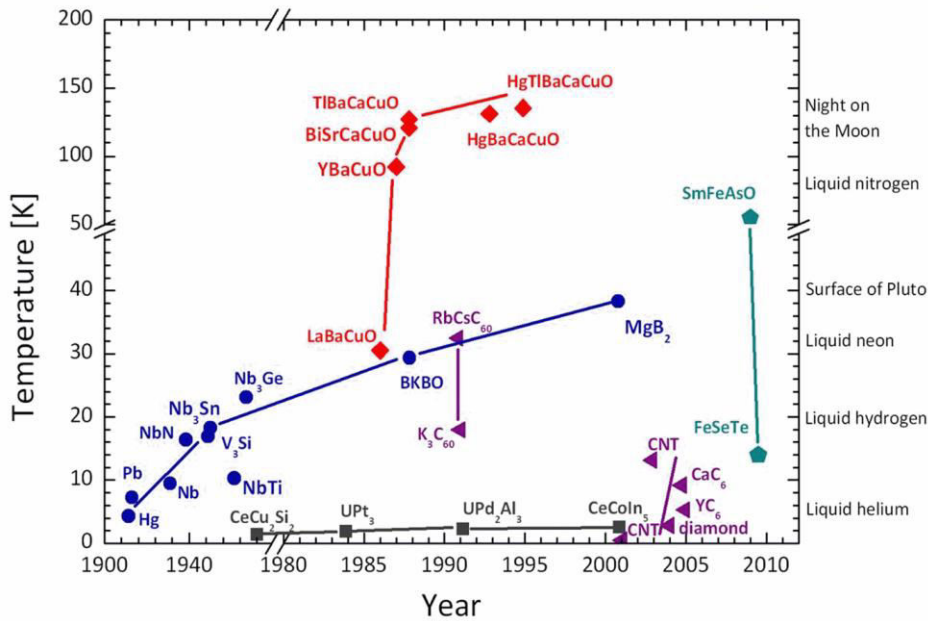


**Fig. 1.3.** Schematic of the critical temperature discoveries of the various superconducting materials over the years.

Different class of materials and the $T_c$ ranges are given in table 1.1.

**Table 1.1.** $T_c$ range of different types of superconductors, where m=1 and 2 and n=1, 2, 3…..

| Notation | Stoicheometry | $T_c$ (K) | Class |
|---|---|---|---|
| Hg-BaCa-Cu-O | $Hg_mBa_2Ca_{n-1}Cu_nO2_{n+m+2}$ | 97-135 | Cuprate based |
| Bi-Sr-Ca-Cu-O | $Bi_mSr_2Ca_{n-1}Cu_nO_{2n+m+2}$ | 34-110 | Cuprate based |
| RE-Ba-Cu-O | $REBa_2Cu_3O_{7-x}$ | 89-96 | Cuprate based |
| RE-Fe-As (O,F) | $REFeAsO_{1-x}F_x$ | 26-55 | Iron based |
| Nb-Sn | $Nb_3Sn$ | 18 | Metallic |
| Nb-Ti | NbTi | 10 | Metallic |
| Nb | Nb | 9.2 | Elemental |
| Hg | Hg | 4.2 | Elemental |
| Ir | Ir | 0.11 | Elemental |

Among all the cuprate superconductors, REBCO has drawn more attention because of low flux creep and easy preparation. Even though the $T_c$'s are little less compared to other HTS cuprates, applications can be realized because $T_c$ of REBCO materials are well above 77 K, the boiling point of $LN_2$. Even though the properties of the LREBCO (where LRE= light rare earth elements such as Nd, Sm, Gd etc.,) materials are better than YBCO, the YBCO superconductors are found to be more interesting because of ease of preparation. YBCO can be prepared in air atmosphere, where as for preparation of LREBCO materials inert atmosphere need to be provided to reduce the formation of solid solutions that deteriorate superconducting properties.

## 1.2. Crystal Structure:

REBCO materials are ceramic in nature, the properties are sensitive to structure; they contain weakly coupled copper oxide ($CuO_2$ and $CuO$) planes. REBCO and most other high temperature cuprate superconductors contain a Group 2 metal (eg, Ca, Ba, Sr) and a heavy metal such as RE, Bi or Hg [19]. These cuprates have a perovskite unit cell in the form $ABO_3$, where oxygen atoms surround the B atoms in octahedral formation, as shown in fig. 1.4. The YBCO unit cell consists of three simple perovskite cubes vertically stacked with Y and Ba in the 'A' sites and Cu in the 'B' sites of an $ABO_3$ perovskite. However the copper is not surrounded by an octahedron of oxygen. Instead some copper sites have 5 oxygen neighbors in a square-pyramidal arrangement whilst others have 4 oxygen neighbors in a square formation [20].
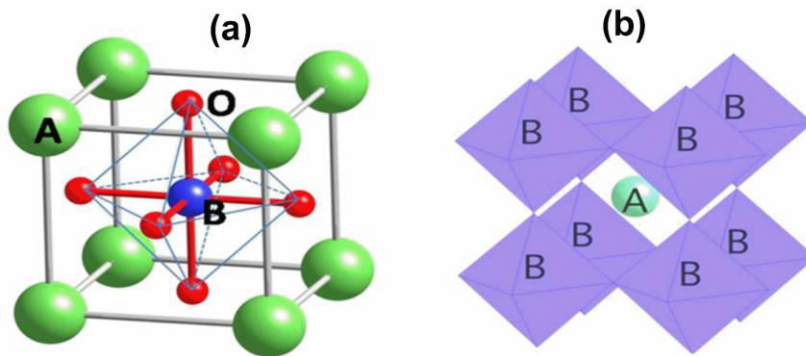


**Fig. 1.4.** The crystal structure of an $ABO_3$ perovskite type with the origin centered at (a) the B-site ion and (b) the A-site ion.

Parent compound of YBCO superconductor is $Y_3Cu^{3+}_3O_9$ (see fig. 1.5) which also contains perovskite units. Doping of Y by Ba leads to structural modification as well as reduction of $Cu^{3+}$ to $Cu^{2+}$ state. This in turn results in a reduction in the number of required oxygen ions and thus creates oxygen vacancies in the structure. This gives a transition temperature of ~ 92 K below which the compound has zero electrical resistance making it a superconductor [21].

$$Y_3Cu^{3+}_3O_9 \rightarrow YBa_2Cu^{3+}_3O_8 \rightarrow YBa_2Cu^{2+}_2Cu^{3+}O_{7-x}$$
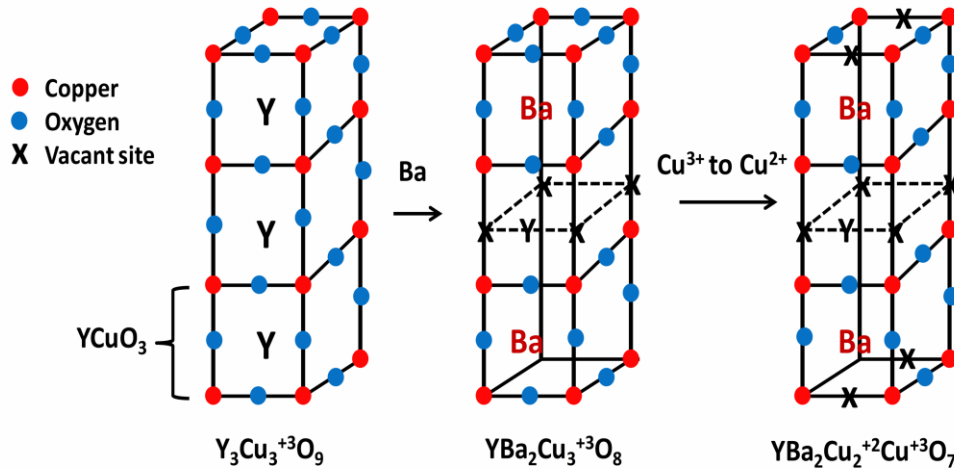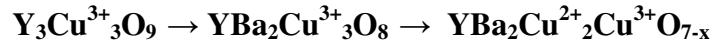


**Fig. 1.5.** Origin of the structure of $YBa_2Cu_3O_{7-x}$ from $Y_3Cu_3O_9$ as a triple-perovskite unit.

The crystal structure of all CuO based HTS consists of two dimensional copper oxide planes that are separated by other atoms like Sr, La, Y or Ba, and some additional oxygen atoms. The atoms in between the layers serve as dopants. For example doping Sr in $La_2CuO_4$ introduces charge carriers (holes) into the $CuO_2$ planes and thus the crystal acquires superconductivity.

The oxygen content in $YBa_2Cu_3O_{7-\delta}$ is extremely important in determining the superconducting properties. Heating the superconductor in oxygen gas can increase the oxygen content in the superconductor. Each oxygen forms an $O^{2-}$ ion by attracting two electrons, which are partly generated from the $CuO_2$ planes, creating vacancy holes in the structure. With increasing hole concentration, the anti-ferromagnetism of the structure decreases to zero and the crystal becomes electrically conductive and superconductivity begins. An optimum $T_c$ of 92 K is obtained for $\delta=0.08$, but $T_c$ falls rapidly if oxygen content is reduced in the structure, and for $\delta > 0.56$, $YBa_2Cu_3O_{7-\delta}$ is not superconducting. Also important

for the superconducting properties of YBCO is the existence of chains of Cu-O atoms, which have metal-like electrical properties and reduce the anisotropy of the superconductor.

Y-Ba-Cu-O system has different phases like $YBa_2Cu_3O_{7-\delta}$ (Y-123, YBCO), $YBa_2Cu_4O_8$ (Y-124), $Y_2Ba_4Cu_7O_{14}$ (Y-247) and $Y_2BaCuO_5$ (Y-211) [22]. Among these phases, Y-123, Y-124 and Y-247 are superconducting phases with $T_c$ ~92 K, ~80 K and ~40 K respectively. Recently $Y_3Ba_5Cu_8O_{18}$ (Y-358) material are reported to show superconductivity with highest $T_c$, among REBCO compounds, of 105 K [23-24].

## 1.3.  Growth of the REBCO superconductors:

Various processes have been employed for the fabrication of bulk high-temperature superconductors.

### 1.3.1.  Sintering:

Sintering is the process of forming a solid mass of material by heat without melting it to the point of liquefaction and is the commonly used technique in ceramic processing which has several advantages in synthesizing the products in desired shapes for various practical applications. In this process due to heat treating the material below its melting point allows the atoms to diffuse across the boundaries of the particles, fusing the particles together and creating one solid piece. For synthesis of REBCO all the precursor powders ($RE_2O_3$, $BaCO_3$ and CuO) are taken in stoicheometric ratios and the mixture is taken to a phase forming temperature below the melting point of material which allows the 123 phase to form. In this process by controlling the heat treatment one can control the microstructural properties such as size of the grains of the material. However, it

has been recognized that, although good $T_c$ values can be easily achieved, $J_c$ values are very small in bulk sintered oxide superconductors [25-27].
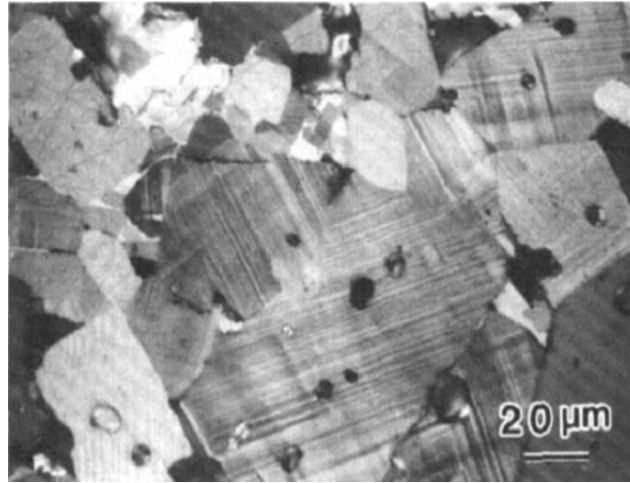


**Fig. 1.6.** SEM image of sintered YBCO [26].

The fig. 1.6 represents the optical micrograph of bulk sintered YBCO. It can be seen that there are many grain boundaries which are coupled with very weak links. Even though the $J_c$ inside each grain is very large, due to the grain boundaries or weak links presents in the samples, $J_c$ drops to zero and the resultant bulk $J_c$ of the material will be very small as compared to single grain $J_c$.

## 1.3.2. Melt Growth Process:

In order to increase the $J_c$, both the elimination of weak links and the introduction of effective pinning centres are necessary. To overcome this weak link problem in sintering process and to get the high $J_c$ through grain alignment in the REBCO materials the melt growth (MG) process is introduced by *Jin* et al,. [28]. MG process involves the heat treatment of the sample assembly to above the peritectic temperature $T_p$ of the RE-123, in this heat treatment the sample undergoes series of phase transformations which are reversible if sufficient time is given for the

system to come to equilibrium. RE-123 decomposes into RE-211 and liquid phases (BaO + CuO), which while cooling form again into RE-123 leaving some RE-211 in composites. In this process the Y-123 phase preform is heated to a temperature which is above the melting point of the Y-123 (1008 $^\circ$C) and cooled subsequently to recrystallize into Y-123 or YBCO composite. The schematic phase diagram for YBCO is shown in fig. 1.7.
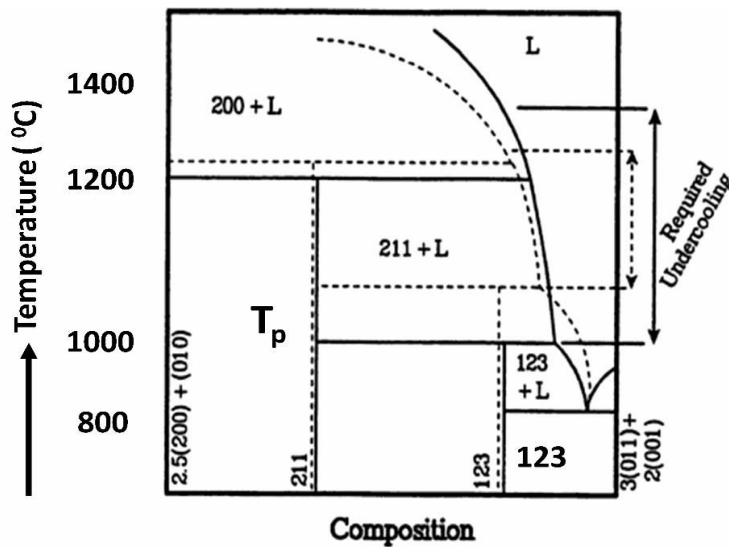


**Fig. 1.7.** Schematic phase diagram of the $YBa_2Cu_3O_{7-\delta}$ (solid lines) and for $NdBa_2Cu_3O_{7-\delta}$ (dashed lines); 123 = $REBa_2Cu_3O_{7-\delta}$; 211 = $RE_2BaCuO_5$; 200 = $RE_2O_3$; 010 = BaO; L= Liquid phases.

From this phase diagram, it is found that there are two kinds of peritectic reactions in this system. At high temperatures above 1200 $^\circ$C, $Y_2O_3$, plus liquid (L: a mixture of BaO and CuO) are stable. On cooling, these two phases react peritectically to produce YBCO [29]. The Y-211 particles are able to orient themselves randomly and evenly in the Y-123 liquid. The mixture is then cooled very slowly, forming a bulk Y-123 crystal with additional Y-211 impurities.

From the micrograph (shown in fig. 1.8) the formation of platelets (continuous) can be observed along with the non-superconducting 211 particles embedded in

123 matrix. Due to peritectic reaction with liquid phases, 211 phase particles become spherical. By melt texturing Y-123, using compact Y-211 absorbant blocks as support, *Salama* and *Sathyamurthy* [30] obtained higher critical current density (18 kAcm$^{-2}$) in spite of numerous remaining high-angle grain boundaries [31]. On the other hand, the large mono domain samples require the use of a low cooling rate, to maintain a stable planar growth front. In the case of Y-123, the maximum growth rate can be increased by decreasing the inter particle spacing between the Y-211 particles close to the solidification interface (through addition of excess Y-211 to the nominal composition, or addition of grain growth inhibitors).
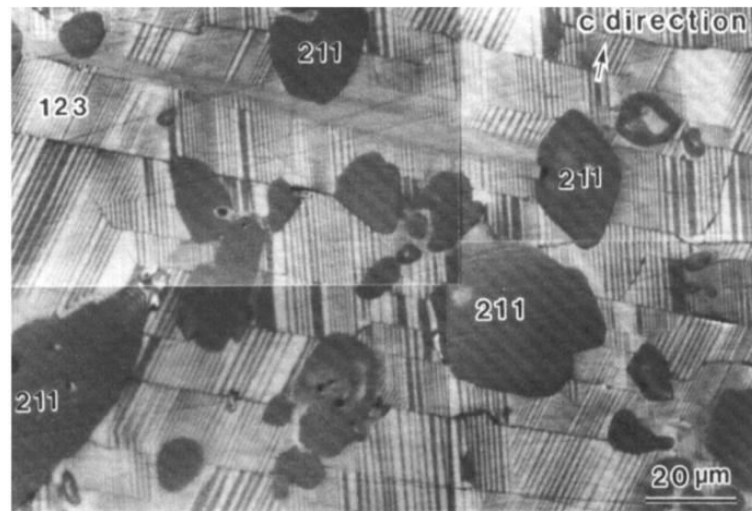


**Fig. 1.8.** SEM image of YBCO processed through MG process. The spherical shape Y-211 phase particles can be seen in Y-123 matrix [28].

Following these observations, a number of modifications to melt growing techniques have been brought about, for example the powder-melt-process (PMP) [32], solid-liquid-melt-growth (SLMG) [33], and melt-quenched pressurized partial-melt-growth (MQPPMG) [34]. Refinement of Y-211 particles and their homogeneous dispersion were the key factors for the improvement of flux pinning in bulk superconductors. To control these parameters, *Murakami et al*, developed

the melt-powder-melt-growth (MPMG) [35] and quench-melt-growth (QMG) [36] processes. These methods achieved fine dispersion of Y-211 particles, which led to improved flux pinning, resulting in large levitation forces between a permanent magnet and MPMG processed Y-123 bulk at liquid nitrogen temperature.

### 1.3.3. Infiltration Growth Process:

Even though the properties of REBCO processed through MG process is better than sintered products, some problems like shrinkage in final products due to liquid out flow and existence of resultant porosity limit the applications of the final products.

High current applications of HTSC superconductors require the synthesis of bulk ceramic materials with large size and different shapes possessing high critical current densities. In combination with the introduction of pinning centres, the numerous processing routes developed in order to increase the mono-domain size allow critical currents up to several hundreds of $kAcm^{-2}$ at 77 K [37] that are quite promising for some of the industrial applications. In MG process because of the chance of unreacted liquid phases to be left back in the matrix, it is not possible to study the effect of different types of dopants.

The infiltration and growth process has been proposed initially by *Chen et al.,* [38] and extensively developed by *Reddy et al*, [39-40] to be an alternative technique for single-domain synthesis that allows finer 211 particle distribution. This method yields obtaining high density RE-123 materials with refined 211-particles well dispersed in the final microstructures [41].
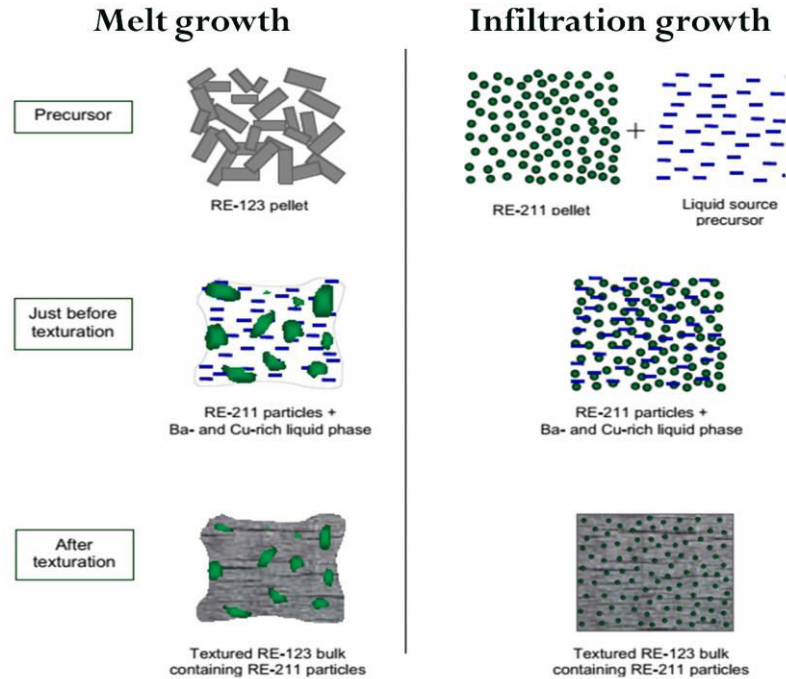
**Fig. 1.9.** A schematic sketch of microstructures comparing MG and IG Processed REBCO materials.

In contrast to the conventional melt-texturing process, this process starts with a Y-211 preform fabricated through any suitable methods for ceramic powder, such as uniaxial compaction, cold isostatic pressing, etc. This Y-211 preform is then provided with a barium-rich liquid phase from a liquid source such as Y-123 pellet. Upon heating these two, kept in contact, above peritectic temperature, barium-rich liquid phase formed in the liquid source specimen will infiltrate into the Y-211 preform and react to form Y-123. The liquid infiltration growth process possesses two advantages compared to the MG process: (1) near-net shape fabrication and (2) the refinement of Y-211 inclusions in the final Y-123 products [42]. *Cloots et al.* reviewed different techniques available for RE-123 bulk fabrication and discussed various parameters that affect the final microstructures in IG and MG processes.   Their comparison of microstructures in MG and IG processed REBCO [43] is displayed in fig. 1.9.

From the microstructures in this image one can observe the following:

(1) The liquid infiltration growth process has resulted in a significantly smaller particle size range for the Y-211.

(2) Y-211 particle distribution in liquid phase for the liquid infiltration growth process is quite uniform, compared to MG process. For this process, these Y-211 particles are preformed and their distribution is pre-determined. However, for the conventional melt-texturing process, the Y-211 particles are generated from the incongruent decomposition of Y-123; the nature of this decomposition is found to result in the large size distribution of Y-211.

(3) No obvious porosity or cavity could be observed in the liquid infiltration growth process. For the conventional melt-texturing process, a certain amount of pores (> 20%) always exist in the final product. This is mainly due to the loss of liquid phase during the process. Presences of these pores are detrimental to the applications based on the bulk transport and mechanical properties.

In the IG process, no liquid out flow occurs and Y-123 does not undergo decomposition, as it does in MG process, and hence the effect of dopants on the growth and properties of RE-123 can be studied effectively. Although IG process has evident advantages, it is necessary to optimize the processing parameters to fabricate high quality Y-123 bulk components of large size. For this, it is essential to understand the various factors that control the microstructural features and promote large critical currents homogeneously throughout the volume of the bulk RE-123.

## 1.4. Factors affecting flux pinning behavior:

The applied magnetic field in a material generates vortex lattice in a superconductor. The interaction of supercurrents with the magnetic field in the flux vortex, causes Lorentz force ($F_L = J \times B$) to be generated. This force drives the vortices down the flux density gradient, causing a flow of flux which creates a voltage. The resistance due to the flux motion is called flux flow resistance, and results in a non-zero resistance state (normal state) in the superconductor [44], destroying the superconductivity. Experimental results show that the magnetization of a Type II superconductor does not change significantly with time, which suggests that there is another force which balances this Lorentz force and prevents flux motion. This is known as the pinning force and is caused by defects or in-homogeneities in the crystal structure of the superconductor, which are called flux pinning centers. The flux lines adapt to the distribution of the defects in the crystal structure and are "pinned" by the defects in the superconductor. In other words, the flux lines can become distorted in order to travel through these pinning centers since it requires less energy to flow through normal regions than to weaken superconductivity in regions that are not normal. Since the introduction of pinning centers in the superconductor inhibits the motion of vortices, zero resistivity can be realized to higher fields in Type II superconductors with flux pinning capabilities [45-46].

It has been proposed that twin planes, stacking faults, oxygen deficient regions, dislocations, and non-superconducting inclusions such as RE-211 can act as pinning centers. It is believed that the fine Y-211 particles will increase the Y-123/Y-211 interfacial area and induce many micro-defects (or stacking faults) around Y-211 particles, which enhance the flux pinning ability and result in a higher $J_c$ value. So it is important to control the size of the initially Y-211 powders for optimizing the microstructures of final samples [47-50].

From theoretical aspects it is believed that the defects smaller than the twin boundary widths are required for the large flux pinning to very high fields [51-52]. It was suggested that the non-superconducting RE-211 particles or other related crystal defects such as dislocations and stacking faults responsible for the increment of $J_c$ might be effective only at low or intermediate fields. However, for achieving enhancement of $J_c$ in low and intermediate fields, improvement of fracture toughness, and reduction of cracks, it is necessary to refine the size of the RE-211 by optimizing the processing route.

## 1.5. Effect of Light Rare Earth doping in YBCO:

Even though the YBCO, commonly used for levitation at 77 K, has a $T_c$ of 91-93 K [53], the pinning performance rapidly drops at temperatures close to $T_c$ and therefore the pinning is insufficient for significant levitation at 90 K. In this aspect, the situation is even worse with BiSrCaCuO, TlBaCuO and other compounds which possess $T_c$ above 100 K, but exhibit rapid fall in $J_c$ much bellow $T_c$, because of flux creep problems [54-55]. These compounds cannot be used for levitation even with liquid nitrogen cooling, due to a low-lying irreversibility line. To date, only the LRE-123 (LRE = light rare earth elements Nd, Sm, Gd etc.,) composites exhibit a sufficiently good pinning performance up to 90 K. This has become possible by designing the inclusion of nanoparticles and nanostripes in these materials [55-56]. The current bulk HTS materials are thus characterized by their very complicated microstructures on the nanoscale.

The pinning provided by the non-superconducting particles of the RE-211 phase is mainly effective at low magnetic fields and high temperatures above 77 K. In this case, the interfaces between RE-123 and RE-211 play an important role in the flux pinning, rather than the RE-211 particles themselves, since their size is much

larger than the coherence length, which is of the order of a few nanometers [56-58].

Survey of literature shows that doping of several light rare earths (LRE) is possible on Y site without compromising on their $T_c$ values. LREs can also occupy Ba-site due to comparable ionic size thus forming solid solutions of $LRE_{1+x}Ba_{2-x}Cu_3O_{7-\delta}$ (called RE/Ba -ss type) with lower $T_c$ values. The presence of such low $T_c$ clusters due to the formation of solid solutions has been confirmed experimentally. *Murakami et al.* have proposed that nano-sized RE-rich clusters of low $T_c$ act as field-induced pinning centers, [59-60] and thus result in the peak effect in the mixed REBCO materials ($\Delta T_c$ pinning). *Hu et al.* have fabricated binary RE –based system such as (Nd, Sm)-Ba–Cu–O and reported that they show rise in $T_c$ and a high $J_c$ [61]. They reported that the higher solubility of Nd resulted in the compositional deviations in the RE-123 matrix at nanoscale and enhance flux pinning [62]. Recently, the mixing of RE elements in the precursor powder [e.g., (Nd, Eu, Gd)–Ba–Cu–O (NEGBCO)] materials has also been proven to be effective in enhancing $J_c$ [63]. Compositional annuli cores [64-65] with a distinct range of the rare earth chemical ratio were found in this material. It is proposed that these cores also affected the pinning properties at high fields and were also regarded as field induced pinning centers.

In literature, YBCO compounds in which ternary LRE elements (a mixture of light rare earth atoms) are added at the Y-site have been shown to exhibit the highest critical current densities among all 123-type superconductors [66-70]. The increase in $J_c$ is due to an additional degree of freedom providing an increased disorder on the Y-site. The compounds also exhibit substitution of the $LRE^{3+}$-ion on the $Y^{3+}$ and on $Ba^{2+}$ site [71] forming solid solutions. The solid solutions are regions where the LRE atoms have substituted for Ba within a unit cell, forming a LRE-rich phase $(LRE)_{1+x}Ba_{2-x}Cu_3O_y$ within   the $LRE-Ba_2Cu3O_y$ (LRE-123 or

LREBCO) matrix. The $(LRE)_{1+x}Ba_{2-x}Cu_3O_y$ phase features a lower $T_c$ than the pure LRE materials [72]. This leads to a spatial variation of the superconducting properties within the sample on the size of several unit cells; implying that nanoclusters are formed within the high-$T_c$ superconducting matrix. In turn, this spatial variations of nano-scale may be responsible for the extraordinary performance of the LREBCO superconductors concerning the increased values of the critical current density especially at elevated applied magnetic fields, as the coherence length ($\xi$) is of the order of 3–5 nm in the (a, b)-plane of LRE superconductors.

Formation of large fraction of solid solutions where LRE ion substitutes $Ba^{2+}$ degrades the superconducting properties [65-66]. Synthesis of LRE-123 compounds by oxygen-controlled melt-growth (OCMG) process suppresses LRE/Ba substitution largely and increases the $T_c$ values of these systems to 96 K, which is the high $T_c$ reported in the RE-123 systems. Solid solutions of (RE, RE')BCO type which show higher $T_c$ values are also reported to form in REBCO compounds. This process not only removed the negative influence of the LRE/Ba substitution on $T_c$, but the low concentration of the remaining LRE/Ba clusters gave rise to a compositional fluctuation [73-74], leading particularly to improvement of pinning at intermediate and high magnetic fields. One of the hypotheses is that compositional fluctuation causes a spatial distribution of $T_c$, which provides $\Delta T_c$ pinning [75-77]. This is observed as pronounced secondary peak in the M-H loops thus enhancing the irreversibility field [78-79]. Thus, one can propose two fundamental pinning mechanisms in bulk LRE-123: the pinning by normal-conducting inclusions operative at low fields; and $\Delta T_c$ pinning due to chemical fluctuations, improving flux pinning at intermediate and high fields.

Based on the above facts, several groups have tried to disperse fine RE-211 or LRE-211 particles in the RE-123 or LRE-123 matrix. As the reaction path in

LRE-123 is identical to that of Y-123, a similar processing technique was used successfully to disperse LRE-211 in the LRE-123 matrix [80-81]. The dispersion of LRE-211 enhanced the flux pinning in low fields but resulted in large particles of about 1–20 µm in diameter in melt grown samples. This caused the high field pinning to be reduced because the relatively large fraction of LRE-211 present in the matrix overshadowed the advantages of compositional fluctuation [82].

In literature, the studies on LRE-123 systems with two, three, and four LRE elements compounded on the LRE site is not well established [83-92]. It was also verified that low-field pinning can be enhanced when an appropriate concentration of fine RE-211 secondary phase particles is added. Studies on $(Nd_{0.33}, Eu_{0.33}, Gd_{0.33})Ba_2Cu_3O_y$ (NEG-123) showed that these materials are suited for high field applications, since it exhibits enhanced microscopic chemical fluctuation in the superconducting matrix and thereby strong pinning [93-95]. Such secondary phase particles also induce the formation of point-like defects (e.g. strains, stacking faults, etc.,) in their vicinity and, as a result, indirectly participate also on the pinning enhancement at intermediate and high fields. As reported recently, NSG-123 system (Eu replaced by Sm) also provides a good performance at liquid nitrogen temperature [96-97], in addition to uniform microstructure and reasonable flux pinning at high fields.

## 1.6. OCMG process:

Peritectic decomposition temperature ($T_p$) of the REBCO or LREBCO depends on the ionic radius of the RE elements. From this table it can be seen that as the ionic radius increases the $T_p$ of the RE increases. In literature it is also observed that mixing two or more RE leads to different $T_p$ depending on the average size of the RE elements. Also the $T_p$ depends on the atmospheric pressure employed for the fabrication of the REBCO/LREBCO superconductors. For instance in 1% $O_2$ – Ar

atmosphere $T_p$ for YBCO is 980 $^o$C, YSm-123 is 1010 $^o$C and 1040 $^o$C for NSG-123 [83, 98].

As mentioned above, the melt processing under low oxygen partial pressure significantly improves the $T_c$ of LRE-123 materials [99-100]. Moreover, it results in a systematic reduction of crystallization temperature that improves the controllability of matrix chemical fluctuations. This in turn results in the generation of an efficient network of nano-scale pinning centers. Each system would have an optimum pressure (pO$_2$) value under which the amount of remaining LRE/Ba clusters is so small that they cannot support the high pinning in the material. In the NEG-123 system, this value seems to be around 0.1% pO$_2$ as $J_c$ and $H_{irr}$ values of the samples melt-processed in 0.1% pO$_2$ are still higher than those of the samples processed in 1% pO$_2$ [30].

*Sakai* and *Murakami et al.*, [101] discussed the effect of atmosphere on formation of pores. Inert gas entrapment during melting also caused pore formation. The control of the composition, atmosphere and heating conditions was effective in reducing the amount of pores. The mechanisms of the gas release from the sample can be summarized to occur: (1) during the orthorhombic to tetragonal phase transition; (2) during the decomposition of the RE123 phase; (3) due to entrapment of the inert gas from the environment; (4) due to evolution of the vapors of the constituent elements. On the other hand, there are two possible mechanisms for the entrapped gas to escape from the sample. One is the diffusion in the solid state, and the other is the discharge of the gas bubbles moving through the liquid phase. They propose that a large amount of oxygen gas gets generated as a result of the orthorhombic to tetragonal phase transformation, however, it can be reduced in advance with simple pretreatment in Ar. Thus, prior to melt processing the precursors should be treated in oxygen-free atmosphere like Ar to remove oxygen to avoid the formation of pores. When the sample is melted in the

inert gas atmosphere at high temperatures, the gas will be trapped in the sample. In this case, the amount of pores increases with the increase in the partial pressure of the inert gas during the melt process. Since the inert gas cannot diffuse out of the sample, it remains inside as pores. Thus it is important to shorten the time for the melted sample exposed to the inert gas atmosphere at high temperatures. Consequently, the key to the fabrication of highly dense REBCO bulk superconductor is the prevention of the inert gas entrapment during melting and the employment of sluggish decomposition process.

## 1.7. Microstructure:

As discussed in earlier microstructure control of HTSC is the key parameter for successful industrial applications of these materials. In the LRE-123 system a large number of crystal defects are present in the 123 matrix that can act as effective pinning centers [102-105]. In addition to the crystal defects, finely dispersed non-superconducting 211 phase particles are known to be effective in enhancing flux pinning at low fields [106-110]. The smaller the size of these particles, the more effective flux pinning is on them. Therefore, the size control of 211 particles is very important in these materials. In this section we discuss the effects of secondary phase content, shape, 123/211 interface, chemical composition of final 211 particles on the mixed REBCO superconducting properties.

The microstructure and compositions of the different phases present in the LREBCO samples were established in literature [111-112]. In fig. 1.10, the TEM microstructure of NSE-123 with 10 and 30 mol% of Gd-211 additions was displayed in (a) and (b) respectively. Two different types of 211 particles were found in LREBCO. TEM-EDX analyses clarified that the large particles consisted of Nd, Sm and Gd on the RE site in different ratios.
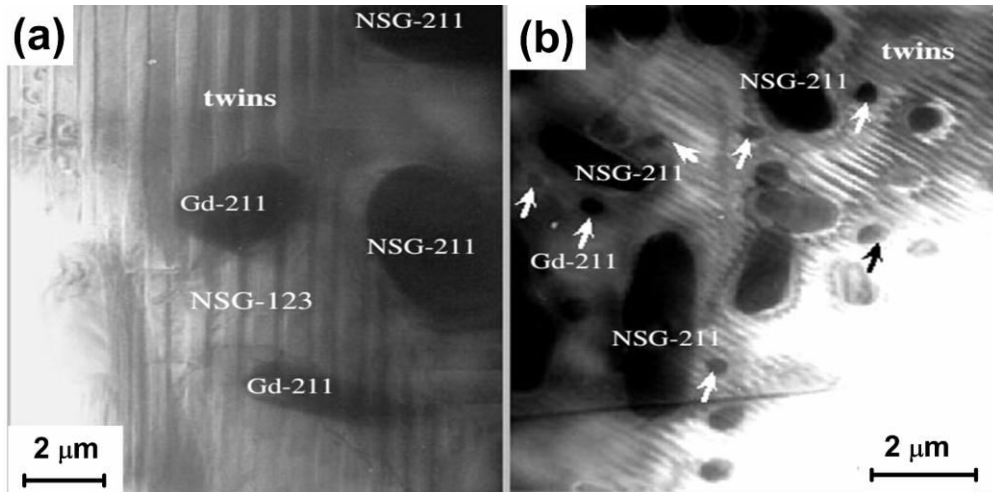
**Fig. 1.10.** TEM image of MG processed NSGBCO samples with the addition of (a) 10 mol % Gd-211 and (b) 30 mol % of Gd-211.

Earlier studies [113-118] on the NEG-123, NSG-123 systems reported a similar effect and suggested that in the partially melted regime there are two kinds of LRE-211 inclusions: one intentionally added as an initial powder and another one produced by the peritectic decomposition of LRE-123.

The surface pinning by the 123/211 interface provides effective flux pinning when the interface is sharp [119]. High resolution TEM images clearly showed clean interfaces between the NSG-123 and Gd-211 without any impurity phase as shown in fig. 1.11. At such a sharp interface, the order parameter rapidly varies over the distance of the coherence length, which gives to a large flux-pinning force. On the other hand, potential nanometric strains around these particles might contribute to high-field pinning [120-121].

The systematic study has been done by doping different RE-211 (Gd-211 and Eu-211) phase particles in NEG-123 show that chemical fluctuations found in different regions which are confirmed through EDS study. However, the chemical ratio started to fluctuate and deviate from 1:1:1 when the amount of Eu-211

exceeded 20 mol%. In the sample with 30 mol% Gd-211 the chemical ratio in the NEG-123 matrix was nearly Nd:Eu:Gd= 1:1:2. EDS analyses proved that the excessive Gd and Eu atoms in the NEG-123 matrix diffused during the peritectic reaction from the Gd-211 and Eu-211 particles to the rare earth sites of the RE-123 matrix. Together with the present results we can conclude that a significant excess of some LRE elements in the NSG matrix deteriorates superconducting properties at high fields and leads to a reduction of the irreversibility field [122-123].
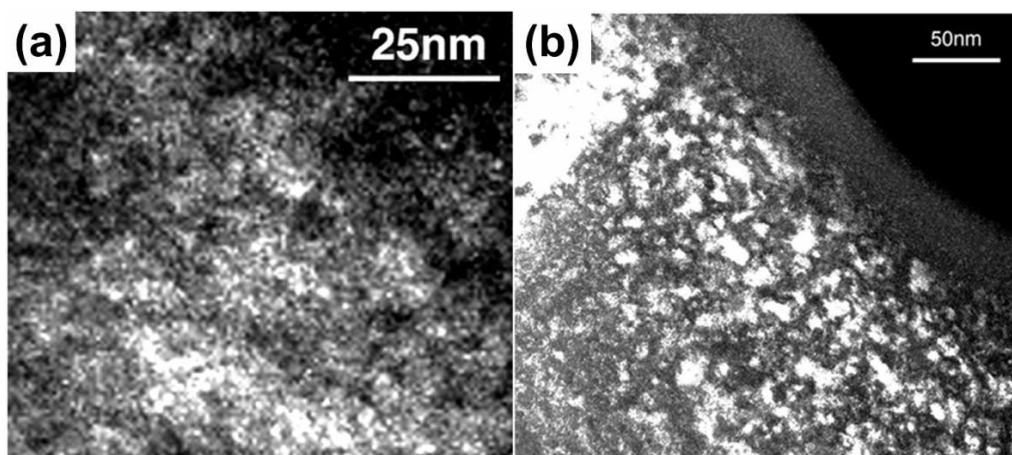


**Fig. 1.11.** TEM dark-field images of NSEBCO superconductors with the addition of 10 and 30 mol% of Gd-211. The white and block contrast in the micrograph reflecting the compositional fluctuations occurred due to RE/Ba substitution.

To date, studies on secondary and ternary light rare earth HTSC compounds is carried out in different systems like (Y, Nd)BCO, (Y, Sm)BCO, NEGBCO, YSNBCO, SEGBCO etc., all prepared by melt growth process. As per our knowledge there are no reports on detailed microstructural work on mixed REBCO samples fabricated using IG process. IG process is an efficient way to study the effects of doping different elements in REBCO compounds on the microstructural and superconducting properties. For this we have carried out extensive microstructural characterizations on compounds of YBCO with LRE

doping and by changing different processing conditions. All these composites were synthesized using POIG process which is developed recently in our group and which was shown to result in along with highly homogeneous distribution of Y-211 phase particle in final products and enhanced $J_c$ up to high fields.

## 1.8. Organization of the thesis:

The present thesis is organized into seven chapters. The contents of the chapters are as follows.

**Chapter I** provides a brief introduction to high temperature superconductors in general and reviews the literature on synthesis and properties of large grained REBCO superconductors. Variations of melt growth processing and Infiltration growth processing methods developed to reduce grain boundaries and create flux pinning centers to enhance the current densities are discussed. Present status of the area and the challenges yet to be resolved are narrated. This chapter also defines the objectives of the present work.

**Chapter II** discusses the experimental techniques used in the present work. Preparation of Y-123 superconductors into which RE elements Sm and NSG are doped for Y using POIG process is discussed. Samples are characterized with regard to their structure, microstructure, and composition of various phases present and their magnetic properties. The ACMS (Alternating Current Measurement System) setup available with Physical Property Measurement System (PPMS-6000, Quantum design make) is used for the initial characterization. Microstructures of metallographically polished samples are studied under a Field Emission Scanning Electron Microscopy (FESEM, ZEISS make, Ultra 55 model) and compositional analysis was done through Energy dispersive Spectroscopy attachment. The X-ray diffraction (XRD) study includes phase identification and lattice parameter calculation. In the present study XRD

patterns of samples were taken using a Cu $K_\alpha$ ($\lambda$ = 1.5405 Å) as the X-ray source; Bruker's AXS Model D8 Advance System and X-ray diffractometer with Co $K_\alpha$ ($\lambda$ = 1.7902 Å) source INEL Model CPS 120 model. Rietveld refinement of unit cell dimensions and contents is carried out using Fullprof program. Magnetic properties of the materials at several temperatures, up to 9 T, are studied using a Vibrating Sample Magnetometer attached to the PPMS.

The next part of the thesis is **Chapter III** that discusses the initial optimization of the infiltration temperature which is shown to have a profound effect on the final microstructure. Quenched studies carried out to study the evolution of grain growth through peritectic temperature are also discussed. The mechanical properties of the processed materials show correlation with hardness and the field dependence of current density, both of which appear to be affected similarly by a network of nanometric defects present in the YBCO composites.

**Chapter IV** discusses introduction of substantial amounts of nanometer-sized particles of $Sm_2O_3$ as a second phase into YBCO being synthesized by POIGP. $Sm_2O_3$ nanoparticles are introduced into the Y-211 preform before POIG processing in two different ways viz. one through formation of a $Sm_2O_3$ gel and the other by chemical substitution of Sm for Y at unit cell level. The first part of the chapter describes a gel and sol-based method to introduce 10, 20 and 30 wt% of $Sm_2O_3$ nanoparticles into Y-211 preform *individually and without agglomeration* using a Nano-dispersive sol-casting method reported elsewhere [124]. These samples are referred to as YSm-10, YSm-20 and YSm-30 respectively. FESEM images demonstrate the successful introduction of individual $Sm_2O_3$ nanoparticles on the Y-211 particle surfaces, without agglomeration even at the high concentrations involved. The $J_c(H)$ curves of the IG processed YSm-samples show that YSm-20 offers the best performance.

The effects of introducing $Sm_2O_3$ nanoparticles on the final microstructure of the POIG-processed (Y, Sm)BCO samples are not always salutary. The particles are demonstrated to promote reaction and sintering between Y-211 grains in the perform before infiltration, which can give rise to porosity in the final samples due to improper infiltration of the liquid phases in extreme cases. The grain coarsening of the Y-211 due to sintering gets carried over to the final microstructure; the resulting Y-211 size is in the range 2-5 microns, unlike in POIG-processed pure Y-123 (i.e. Y-123 without $Sm_2O_3$ addition), which is mostly below one micron. POIG processing of pure YBCO without any dopants is also carried out in Ar atmosphere for comparison.

The second part of this chapter discusses POIG processing of ($Y_{1.6}$, $Sm_{0.4}$)$Ba_2Cu_3O_y$, called YSm20-C. Atomic level mixing of Y and Sm was expected in this case, and thus the problems associated with the sintering of Y-211 particles and the resultant blocking of liquid phase movement into perform, was expected to be eliminated. But, the microstructure and $J_c(H)$ performance of this sample are found to be far inferior to YSm-20 synthesized by NDSC method discussed above. The effect of doping 0.1% nano- sized $Nb_2O_5$ to YSm-20 was also studied.

In **Chapter V**, we discuss the work done on the effect of introducing 20 wt. % of NSG-211, which is a mixture of three REs, viz. Nd, Sm, and Gd, into Y-211. Compounding of three REs (Nd, Sm and Gd) in YBCO was chosen to increase the lattice mismatch effects further as compared to singly-doped RE-211 studied in Chapter IV. This sample is referred to as YNSG. The $J_c$ values are found to be indeed higher than for YSm- series. $J_c$ curves as a function of H remained flat up to very high magnetic fields, for instance $J_c > 1$ kAcm$^{-2}$ up to nearly 7 T.

**Chapter VI** discusses the salient features observed in the microstructures and magnetic properties of various samples studied in the earlier chapters. Detailed EDS studies showed that in the microstructures of the YSm- series and YNSG superconductors, where dopants are added externally, bright Y-rich regions are seen within the YSm-211 particles. On the contrary, in YSm20-C, where Sm is chemically substituted for Y, bright regions are found smeared throughout the YSm-211 particles. Probable mechanism is proposed.

Another important feature observed in the microstructures of the Ar-processed samples is the undesirable uniform presence of abundant spherical porosity in the microstructures. The geometry of the pores suggests association with the evolution of gases at the texturing stage of the IG process. The presence of such porosity in the microstructure must have a major impediment to achieving high $J_c$, especially to high fields, and could have affected the reproducibility of results at various centers of research on $RE_m$-123 samples. This is because such samples necessarily had to be processed in inert atmosphere to prevent solid solution forming.

Murakami's group had discussed the possibility of evolution of either oxygen or entrapped argon during cooling through the peritectic temperature to be the reason for spherical porosity [101]. Choosing YNSG that showed the best current density to high fields as a model system, some experiments with modified heat-treatments are carried out to assess the effect of gases on the nature and extent of porosity in the processed samples. A detailed analysis of various microstructures that resulted from different processing conditions is presented in this chapter.

Magnetic measurements carried out using PPMS have provided the field dependence of current density that is used to assess the superconductor performance for various applications. Our results show that doping 20 wt. % Sm

for Y (YSm-20 sample) shows better flux pinning properties than YBCO; YNSG with mixed rare earth element doping exhibits the highest $J_c(0)$ of nearly 21.5 kA/cm$^2$ at 77 K. This demonstrates the effective pinning due to lattice mismatch defects that are on nano-scale. $J_c(H)$ curves also remain reasonably flat to high fields. Earlier reports of $J_c(0)$ of 18 kA/cm$^2$ that remained flat to high fields, observed in YBCO processed by POIGP in air (YBCO-Air), were due to the presence of defects in wide size range originating from twinning [125]. It is interesting to note that the present samples YSm-20 and YNSG show flat $J_c(H)$ performance in spite of considerable porosity and absence of twinning and this can be attributed to lattice mismatch defects contributing to flux pinning at high fields. Further work on process modifications that can minimize porosity in the samples is also discussed. Correlation of $J_c(H)$ curves obtained in different samples with their microstructures, and discussion on the factors that contribute to flux pinning at different field regimes is presented.

In summary, the present work is aimed at a systematic study of the microstructures and $J_c(H)$ in Y-123 samples when Yttrium is replaced by other rare earths. Introduction of RE for Y was done by different methods into Y-211 preform which was subjected to Preform Optimized Infiltration Growth processing. This process enables incorporation of nano-dopants into 211 preform. Detailed characterization of various samples, viz. crystal structures using XRD, microstructures using FESEM and magnetic properties using PPMS was carried out. A summary of the results and the conclusions drawn are presented in **Chapter VII**.

# References:

1. http://www.superconductors.org/Uses.htm

2. H. Kamerlingh Onnes, research notebooks 56-57, Kamerlingh Onnes Archive, Boerhaave Museum, Leiden, the Netherlands, H Kamerlingh Onnes, Leiden Comm. 120b 122b, 124c, (1911).

3. http://en.wikipedia.org/wiki/Heike_Kamerlingh_Onnes

4. W. Buckel, R. Kleiner, Supraleitung – Grundlagen and Anwendungen, WILEY-VCH Verlag, Weinheim (2013).

5. W. Buckel, R. Kleiner, Superconductivity - Fundamentals and Applications, WILEY-VCH Verlag, Weinheim (2004).

6. T. H. Geballe, Science **293** (2001) 22.

7. E.A. Ekimov, V.A. Sidorov, E.D. Bauer, N.N. Mel'nik, N.J. Curro, J.D. Thompson and S.M. Stishov, Nature **428** (2004) 542.

8. C. Buzea and T. Yamashita, Supercond. Sci. Techn. **14** (2001) R115.

9. W. Meissner and R. Ochsenfeld, Naturwissenschaften **21** (1933) 787.

10. J. Bednorz and K.A. Muller, Z. Phys. B: Cond. Matter. **64** (1986) 189.

11. M.K. Wu, J.R. Ashburn, C.J. Torng, P.H. Hor, R.L. Meng, L. Gao, Z.J. Huang, Y.Q. Wang and C. W. Chu, Phys Rev Lett **58** (1987) 908–910.

12. H. Maeda, Y. Tanaka, M. Fukutomi and T. Asano, Jpn J Appl Phys **27** (1988) L209–L210.

13. Z.Z. Sheng and A.M. Hermann, Nature **332** (1988) 55–58.

14. C.W. Chu, L. Gao, F. Chen, Z.J. Huang, R.L. Meng & Y.Y. Xue, Nature **365** (1993) 323 – 325.

15. Mourachkine, Andrei. Room-temperature superconductivity. (Cambridge, UK: Cambridge International Science Pub., (2004). p. 5–7.

16. J.B. Ketterson and S.N. Song, Superconductivity. (Cambridge: Cambridge University Press, 1999)

17. Sheahen, P. Thomas, Introduction to high-temperature superconductivity. (New

    York: Kluwer Academic, 2002.) p. 21–22. To Review on Superconducting Materials, Roland Hott, Reinhold Kleiner, Thomas Wolf & Gertrud Zwicknagl, to be published in "Handbook of Applied Superconductivity", Wiley-VCH.

18. Ernst Helmot Brandt, Physica C **369** (2002) 10-20.

19. Buckel, Werner, and Reinhold Kleiner. Superconductivity: fundamentals and applications. 2nd rev. and enl. ed. (Weinheim: Wiley-VCH 2004). p. 351–443.

20. http://nptel.ac.in/courses/113104005/lecture4/4_5.htm

21. D.M. Smyth, PP.1-10 in ceramic superconductors II. Research Update 1988, M.F.Yan, Ed. The American Ceramic Society, (1988).

22. A. Baranauskas, D. Jasaitis, A. Kareiva, R. Haberkorn and H.P. Beck, J. Euro. Ceram. Soc. **21** (2001) 399.

23. S. Gholipour, V. Daadmehr, A.T. Rezakhani, H. Khosroabadi, F. Shahbaz Tehrani and R. Hosseini Akbarnejad, J. Supercond. Nov. Magn. **25** (2012) 2253–2258.

24. A. Aliabadi, Y. Akhavan-Farshchi and M. Akhavan, Physica C **249** (2009) 2012.

25. M. Murakami, Supercond. Sci. Technol. **5** (1992) 185–203.

26. D.C. Larbalestier, S.E. Babcock, X. Cai, M. Daeumling, D.P. Hampshire, T.F. Kelly, L.A. Lavanier, P.J. Lee and J. Seuntjens, Physica C **153-155** (1988) 1580.

27. F. Stucki, P. Brüesch, T. Baumann, Physica C **153-155** (1988) 200.

28. S. Jin, T.H. Tiefel, R.C. Sherwood, R.B. van Dover, M.E. Davis, G.W. Kammlott and R.A. Fastnacht, Phys. Rev. B **37** (1988) 13.

29. M. Murakami, M. Morita, K. Doi, K. Mivamoto and H.L. Hamada, Japan. J. Appl. Phys. **28** (1989) L399.

30. K. Salama and S. Sathyamurthy, Supercond. Sci.Technol. **11** (1988) 954.

31. M.K. Mironova, G.Du, I.A. Rusakocva and K. Salama, Physica C **271** (1996) 15.

32. L. Zhou, P. Zhang, P. Ji, K. Wang, J. Wang and X. Wu, Supercond. Sci. Technol. **34** (1990) 90.

33. D. Shi, S. Sengupta, J.S. Lou, C. Varanasi and P.J. Mc Ginn, Physica C **213** (1993) 179.

34. S. Hu, H. Hojiaji, A. Barkatt, M. Boroomand, M. Hung, A.C. Buechele, A.N. Thorpe and D. Davis, HTS Material, Bulk Processing and Bulk Applications ed C W Chuet al (Singapore: World Scientific) (1992) p 313.

35. M. Murakami, Mod. Phys. Lett. B **41** (1990) 63.

36. M. Murakami, S. Gotoh, H. Fujinoto, K. Yamaguchi, N. Koshizuka and S. Tanaka, Supercond. Sci. Technol. **4** (1991) S49.

37. M. Muralidhar, N. Sakai, M. Jirsa, M. Murakami and I. Hirabayashi, App. Phys. Lett. **92** (2008) 162512.

38. Y.L. Chen, H.M. Chan, M.P. Harmer, V.R. Todt, S. Sengupta and D. Shi Physica C **234** (1994) 232–6.

39. E.S. Reddy and T. Rajasekharan, J. Mater. Res. **130** (1998) 2472

40. E.S. Reddy and T. Rajasekharan, Supercond. Sci. Technol. **11** (1998) 523

41. E.S. Reddy and T. Rajasekharan, Physica C **316** (1999) 279.

42. H. Fang, Y.X Zhou, K. Ravi-Chandar and K. Salama, Supercond. Sci. Technol. **17** (2004) 269–273.

43. R. Cloots, T. Kutzarova, J.P. Mathieu and Ausloos, Supercond. Sci. Technol **18** (2005) R9.

44. A.M. Campbell and J.E. Evetts, Adv. Phys. **21** (1972) 199.

45. M. MurakamI, Melt Processed High temperature Superconductors (World Scientific, Singapore) (1992)

46. T. Matsushita Flux Pinning in Superconductors (Springer-Verlag Berlin Heidelberg) (2007)

47. L. Zhou, S.K. Chen, K.G. Wang, X.Z. Wu, P.X. Zhang and Y. Feng, Physica C **363** (2001) 99−106.

48. M. Murakami, S. Gotoh, H. Fujimoto, K. Yamaguchi, N. Koshizuka, S. Tanaka, Supercond. Sci. Technol. **4** (1999) S93.

49. S.K. Chen, L. Zhou, K.G. Wang, X.Z. Wu, P.X. Zhang, Y. Feng, Physica C **377** (2002) 571.

50. B.H. Jun, S.A. Jung, S.D. Park, B.J. Park, Y.H. Han, C.J. Kim, Physica C **471** (2011) 876–879.

51. M. Nakamura, T. Hirayama, Y. Yamada, Y. Ikuhara and Y. Shiohara, Jpn. J. Appl. Phys. **35** (1996) 3882.

52. G. Krabbes, G. Fuchs and W.F. Canders, High Temperature Superconductor Bulk Materials: Fundamentals    Processing    Properties Control Application Aspects  (Wiley, GmbH, KGaA, Weinheim)  (2005).

53. S. Jin, A. Fastnacht, T.H. Tiefel, R.C. Sherwood, Phys. Rev. B **37** (1988) 5828-5830.

54. Z.Z. Sheng and A.M. Hermann, Nature **332** (1988) 138-139.

55. H. Maeda, Y. Tanaka, M. Fukufomi and Asano, Jpn. J. Appl. Phys. **27** (1988) L209-L210.

56. M. Muralidhar, N. Sakai, N. Chikumoto, M. Jirsa, T. Machi, Y. Wu and M. Murakami, Phys. Rev. Lett. **89** (2002) 237001.

57. M. Muralidhar, Y. Wu, N. Sakai, M. Murakami, M. Jirsa, T. Nishizaki and N. Kobayashi, Supercond. Sci. Technol. **15** (2002) 1357-1363.

58. M.R. Koblischka, M. Winter, P. Das, A. Koblischka-Veneva, M. Muralidhar, T. Wolf, N. Hari Babu, S. Turner, G. van Tendeloo and U. Hartmann, Physica C **469** (2009) 168–176.

59. M. Murakami, S.I Yoo, Takamitsu Higuchi, Naomichi Sakai, Jurgen Weltz, Naoki Koshizuka and S. Tanaka Jpn. J. Appl. Phys. **33** (1994) L715-L717.

60. Shih-Yun Chen, Yung-Sheng Hsiao, Chi-Liang Chen,Der-Chung Yan, In-Gann Chen and Maw-KuenWu, Mater. Sci. Eng. B **151** (2008) 31–35

61. C. Varanasi, P.J. M.C Ginn, H.A. Blackstead, D.B. Pulling, J. Electronic mater. **24** (1995) 12.

62. Shih-Yun Chen, In-Gann Chen, Yang-Chung Liao and Maw-Kuen Wu, J. Mater. Res. **20** (2005) 2.

63. M. Muralidharan and M. Murakami, Supercond. Sci. Technol. **13** (2000) 1315-1321.

64. T. Saitoh , K. Segawa, K. Kamada , N. Sakai , T. Segawa , S.I. Yoo , M. Murakami, Supercond. Sci. Technol. **22** (2009) 075012; Physica C **288** (1997) 141–147.

65. M. Oda, X. Yao, Y. Yoshida and H. Ikuta, Supercond. Sci. Technol. **22** (2009) 075012

66. M. Muralidhar, M.R. Koblischka, T. Saitoh and M. Murakami, Supercond. Sci.Technol. **11** (1998) 1349.

67. M.R. Koblischka, M. Muralidhar and M. Murakami, Appl. Phys. Lett. **73** (1998) 2351.

68. S.Y. Chen, A. Gloter, C. Colliex, J.G. Chen and M.K. Wu, IEEE Trans. Appl. Supercond. **17** (2007) 2957.

69. D.A. Cardwell and N. Hari Babu, Physica C **445** (2006) 1.

70. S. Awaji, N. Isono, K. Watanabe, M. Muralidhar, M. Murakami, N. Koshizuka and K. Noto, Supercond. Sci. Technol. **17** (2004) S6.

71.   R.W. McCallum, M.J. Kramer, K.W. Dennis, M. Park, H. Wu and R. Hofer, J. Electronic Mater. **24** (1995) 1931.

72.   H. Wu, K.W. Dennis, M.J. Kramer, R.W. McCallum, Appl. Supercond. **6** (1998) 87.

73.   T. Egi, J.G. Wen, K. Kuroda, H.Unoki and N. Koshizuka, Appl. Phys. Lett. **6** (1995) 72406.

74.   N. Chikumoto, J. Yoshioka and M. Murakami, Physica C **291** (1997) 79.

75.   G. Blatter, M.V. Feigelman, V.B. Geshkenbein, A.I. Larkin and V.M. Vinokur, Rev. Mod. Phys. **66** (1994) 1125.

76.   D. Dew-Hughes, Philos. Mag. **30** (1974) 293.

77.   A.M. Campbell and J.E. Evetts, Adv. Phys. **21** (1972) 199.

78.   M. Jirsa, M.R. Koblischka, T. Higuchi, M. Muralidhar and M. Murakami M Physica C **338** (2000) 235.

79.   A.J.J. Van Dalen, M.R. Koblischka, K. Sawada, H. Kojo, T. Higuchi and M. Murakami, Supercond. Sci. Technol. **9** (1996) 659.

80.   G.W. Kammlott, T.H. Tiefel and S. Jin, Appl. Phys. Lett. **56** (1990) 2459.

81.   N. Sakai, S.I. Yoo and M. Murakami, J. Mater. Res. **10** (1995) 1611.

82.   J.C.L. Chow, H.T. Leung, W. Lo and D.A. Cardwell, Supercond. Sci. Technol. **11** (1998) 369.

83.   T. Saitoh, K. Segawa, K. Kamada, N. Sakai, T. Segawa, S.I. Yao and M. Murakami, Physica C **288** (1997) 141.

84.   K. Iida, M. Muralidhar and M. Murakami, Supercond. Sci. Technol. **13** (2000) 683.

85.   S. Nariki, S.J. Seo, N. Sakai and M. Murakami, Supercond. Sci. Technol. **13** (2000) 778.

86.   M. Muralidhar, M.R. Koblischka, T. Saitoh and M. Murakami, Supercond. Sci. Technol. **11** (1998) 1349.

87. M.R. Koblischka, M. Muralidhar and M. Murakami, Appl. Phys. Lett. **73** (1998) 2351.

88. M. Muralidhar, M. Murakami, K. Segawa, K. Kamada and T. Saitho, (2000) United States Patent, Patent Number 6063 753

89. M. Muralidhar, M.R. Koblischka, P. Diko and M. Murakami, Appl. Phys. Lett.**76** (2000) 91.

90. A.K. Pradhan, M. Muralidha, M.R. Koblischka, M. Murakami, K. Nakao and N. Koshizuka, Appl. Phys. Lett. **75** (1999) 253.

91. A. Das, S. Koshikawa, T. Fukuzaki, M. Muralidhar and M. Murakami, Appl. Supercond. **6** (1998) 183.

92. A. Hu, N. Sakai and M. Murakami, Appl. Phys. Lett. **78** (2001) 2539.

93. M. Jirsa, M. Muralidhar and M. Murakami, Physica C **357–360** (2001) 489.

94. M. Muralidhar, M. Jirsa, K. Iida and M. Murakami, Physica C **357–360** (2001) 661.

95. M. Muralidhar, M. Jirsa, S. Nariki and M. Murakami, Supercond. Sci. Technol. **14** (2001) 832.

96. M. Muralidhar, S. Nariki, M. Jirsa, Y. Hu and M. Murakami, Appl. Phys. Lett. **80** (2002) 1016.

97. M. Muralidhar, S. Nariki, M. Jirsa and M. Murakami, Physica C **378–381** (2002) 746.

98. M. Muralidhar, H.S. Chauhan, T. Saitoh, K. Kamada, K. Segawa and M. Murakami, Supercond. Sci. Tec. **10** (1997) 663.

99. M. Murakami, N. Sakai, T. Higuchi and S.I. Yoo, Supercond. Sci. Technol. **9** (1996) 1015.

100. H. Wu, K.W. Dennis, M.J. Kramer and R.W. McCallum, Appl. Supercond. **6** (1998) 87.

101. N. Sakai, D. Ishihara, K. Inoue and M. Murakami, Supercond. Sci. Technol. **15** (2002) 698–701.

102. P.H. Kes, A. Pruymboom, J. van der Berg and J.A. Mydosh, Cryogencis **29** (1989) 228.

103. K. Yamaguchi, M. Murakami, H. Fujimoto, S. Gotoh, Y. Shiohara, N. Koshizuka and S. Tanaka, J. Mater. Res. **6** (1991) 1404

104. V. Selvamanickam, M. Mironova, S. Son and K. Salama, Physica C **208** (1993) 238.

105. M. Daumling, J.M. Seuntjens and D.C. Larbalestier, Nature **346** (1990) 332.

106. M. Murakami, S. Gotoh, H. Fujimoto, K. Yamaguchi, N. Koshizuka and S. Tanaka, Supercond. Sci. Technol. **4** (1991) S43.

107. M. Chopra, S.W. Chan, R.L. Meng and C.W. Chu, J. Mater. Res. **11** (1996) 1616.

108. M. Muralidhar, M.R. Koblischka and M. Murakami, Phys. Status Solidi (a) **171** (1999) R7.

109. Delamare, I. Monot, J. Wang, J. Provost and Desgardin, Supercond. Sci. Technol.**11** (1996) 534.

110. N. Vilalta, F. Sandiumenge, S. Pinol and X. Obradors, Supercond. Sci. Technol. **12** (1997) 38.

111. A.M. Campbell, J.E. Evetts and D. Dew-Hughes, Philos. Mag. **30** (1968) 293

112. M. Murakami, K. Yamagauchi, H. Fujimoto, N. Nakamura, T. Taguchi, N. Koshijuka and S. Tanaka, Cryogenics **32** (1992) 930.

113. M. Muralidhar, M.R. Koblischka and M. Murakami, J. Appl. Phys. **7** (1999) 99.

114. M. Murakami, N. Sakai, T. Higuchi and S.I. Yoo, Supercond. Sci. Technol. **9** (1996) 1015.

115. E. Sudhakar Reddy and T. Rajasekharan, Supercond. Sci. Technol. **11** (1998) 523.

116. S. Nariki, N. Sakai and M. Murakai, Physica C **357–360** (2001) 629.

117. M. Muralidhar, S. Nariki, M. Jirsa, Y. Hu and M. Murakami, Appl. Phys. Lett. **80** (2002) 1016.

118. M. Muralidhar, M. Jirsa, Y. Wu and M. Murakami, Physica C **378–381** (2002) 742.

119. M. Muralidhar, M.R. Koblischka and M. Murakami, Phys. Status Solidi (a) **171** (1999) R7.

120. M. Murakami, Melt Processed High-Temperature Superconductors (Singapore: World Scientific) 1992.

121. V. Zablotskii, M. Jirsa and P. Petrenko, Phys. Rev.B **65** (2002) 2245081.

122. M. Muralidhar and M. Murakami, Supercond. Sci. Technol. **13** (2000) 1587.

123. M. Muralidhar and M. Murakami, Physica C **309** (1998) 39.

124. P.M. Swarup Raju, Ph.D. Thesis (2012) "Infiltration growth processing of YBCO nano-composites: Shape forming, microstructural and magnetic studies".

125. N. Devendra Kumar, T. Rajasekharan, Ravi C. Gundakaram and Vummethala Seshubai, IEEE Transactions on Applied Superconductivity **21** (2011) 6.

# Chapter II

# Experimental methods

Objective of this work was to enhance flux pinning and identify the factors that control it at high fields in infiltration and growth (IG) processed $(Y, RE)Ba_2Cu_3O_{7-\delta}$ (RE = rare earth elements) bulk superconductors, in which Sm and mixed RE elements are substituted in place of Y. Various experimental methods are used to synthesize the samples chosen for study and investigate their structural, microstructural and magnetic properties. Among them, structural characterization was carried out for all synthesized samples by recording X-ray Diffraction (XRD) patterns and Rietveld refinement is done to evaluate the lattice parameters and volume of the unit cell. Microstructural and compositional investigations were carried out employing the Field Emission Scanning Electron Microscopy (FESEM) and Energy Dispersive Spectroscopy (EDS). Physical Property Measurement System (PPMS) with Vibrating sample magnetometer (VSM) facility is employed for measuring the magnetic moment as a function of magnetic field for the determination of critical current density of superconducting samples at various temperatures. The superconducting-to-normal transition temperature and its width are often obtained from ac susceptibility measurements which are carried out using ACMS facility on the PPMS system. All of the techniques are briefly introduced below. For some of the samples mechanical properties such as hardness and elastic modulus are determined by using Nano-Indentation measurement.

## 2.1. Furnaces used for processing samples:

In the present work, different home-made furnaces with re-crystallized $Al_2O_3$ muffle were used for sintering the precursor powders RE-123 and $RE_2BaCuO_5$

(RE-211). For synthesizing various YBCO and (Y, LRE)Ba$_2$Cu$_3$O$_7$ samples by infiltration and growth process (IGP), furnace was set up with a long Al$_2$O$_3$ muffle and commercial grade Ar atmosphere was purged through the hot zone. For oxygenating the processed samples another furnace was set up with a quartz muffle of length ~ 100 cm introduced into the Al$_2$O$_3$ muffle. For gas purging, the muffles of the furnace after loading with the samples was sealed with rubber cork and plaster of Paris cloth and sealed with Teflon tapes. To insulate the caps from the hot zone and to maintain stability of temperature in the hot zone, fire brick separators and quartz wool were placed far away on both sides of the hot zone. Kanthal APM wires were used as heating elements. Chromel– Alumel thermocouples were used for temperature measurements. Eurotherm make temperature controller (model 2404) and thyristor (model TE10A) were used for controlling the temperature in the furnaces to an accuracy of ± 2 °C. A Schematic picture of the furnace along with the temperature controller and thyristor are shown in fig. 2.1.
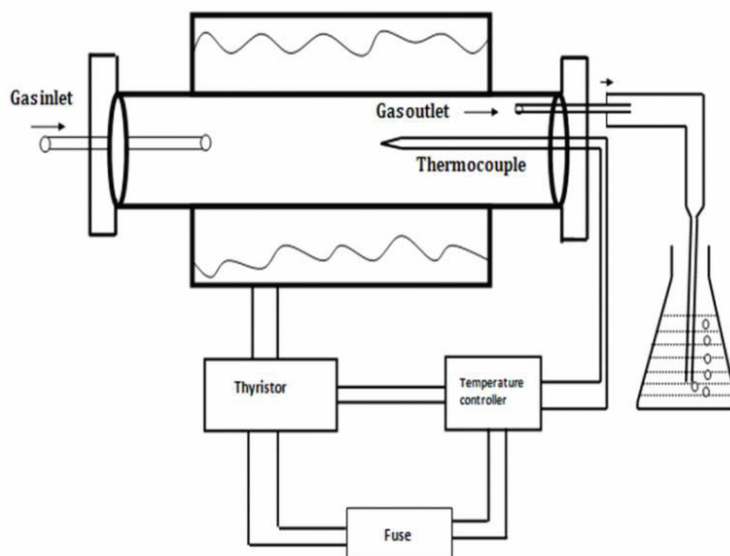


**Fig. 2.1.** A schematic diagram of the furnace used.

The heat profiles of the furnaces were measured through temperature as a function of depth along the muffles and are shown in figs. 2.2 (a) and (b).
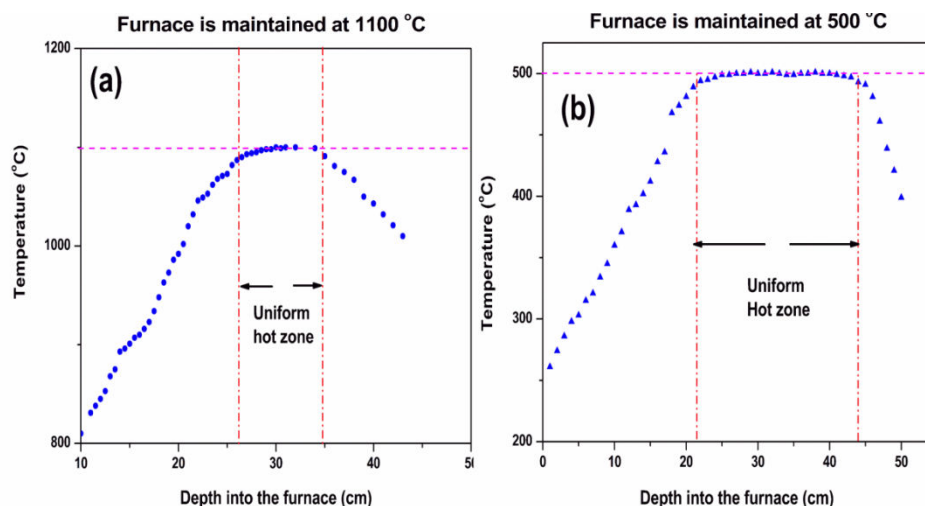


**Fig. 2.2.** The heat profiles showing the temperature distribution obtained along the length of the muffle in tubular furnaces used for **(a)** sintering powders / IGP and **(b)** oxygenation.

## 2.2.   Sample Preparation:

The precursor powders of $YBa_2Cu_3O_7$ (Y-123), $Y_2BaCuO_5$ (Y-211) and $(Nd_{0.66}, Sm_{0.66}, Gd_{0.68})BaCuO_5$ (NSG-211) are synthesized by chemical methods from $Y_2O_3$, $BaCO_3$, CuO powders. Chemical synthesis ensures homogeneity in the composition of the powders compared to those produced by solid state routes. An additional advantage is the possibility of producing very fine powders through combustion synthesis [1-2]. In order  to prepare powders of Y-123 and RE-211, Rare earth oxide ($RE_2O_3$) of Indian Rae-Earth make, Barium  Carbonate ($BaCO_3$) and Copper Oxide (CuO) of E-Merck make, each of them of 99.99% purity were weighed out in stoicheometric ratios and were dissolved in nitric acid ($HNO_3$) to make corresponding nitrates. The mixture was mixed well on a magnetic stirrer to get a clear solution. Requisite amount of citric acid was added to the nitrate

precursor solution along with a small amount of chelating agent Ethylene glycol. The $p^H$ of the solution was adjusted to 8 by adding appropriate amounts of ammonia ($NH_3$). The resultant gel solution then was kept for combustion on a hot plate at 250 $^o$C to get the voluminous powders.

To form the requisite phases of Y-123 and RE-211, the powders were sintered at 900 $^o$C and 950 $^o$C for 12 hours respectively. Sub micron sized RE-211 particles were observed through FESEM image which is recorded at a magnification of 10 kX shown in fig. 2.3 (a) and for Y-123 phase particles also shown in fig. 2.3 (b).
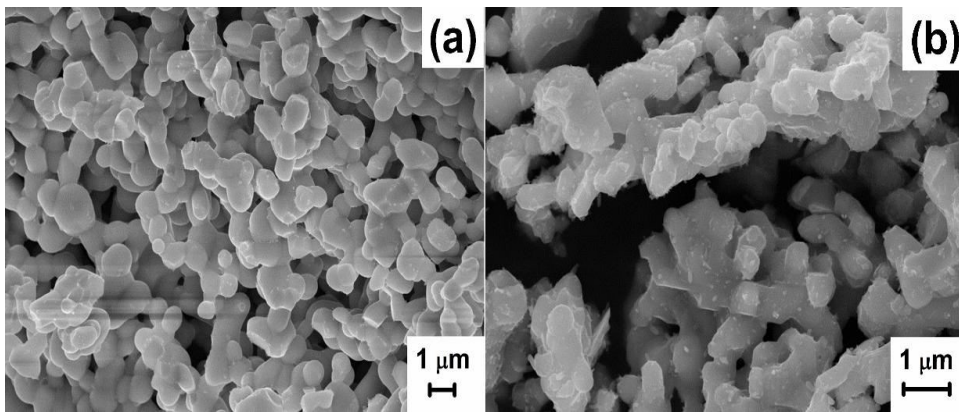


**Fig. 2.3.** FESEM images obtained from sintered Y-211 and Y-123 powders used in the present experiments are shown. The micrograph shows that the Y-211 particles are of size in the range 400 nm – 1μm.

## 2.3. Fabrication of YBCO/(Y, LRE)BCO superconductors by the modified POIGP:

Infiltration Growth (IG) process enables fabrication of REBCO products with near-net shape and overcomes defects like shrinkage, cracks, pores etc., [3-4]. However, this process suffers from serious problems like in-homogeneities in the distribution of Y-211 particles [5-6] and hence often results in non-uniform current densities [7-8] across the volume of the samples. Preform optimized IG

process (POIGP) recently developed in our group offers products without any macro defects such as porosity, cracks along with homogenously distributed fine sized Y-211 phase particles in the final compositions. In this process a pressure of 460 MPa is applied to make preforms and the sintering temperatures in the heat treatment schedule are optimized to strengthen the preforms to support liquid phase infiltration. Processed samples support high $J_c$ up to high fields owing to enhanced flux pinning caused by the presence of submicron sized Y-211 particles and wide spread twinning with twin widths of 25-100 nm present throughout the sample. For these reason we have adopted this process to synthesize all the present samples.

### 2.3.1. Preform Fabrication:

Sintered powders of Y-123 and Y-211 were compacted into pellets of dimensions of 16 mm X 16 mm X ~ 15 mm and 16 mm X 16 mm X ~ 8 mm respectively by applying uni-axial pressure. For this purpose, a hydraulic press was used. The preforms were made at the optimized compaction pressure of 460 MPa.

### 2.3.2. Sample assembly and heat treatments:

Bulk (Y, LRE)BCO samples are fabricated employing modified Infiltration Growth process. A schematic of the sample assembly employed is shown in fig. 2.4. The RE-211 preform is supported on thin layers of $Y_2O_3$, Yttria-Stabilized Zirconia (YSZ) and alumina ($Al_2O_3$) to minimize the outflow of liquid phases during heat treatment. The presence of $Y_2O_3$ and YSZ layers also help in avoiding contamination of the sample by alumina at elevated temperatures. Y-123 pellet, which is the source of liquid phases, is placed above the RE-211 preform.
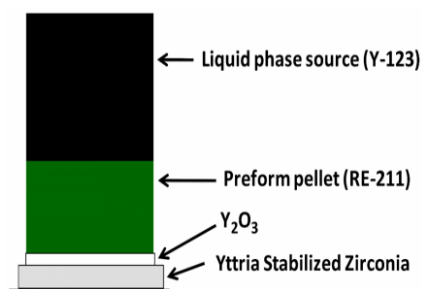
**Fig. 2.4.** Assembly for POIG processing of the samples.

The sample assembly arranged as described above is heat-treated in a tubular muffle furnace, which has a uniform hot-zone of ~ 60 mm. The cooling rates used during heat treatment schedule of POIGP was modified for synthesizing (Y, LRE)BCO, compared to that for YBCO, keeping in mind that the peritectic temperatures differ based on the RE elements chosen and also the atmosphere selected. The heat treatment schedules thus used for YBCO and (Y, LRE)BCO are shown in fig. 2.5.
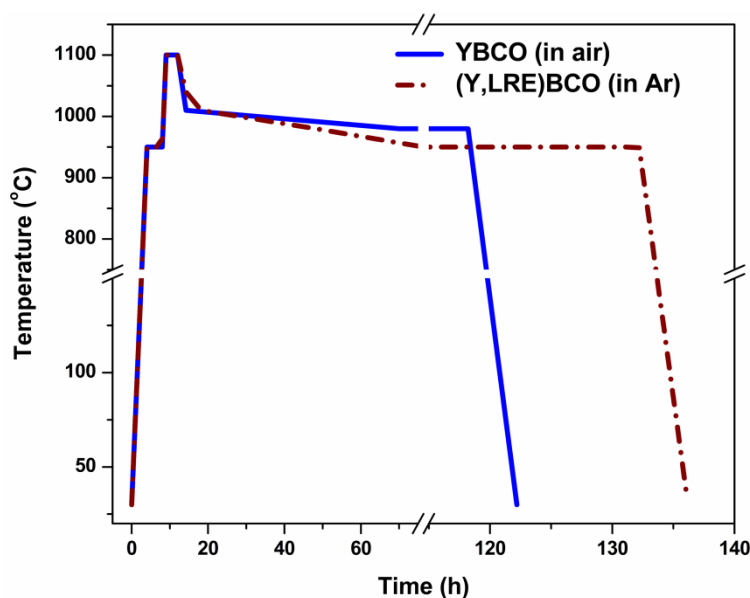


**Fig. 2.5.** Heat treatment schedules of YBCO (in air) and for (Y, LRE)BCO (in Ar).

The POIG processed samples thus prepared were characterized as discussed below.

## 2.4.   X-ray diffraction analysis:

Solid matter can be categorized as amorphous and crystalline materials. Those materials in which the atoms are arranged in random directions similar to the disorder present in a liquid are known as amorphous materials. Crystalline materials are those materials in which the atoms are arranged in a regular pattern, and there is a smallest volume element that by repetition in three dimensions describes the crystal. This smallest volume element is called a unit cell. The dimension of the unit cell is described by three axes: *a, b, c* and the angles between them *α, β, γ.*

An electron in an alternating electromagnetic field will oscillate with the same frequency as the field. When an X-ray beam hits an atom, the electrons around the atom starts to oscillating with the same frequency as the incoming beam. In almost all directions interference is destructive, that is, the combining waves are out of phase and there is no resultant energy leaving the solid sample. However, the atoms in a crystal are arranged in a regular pattern, and in some particular directions interference is constructive, i.e., the waves are in phase and well defined X-ray beams leave the sample in specified directions. Hence, a diffracted beam may be described as a beam composed of a large number of scattered rays mutually reinforcing one another. English physicists *Sir W.H. Bragg* and his son *Sir W.L. Bragg* [9-10] developed the relationship, *nλ = 2d sinθ* in 1913 to explain why the cleavage faces of crystals appear to reflect X-ray beams at certain angles of incidence (*θ*). The variable d is the distance between atomic layers in a crystal, and the parameter λ is the wavelength of the incident X-ray beam and n is an integer giving the order of reflection. This observation is an example of X-ray

wave interference, commonly known as X-ray diffraction (XRD), and was the direct evidence for the periodic atomic structure of crystals. In 1919 *A. W. Hull* pointed out that *"every crystalline substance gives a pattern; the same substance always gives the same pattern; and in a mixture of substances each produces its pattern independently of the others"*. The X-ray diffraction pattern of a pure substance, therefore, acts like a fingerprint of the substance. Thus, the powder diffraction method is a powerful tool suited for characterization and identification of polycrystalline phases.

Ideally, the sample consists of random distribution of all possible (*h, k, l*) planes. Only crystallites having reflecting planes (*h, k, 1*) parallel to the specimen surface will contribute to the reflected intensities and each possible reflection from a given set of *h, k, l* planes will have an equal number of crystallites contributing to it. In order to produce all possible reflections, X-ray is scanned through the glancing angle θ on the sample. The schematic description of Bragg's law is represented in fig. 2.6.
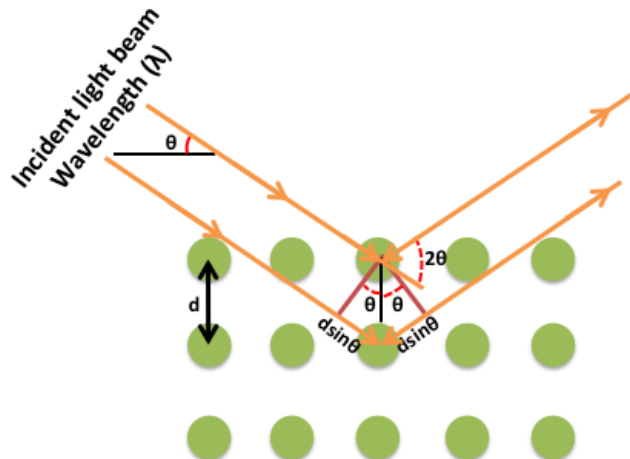


**Fig. 2.6.** Schematic description of Bragg's Diffraction Law.

The most common use of powder diffraction includes phase identification and lattice parameter calculation. The phase identification of compounds consists of identification of phases using search-match utility and estimation of the amount of crystalline phases present in the samples. Phase identification of the samples was performed using *X'Pert High score* software with support of the *ICDD PDF 1I* database. Different phases (vol.%) formed in the samples, the lattice parameters and unit cell volumes were quantitatively estimated from the XRD patterns using the TOPAS and Fullprof programs through Rietveld refinement process.

In the present study powder XRD patterns of samples were taken using a Cu $K_\alpha$ as the X-ray source ($\lambda$ =1.5404 Å); Bruker's AXS Model D8 Advance System or an X-ray diffractometer with Co $K_\alpha$ ($\lambda = 1.7889$ Å) source INEL Model CPS 120.

## 2.5. Microstructural Characterizations:

Microstructural properties provide information on the key parameters responsible for enhancement of $J_c$ in superconductors. Microstructural analysis of complex non-stoicheometric material has a lot of challenges. In order to prepare specimens for microstructural characterization, the samples were sliced into thin sections using a low speed diamond saw (model Isomet 1000, Buehler-make). The specimens extracted from the samples were mounted in bakelite and ground on silicon carbide papers (600, 800, 1000 and 1200 grits) to a flat surface. They were further polished on polishing cloth on the rotating wheel of a Buehler polishing machine, using different grades (6, 3, 1, 0.25 μm) of diamond paste as grinding media. Kerosene was used as a lubricant during polishing. The surface was cleaned after every stage of polishing. Polishing time at each stage ranged from 2 to 30 minutes with silicon carbide paper and 0.5-2 hours with diamond paste. The polished surface of the sample was then cleaned with methanol and dried in hot air. In the present study, no etching

was done to the polished surface of the samples. The micrographs thus obtained were characterized for various microstructural parameters using quantitative metallographic methods as explained below. Scanning Electron Microscope (SEM) and Energy Dispersive X.ray Spectrometer (EDS) are the tools used to perform microanalysis on these materials such as observe the grain size, presence of secondary phases and their distribution, defects an voids, twinning, etc.

### 2.5.1. Field Emission Scanning Electron Microscope:

FESEM is one of the most versatile and well known analytical techniques for microstructural studies. Compared to conventional optical microscope, an electron microscope offers advantages including high magnification, large depth of focus, great resolution and ease of sample preparation and observation. Electrons generated from an electron gun enter a surface of a sample and generate many low energy secondary electrons. The intensity of these secondary electrons is governed by the surface topography of the sample. An image of the sample surface is therefore constructed by measuring secondary electron intensity as a function of the position of the scanning primary electron beam.

The FESEM employs a high-energy electron beam (in keV) and helps in imaging the topography of the sample surface by operating in a raster scan mode. In the case of a FESEM, a field-emission cathode in the electron gun of a FESEM provides narrower probing beams at low as well as high electron energy, resulting in both improved spatial resolution and minimized sample charging and damage. The electrons, when they interact with the atoms of the sample, produce secondary electrons, back-scattered electrons, transmitted electrons, characteristic X-rays etc. A typical schematic sketch representing the above mentioned processes are shown in fig. 2.7. Separate detectors are present to pick up the

information from each of these processes. The secondary electron imaging can produce very high-resolution images of a sample surface, revealing details even in the size range 10 - 100 nm. Due to the very narrow electron beam, FESEM micrographs have a large depth of field yielding a characteristic three-dimensional appearance useful for understanding the surface structure of a sample.
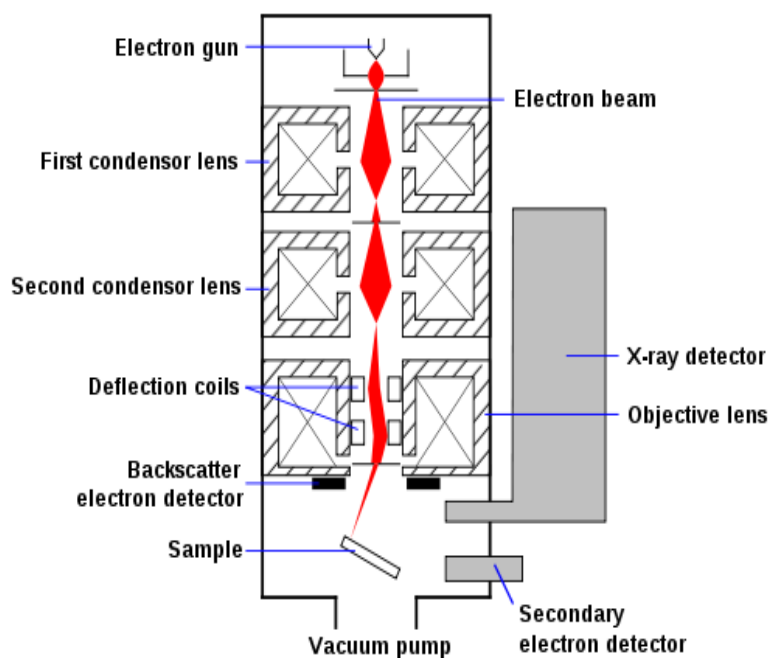


**Fig. 2.7.** A schematic picture showing emission of electron beam and presence of various detectors in an FESEM.

Electron beam of very high energies are employed in order to visualize the sub-surface structures while low energy BSE detection is quite useful for high resolution investigation of specimen that accumulate surface charge, in spite of thin gold coating. This is met through a new In-lens detection system. In order to reduce aberrations and sensitivity to interfering stray-fields the electron optical column is equipped with a positively biased booster that shifts the energy of the

primary electrons. The incident beam is focused by a combination of a magnetic lens with an axial gap that avoids field leakage to the specimen and an electrostatic retarding together with the grounded pole piece cap. Shortly before the electrons hit the specimen they are decelerated down to the desired primary energy. A suitable explanation for the reduction of spherical and chromatic aberrations is that the electron beam is focused by the objective lens at higher energies and smaller electron beam diameters. Another advantageous effect of this arrangement is the collection of secondary electrons emerging from the sample surface attracted and accelerated by the positively biased electrode of the beam booster and finally projected onto the In-lens detector. Characteristic X-rays are emitted when the electron beam removes an inner shell electron from the sample, causing a higher energy electron to fill the shell and release energy. These characteristic X-rays are used to identify the composition and measure the abundance of elements in the sample.

In the present work, a Field Emission Scanning Electron Microscope (model Ultra 55, Carl Zeiss-make) along with Energy Dispersive Spectrometry (EDS) was employed for obtaining the micrographs. The working distance for most of the cases was in the range 4 -10 mm. The charging effects of the electron beam on the sample were bypassed by either gold coatings or by creating a silver paint / strip channel from the holder to the sample.

## 2.5.2. Energy Dispersive X-ray Spectroscopy:

To get the composition of different phases observed through microstructural studies in the samples, they were individually selected and investigated through EDS. Through different techniques like point scan, area scan, line scan and mapping on the sample, relative amounts of different elements present in each of the phases is estimated.

Energy Dispersive X-Ray Spectroscopy (EDS) is an analytical technique that qualitatively and quantitatively identifies the elemental composition of materials analyzed in FESEM. EDS analyzes the top two microns of the sample with a spatial resolution of one micron. Beryllium windowed EDS detect all elements with atomic numbers greater than oxygen at concentrations greater than 0.1%. "Windowless" EDS detectors can also detect carbon, nitrogen and oxygen at concentrations greater than 1.0%. EDS displays the distribution of elements as either dot maps or line profiles with a spatial resolution of one micron.

When the electron beam of the FESEM is scanned across the sample, it generates X-rays from the atoms. X-rays are produced as a result of the ionization of an atom by high-energy radiation wherein an inner shell electron is removed. To return the ionized atom to its ground state, an electron from a higher energy outer shell fills the vacant inner shell and, in the process, releases an amount of energy equal to the potential energy difference between the two shells. This excess energy, which is unique for every atomic transition, will be emitted by the atom either as an X-ray photon or will be self absorbed and emitted as an Auger electron. The energy of each X-ray is characteristic of the atom from which it escapes. The EDS system collects the x-rays, sorts them by energy and displays the number of X-rays versus their energy. This qualitative EDS spectrum can be either photographed or plotted. This data can then be further analyzed to produce either an area elemental analysis (displayed as a dot map) or a linear elemental analysis (displayed as a line scan) showing the distribution of a particular element on the surface of the sample. The EDS data can be compared to either known standard materials or computer-generated theoretical standards to produce either a full "quantitative" or a "semi-quantitative" analysis. The location of the peaks on the energy scale identifies the elements. The peak heights vary because each transition has different probability of occurring and the detector's efficiency is a

function of energy. The EDS spectrum has a peak width because the energy dispersion is a statistical event, i.e. every photon does not produce the same number of electron - hole pairs and there is thermal noise caused by the amplification process.

## 2.6. Methods used for superconductor characterization:

### 2.6.1. ac susceptibility measurement:

AC magnetic susceptibility (ACMS) is the standard tool for determining the magnetic field effect on the superconductor. The diamagnetic nature of superconductor is a bulk effect and is not a surface effect, which can be confirmed by ac susceptibility measurement. In the fully superconducting state, the sample is a perfect diamagnetic and so $\chi' = -1$. Typically, the onset of a significant nonzero $\chi'$ is taken as the superconducting transition temperature.

ACMS is useful for the evolution of the superconductivity with magnetism by applying an oscillating external magnetic field. The contribution of different phases to the diamagnetism can be activated by applying small field. The property of perfect diamagnetism is exploited in this method to estimate the $T_c$ of the superconductors, low $T_c$ phases present in the materials, using the PPMS (quantum design) with ACMS (Alternating Current Magnetic Susceptibility) set up. The PPMS ACMS consists of a pair of pick-up coils with opposite winding directions connected in series. The coils are located one above the other with a small separation between them. The sample is fixed to the end of a sample rod that is connected to a linear actuator which moves the sample vertically from one coil to the other. Under applied field, the sample has some magnetic moment and the motion of the sample with respect to the coils generates an emf (V) according to Faraday's law of induction.

The response of the secondary as a function of temperature is measured and various properties such as onset $T_c$, broadness which is due to the presence of low $T_c$ phases and solid solutions and the superconducting fractions in the materials are calculated. As soon as the superconducting to normal state transition takes place, the signal in the secondary suddenly rises, the temperature at which this transition takes place is the $T_c$ of the material.

Due to this, a voltage proportional to the frequency is induced in the secondary coil. The in-phase and out-of-phase components (w.r.t. the driving current of the primary coil) of the voltage are proportional to the real $\chi'$ (diamagnetic response) and imaginary $\chi''$ (power loss) components of the susceptibility respectively. We have used this technique extensively while characterizing the superconducting properties of (Y, LRE)BCO.

AC susceptibility is the magnetization response of a material in an AC magnetic field and can be expressed by the following equation 2.1.

$$\chi = \frac{dM}{dH_{ac}} \qquad \text{...............} \quad \textbf{(2.1)}$$

Where $\chi$ is the magnetic susceptibility, M is the magnetization of the sample and H is the AC magnetic field.

A block diagram of a typical mutual inductance set up used for measuring susceptibility as a function of temperature of a sample is shown in fig. 2.8.
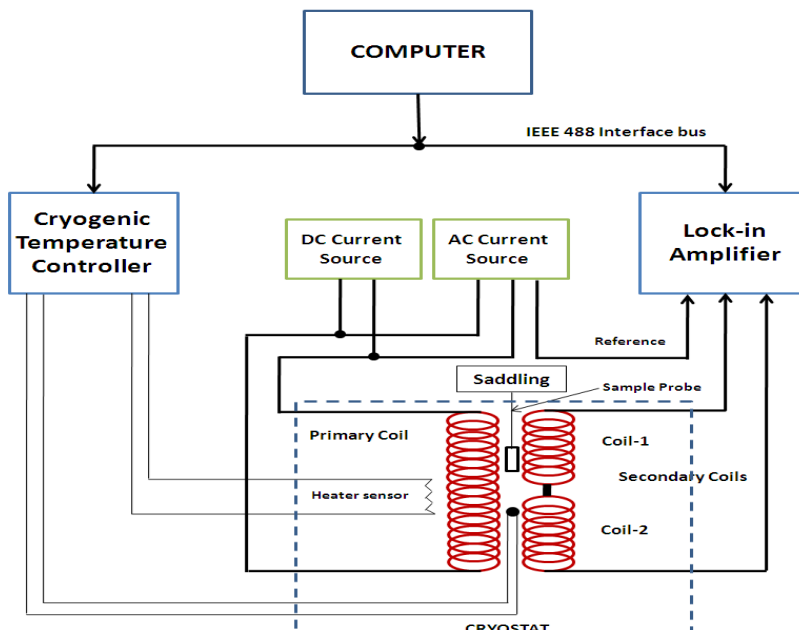
**Fig. 2.8.** Block diagram of ac susceptibility measurement system.

The property of perfect diamagnetism is exploited in this method to estimate the $T_c$ of the superconductors, low $T_c$ phases present in the materials, employing the PPMS ACMS (Alternating Current Magnetic Susceptibility (quantum design). We have used this technique extensively to characterize the superconducting properties of (Y, LRE)BCO samples.

If the applied ac voltage is $H = H_o \cos \omega t$, where ω is the angular frequency (=2πf), the resulting magnetization amounts to

$$M = H_o(\chi' \cos\omega t + \chi'' \sin\omega t) \ldots\ldots\ldots (2.2)$$

Where $\chi'$ and $\chi''$ represent the real and imaginary components of the fundamental ac susceptibility. The fundamental principle on which this measurement works is based on the mutual induction (Faraday's law)

$$\nabla \times E = -\frac{\partial B}{\partial t} \dots\dots\dots (2.3)$$

Basically the assembly comprises of a mutual inductance coil assembly with two secondary coils co-axially mounted in a primary solenoid. The two secondary coils are identical and are connected in opposition in order to cancel the voltages induced by the ac field itself. A constant current source is employed to drive an ac current in the primary solenoid. The field produced by a current with r.m.s. value '$I_{rms}$' in a solenoid is given by

$$\mathbf{H_{rms}} = \frac{\mu_o N_p I_{rms}}{L_p} \dots\dots\dots (2.4)$$

where $N_p$ is the number of turns in the primary coil, $L_p$ is the length of the primary coil (in cm) and $I_{rms}$ is the root mean square (rms) value of the ac current through the primary coil. The field amplitude $H_{ac}$ (in Oe) is $\sqrt{2}\, H_{rms}$.

If the secondary coils are ideally made i.e. both the coils are made under similar conditions (number of turns, diameter, etc.), no voltage will be detected by the lock-in amplifier when the coil assembly is empty. But, in practice, the net output from the secondary coils is often non-zero and is temperature dependent. This is eliminated by measuring and subtracting the back ground voltage from the signal measured after introducing the sample in similar conditions. Additionally, there is a need to correct the extraneous phase shifts arising from various sources in the setup. This is done by shifting the phase of the references so as to obtain $\chi^{''} = 0$ well above $T_c$ as well as well below $T_c$.

When the induced voltages in the secondary is sensed at the input of the dual phase lock-in amplifier, it gives out a signal in the form of dc voltages $\epsilon_r$ and $\epsilon_i$ proportional to the real and imaginary parts of $M$ that are in-phase and out-of

phase, respectively, with respect to the reference signal which is in-phase with the applied field H.

From the measured $\epsilon_r$ and $\epsilon_i$, the real and imaginary components of the ac susceptibility $\chi_r$ and $\chi_i$ are determined using the formulae shown in Eq. 2.5 to Eq. 2.6.

$$\chi_r = \frac{\epsilon_r}{\alpha\omega AN\mu_0 H_m(1-D)} \ldots\ldots\ldots (2.5)$$

$$\chi_i = \frac{\epsilon_i}{\alpha\omega AN\mu_0 H_m(1-D)} \ldots\ldots\ldots (2.6)$$

Here N is the number of turns in the secondary across the sample, $H_m$ is the amplitude of the applied ac field, $A$ is the area of the cross-section of the sample, D is the demagnetization factor and $\alpha$ is the filling factor [11]. The absolute values of the ac susceptibility for non-zero demagnetization D values are calculated using the expressions given by Murphy et al. [12].

The property of perfect diamagnetism is exploited to estimate the $T_c$ of the superconductors and detect low $T_c$ phases if present in the materials in employing the PPMS ACMS (Alternating Current Magnetic Susceptibility (quantum design) facility.

### 2.6.2. M-H hysteresis loops and critical current density measurements:

The critical current density ($J_c$) in type-II superconductors can be estimated by analyzing the magnetization using critical state model proposed by C.P. Bean [13]. The model assumes that the penetrated super-currents flow with a density equal to $J_c$ independent of the local internal field. If this magnitude of the current flows everywhere in the specimen, it is in the critical state. The process of

magnetization of a slab of thickness 2a in a field parallel to its surface is shown in fig. 2.9, when the current density is independent of the external field.
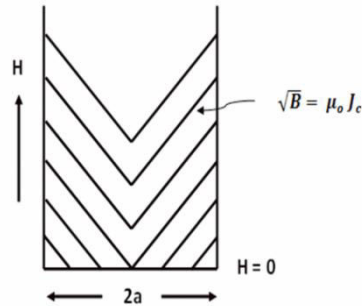


**Fig. 2.9.** Magnetization process of thin slab of thickness 2a in a field parallel to the surface [13].

The field within the specimen decreases linearly with distance, if the material is in critical state. The Maxwell's equation is

$$\sqrt{B} = \mu_0 J_c \quad \ldots\ldots\ldots\text{ (2.7)}$$

Where $J_c$ is the critical current density in $Am^{-2}$, B is the magnetic induction in Tesla and $\mu_o$ is the absolute permeability.

The local internal field $H_i$ is given as

$$H_i = \frac{B}{\mu_o} \ldots\ldots\ldots\text{ (2.8)}$$

Where $B$ is the macroscopic local flux density.

The local magnetization $M_i$ becomes, $M_i = H_i$ - H, where H is the applied field. The total magnetization $M$ is the average of $M_i$, over the sample cross-section.

If we consider the magnetization for two stages namely

(i) $0 < H < H^*$ and (ii) $H^* < H$

Where $H^*$ is the applied magnetic field at which the internal field reaches the centre of the specimen.

For an infinite slab, the initial magnetization curve M(H) becomes

$$M(H) = -H + \frac{H^2}{2J_c a}, for\ 0 < H < H^* \qquad \text{..........} \quad 2.9$$

$$M(H) = -\frac{J_c a}{2}, for\ H^* < H \qquad \text{.........} \quad 2.10$$

The reverse curve for high -$H_m$ ($H^* < H_m$) case is given by

$$M(H) = -\frac{J_c a}{2} + H_m - H - \frac{(H_m - H)^2}{4J_c a}, for\ H_m - 2H^* < H < H_m$$

$$\text{.........} 2.11$$

$$M(H) = \frac{J_c a}{2}, for\ -H_m - H < H_m - 2H^* \qquad \text{............} \quad 2.12$$

Where H is the applied magnetic field, $H_m$ is the maximum applied field and 2a is the thickness of the slab.

When $H_m > 2H^*$, $J_c$ is related to the magnetization $M$ for slab of thickness 2a as

$$M(H^+) - M(H^-) = J_c a \qquad \text{...............} \quad (2.13)$$

Therefore $J_c$ can be determined by measuring the width of an M-H hysteresis loop at a given field. The discussion made above is applicable only if the sample is considered as an infinite slab.

For the orthorhombic geometry

$$M(H)^+ - M(H)^- = J_c b \left(1 - \frac{b}{3a}\right) \text{.......... (2.14)}$$

### 2.6.3. Calculation of $J_c$ from M-H loops:

Magnetization hysteresis loops representing magnetization (M) as a function of applied magnetic field (H) were recorded on the samples at various cryogenic temperatures using a Physical Property Measurement System (PPMS) of Quantum design make.
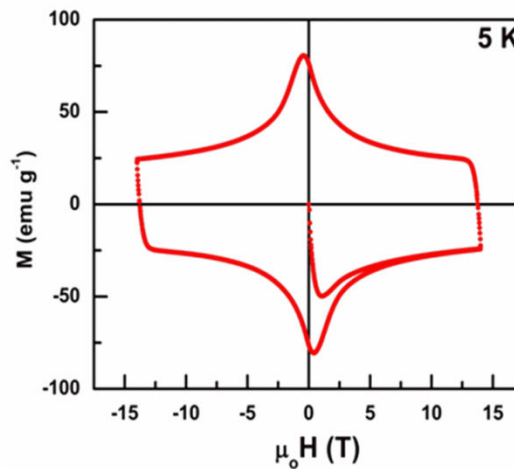


**Fig. 2.10.** A typical magnetic hysteresis (M-H) loop obtained from an IG processed YBCO superconductor at 5 K [14].

The specimens used for the measurements were of size approximately 2 mm x 2 mm x 5 mm, which were cut such that their long dimension was normal to the pressed surface of the samples. The samples were exposed to magnetic fields of up to 9 Tesla generated by superconducting magnet in order to record the field dependences of magnetization. A typical M-H loop obtained for a superconductor is shown in fig. 2.10.

Critical current densities ($J_c$) of the samples were determined following extended Bean's critical State model using the relation [15-16]:

$$J_c = \frac{20\,\Delta M}{d} \quad \ldots\ldots\ldots (2.15)$$

where $\Delta M = M^+ - M^-$ (in emu/cc), $d = b\left(1 - \dfrac{b}{3a}\right)$; $a > b$ and a, b are broad and narrow dimensions of the sample (in cm).

## 2.7. Mechanical properties:

A TI 900 Tribo-Indenter, Hysitron make, was used for the nano hardness ($H_n$) and elastic modulus ($E$) measurements. $H_n$ and E measurements were carried out at 16 different points on each polished sample. Nanoindentation studies at low applied loads enable the determination of $H_n$ and $E$ of each of the phases present in the superconductor composite separately, unlike measurements at high applied loads which create indentations with sizes bigger than the size of Y-211 inclusions [17]. The samples were indented by a Berkovich-type pyramidal diamond tip with a maximum load of 8,000 µN for each indent. The relations given by Oliver and Pharr [18] were used for analyzing load–displacement data recorded at indentations to determine reduced Young's modulus ($E_r$) and nano hardness ($H_n$) values. To overcome the error due to choice of indenter, reduced modulus $E_r$ is defined for non-rigid indenters based on the load-displacement behavior [17-18].

**Nanoindentation:** It enables mechanical probing of a material surface to nanometric-scale depths, while simultaneously monitoring LOAD and DEPTH.

1. Mechanics of small volumes: Understanding whether thin films, lines, dots have different mechanical properties than bulk counterparts

2. Material physics: Measuring deformation processes such as dislocation nucleation, crack growth, etc.

In indentation an indenter tip (Berkovich, Sphero-conical, Knoop or cube cornor), normal to the sample surface with a known geometry is driven into the sample by applying an increasing load up to some preset value. The load is then gradually decreased until partial or complete relaxation of the sample has occurred. The load and displacement are recorded continuously throughout this process to produce a load-displacement curve from which the nano-mechanical properties such as $H_n$, $E_r$, stress-strain studies of the sample material can be calculated. Nanoindentation tester can be used in a mapping mode to take data automatically from a variety of locations on the sample. For the present work Berkovich indenter is used for all measurements. The photograph of the instrument used for indentation and the    schematic of the basic Hysitron tribo-indenter system are displayed in fig. 2.11 (a) and (b) respectively.
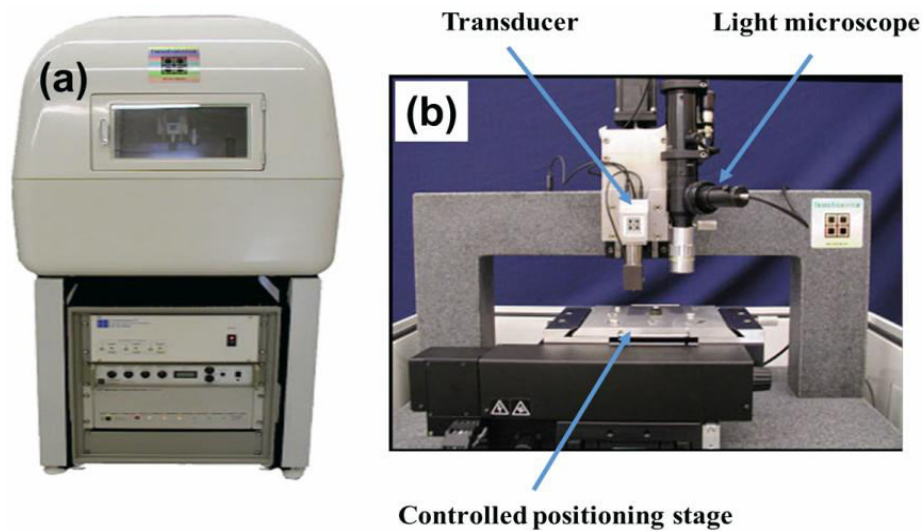


**Fig. 2.11.** (a) Photograph of Nanoindentation instrument and (b) a schematic image of the nano-indenter system.

The nano hardness ($H_n$) and reduced young's modulus ($E_r$) values were calculated as a function of penetration depth using a method of Oliver and Pharr. In this method the contact depth ($h_c$) is given as

$$h_c = h_{max} - \varepsilon \frac{P}{S} \quad \text{............. (2.16)}$$

Where $\varepsilon$ is a parameter, for Berkovich indenter the value of $\varepsilon$ is 0.75 and $S$ is contact stiffness and $P$ is applied load. In the present study $P_{max}$ is 8000 mN. The expression for $S$ is

$$S = \frac{dP}{dH_n} = 2 E_r \frac{\sqrt{A_c}}{\sqrt{P}} \quad \text{.............. (2.17)}$$

Where $A_c$ is the contact area of the indenter. The expression for $A_c$ is

$$A_c = 24.56\, h_c^2 \quad \text{............... (2.18)}$$

$E_r$ is given by

$$\frac{1}{E_r} = \frac{1-v^2}{E} - \frac{1-v_i^2}{E_i} \quad \text{............. (2.19)}$$

Where, $v$, $E$ are poisson ratio and young's modulus of the sample and $E_i$ (1141 GPa) and $v_i$ (0.07) are the corresponding parameters for the Berkovich diamond indenter. In general $v$ is set equal to 0.3 for YBCO [17-18].

The nanohardness ($H_n$) is defined as the mean contact pressure under the condition of the indenter at maximum load ($P_{max}$): The nano hardness is calculated using the equation shown below.

$$H_n = \frac{P}{24.56\, h_c^2} \quad \text{.................. (2.20)}$$

In summary, in this chapter different experimental facilities and techniques by which the present thesis work has been carried out are introduced and the physical properties that can be derived from them are described.

**References:**

1. G. Kordas, K. Wu, U.S. Brahme, T.A. Friedmann and D.M. Ginsberg, Mater. Lett. **5** (1987) 417.

2. L.C. Pathak and S.K. Mishra, Supercond. Sci. Technol. **18** (2005) R67.

3. E. Sudhakar Reddy and T. Rajasekharan, Supercond. Sci. Technol. **11** (1998) 523.

4. R. Cloots, T. Koutzarova, J.P. Mathieu and M. Ausloos, Supercond. Sci. Technol. **18 (**2005) R9.

5. Y.L. Jiao, L. Xiao, H.T. Ren, M.H. Zheng and Y.X. Chen, Physica C **386** (2003) 266.

6. J.C.L. Chow, H.T. Leung, Lo Wai and D.A. Cardwell, J. Mater. Sci. **33** (1998) 1083.

7. K. Iida, N. Hari Babu, Y. Shi and D.A. Cardwell, Supercond. Sci. Technol. **18** (2005) 1421.

8. S.Y. Chen, Y.S. Hsiao, C.L. Chen, D.C. Yan, I.G. Chen and M.K. Wu, Mater. Sci. Eng. B **151** (2008) 31.

9. W.L. Bragg, Proc. Camb. Philos. Soc. **17** (1913) 43-57.

10. W.L. Bragg, Proc. R. Soc. A **89** (1913) 248-277.

11. M. Couach and A. F. Khoder, Magnetic Susceptibility of Superconductors and other Spin Systems edited by Hein R A, Francavilla T L and Liebenberg D H 1992 (Plenum, Neyork)

12. S.D. Murphy, K. Renouard, R. Crittenden and S. M. Bhagat, Solid State Commun. **69** (1989) 367.

13. C.P. Bean, Phys. Rev. Lett. **8** (1962) 250.

14. Ph.D. Thesis entitled "Enhanced Flux Pinning to High Fields in YBCO and YBCO/Ag Superconductors through Preform Optimization in Infiltration and Growth Process" by N. Devendra Kumar, (2011), University of Hyderabad.

15. D.X. Chen and R.B. Goldfarb, J. Appl. Phys. **66** (1989) 2489.

16. M. Murakami, M. Morita, K. Doi and K. Miyamoto, Jpn. J. Appl. Phys. **28** (1989) 1189.

17. Joan Josep Roa Rovira, Ph.D. thesis, Mechanical Properties of HTSC at Micron/Nanometric Scale, University of Barcelona, page No.58 (Chapter 1) (2010).

18. W.C. Oliver, and G.M. Pharr, J. Mater. Res. **7** (1992) 1564.

# Chapter III

# Study of growth mechanism and the effect of infiltration temperature on the properties of Preform Optimized Infiltration Growth processed YBCO superconductors

In this chapter we have discussed the initial work done to assess the growth mechanism and the effect of infiltration temperature on the physical properties (structural, microstructural, mechanical and magnetic) of preform optimized infiltration growth (POIG) processed YBCO superconductors. The objective of the present work is to

a) Understand the peritectic reaction and growth mechanism of YBCO superconductors in IG process by investigating the ingots quenched from different temperatures.

b) Study the effect of infiltration temperature on the properties of YBCO synthesized by POIG process.

c) Examine the results and draw correlations, if any, between microstructural, mechanical and magnetic properties measured.

## 3.1. Introduction:

$REBa_2Cu_3O_{7-\delta}$ (REBCO, where RE=Y, Gd, Sm, Nd etc.,) is one of the widely studied high temperature superconductor (HTS) systems. Their critical temperatures ($T_c$) above which superconductivity is lost are higher than the boiling point of liquid nitrogen ($T_c \sim 92$ K, for YBCO), and they have the least flux creep among all HTS [1-2] systems.

Sintering is the commonly used technique in ceramic processing and it allows

formation of different shapes needed for various practical applications. However, it has been realized that, although good $T_c$ values can easily be achieved, critical current density ($J_c$) values are very small in bulk sintered oxide superconductors [1-3]. Melt textured REBCO materials [4-6] have superior current carrying capacities due to the elimination of most of the weak links and due to texturing/alignment of the grains. Even though, the properties of YBa$_2$Cu$_3$O$_{7-\delta}$ (Y-123) processed by melt texturing are substantially better than those of sintered Y-123, the melt texturing technique poses several problems which are severe enough to block many applications. The incongruent melting of REBCO produces liquid phases, which tend to diffuse out to the exterior of the components as a result of their low viscosity. In the case of samples exceeding a few centimetres in dimensions, the problem is very severe and leads to products with defects like distortions, cracks, and macro and micro porosities. The depletion of liquid phases from the interior of the material will not only alter the stoichiometry but also hinder the grain growth and texturing process of YBCO. These drawbacks therefore limit the fabrication of components of large and complex shapes. The only shapes reported so far by melt processing in the literature are either those of disks or bars [4-6]. Due to their ceramic nature, and due to various kinds of defects mentioned above, the melt processed Y-123 materials pose difficulties in machining into different suitable shapes for applications. The possibilities of using the bulk RE-123 material for applications would be aided by the availability of a process which allows the fabrication of near-net-shaped and large-sized components without internal defects and with superconducting properties at least comparable to the existing melt processed samples.

With the aim of overcoming the difficulties associated with the MG process, the Infiltration Growth (IG) process was developed [7]. It allows near-net shape

fabrication of REBCO simultaneous with microstructures that support high current density [8]. The IG process involves the infiltration of liquid phases ($BaCuO_2$ and $CuO$) into a porous preform of the primary $RE_2BaCuO_5$ (RE-211) phase and subsequent reaction between them to form RE-123 on cooling below the peritectic formation temperature [9-10]. The reaction occurring between RE-211 and the liquid phases is shown below.

$$RE_2BaCuO_5 + 3BaCuO_2 + 2CuO \rightarrow 2REBa_2Cu_3O_{7-\delta}$$
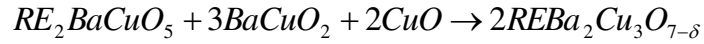
Though the IG process has many advantages compared to the MG process like the minimization of shrinkage, cracks and distortions in the final product, various reports discuss the occurrence of inhomogeneity in the distribution of $Y_2BaCuO_5$ (Y-211) particles in the YBCO matrix [7-13]. This causes a wide variation, across the sample volume, in the microstructure and the current densities [12, 14]. The problem of inhomogeneity in the RE-211 distribution and hence of the non-uniformity in $J_c(H)$, occurs even in MG processed samples [15-17]. In MG process an extent of 2-30% porosity is reported in literature [18-24], which is attributed to the oxygen gas evolution during peritectic decomposition of RE-123 into RE-211 and liquid phases. Both *Mahmood et al*. and Iida et al. [14, 26] have reported a residual porosity of only up to ~ 1% in IG processed REBCO samples and this is because no oxygen gets released during IG process [27-30]. Though the pore size and their density in the RE-123 samples can be much reduced by employing IG process, the extent of reduction depends on the conditions used for their fabrication. *Devendra et al.* [31-32] reported porosity as low as ~ 0.2% in the optimized YBCO samples processed using a modified IG process. Modifications were made to the IG process paying special attention to the stability of the preform used in the process. This modified process was named as "Preform Optimized Infiltration

and Growth Process (POIGP)". The Y-211 preforms used were made under relatively higher compaction pressures (460 MPa) and were sintered at 950 $^{o}$C for an optimum duration prior to the liquid phase infiltration, so as to offer enough mechanical rigidity during the infiltration process. Thus POIGP led to microstructures with minimal porosity and a homogenous distribution of Y-211 inclusions in the superconducting Y-123 matrix [31].

The POIG process involves heat treatment to 1100 $^{o}$C to render sufficient infiltration and was found to yield good YBCO samples with considerable $J_c$ sustained to high fields (i.e. flat $J_c$ to high fields). However, these samples are found to exhibit [103] texture [32], unlike the [00l] texture reported in seeded melt textured REBCO samples [33-35]. Since the source pellet Y-123 melts at 1008 $^{o}$C and the Nd-123 seed melts at 1065 $^{o}$C, seeded growth giving rise to [00l] texture is not feasible if infiltration of liquid phases is carried out at 1100 $^{o}$C in POIG process. Hence, it is worth investigating the pros and cons of selecting a lower infiltration temperature ($T_i$) during the POIG process, with regard to the properties of the resultant YBCO, in order to envisage seeded growth during POIGP.

While $T_c$ is an intrinsic property, field dependence of $J_c$ strongly depends on the microstructure of the end product which in turn depends on the processing conditions [36]. To obtain high quality REBCO materials for practical applications reproducibly, an understanding of the fundamental factors responsible for achieving favourable microstructures in REBCO superconductors is essential [37-38].

There are several reports on the nucleation of $Y_2BaCuO_5$ (Y-211) from YBCO melt and their growth in melt-grown REBCO materials. It is established that the peritectic recombination of Y-211 and liquid phases forms Y-123 phase [38-43]

along with some amount of remnant liquid phase or Y-211 depending on the choice of the starting composition. Homogenous distribution of fine Y-211 particles in the matrix of Y-123 contributes to the much needed flux pinning caused by defects created at Y-211/Y-123 interface. Presence of an optimum content of fine-sized RE-211 inclusions uniformly distributed in the matrix of RE-123 is known to improve the flux pinning and enhance the magnitude of $J_c$ and lead to superior field dependence of $J_c$ [12, 44]. The most efficient way to fulfil these requirements is to control the size of the Y-211 particles in the molten state, prior to the grain growth of Y-123 [45].

Numerous empirical processes have been developed for optimizing the size; content and morphology of Y-211 particles in melt processed YBCO. It has been reported that finer the starting extra Y-211 added to Y-123 (in the precursor powder), the finer will be the size of residual Y-211 particles in the end product obtained after melt processing [46]. Both the starting composition of the precursor powder and the thermal profile used to melt process influence the size and morphology of the Y-211 particles [47-49].

In the MG process, the Y-123 decomposes into Y-211 and liquid phases; which later recombine while being cooled below peritectic temperature ($T_p$). This process involves outflow of liquid phases during melting and hence fails to provide a means to study the mechanism of the recombination. On the other hand, in IG process liquid phases infiltrate into Y-211 preform and when cooled through $T_p$ they react with Y-211 particles and form Y-123 matrix with finer unreacted Y-211 particles left back in the matrix. Hence IG process gives an opportunity to investigate reaction mechanism [31, 50] and the factors that control the Y-211 particle size. Uniform distribution of fine sized Y-211 particles of ~ 1-2 μm size can be observed in IG processed products [51], when

compared to a size range of 0.5 –3 μm achieved on adding grain refiners like Pt and $CeO_2$ in MG process [52-56].

In order to choose appropriate processing conditions, mechanism of growth of Y-123 and the resultant dispersion and size of Y-211 particles in Y-123 matrix have been studied in this chapter by quenching the samples from selected temperatures during IG process as described in section 3.2. The effect of choosing a lower infiltration temperature is discussed in section 3.3.

## 3.2    Growth mechanism through quenching:

The vertical furnace used for quenching the samples is shown in fig. 3.1 (a) and the heat treatment schedule used for quenching the samples into liquid nitrogen ($LN_2$) is given in fig. 3.1 (b).
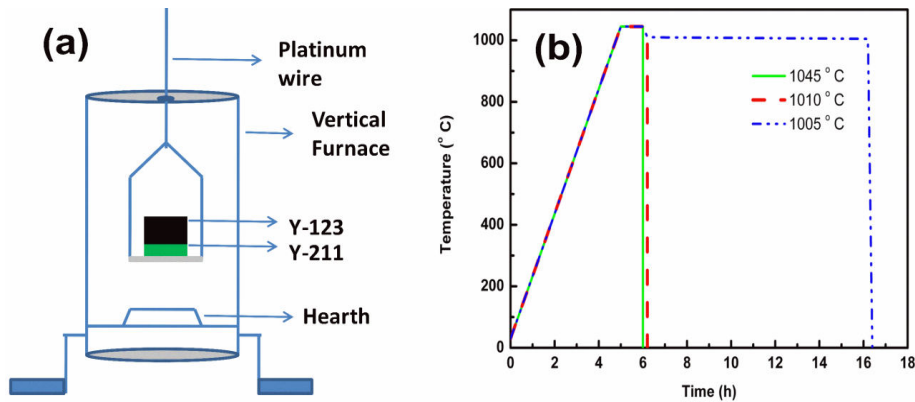


**Fig. 3.1.** (a) Vertical furnace with alumina muffle, used for quench experiments. (b) The heat treatment schedules for quenching the samples.

The Y-211 and Y-123 pellets were assembled as shown in fig. 3.2 for the POIG process. The pellets were supported on inert substrates to prevent liquid phase loss and to avoid contamination from the alumina crucible used [31].
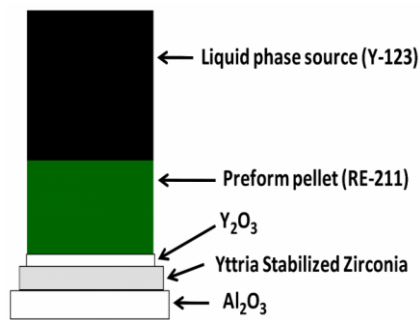
**Fig. 3.2.** The sample assembly used in POIGP. Y-123, which is the liquid phase source, is kept on top of a Y-211 pellet pressed under an optimum pressure of 460 MPa. They are supported on top of a thin Yttria pellet and dense plates of Yttria stabilized Zirconia and alumina as shown.

Details of the three samples chosen for study are given below. All three sample assemblies were ramped to 1045 $^{o}$C in 4 hours and were maintained there for 1 hour for liquid phase infiltration into Y-211 preform.

**S45:** The first sample was quenched into $LN_2$ from 1045 $^{o}$C. Resultant sample is S45.

**S10:** The second sample assembly after a dwell at 1045 $^{o}$C for 1 hour as given for S45, was cooled to 1010 $^{o}$C within 0.2 hour time and was quenched into $LN_2$ resulting in sample S10.

**S05:** The third sample assembly after a dwell at 1045 $^{o}$C for 1 hour followed by cooling to 1010 $^{o}$C in 0.2 hour as for S10, was further cooled to 1005 $^{o}$C, which is below the peritectic temperature of 1008 $^{o}$C, slowly at a cooling rate of 0.5 $^{o}$C/h and was quenched into $LN_2$ to obtain sample S05.

Microstructural characterization and the compositional analysis were performed using FESEM and EDS facilities. The Y-211 particles in the matrix of Y-123 were observed under FESEM using an in-lens detector.

### 3.2.1    Microstructural characterization:

The present investigation details the formation of Y-123 phase at various stages of IG process. It is interesting to observe the initial particle size and morphology of Y-211 particles prior to examining the final microstructure. FESEM image recorded at 25 kx magnification on the Y-211 powder sintered at 950 $^o$C for 12 h is shown in fig. 3.3 (a) and the corresponding histogram is shown in fig. 3.3 (b). It is observed from fig. 3.3 (a) that the Y-211 particles are spherical in morphology and are fused with one another after sintering at 950 $^o$C.
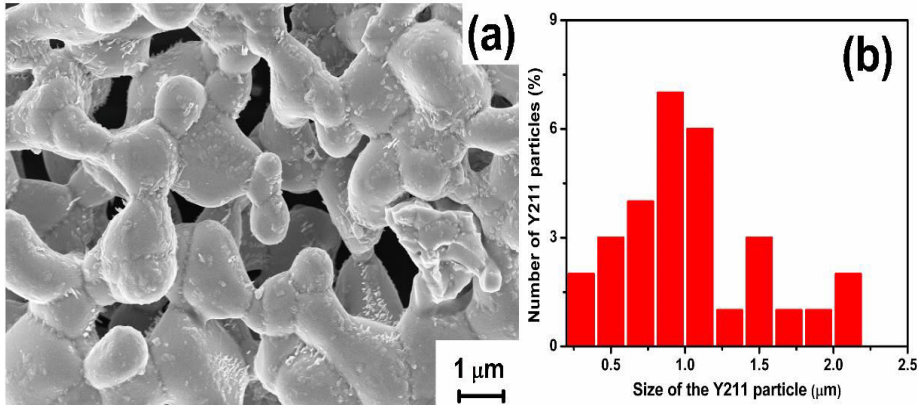


**Fig 3.3.** (a) FESEM image for Y-211 powder sintered at 950 $^o$C obtained at a magnification of 25 kX, (b) The histogram for Y-211 particle size, the average size of the Y-211 particles is ~ 1 μm. The Y-211 particles after sintering are rounded and fused among themselves to some extent.

Optical images recorded in the quenched samples S-45, S-10 and S-05 are shown in figs. 3.4 (a), (b) and (c).
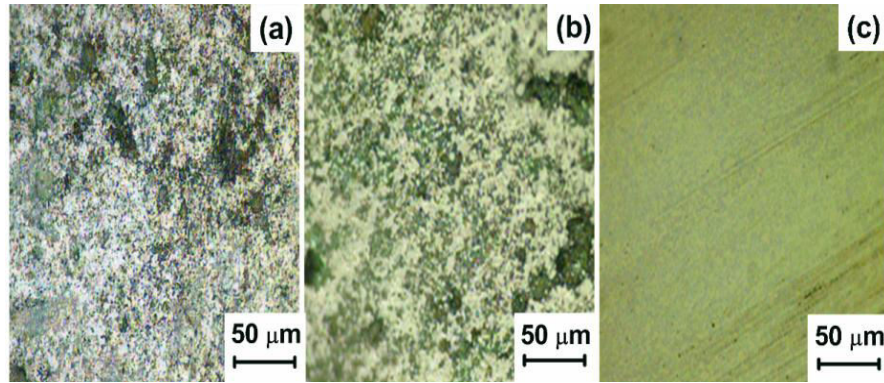
**Fig. 3.4.** Optical micrographs of the differently quenched S45, S10 and S05 samples are shown in figs (a), (b) and (c) respectively.

On first look one observes the following.

Optical images at different magnifications show that there are no gaps between Y-211 particles which are much closely spaced. We can also observe the presence of dark color phase (which could be unreacted liquid phases) that are infiltrated into the Y-211 preform in (a) and (b). We note here that in the case of S45, after allowing infiltration of liquid phases at 1045 $^{o}$C we did not give much time to react with Y-211 particles and also the temperature used for quenching is much above the peritectic temperature of YBCO.

Figs. 3.5 (a), (b), and (c) show the micrographs of S45 sample obtained under magnifications of 5, 10, and 20 kx respectively. Distribution of Y-211 particles can be seen to be uniform within the bulk of the sample and large pores can also be observed. Fig. 3.5 (b) shows that most of the Y-211 particles have sharp edges and the size of Y-211 particles is > 2 $\mu$m. Fig. 3.5 (c) shows the presence of liquid phases around the Y-211 particles.
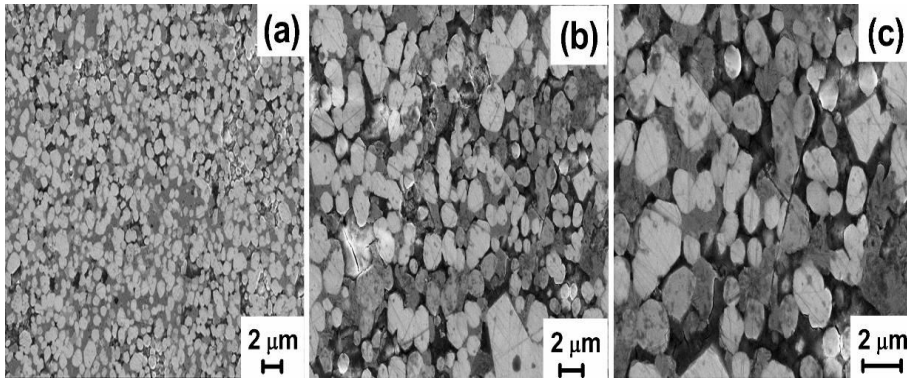
**Fig 3.5.** FESEM images from S45, which was quenched from 1045 °C. Some amount of liquid phase infiltration can be observed. It can be observed that Y-123 matrix is not formed.

Figs. 3.6 (a), (b), and (c) show the micrographs of S10 at magnifications of 5, 10, and 20 kx. Homogenous distribution of Y-211 particles and the presence of infiltrated liquids around Y-211 particles are seen. Fig. 3.6 (b) shows that sharp edges of the Y-211 particles are getting rounded up indicating that Y-211 particles have started reacting with liquid phases. Fig. 3.6 (c) shows that the infiltrated liquid phases filled the gaps between the Y-211 particles completely unlike in S45 where there were un infiltrated regions.
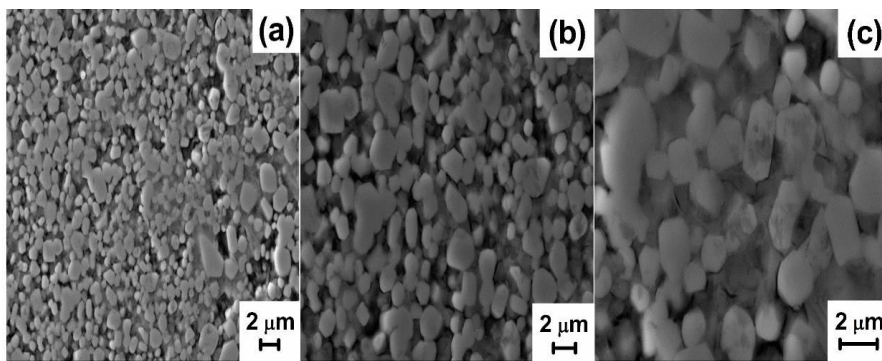


**Fig. 3.6.** FESEM micrographs of S10, are shown at increasing magnifications in figs. (a) to (c). It can be observed from fig. (c) that the sharp edges of Y-211 particles are rounded; the particles are still of the same size as in fig. 3.5.

Unlike S45 and S10, the sample S05 was allowed to cool slowly through $T_p$. A continuous Y-123 matrix with spherical Y-211 particles is observed in S05 indicating that the peritectic reaction has progressed by cooling to 1005 $^o$C. A homogeneous distribution of Y-211 particles can be observed in fig. 3.7 (a) and (b) at a magnification of 5 kx and 10 kx. FESEM micrograph at magnification of 20 kx, shown in fig. 3.7 (c), indicates that most of the Y-211 particles are spherical and are less than 1 μm in size, which is advantageous to increase Y-123/Y-211 interface defect density which would enhance the magnetic flux pinning.
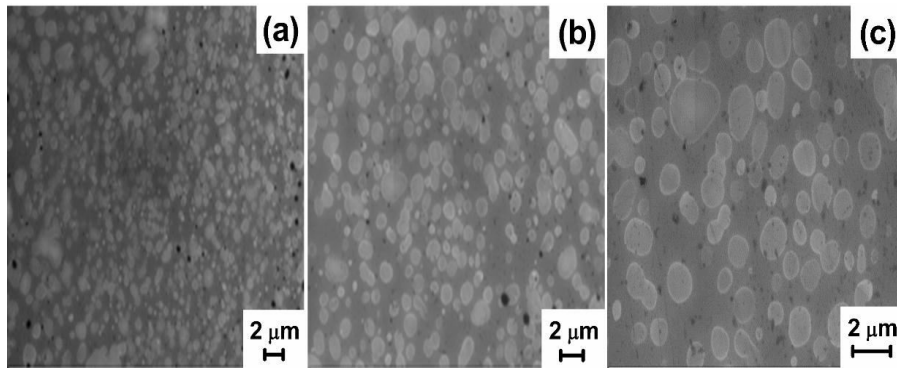


**Fig. 3.7.** FESEM of S05. The formation of Y-123 and uniform distribution of fine Y-211 particles in the Y-123 matrix can be seen. The Y-211 particles are spherical in shape and are smaller (< 1 μm) after the peritectic reaction with liquid phases.

In order to understand the origin of the occurrence of sharp edges of Y-211 particles in S45, we closely examined the microstructure of Y-211 pellet after it is pressed from Y-211 powder, and before infiltrating liquid phases which is shown in fig. 3.8.
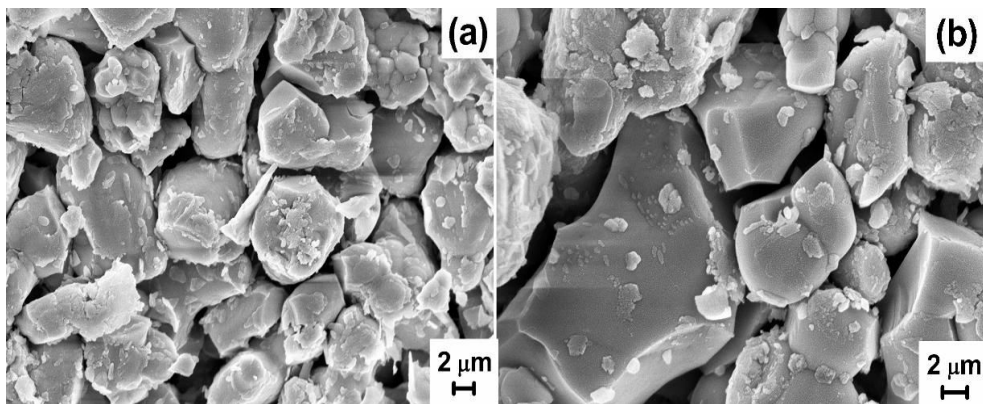
**Fig. 3.8.** FESEM micrographs of Y-211 powder after pressing into a pellet, before further heat treatments. Sharp edges have been for these particles due to cracking in the pressing process.

Fused Y-211 particles which were spherical in sintered powder (fig. 3.3 (a)) are found to be broken with sharp edges when pressed into pellet, as can be seen in figs. 3.8 (a) and (b). In fig. 3.8 (b), the sharp edges of the broken Y-211 particles which are of sizes around 1-2 μm can be seen. The applied pressure of 460 MPa seems to have broken the Y-211 particles.

### 3.2.2. Elemental Analysis:

An examination of the composition of the matrix region between Y-211 particles in a line scan has led to the following results as shown for S05, S10 and S45 samples in figs. 3.9 (a), (b) and (c) respectively.
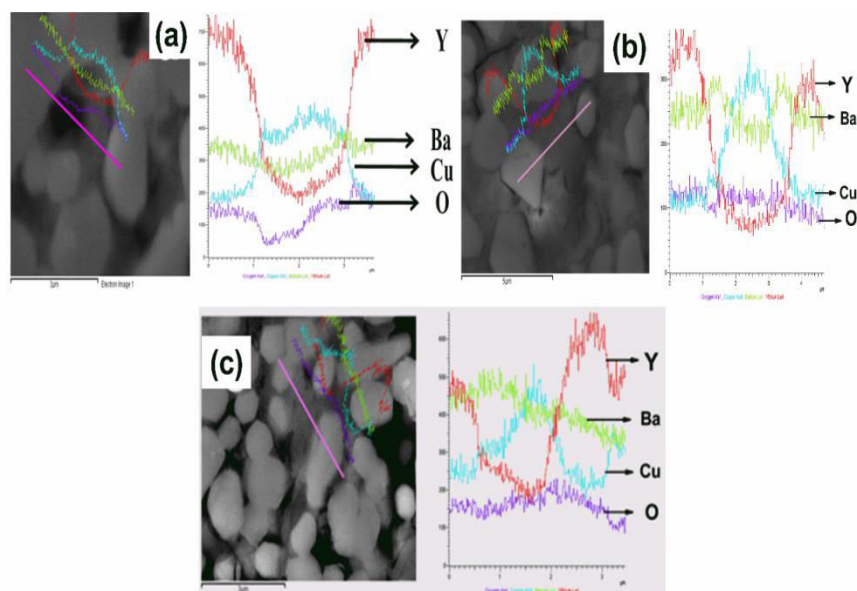
**Fig 3.9.** EDS line analysis of S05, S10 and S45. In S05 the matrix region between Y-211 particles Y-123 as deduced from the composition graph shows the ratio of elements Y: Ba: Cu to be nearly 1:2:3. In S10 and S45, we observe that liquid phases with high Ba and Cu content are present in the matrix region.

### 3.2.3. Structural Analysis:
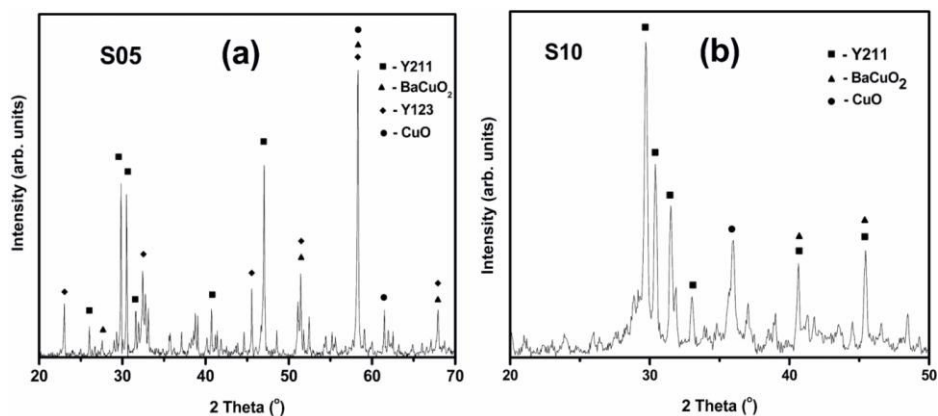


**Fig. 3.10.** XRD patterns of S05 and S10 with the Bragg peaks corresponding to Y-211, $BaCuO_2$, CuO and Y-123 phases marked.

In fig. 3.10 (a) all peaks are indexed to Y-211, $BaCuO_2$, CuO and Y-123 phases, taken from JCPDS file numbers 811199, 790838, 895899, and 898867 respectively. In fig. 3.10 (b) peaks corresponding to Y-123 phase which is in agreement with the EDS results that Y-123 has not formed in S10 sample. In both the XRD patterns Y-211 phase was dominant. But in S05 sample Y123 phase was found along with Y211 and $BaCuO_2$ phases due to prolonged heat treatment.

### 3.2.4. Discussion:

From the FESEM images recorded on sintered Y-211 powder, it is evident that due to sintering at a temperature of 950 $^o$C, all spherical Y-211 particles in the powder form are fused. From histogram it is clear that the starting sizes of the Y-211 phase particles are of the order of 500 nm to 1 μm.

EDS study confirms the formation of Y-123 in the matrix region in S05, whereas in case of S10 and S45 there is infiltration of liquid phases into the Y-211 preform but formation of Y-123 matrix is not seen. This shows that the quenching temperatures of these samples are 1010 $^o$C and 1045 $^o$C, which are above $T_p$ and hence Y-123 matrix formation has not commenced in these S10 and S45 samples. The composition of the precipitates is inferred in all the samples to be Y-211 from EDS studies. These results agree with the conclusions drawn from the microstructural studies. Structural study through XRD is also confirmed the formation of Y-123 phase in S05 along with the traces of Y-211 and liquid phases (BaO+CuO). Whereas in S10 only Y-211 and liquid phases were found.

From the FESEM images in S05 sample we can observe the formation of platelets and also the continuous Y-123 matrix with homogenously distributed

Y-211 particles. But in the case of S10 we observe the unreacted infiltrated liquid phases in the Y-211 preform (confirmed through EDS) and there is not much space present in between the Y-211 particles, which have got rounded up. Since the temperature used for quenching is just above the peritectic temperature of YBCO, the observations suggest that the peritectic reaction is just about to start. Sharp edges of Y-211 observed in S45 suggest that there is no reaction between Y-211 and liquid phases as the sample was quenched from 1045 $^{o}$C, which is much above the $T_p$.

Quench studies of IG processed YBCO samples show that the fused Y-211 particles in sintered powder are broken during pelletization, forming sharp edged individual particles. The Y-211 particles have very sharp edges in S45 which are less sharp in S10 as the peritectic reaction is about to start. In S05, the Y-211 particles became spherical and got refined to < 1 μm size because of peritectic reaction during slow cooling from 1010 $^{o}$C to 1005 $^{o}$C, which is below $T_p$. These results are supported by micro-structural, compositional, which revealed that sufficient liquid phases infiltration and Y-123 phase formation in the matrix region led to very fine and spherical Y-211 precipitates uniformly distributed, as seen in S05.

## 3.3.    Effect of Infiltration temperature on the properties of Infiltration Growth Processed YBCO superconductor:

The importance of optimizing the fabrication of the Y-211 preform in achieving high current densities to high magnetic fields has recently been established [31-32]. Here we have investigated the effect of the choosing the infiltration temperature to be 1100 $^{o}$C (sample Y-1) and 1040 $^{o}$C (sample Y-2) on the microstructure, magnetic properties and mechanical strength of POIG processed YBCO superconductor. The reason for such a study stems from the observation

that a $T_i$ of 1100 °C being well above the $T_p$ of the seed crystal (even Nd-123) and hence will not be effective in fabricating single domain components by POIG process. A study of lower $T_i$ is aimed at facilitating infiltration below $T_p$ = 1048 °C of the seed crystal.

Hence, in the present work we have compared the results of subjecting the sample assembly to a $T_i$ of 1040 °C with those subjected to $T_i$ of 1100 °C. Sintered powders of Y-123 and Y-211 were taken in 2:1 ratio and were compacted into pellets separately under an optimum pressure of 460 MPa. The Y-211 and Y-123 pellets were assembled as shown in fig. 3.2 for the POIG process [31].

Two different samples Y-1 and Y-2 are prepared by POIG process by following the heat-treatment schedules with infiltration temperatures 1100 °C and 1040 °C as shown in fig. 3.11.
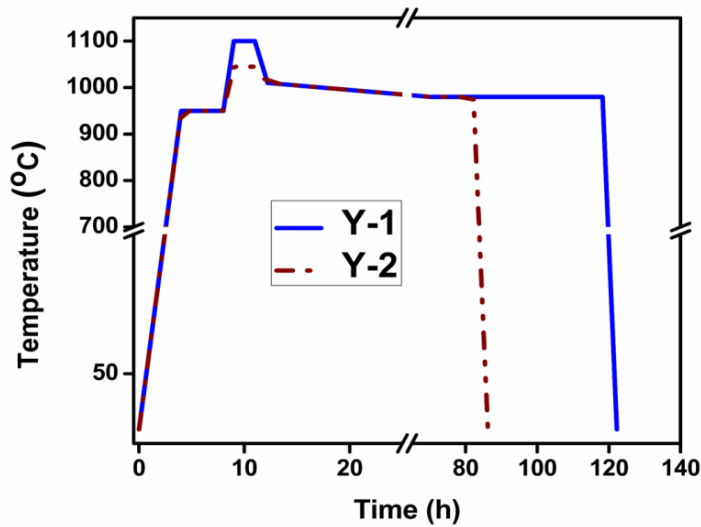


**Fig. 3.11.** The heat treatment schedules followed to synthesize the samples Y-1 and Y-2. The only difference between the two heat treatments is the infiltration temperature. For sample Y-1, $T_i$ was 1100 °C, and for sample Y-2, it was 1040 °C.

The POIG process involves heat treating the sample assembly to $T_i$ where infiltration of liquid phases takes place into Y-211 preform, followed by cooling to 1010 $^o$C, and slow cooling from 1010 $^o$C to 980 $^o$C. Then the samples were furnace cooled. The samples thus obtained were oxygenated in a tubular furnace at 460 $^o$C in flowing oxygen for 100 h [31]. The temperature of the furnace was controlled and monitored using a Eurotherm make temperature controller (model 2404) and a thyristor (TE10A). Photographs of the IG processed samples Y-2 and Y-1 are shown in fig. 3.12 .



**Fig. 3.12.** (a) IG processed sample Y-2 prepared starting with a preform infiltrated at 1040 $^o$C and (b) IG processed sample Y-1 prepared starting with a preform infiltrated at 1100 $^o$C.  The arrows point to the final POIG processed samples.

### 3.3.1.  Structural properties:

Processing the samples to 1100 $^o$C does not permit seeded growth which is generally used to achieve [00l] texture. The XRD pattern recorded in sample Y-1 and Y-2 are shown in fig. 3.13. It can be seen that both the samples are textured in [103] direction.
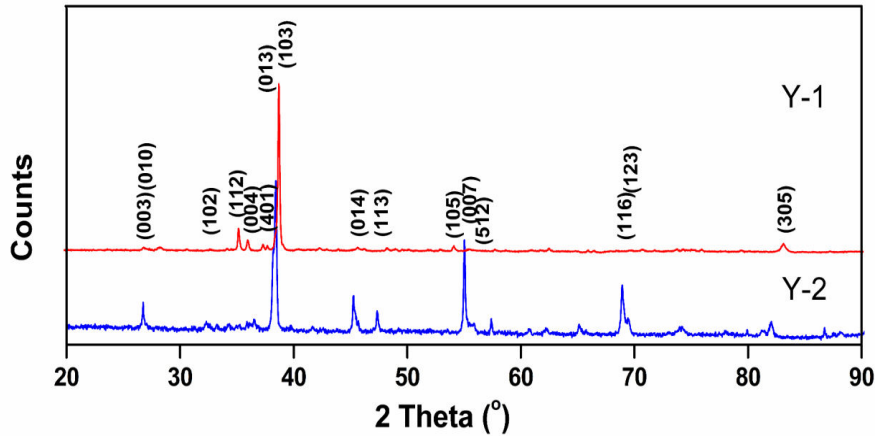
**Fig. 3.13.** XRD patterns from sample Y-1 and Y-2 showing [103] texture.

## 3.3.2. Microstructural properties:
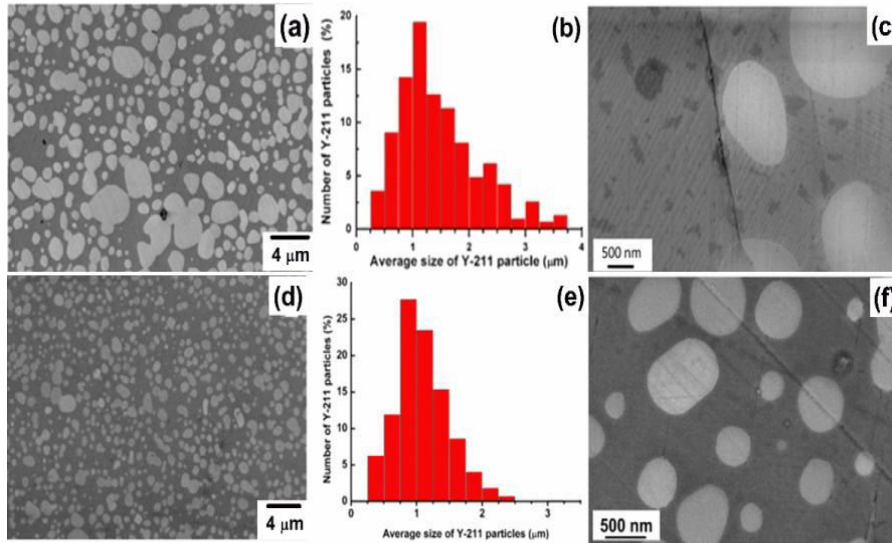


**Fig. 3.14.** Y-211 particles are distributed uniformly in the Y-123 matrix of the samples (a) in Y-1 and (b) in Y-2. The histograms for Y-211 particle size distribution in Y-1 and Y-2 are shown in (b) and (e) respectively. It can be observed that a substantial number of Y-211 particles are of size below 1 µm in both the samples; in the sample Y-2 for which the infiltration temperature was lower, the Y-211 particles are finer in size. Twinning is observed in the Y-123 matrix of sample Y-1 (fig. c), and not observed in sample Y-2 (fig. f).

Analysis of the microstructures was carried out in samples Y-1 and Y-2 to assess the distribution and size of the non-superconducting Y-211 particles in the superconducting Y-123 matrix using Carl Zeiss-Axio Vision image processing software on the micrographs obtained from FESEM.

FESEM images obtained in samples Y-1 and Y-2 are shown in fig. 3.14 (a-c) and (d-f) respectively. The Y-211 particles can be seen to be fine, spherical and uniformly distributed in the Y-123 matrix in both the samples. From histograms it is clear that the distribution of Y-211 shows that majority of the particles are in the range of 0.5–1.5 μm in both the samples.

### 3.3.3. Magnetic properties:
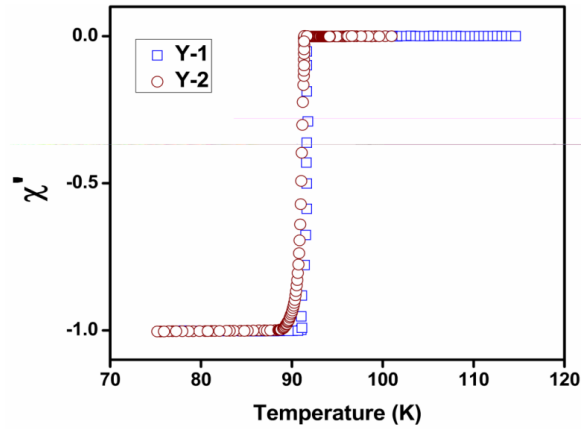


**Fig. 3.15.** The temperature dependence of in phase component of the ac susceptibility ($\chi^{'}$) in samples Y-1 and Y-2.

The temperature dependence of the in-phase components of ac susceptibility ($\chi^{'}$) measured at 33 Hz for the two samples are shown in fig. 3.15. The figure reveals onset of $T_c$ to be at 91.6 K in sample Y-2 with a small tail region close to $T_c$ (zero) indicating possible existence of minor amounts of lower $T_c$ phases which could be oxygen deficient phases [14, 57]. For Y-2 sample onset of a

sharp superconducting transition is found at 92.1 K in sample Y-1. The transition width ($\Delta T_c$) is nearly 0.7 K for Y-1 and 2.5 K for Y-2 sample as measured between 10 % to 90 % increase of diamagnetic susceptibility.

M-H loops were recorded in the samples at different temperatures sweeping the magnetic field in the range 0-8 Tesla for both the samples (Y-1 and Y-2) using a physical property measurement system (PPMS). $J_c$ was calculated by following extended Bean's Critical State model [58-60], using the formula $J_C = \dfrac{20\Delta M}{d}$ Acm$^{-2}$. Here $\Delta$M (in emu/cc) is the difference in the hysteretic magnetization between the curves obtained while increasing and decreasing the magnetic fields ($\Delta$M= M$^+$- M$^-$) and $d = b\left(1 - \dfrac{b}{3a}\right)$ is the reduced dimension, where '$a$' and '$b$' are the planar dimensions (in cm) of the sample with $a \geq b$. The dimensions of the specimens used in magnetization measurements were $a =$ 2 mm, $b$=1.5 mm, and $c$=5 mm, for samples Y-1 and Y-2.
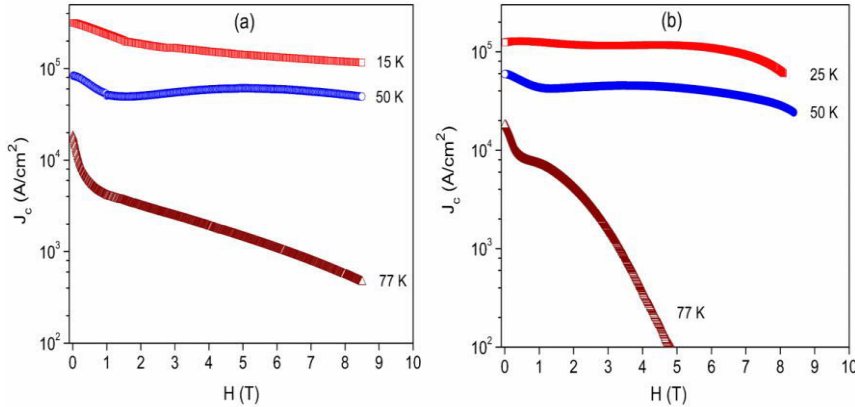


**Fig. 3.16.** (a) and (b) shows magnetic field dependence of $J_c$ at different temperatures for samples Y-1 and Y-2 respectively. It can be observed that the $J_c$ of sample Y-2 ($T_i$ = 1040 $^o$C) is not sustained to very high magnetic fields as for the sample Y-1. This is in spite of a finer Y-211 distribution in the former case.

To estimate the critical current densities, magnetic hysteresis loops were recorded for which the magnetic field (H) was applied normal to the pressed surface of the sample and was varied up to 14 T and 9 T at different temperatures for samples Y-1 and Y-2 respectively. The field dependences of $J_c$ at different temperatures are shown in fig. 3.16.

At temperatures of 50 K and below, high $J_c$ values were retained up to the maximum applied fields of 8 T for both the samples. On the other hand at 77 K, the $J_c$ is found to decrease rapidly beyond 2 T for sample Y-2. Sample Y-2 showed a zero-field $J_c(0)$ of ~ 126.4 kA/cm$^2$ at 25 K which decreased to ~ 18.1 kA/cm$^2$ when warmed up to 77 K. Sample Y-1 showed $J_c(0)$ of 316 kA/cm$^2$ at 15 K which reduced to 18.2 kA/cm$^2$ at 77 K. It is evident from figs. 3.16 (a) and (b) that the performance of sample Y-1 which exhibited a flat $J_c$ better than 1 kA/cm$^2$ at 77 K up to 7 T is superior to that of sample Y-2. Microstructural and magnetic properties of the samples Y-1 and Y-2 are compared in Table 3.1.

**Table. 3.1.** Microstructural and magnetic properties of the samples Y-1 and Y-2.

| | Y-1 | Y-2 |
|---|---|---|
| $T_i$ ($^{\circ}$C) | 1100 | 1040 |
| $T_c$ (K) | 92.1 | 91.6 |
| $\Delta T_c$ (K) | 0.7 | 2.5 |
| Y- 211 size ($\mu$m) | 1 - 1.25 | 0.75 - 1 |
| $J_c$ (0) at 77 K (kA/cm$^2$) | 18.2 | 18.1 |
| Width of twins (nm) | 25 - 100 | -- |
| Macro porosity (%) | 0.2 | 2.7 |
| Vol. % of Y-211 | 46.3 | 43 |

### 3.3.4. Mechanical properties:

The development of bulk high-temperature superconductors (HTSC) and their applications has today come to a point where the mechanical response to high magnetic fields is as important as their critical-current density and large-grain property. In fact, in the currently produced centimetre-sized single-domain HTSC bulks with strong pinning, leading to high critical current density, the pinning induced strain can be so huge that it threatens the mechanical stability of the material [5]. For trapped field applications of oxide superconductors, materials with high $J_c$ as well as high mechanical strength are required. Therefore, the major research objective is to improve the mechanical properties simultaneous with their critical currents in REBCO materials.

It is observed while cutting the samples Y-1 and Y-2 for microstructural studies that Y-2 is brittle, while Y-1 with superior $J_c(H)$ is quite hard. This section presents a systematic evaluation of mechanical properties at local level in Y-1 and Y-2. Surface indentation experiments carried out by a nano-indenter were used to probe the mechanical properties of the solid surface by measuring the nano-scale penetration depth of the indenter and the applied force; such information is highly valuable to assess the influence of local stresses and the robustness of the ceramic surface [61-65]. Though it probes on the surface, polished section from interior gives information on local stresses/strength on selected phases/regions/grains. For the measurement of hardness ($H_n$) and elastic modulus ($E_r$) a nanoindenter, TI 900 Tribo-Indenter, Hysitron make, was used. The measurements were carried out at 16 different points on each polished sample. Nano-indentation studies at low applied loads enable the determination of $H_n$ and $E_r$ of each of the phases in the superconductor composites, separately. This would be unlike in measurements at high applied loads which would create indentations of sizes bigger than the size of the Y-211

inclusions [66]. The samples were indented by a Berkovich-type pyramidal diamond tip with a maximum load of 8,000 μN for each indent. Oliver and Pharr [61-62] method was used to analyze the load–displacement data recorded during indentation, to determine $E_r$ and $H_n$ values. To overcome the error due to the choice of the indenter, reduced modulus $E_r$ is defined for non-rigid indenters based on the load-displacement behaviour, through the equation.

$$\frac{1}{E_r} = \frac{(1 - v^2)}{E} + \frac{(1 - v_i^2)}{E_i}$$

Where $E$ and $v$ are Young's modulus and Poisson's ratio for the specimen and $E_i$ (1141 GPa) and $v_i$ (0.07) are the corresponding parameters for the Berkovich diamond indenter. In general $v$ is set equal to 0.3 for YBCO [61-62, 66].
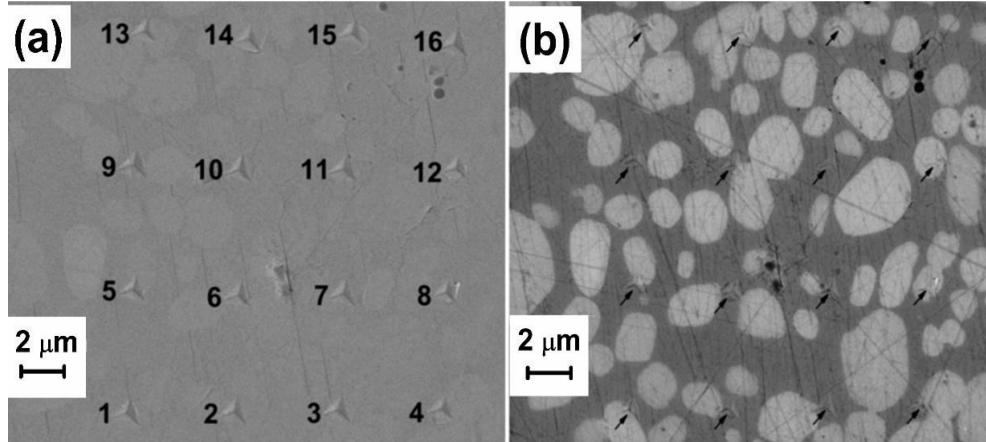


**Fig. 3.17.** FESEM images recorded after nano-indentation in Y-1 using (a) SE and (b) in-lens detectors. The SE image in (a) clearly shows the position of the indent and in (b) the microstructure of the same region can be clearly seen. In (a) serial numbers are provided for each indent, and in (b) position of the indents are pointed out with arrow marks.

The nano-indentation marks are clearly visible as seen in fig. 3.17 (a), when recorded using the secondary electron mode. The same area is observed using

the in-lens mode of the FESEM to observe the Y-211 grains (fig. 3.17 (b)). From 16 measurements, the indents falling on Y-123 matrix and the Y-211 grains are selectively studied, ignoring those located partially on Y-123 and Y-211. The $H_n$ and $E_r$ values were then determined at different indents formed exclusively on the Y-123 superconductor matrix phase and on the Y-211 grains.

Similar measurement is carried out for sample Y-2, FESEM images of Y-2 sample after indentation measurements are shown in figs. 3.18.
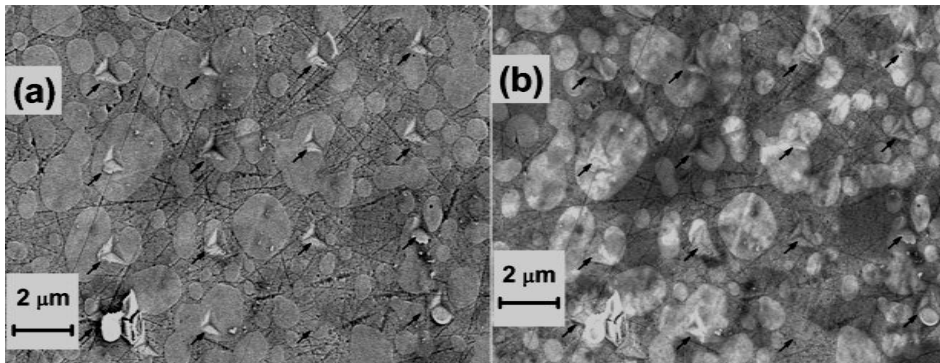


**Fig. 3.18.** FESEM image of Sample Y-2 recorded after indentation using SE and in-lens detectors are shown in (a) and (b) respectively.

### 3.3.5. Discussion:

From the microstructural studies it can be understood that compared to sample Y-1, sample Y-2 shows presence of a large number of fine particles < 0.5 μm, while Y-1 shows considerable number of Y-211 particles larger than 2 μm, which could be because higher temperature of operation promotes grain growth. The above microstructural studies demonstrate a clear improvement in producing uniform distribution of fine Y-211 particles in both the samples Y-2 and Y-1 processed by POIGP, even without adding any grain refiners like Pt and $CeO_2$, when compared to various reports in literature on samples made using MG and IG processes [13, 15, 17, 67]. Higher $T_i$ appears to have resulted

in sufficient amount of infiltration into Y-211 preform reducing the extent of macro defects to 0.2% in sample Y-1 compared to 2.7 % in sample Y-2. Additionally, widespread twinning is observed in Y-1. The sizes of the twin widths are of the order of 25-100 nm, whereas twinning is not observed in Y-2.

The structural of the both the samples (Y-1 and Y-2) resulted in (103) direction. We believe that due to slow cooling (0.5 $^o$C/h) both the samples (Y-1 and Y-2) have crystallized in [103] structure. Some peaks were indexed to Y-211 phase, while no other impurity phases were found to be present.

Though both the samples Y-1 and Y-2 show equally good distribution of Y-211 in Y-123 matrix and considerable zero field $J_c$, sample Y-1 shows better field dependence of $J_c$ which is flat up to 7 T at 77 K. But $J_c(H)$ curve of Y-2 sample shows a rapid fall at high fields. The fact that the Y-211 particles are fine and spherical is expected to contribute to considerable flux pinning and enhancement of $J_c$ due to large Y-123/Y-211 interfacial defects [57]. This result is attributed to the microstructural properties that even though the distribution of Y-211 particles sizes are comparable in both samples, no twinning is observed in Y-2 sample which also exhibits macro-porosity.

Even though all Y-211 powders used for fabricating the YBCO samples were prepared by same method, due to processing at different temperatures it is observed that the hardness values at of Y-211 site got modified. It can be noticed in Y-2 that due to processing at lower $T_i$, a lower hardness value of 10.94 GPa on an average is observed. FESEM images of Y-2 after indentation has been done are displayed in fig. 3.18.

The mechanical properties of different phases (Y-123 and Y-211) of both the samples are presented in Table 3.2. We observe from the Table 3.2 that the $H_n$

and $E_r$ have average values of around 17.7 GPa and 290 GPa respectively for Y-123 phase and 23.0 GPa and 302 GPa for Y-211 phase, in sample Y-1. For sample Y-2, the corresponding values are considerably lower at 9.5 GPa and 145 GPa respectively for Y-123 phase and 10.9 GPa and 140 GPa for Y-211 phase.

**Table. 3.2.** Mechanical properties of Y-1 and Y-2 measured on the Y-123 and Y-211 phases in both the samples.

### Y-123

| | Y-1 | | Y-2 | |
|---|---|---|---|---|
| Meas. No. | $H_n$ (GPa) | $E_r$ (GPa) | $H_n$ (GPa) | $E_r$ (GPa) |
| 3 | 17.3 | 288 | 8.6 | 150 |
| 6 | 17.0 | 292 | 10.7 | 137 |
| 7 | 17.4 | 289 | 9.3 | 144 |
| 9 | 19.0 | 291 | 9.0 | 148 |
| 11 | 17.1 | 290 | 9.6 | 146 |
| 13 | 18.6 | 289 | 9.9 | 147 |
| Avg. | 17.7 | 290 | 9.5 | 145 |

### Y-211

| | Y-1 | | Y-2 | |
|---|---|---|---|---|
| Meas. No. | $H_n$ (GPa) | $E_r$ (GPa) | $H_n$ (GPa) | $E_r$ (GPa) |
| 8 | 19.9 | 294 | 10.2 | 114 |
| 12 | 24.8 | 309 | 11.4 | 153 |
| 14 | 23.5 | 303 | | |
| 15 | 23.6 | 304 | 11.2 | 152 |
| Avg. | 23.0 | 302 | 10.9 | 140 |

Mechanical properties of composite (average values of 16 indents) and different phases are compared with the values from literature and are given in Table 3.3. From this table it can be observed that the mechanical properties of the sample Y-1 are superior to the Y-2 and also the MG and IG processed samples reported in literature [68].

We attribute higher hardness of the sample Y-1 to be correlated to (a) high density of nanometric defects associated with twinning in matrix, starting at the twin boundaries, in the highly dense crossing-twin network in the superconductor and (b) minimization of macro defects after facilitating

infiltration at 1100 °C. It is worthwhile to note that enhancements in mechanical strength simultaneous with high $J_{c\ to}$ high fields seems to be originating from a stress field caused by uniform distribution of defects in a wide size range.

**Table 3.3.** Comparison of mechanical properties with those reported in the literature.

| Sample | Applied load (mN) | Phase | $H_n$ (GPa) | $E_r$ (GPa) | Reference |
|--------|-------------------|-------|-------------|-------------|-----------|
| Y-1 | 8 | Y-123 | 17.7 | 290 | Present study |
| | | Y-211 | 23.0 | 302 | |
| | | Composite | 19.2 | 292 | |
| Y-2 | | Y-123 | 9.5 | 145 | |
| | | Y-211 | 10.9 | 140 | |
| | | Composite | 9.7 | 141 | |
| Bridgman | 10 | Y-123 | 11.4 | 185 | [64] |
| | | Composite | 15.3 | 201 | |
| MTMG | | Y-123 | 11.0 | 192 | |
| | | Composite | 14.9 | 206 | |
| Thin film | 2 | Composite | 8.5 | 210 | [65] |

The results obtained on the two samples Y-1 and Y-2 subjected to infiltration temperatures, $T_i$ of 1100 °C and 1040 °C respectively are compared. Though both the samples Y-1 and Y-2 show equally good distribution of Y-211 in Y-123 matrix and considerable zero field $J_c$, sample Y-1 shows better field dependence of $J_c$ which is flat up to 7 T at 77 K and it also exhibits higher hardness. Though YBCO samples with [00l] texture are reported to yield higher zero field $J_c$ values when field is applied along c-axis, heat treatment at 1100 °C is found, from the present work to yield higher hardness and retention of high $J_c$ to high fields. Infiltration at higher temperature is found to yield highly dense composites with minimal macro-defects and higher hardness of 19.2 GPa in sample Y-1. The occurrence of higher hardness, simultaneous with retention of considerably high current density to high fields in sample Y-1 has definite

advantages for trapped field applications.

**References:**

1. D.C. Larbalestier, Physics Today **6** (1991) 74.

2. D.C. Larbalestier, S.E. Babcock, X. Cai, M. Daeumling, D P. Hampshire, T.F. Kelly, L. Lavanier, P.J. Lee and J. Seuntjens, Physica C **153-155** (1988) 1580.

3. R. Flukiger, T. Muller, W. Goldacker, T. Wolf, E. Seibt, I. Apfelstedt and H. Kupfer, W. Schauer, Physica C **153-155** (1988) 1574.

4. R.L. Meng, C. Kinalidis, Y.Y. Sun, L. Gao, Y.K. Tao, P.H. Hor and C.W. Chu, Nature **345** (1990) 326.

5. J.G. Larsen, N.E. Dam, C.S. Jacobsen, H.D. Baerendtsen and J.G. Sommerschield, Physica C **217** (1993) 135.

6. D. Shi, K. Lahiri, J.R. Hull, D. LeBlanc, M.A.R. LeBlanc, A. Dabkowski, Y. Chang, Y. Jiang, Z. Zhang and H. Fan, Physica C **246** (1995) 253.

7. E. Sudhakar Reddy and T. Rajasekharan, J. Mater. Res. **13** (1998) 2472.

8. R. Cloots, T. Koutzarova, J.P. Mathieu and M. Ausloos, Supercond. Sci. Technol. **18** (2005) R9.

9. N. HariBabu, T. Rajasekharan and V. SeshuBai, Eur. Phys. J. B. **4** (1998) 55.

10. E. Sudhakar Reddy and T. Rajasekharan, Supercond. Sci. Technol. **11** (1998) 523.

11. T. Miyamoto, J. Katagiri, K. Nagashima, M. Murakami, IEEE Trans. Appl. Supercond. **9** (1999) 2066.

12. S. Meslin, J.G. Noudem, Supercond. Sci. Technol. **17** (2004) 1324.

13. K. Iida, Hari N. Babu, T.D. Withnell, Y. Shi, S. Haindl, H.W. Weber and D.A. Cardwell, Physica C **445–448** (2006) 277.

14. K. Iida, N. HariBabu, Y. Shi and D.A. Cardwell, Supercond. Sci. Technol. **18** (2005) 1421.

15. Y.L. Jiao, L. Xiao, H.T. Ren, M.H. Zheng and Y.X. Chen, Physica C **386** (2003) 266.

16. J.C.L. Chow, H.T. Leung, W. Lo and D.A. Cardwell, J. Mater. Sci. **33** (1998) 1083.

17. A. Endo, H.S. Chauhan and Y. Shiohara, Physica C **273** (1996) 107.

18. E. Mendoza, T. Puig, E. Varesi, A.E. Carrillo, J. Plain and X. Obradors, Physica C **334** (2000) 7.

19. P. Diko, G. Krabbes and C. Wende, Supercond. Sci. Technol. **14** (2001) 486.

20. J. Maeda, T. Izumi and Y. Shiohara, Supercond. Sci. Technol. **12** (1999) 232.

21. K. Iida, N. Hari Babu and D.A. Cardwell, Supercond. Sci. Technol. **20** (2007) 1065.

22. C.E. Foerester, E. Lima, P. Rodrigues, F.C. Serbena, C.M. Lepinski, M.P. Cantao, A.R. Jurelo and X. Obradors, Braz. J. Phys. **38** (2008 ) 341.

23. H. Fujimoto, IEEE Trans. Appl. Supercond. **19** (2009) 2933.

24. N. Hari Babu, K. Iida, A. Briffa, Y.H. Shi, L.S. Matthews and D.A. Cardwell, IEEE Trans. Appl. Supercond. **17** (2007) 2953.

25. R. Gopalan, T. Rajasekharan, G. Rangarajan and N. Hari Babu, Physica C **244** (1995) 106.

26. A. Mahmood, B. H. Jun, H. W. Park and C. J. Kim, Physica C **468** (2008) 1350.

27.   K. Iida, N. Hari Babu, Y. Shi and D.A. Cardwell, Supercond. Sci. Technol. **20** (2007) 1065.

28.   S. Meslin and J.G. Noudem, Supercond. Sci. Technol. **17** (2004) 1324.

29.   H. Fang, Y.X. Zhou, K. Ravi-Chandra and K. Salama, Supercond. Sci. Technol. **17** (2004) 269.

30.   S. Meslin, K. Iida, N.H. Babu, D.A. Cardwell and J.G. Noudem, Supercond. Sci. Technol. **19** (2006) 711.

31.   N. Devendra Kumar, T. Rajasekharan, K. Muraleedharan, A. Banerjee and V. Seshubai,    Supercond. Sci. Technol. **23** (2010) 105020.

32.   N. Devendra Kumar, T. Rajasekharan, C. Ravi. Gundakaram, V. Seshubai, IEEE Transactions on Applied Superconductivity **21** (2011) 3612.

33.   M. Morita, S. Takebayashi, M. Tanaka, K. Kimura, K. Myamoto and K. Sawano, Adv. Supercond. **3** (1991) 733.

34.   J-Ph Mathieu, I Garcia Cano, T. Koutzarova, A. Rulmont, Vanderbemden Ph, D. Dew-Hughes, M. Ausloos and R. Cloots, Supercond. Sci. Technol. **17** (2004) 169.

35.   R. Cloots, T. Koutzarova, J-Ph Mathieu and M. Ausloos, Supercond. Sci. Technol. **18** (2005) R9.

36.   L.F. Cohen, J.T. Totty, G.K. Perkins, R.A. Doyle and K. Kadowaki, Supercond. Sci. Technol. **10** (1997) 195.

37.   F. Frangia, T. Higuchi, M. Deguchi and M. Murakami, J. Mater. Res. **10** (1995) 2241.

38.   C.A. Bateman, L. Zhang, H.M. Chan and M.P. Harmer, J. Am. Ceram. Soc. **75** (1992) 1281.

39.   M.J. Cima, M.C. Flemings, A.M. Figueredo, M. Nakade, H. Ishii, and H.D. Brody, J. Appl. Phys. **72** (1992) 179.

40.   T. Izumi, Y. Nakamura and Y. Shiohara, J. Mater. Res. **7** (1992) 1621.

41. M.A. Rodriguez, B.J. Chen and R.L. Snyder, Physica C. **195** (1992) 185.

42. A. Goyal, K.B. Alexander and D.M. Kroeger, Physica C. **210** (1993) 197.

43. E. Sudhakar Reddy, N. HariBabu, Y. Shi and D.A. Cardwell, Supercond. Sci. Technol. **17** (2004) L1.

44. N. Devendra Kumar, P. Missak Swarup Raju, S. Pavan Kumar Naik, T. Rajasekharan and V. Seshubai, J. Low. Temp. Phy. **174** (2014) 113-127.

45. P.J. Smith, D.A. Cardwell, N.H. Babu, W.W. Zhou and Y.H. Shi, Supercond. Sci. Technol. **13** (2000) 1526.

46. C. Varanasi, P.J. McGinn and S. Sengupta, J. Electron. Mater. **23** (1994) 1143.

47. G. Krabbes, P. Schatzle, W. Bieger and G.G. Fuchs, Appl. Supercond. **6** (1998) 61.

48. I. Monot, J. Wang, M.P. Delamare, J. Provost and G. Desgardin, Physica C **267** (1996) 173.

49. Y.L. Chen, H.M. Chan, M.P. Harmer, V.R. Todt, S. Sengupta and D. Shi, Physica C **234** (1994) 232.

50. Chan-Joong Kim, Hee-Gyoun Lee, Ki-Baik Kim and Gye-Won Hong, J. Mater. Res. **10** (1995) 2235.

51. Y.L. Jiao, L. Xiao, H.T. Ren, M.H. Zheng and Y.X. Chen, Physica C **386** (2003) 266.

52. D. Volochova´n, P. Diko, V. Antal, M. Raduˇsovska and S. Piovarcˇl, Journal of Crystal Growth **356** (2012) 75.

53. N. Ogdwa, I. Hirdbayashi and S. Tanaka, Physica C **177** (1991) 101.

54. N. Ogawa, M. Yoshida, I. Hirabayashi and S. Tanaka, Supercond. Sci. Technol. **5** (1992) S89.

55. Michael J. Cima, Met-ton C. Flemings, Anacleto M. Figueredo, Masahiko Nakade, Hideo Ishii, Harold D. Brady and John S. Haggerty, J. Appl. Phys. **71** (1992) 1868.

56. Y. Shiohara and A. Endo, Materials Science and Engineering **R19** (1997) 1–86.

57. M. Daeumling, J.M. Seutjens and D.C. Larbalestier, Nature **346** (1990) 332.

58. C.P. Bean, Phys. Rev. Lett. **8** (1962) 250.

59. E.M. Gyorgy, R.B. van Dover, K.A. Jackson, L.F. Schneemeyer and J.V. Waszczak, Appl.

    Phys. Lett. **55** (1989) 283.

60. Tom H Johansen, Supercond. Sci. Technol. **13** (2000) R121–R137.

61. W.C. Oliver, G.M. Pharr, J. Mater. Res **19** (2004) 3-20.

62. G.M. Pharr, Mater. Sci. Eng. A **253** (1998) 151–159.

63. D.B. Sirdeshmukh, L. Sirdeshmukh, K.G. Subhadra, Micro-and Macroproperties of Solids, Springer, New York, 2006.

64. C.A. Schuh and T.G. Nieh, Acta Mater. **51** (2003) 87–99.

65. Y. He, J.Z. Zhang, W.Q. Yao, D.Q. Li, X. Teng, J. Surf. Sci. **255** (2009) 4484–4490.

66. D. Joan Josep Roa Rovira, Ph.D. Thesis, "Mechanical properties of HTSC at micron/nanometric scale", University of Barcelona, 2010, Chapter 1, page No. 58.

67. D.F. Lee, V. Selvamanickam and K. Salama, Physica C **202** (1992) 83.

68. Ya. M. Soifer, A. Verdyan, J. Azoulay, M. Kazakevich and E. Rabkin, Physica C, **402** (2004) 80.

# Chapter IV

## Structural, microstructural and magnetic studies of POIG processed (Y, Sm)BCO superconductors

The aim of the present chapter is to study the effect of introducing samarium (Sm) at Y site into bulk YBCO samples, either through doping nanometric $Sm_2O_3$ particles or by chemical substitution. This was done by causing modifications to the $Y_2BaCuO_5$ (Y-211) preforms, which were then subjected to POIG process under commercial grade Ar atmosphere (1% $O_2$ in Ar). The objective is to study the structural, microstructural and magnetic properties of the POIG processed (Y, Sm)$Ba_2Cu_3O_{7-\delta}$ ((Y, Sm)BCO or YSm-123) superconductors and to look for possible correlations among the various observations.

### 4.1. Introduction:

It is known that to enhance the $J_c$ -$H$ performance of REBCO superconductors at 77 K, the number of effective pinning centres should be increased in addition to having a material with critical temperature ($T_c$) well above 77 K. The coherence length of the $REBa_2Cu_3O_{7-\delta}$ (REBCO or RE-123; RE stands for rare earth elements) superconductors is on the nanoscale [1-4]. Hence, defects created at the interface of non superconducting phase $RE_2BaCuO_5$ (RE-211) particles with RE-123 matrix [5], dislocations [6], twins and stacking faults [7] present in the samples have been identified to be effective as flux pinning centres. [8]. Creation of stress field associated with compositional fluctuations in the nano-scale is also reported to be beneficial for flux pinning [9-10].

An examination of the literature shows that nanometre-sized additives in REBCO directly serve as flux pinning centres due to their small size. Many investigators

have introduced nanoparticles of various dopants in REBCO materials. For instance, $Y_2O_3$ [11], $ZrO_2$ [12], $BaCeO_3$ [13], $Al_2O_3$ [14] and NiO [15], have been introduced as fine second phase particles in the Y-123 matrix. $Y_2Ba_4CuMO_y$ (M=U, Nb, Ta, Mo, W, and Re) [16] nanoparticles have been introduced into the YBCO matrix by other groups during melt processing and IG processing. Most often, the expectation has been that the particles themselves would serve as pinning centres, but in cases like ceria, Zirconia, barium cerate etc. reactions with the Y-123/Y-211 system leading to refinement of Y-211 particles has been observed [17-19]. However, highest current densities ($J_c$) reported in melt grown samples are mixed rare earth based copper oxide superconductors doped with nanometre-sized, non interacting materials. For instance, Melt processed ($Nd_{0.33}$, $Eu0_{.33}$, $Gd_{0.33}$)$Ba_2Cu_3O_{7-\delta}$ (NEG-123) superconductor with 35 mol.% of nanometre-sized (70 nm) Gd-211 and 0.1 mol.% of nanometre-sized $NbO_3$ are reported to exhibit the highest $J_c$ of 600 kA/cm$^2$ at 77 K in zero field and 200 kA/cm$^2$ at 4 T [10].

In REBCO systems, where RE represents the light rare-earth elements (LRE) like La, Nd, Sm, Eu, etc., it is observed that some of the LRE$^{3+}$ ions can occupy the Ba$^{2+}$ sites because their ionic radii are close to each other. Increasing replacement of Ba$^{2+}$ sites is found to result in a deterioration of superconducting properties, and substantial reduction of critical temperature especially at high substitution levels [20-25]. Subsequent investigations led to the observation that modified synthesis either under reduced oxygen partial pressures or usage of excess Ba (in the form of precursors such as BaO, $BaO_2$, $BaCuO_x$ etc.) can effectively suppress the substitution of RE at Ba site. In other words, such a process suppresses formation of solid solutions of the $LRE_{1+x}Ba_{2-x}Cu_3O_y$ (RE/Ba -ss) type and permits local compositional fluctuations of $(RE_{1-x}, RE'_x)BCO$ (RE/RE' -ss) type in the processed samples [26], where RE and RE$^1$ are different rare earth elements in

mixed REBCO samples.

Enhancement of $J_c$ in these materials gives rise to the assumption that an additional pinning mechanism may be acting in this type of materials. There are some reports that discuss the sources of flux pinning in medium field regions (2-5 T) in the REBCO materials. Several groups have reported the presence of lower or higher $T_c$ clusters, compared to 92 K of stoicheometric REBCO, due to the formation of $(RE_{1-x}, RE'_x)BCO$ or $RE_{1+x}Ba_{2-x}Cu_3O_y$ solid solutions through EDS measurements [27]. Murakami group have proposed that nano-sized RE-rich clusters act as field-induced pinning centres, [27] and thus result in an enhancement in $J_c$ at high fields, referred to as the peak effect in the REBCO materials. Recently, the mixing of RE elements as in NEG-123 materials has also been proven to be effective in enhancing $J_c$ [28]. Regions of compositional segregation within RE-211 particles, called annuli cores, [29-30] with a distinct range of the rare earth chemical ratio were found in this material. These cores strongly affect the pinning properties at moderate fields and were also regarded as field induced pinning centres. Similar compositional variations are reported in the (Nd, Sm)-Ba–Cu–O system [31]. Since these nanoscale compositional fluctuations were formed during the peritectic transformation, the reaction mechanisms between these nano particles and the matrix are important [8].

The pinning mechanism in $RE_{1+x}Ba_{2-x}Cu_3O_y$ solid solutions might be a result of partial substitution of Nd for Ba as observed by TEM studies in single Nd-123 crystals [32]. The formation of vacancies on barium sites may also contribute to pinning, assuming that point defects of substitutional type and vacancies in the barium sub lattice interact to create clusters, the size of which is of the order of the coherence length in these materials. High $J_c$ values combined with decreasing $B_{irr}$ in $(Nd, Y)Ba_2Cu_3O_{7-\delta}$ (NdY-123) compared to Y-123 are observed in oxygen deficient Y-123 and $NdBa_2Cu_3O_{7-\delta}$ (Nd-123) single crystals [33] due to the

presence of lower $T_c$ phases. A similar behavior is expected in the composite materials with a defect concentration generated by the substitution of Nd or Sm on barium sites. The optimization of the oxygen content in these materials was shown to lead to an increase in the $J_c$ values at higher applied magnetic fields.

The (Y, Sm)-Ba-Cu-O samples fabricated in melt growth process reveal annuli cores within larger (Y, Sm)$_2$BaCuO$_5$ (YSm-211) inclusions which consist of Sm rich areas surrounded by Y rich zones. The distribution of the inclusions is not homogeneous. The YSm-211 inclusions in (Y, Sm)Ba$_2$Cu$_3$O$_{7-\delta}$ (YSm-123) matrix are of size ~5 μm which exist together with elongated ones of 10–20 μm. The pinning is dominated by the interfacial defects around the (Sm, Y)-211 inclusions [34].

It is reported that the presence of Sm results in the formation of compositional fluctuations (RE/RE$^{'}$ -ss) causing variation of $T_c$ across different regions in the matrix which can act as effective pinning centers at higher fields. This provides $\Delta T_c$ pinning and contributes to the peak effect observed in $J_c$–$H$ curves. This result demonstrates a possible way to introduce peak effect in YBCO materials and thus enhance the applications in high field regions [35]. To understand the effect of varying the extent of Sm doping in YBCO sample, different amounts of Sm$_2$O$_3$ was doped into MG processed YBCO materials by means of nano-scale Sm$_2$O$_3$ addition to YBCO powders. The amounts of nanometric YSm-211 is varied from 0.1 to 0.4 mol.% [35]. It has been reported that the solubility of Sm in liquid phases is higher than Y at high temperatures. As a consequence, Sm diffuses and dissolves into the liquid phase and then takes part in the growth of RE-123 phase.

Most of the works reported on substituted REBCO superconductors have been on melt grown samples. Work on mixed RE superconductors prepared by infiltration

growth (IG) process has been very limited. As of now there is no clear understanding as to why and how these annuli cores representing compositional segregation, seen as formation of bright and dark regions within RE-211 particles, occur in mixed REBCO superconductors. One of the aims of this work is to study if introduction of Sm into Y-211 preform results in formation of annuli cores and whether compositional fluctuations occur in the matrix after IG process and lead to enhancement in $J_c$. In the present work, the effect of introducing Sm (into YBCO) at nano scale is investigated systematically, with regard to the structural, micro-structural and magnetic properties of the POIG processed (Y, Sm)BCO system as discussed below.

## 4.2. Systems studied in this chapter and methods of synthesis:

### 4.2.1. Systems studied in this chapter:

In order to substitute Sm at Y site as in (Y, Sm)BCO system, two different processing routes were chosen. Effect of adding small amounts of nano $Nb_2O_5$ powder to preform was also investigated. The systems studied in the present chapter are described below

(i) Addition of different amounts of nano $Sm_2O_3$ sol into Y-211 preform powder as discussed in section 4.2.2. The pellets of the resultant preform powders were subjected to POIGP. The optimum composition with the best $J_c(H)$ performance is identified.

(ii) The chosen optimum composition is synthesized using Chemical substitution of Sm for Y as discussed in section 4.2.3.

(iii) Further addition of 0.1 wt % of nano powders of $Nb_2O_5$ to the optimal composition is rendered and the $J_c(H)$ performance is investigated as

discussed in section 4.2.4.

## 4.2.2. Addition of nano $Sm_2O_3$ to synthesize (Y, Sm)BCO preform powders:

Y-123 and Y-211 powders were synthesized following a chemical route employing citrate method which is discussed in section 2.2 of chapter 2. A sol containing nano $Sm_2O_3$ particles were prepared by sol-gel process. For this $Sm_2O_3$ powder was dissolved in $HNO_3$ on magnetic stirrer and ammonia was added to the solution to adjust $p^H$ to 8. This solution was washed several times using double distilled water and was ultrasonicated for 30 minutes. The $Sm_2O_3$ particles were then observed to be dispersed in solution homogenously. The nano $Sm_2O_3$ sol was then added to Y-211 powder in varied amounts of 0, 10, 20 and 30 wt.% along with premix solution employing Nano Dispersive Sol Casting (NDSC) method. This method enables introduction of nano-particles into Y-211 preform without agglomeration [17]. For this, premix solution was prepared by dissolving an organic monomer, methacrylamide (MAM) and a cross linker, N, N'-methylenebisacrylamide (MBAM) in distilled water. The concentration of organics in premix solution was 16 wt%, and the mass ratio of MAM: MBAM was 6:1 that can promote the formation of a relatively rigid cross-linked gel network between $Sm_{2O3}$ particles. This solution was then mixed using homemade tumbling machine with solution to ball volume ratio as 1:1 for 12 hours. Polymerization was activated by adding chemical initiator, ammonium per sulphate (APS) whereas a catalyst, N.N.N', N'- tetramethylenediamine (TEMED) was used to control the kinetics of the mixture. This mixture was then dried at 70 $^o$C in a hot air oven. Dried powders were then sintered for 2 hours at 600 $^o$C to remove the carbon related compounds. The resultant YSm-211 preform powders are referred to as YSm-10—211, YSm-20—211 and YSm-30—211 respectively, corresponding to x wt % nano $Sm_2O_3$ addition to (100-x) wt % Y-211, with x=10, 20 and 30.

### 4.2.3. Chemical substitution: Synthesis of $(Y_{1.6}, Sm_{0.4})BaCuO_5$ preform powder:

The YSm-20 sample was found to be optimum from $J_c(H)$ performance after POIG process, as will be discussed in section 4.4. This composition was chosen for an alternate synthesis through chemical substitution route to compare the microstructural features and $J_c(H)$ performance in both the cases. For this purpose, $(Y_{1.6}, Sm_{0.4})BaCuO_5$ powders were prepared by chemical combustion route using citrate precursors (as discussed in chapter 2, section 2.2.) by taking stoicheometric ratios of $Y_2O_3$, $Sm_2O_3$, $BaCO_3$ and $CuO$. After the combustion, powders were collected and sintered at 950 $^o$C for 12 hours and the resultant preform powders are referred to as (YSm-20-C-211), where C stands for Chemical substitution.

### 4.2.4. Synthesis of (Y, Sm)BCO with 20 wt.% $Sm_2O_3$ and 0.1 wt.% doping of $Nb_2O_5$:

$Nb_2O_5$ sol is prepared through dissolving $NbCl_5$ powder (Alfa Aeser Puratronic make, 99.999 purity, metal basis) in double distilled water and dried. 0.1 wt.% $Nb_2O_5$ powder was added to the YSm-20-211 preform powder (prepared by mixing 20 wt.% nano $Sm_2O_3$ sol to Y-211 powder). The resultant preform is referred as YSm-20-Nb-211.

The various YSm-211 preform (mixture of Y-211 and nano $Sm_2O_3$ particles or Sm) powders discussed above were compacted into pellets under an optimum pressure of 460 MPa as suggested by *Devendra et al.* [25]. The Y-123 powder which is a source of liquid phases during POIGP was taken as twice the amount of YSm-211 preform pellet and was also pressed separately. The pellets were supported on inert substrates to prevent liquid phase loss and to avoid contamination from the alumina crucible used. The arrangement of preforms for synthesizing the samples is shown in fig. 4.1.

### 4.2.5. Heat treatment schedule:

It is known that the peritectic decomposition temperatures ($T_p$) of the RE-123 varies with the ionic radius of the RE element involved and the atmosphere. For instance, $T_p$ of Y-123 is 1005 $^o$C and Sm-123 is 1054 $^o$C when processed in air while it is 980 $^o$C and 1005 $^o$C in argon with 1% $O_2$ and 950 $^o$C and 980 $^o$C in argon with 0.1% $O_2$ atmosphere. Thus it was found that $T_p$ of YBCO decreased by about 30 $^o$C in a 1% $O_2$ in Ar (commercial grade Ar) atmosphere and decreased by 60 $^o$C in a 0.1% $O_2$ in Ar atmosphere compared to that measured in air [29]. It was also observed that the $T_p$ of (RE, RE')-123 composites increases linearly with an increase in the ionic radius of the RE element. This suggests that (RE, RE')-123 composites form a complete solid solution, which enables us to control $T_p$ according to the radius ratio or the kind of rare earth elements being used.
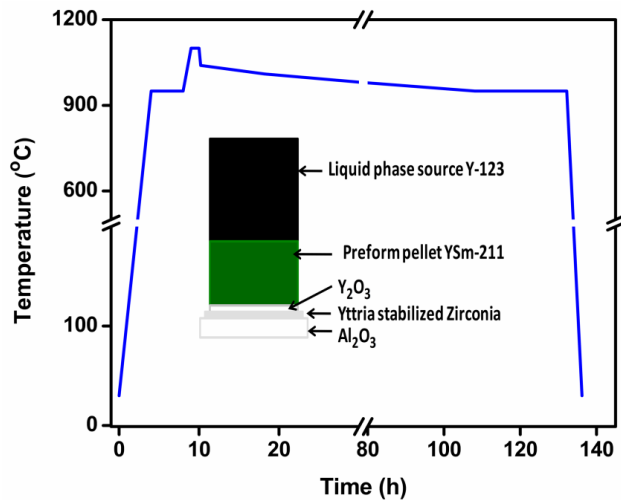


**Fig. 4.1.** Heat treatment schedule followed to synthesize the (Y, Sm)BCO samples.

The heat-treatment schedule used for fabricating the (Y, Sm)BCO samples is shown in fig. 4.1. To avoid the formation of solid solutions like $Sm_{1+x}Ba_{2-x}Cu_3O_{7-\delta}$ which are of lower $T_c$, heat treatment was carried out in commercial grade Ar atmosphere. In this heat treatment two stages of slow cooling was followed to

grow (Y, Sm)BCO superconductors. The POIG processes involves heat treating the sample assembly (shown as inset in fig. 4.1) initially to 950 $^{o}$C for strengthening the preforms and then raise the temperature to 1100 $^{o}$C ($T_i$) where infiltration of liquid phases takes place into YSm211 preform. This was followed by rapid cooling to 1040 $^{o}$C, and slow cooing from 1040 $^{o}$C to 980 $^{o}$C with a cooling rate of 1 $^{o}$C/h and from 980 $^{o}$C to 950 $^{o}$C with a cooling rate of 0.5 $^{o}$C/h and was maintained at 950 $^{o}$C for 24 hours for completion of grain growth and was furnace cooled to room temperature. Slow cooling was done relatively to lower temperatures because in Ar atmosphere $T_p$ of RE-123 materials come down. Peritectic temperature of these (Y, Sm)BCO in commercial grade Ar is 1005 $^{o}$C, as reported in melt grown samples [29, 35] .

The oxygen absorption or oxygenation process in highly dense RE-123 samples and single crystals are very slow compared to porous materials or those materials which are in the powder form [36]. The samples thus obtained were oxygenated in a tubular furnace at 460 $^{o}$C in flowing oxygen for a long duration of 110 h, to form the superconducting orthorhombic phase.

### 4.2.6. End products:

The series of (Y, Sm)BCO or YSm-123 superconductors are prepared by POIG processing the corresponding preforms as described below under commercial grade Ar atmosphere (hereafter referred to as 'under argon'), unless specified otherwise. The products thus obtained are highlighted below.

**YSm-10:** is the superconductor prepared using YSm-10 - 211 preform under argon atmosphere.

**YSm-20:** is the superconductor prepared using YSm-20 - 211 preform under argon atmosphere.

**YSm-30:** is the superconductor prepared using YSm-30 - 211 preform under argon atmosphere.

**YSm-20-C:** is the superconductor prepared using YSm-20-C - 211 preform under argon atmosphere.

**YSm-20-Nb:** is the superconductor prepared using YSm-20-Nb - 211 preform under argon atmosphere.

**YBCO-Ar:** In order to evaluate the role of processing conditions realistically, YBCO was also POIG processed under argon without any Sm maintaining the same heat treatment schedule.

## 4.3. Characterization techniques:

Structural studies on oxygenated (Y, Sm)BCO samples were carried out employing X-ray diffraction (XRD) patterns recorded using Cu $K_\alpha$ as the X-ray source ($\lambda$=1.5406 Å) in Bruker's AXS Model D8 Advance System. The polished surface (down to 0.25 μm size) of each of the samples was examined using a field-emission scanning electron microscope (FESEM; Zeiss-make Ultra 55 model). An in-lens detector was used to observe YSm-211 particles in the matrix of YSm-123.

Superconducting transition temperature ($T_c$) of the processed samples was characterized by measuring temperature dependence of ac susceptibility with the help of ACMS attachment on Quantum design make physical property measurement system (PPMS). M-H loops were recorded in the samples at different temperatures (25 K, 50 K, 65 K and 77 K) sweeping the magnetic field in the range 0-9 Tesla for all samples using the VSM attachment on the PPMS system. $J_c$ was calculated following extended Bean's Critical State model [37-38],

using the formula $J_C = \dfrac{20\Delta M}{d}$ Acm$^{-2}$. Here $\Delta M$ (in emu/cc) is the difference in the hysteretic magnetization between the curves obtained while increasing and decreasing the magnetic fields ($\Delta M = M^+ - M^-$) and $d = b\left(1 - \dfrac{b}{3a}\right)$ is the reduced dimension, where 'a' and 'b' are the planar dimensions (in cm) of the sample with a ≥ b. The dimensions of the specimens used in magnetization measurements were a = 3 mm, b=2 mm, c=5 mm.

## 4.4. Results on (Y, Sm)BCO samples POIG processed after addition of nano Sm$_2$O$_3$ particles to Y-211 powders in preform:

### 4.4.1. Observations on preform powders:
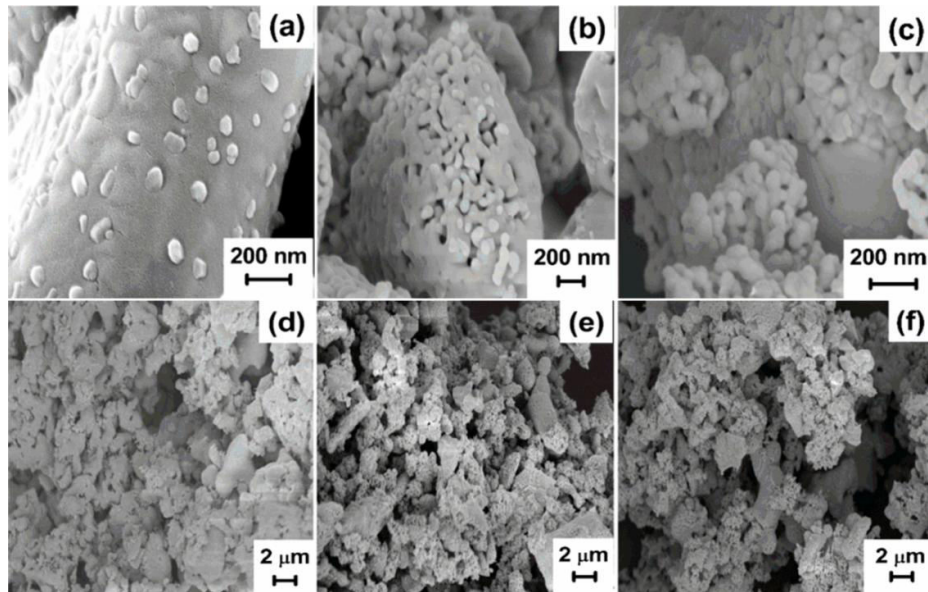


**Fig. 4.2.** FESEM images of (a) and (d) YSm-10, (b) and (e) YSm-20 and (c) and (f) YSm-30 powders sintered at 950 $^\circ$C. The figures in the lower panel are at lower magnifications. The figures in the upper panel are at higher magnifications. Sm$_2$O$_3$ nano particles added to Y-211 can be seen to be distributed individually and without agglomeration on the Y-211 surface in (a). In (b) and (c) such particles are too numerous to individually resolved.

Preform powders were prepared by adding $Sm_2O_3$ sol in different amounts (x wt%, x= 0, 10, 20 and 30) to Y-211 powder (of 100-x wt.%), mixing it intimately and sintering the mixture at 950 $^{o}$C for 1 h as discussed in section 4.2.2. The distribution of the $Sm_2O_3$ particles in YSm-211 preform has been studied before pelletizing the powders and subjecting them to IG process. FESEM images of the sintered powders of YSm-10, YSm-20 and YSm-30 in Y-211 are shown in fig. 4.2. It is clear that the $Sm_2O_3$ particles are distributed homogenously onto Y-211 particles in all the three preforms and the $Sm_2O_3$ particle sizes are of the order of 50 - 80 nm. From the FESEM images it suggests that there is some reaction between nano $Sm_2O_3$ and Y-211 particles during sintering so that the nano $Sm_2O_3$ particles get embedded onto the surface of Y-211 particles.

### 4.4.2. Structural characterization:
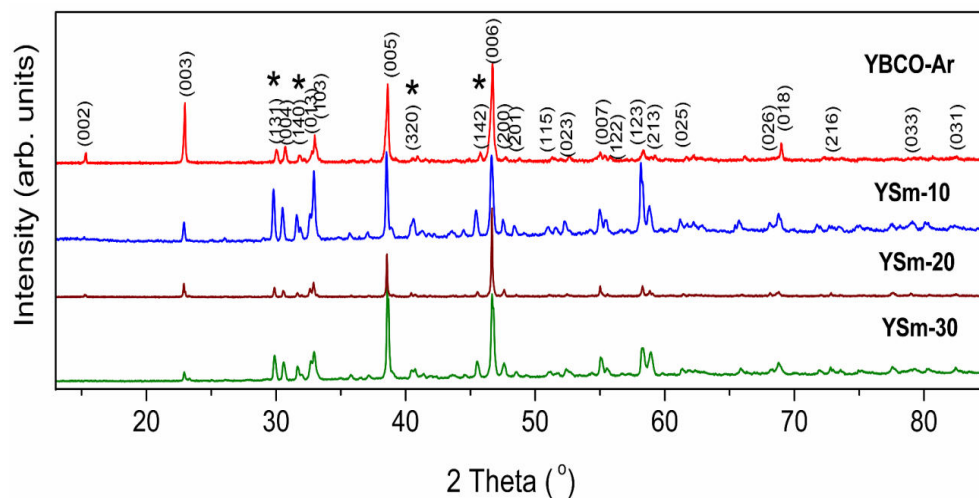


**Fig. 4.3.** XRD patterns obtained from YBCO-Ar, YSm-10, YSm-20 and YSm-30 samples are shown. The patterns were obtained using Cu $K_{\alpha}$ radiation. The Bragg peak positions corresponding to the 211 minority phases are indicated by (*).

Fig. 4.3 shows the XRD patterns for YBCO-Ar, YSm-10, YSm-20 and YSm-30 composites. The FULLPROF program was used to determine the lattice

parameters of the composites from the corresponding X-ray diffractograms. The profile matching with the program confirms that the majority phase in all the XRD patterns have crystallized with Pmmm space group. The prominent reflections could be indexed to orthorhombic structure for all samples. YSm-211 phase is found to be present as the minor phase coexisting with YSm-123 phase. In all the samples [00l] texture was observed even without any seeding. In order to analyze the lattice parameters accurately relatively strong reflections with no overlap were considered. Extra peaks due to additional phases are seen in YSm-10 and YSm-30 samples, unlike in YBCO-Ar and YSm-20 samples. No diffraction peaks corresponding to liquid phases are found indicating that the peritectic reaction is complete. On increasing the concentration of Sm into Y-211 preform, a relative shift in the peak positions toward smaller angles has been observed suggesting a change in the lattice constants.

**Table 4.1.** Lattice parameters and cell volumes of YBCO-Ar, YSm-10, YSm-20 and YSm-30 samples.

| Sample | Lattice parameters $\text{Å}$ | | | Cell volume $\text{Å}^3$ |
|---|---|---|---|---|
| | a | b | c | |
| YBCO-Ar | 3.810 | 3.886 | 11.697 | 172.2 |
| YSm-10 | 3.810 | 3.887 | 11.652 | 172.5 |
| YSm-20 | 3.811 | 3.888 | 11.650 | 172.6 |
| YSm-30 | 3.814 | 3.895 | 11.689 | 173.6 |

Lattice parameters for YBCO-Ar, YSm-10, YSm-20 and YSm-30 are presented in Table-4.1. The accuracy in the determination of the lattice parameters of the multi-phase systems studied here is $\pm 0.3$ Å.

### 4.4.3.  Temperature dependence of ac susceptibility:
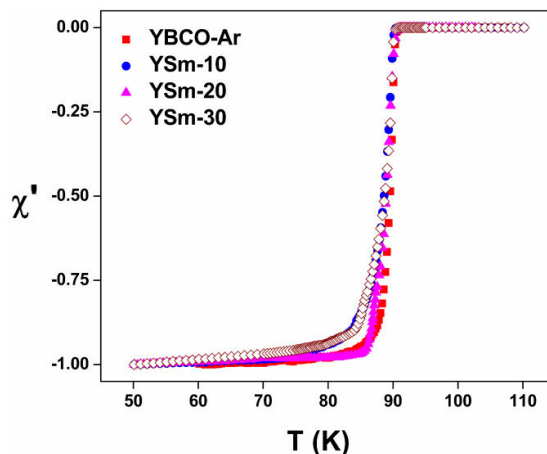


**Fig. 4.4.** Temperature dependence of the real part of ac susceptibility ($\chi'$) for YBCO-Ar, YSm-10, YSm-20 and YSm-30 samples.

Temperature dependence of ac susceptibility in the three samples of (Y, Sm)BCO system and YBCO-Ar are measured as discussed in section 2.5 in chapter 2 and are shown in fig. 4.4. Onset of $T_c$ was measured to be at 91.0 K, 90.39 K, 90.71 K and 90.51 K and width of the transition temperature was 2.5 K, 5.5 K, 2.5 K and 5.7 K for YBCO-Ar, YSm-10, YSm-20 and YSm-30 samples respectively. Broader transition widths at $T_c$ and a tail region below the sharp drop at $T_c$ are found for YSm-10 and YSm-30 as compared to YSm-20 and YBCO-Ar samples.

### 4.4.4.  Microstructural properties of processed samples:

FESEM image of YBCO-Ar sample which is recorded at a magnification of 5 kX using in-lens mode detector is displayed in fig. 4.5 (a) and the corresponding histogram showing particle size distribution is shown in fig. 4.5 (b). It can be seen that the size of Y-211 phase particles is of the order of 0.5 to 4 μm with majority being of 1-2 μm size. It can be seen that many pores of spherical shape (spherical porosity) exist throughout the sample.
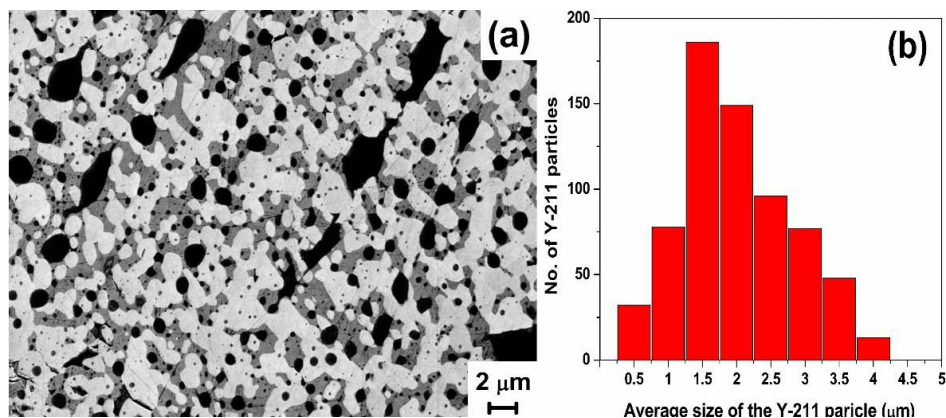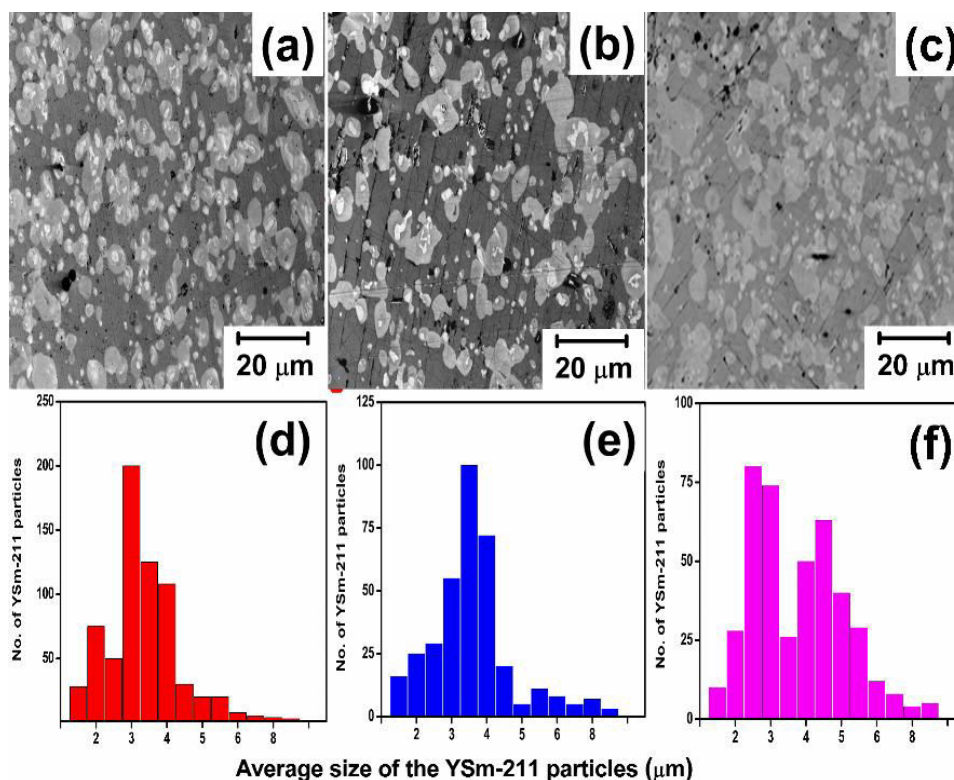
**Fig. 4.5.** FESEM image from YBCO-Ar, and the corresponding Y-211 particle size histogram, is shown in (a) and (b) respectively.

The FESEM images of all (Y, Sm)BCO samples are shown in fig. 4.6 which are recorded at 2 kX magnification. Correlating the microstructural features to those in literature we identify the inclusions to be YSm-211 embedded in (Y, Sm)BCO matrix. However elemental analysis was carried out and the results are presented in section 4.7.2.2 of this chapter.

Corresponding histograms indicate the distribution of YSm-211 particles in a size range of 2-7 µm. The distribution is narrow for YSm-20 while in YSm-10 and YSm-30 with relatively lower and higher concentrations of Sm distribution is wider, indicating that the refinement of the YSm-211particles is more effective in YSm-20. In all (Y, Sm)BCO samples spherical porosity is observed. In addition, defects or non-spherical porosity is also observed. The extent of porosity is estimated using the Axiovision software and are tabulated in Table 4.2.

**Fig. 4.6.** FESEM images obtained from the samples YSm-10 YSm-20 and YSm-30 using In-lens detector are shown in (a), (b) and (c) respectively. In all the images, the presence of YSm-211 particles can be seen in the YSm-123 matrix. The corresponding 211 particle size histograms are shown in figs. (d), (e) and (f) respectively.

The FESEM images of all (Y, Sm)BCO samples which are recorded at 5 kX magnification are shown in fig. 4.7. All micrographs exhibit presence of brighter regions (cores) which are surrounded by darker regions within the precipitates (or inclusions which are the YSm-211 particles). Similar core formation is reported, in MG processed (Sm, Y)BCO system, to be arising from compositional segregation [34]. No reports of annuli cores exist in literature in IG processed REBCO superconductors, to the best of our knowledge.
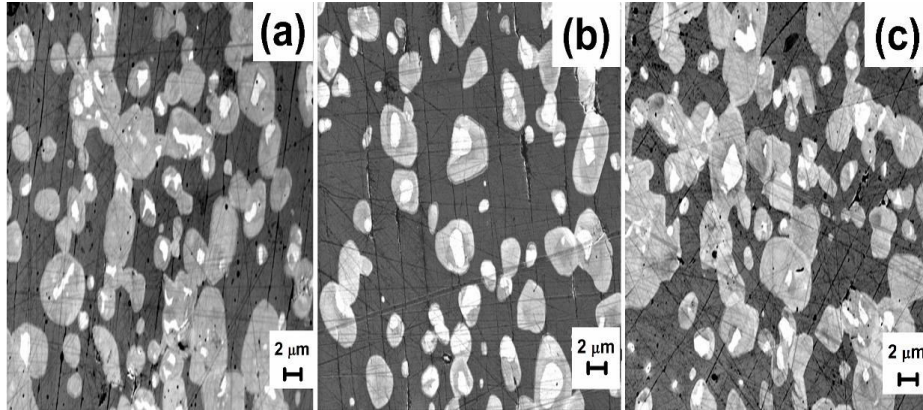
**Fig. 4.7.** FESEM images obtained from the samples YSm-10 YSm-20 and YSm-30 (at 5 kX) are shown in (a), (b) and (c) respectively. In all images YSm-211 particles can be seen in YSm-123 matrix. The micrographs obtained at higher magnifications than those in fig. 4.6 are intended to clearly show the Y-211 core region (bright) in the YSm-211 particles.

**Table 4.2:** $T_c$ onset and transition widths ($\Delta T_c$) obtained from ac susceptibility measurements for YBCO-Ar, YSm-10, YSm-20 and YSm-30 samples. YSm-211 phase content (Vol. %), YSm-211 particle size-range, and porosity in the matrix estimated from microstructural studies, are also shown.
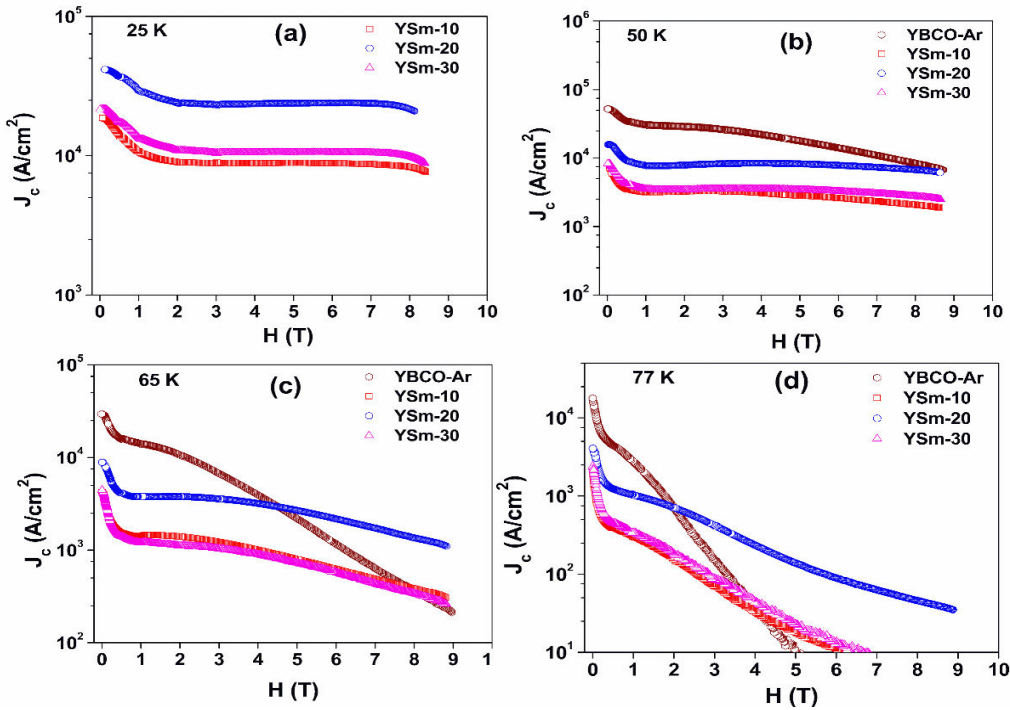
|  | YBCO-Ar | YSm-10 | YSm-20 | YSm-30 |
|---|---|---|---|---|
| $T_c$(K) | 91.0 | 90.39 | 90.71 | 90.51 |
| $\Delta T_c$(K) | 2.5 | 5.5 | 2.5 | 5.7 |
| Vol. % of RE-211 | 46.8 | 40.3 | 35.5 | 49.0 |
| RE-211 size (μm) | 0.5-4 | 2 - 5 | 2 - 4 | 2 - 7 |
| Porosity (%) | 6.8 | 3.9 | 6.0 | 7.2 |

Onset of transition ($T_c$), superconducting transition width ($\Delta T_c$), porosity, the volume fraction of RE-211 (i.e. Y-211 or YSm-211) particles and their size range observed in the processed samples of YBCO-Ar, YSm-10, YSm-20 and YSm-30 are presented in Table 4.2. Average content of YSm-211 particles is calculated in

an area scan of 60000 μm$^2$ in the FESEM image with the help of Axiovision software and is presented in Vol.%.

### 4.4.5. Magnetic properties of the (Y, Sm)BCO superconductors:

### 4.4.5.1. Field dependence of critical current densities:



**Fig. 4.8**. The field dependence of $J_c$ at temperatures 25 K, 50 K, 65 K and 77 K (for YBCO-Ar, YSm-10, YSm-20 and YSm-30 POIG processed samples) are shown in figs. (a), (b), (c) and (d) respectively. YBCO-Ar shows maximum $J_c$ at zero field ($J_c(0)$) in comparison with other samples at all temperatures. Among all (Y, Sm)BCO samples, YSm-20 showed the best performance and it supported significantly larger $J_c$ up to high magnetic fields at all temperatures.

The field dependence of critical current density ($J_c(H)$) are determined from M-H loops recorded in YBCO-Ar and (Y, Sm)BCO samples. $J_c$ $(H)$ curves obtained for the YBCO-Ar, YSm-10, YSm-20 and YSm-30 at different temperatures (at 25,

50, 65 and 77 K) with the applied magnetic field parallel to the pressed direction are shown in fig. 4.8. (a-d). It is observed that the YSm-20 sample exhibits superior $J_c(H)$ at all temperatures. Zero field $J_c$ at 77 K for the YBCO-Ar, YSm-10, YSm-20 and YSm-30 is found to be 17.8 kA/cm$^2$, 2.0 kA/cm$^2$, 4.1 kA/cm$^2$ and 2.4 kA/cm$^2$ respectively. $J_c > 1$ kA/cm$^2$ is observed up to 1.75 T for YBCO-Ar, 1.25 T for YSm-20 and up to 0.2 T in YSm-10 and YSm-30 samples at 77 K while at 65 K, $J_c > 1$ kA/cm$^2$ was observed all the way to 9 T for YSm-20, while it is up to 6.2 T, 4.1 T and 3.5 T for YBCO-Ar, YSm-10 and YSm-30 samples respectively. It can be seen that the $J_c(H)$ performance at high fields is the best for YSm-20 sample.

The calculated $J_c(0)$ at different temperatures for the samples YBCO-Ar, YSm-10, YSm-20 and YSm-30 are given in Table 4.3.

**Table 4.3:** Current density at zero field ($J_c(0)$) for the YBCO-Ar, YSm-10, YSm-20 and YSm-30 samples at 25 K, 50 K, 65 K and 77 K.

| $J_c(0)$ (kA/cm$^2$) \ T (K) | 77 | 65 | 50 | 25 |
|---|---|---|---|---|
| YBCO-Ar | 17.8 | 29.4 | 52.0 | -- |
| YSm-10 | 2.0 | 4.2 | 7.3 | 18.7 |
| YSm-20 | 4.1 | 8.9 | 15.8 | 41.7 |
| YSm-30 | 2.4 | 4.5 | 8.3 | 21.7 |

### 4.4.5.2. Flux pinning properties:

Flux pinning force ($F_p$) in (Y, Sm)BCO samples was calculated using the relation $F_p(H) = J_c*B$ [39, 40-41]. For normalization of the $F_p$ curves with respect to maximum pinning force ($F_{p\ max}$) the normalized flux pinning force ($F_p/ F_{p\ max}$) plotted as a function of applied field for all the samples are shown in fig. 4.9. An enhancement of $J_c$ in high fields can be observed from the curves in all (Y,

Sm)BCO samples compared to YBCO-Ar. The peak position of H $(F_p/F_{p\ max})_{max}$ at 77 K for YSm-20 was observed at 2.1 T, while for YBCO-Ar it is at 1 T. For YSm-10 and YSm-30 samples, the peak field was observed at 1.5 T.
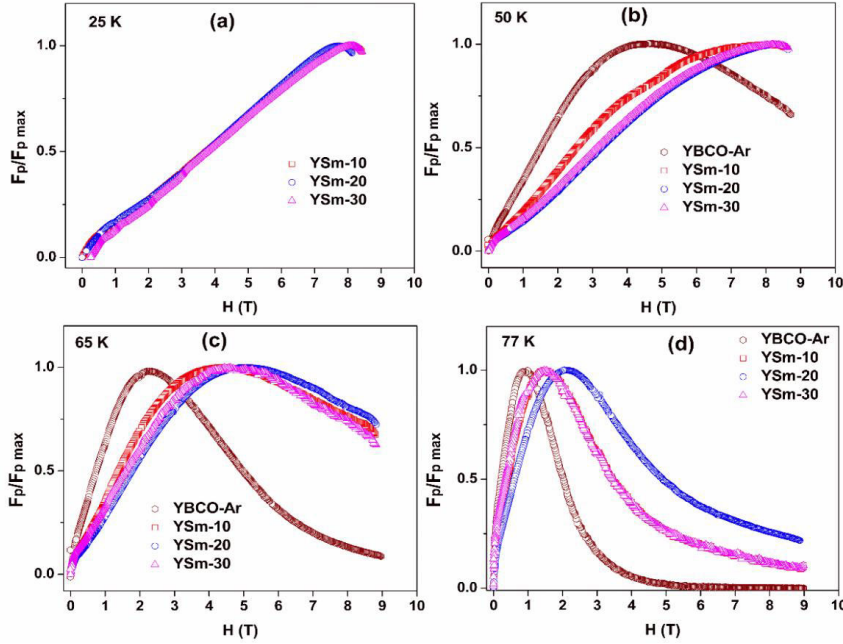


**Fig. 4.9.** The field dependence of the normalized flux pinning force $F_p$ / $F_{p\ max}$ for the samples YBCO-Ar, YSm-10, YSm-20 and YSm-30 at temperatures 25 K, 50 K, 65 K and 77 K are shown in figs. (a), (b), (c) and d). The curve for sample YSm-20 peaks at the maximum field of 2.1 T at 77 K.

## 4.5. Results on YSm -20-C sample processed through Chemical substitution of Sm for Y and comparison with those of YSm-20 presented in Sec. 4.4:

In earlier section, nano $Sm_2O_3$ was added in the form of sol to Y-211 powders in preform, which after POIG processing has led to annuli core formation within YSm-211 inclusions in YSm-123 matrix. Such cored YSm-211 with compositional fluctuations are observed in all (Y, Sm)BCO superconductors as seen in figs. 4.7. To investigate the possibility of distributing Sm more uniformly throughout the matrix, at the unit cell level, Sm was chemically substituted for Y,

rather than through addition of nano $Sm_2O_3$ to Y-211. For this purpose, $(Y_{1.6}Sm_{0.4})$-211 powders were prepared in citrate route, pressed and POIG processed to form YSm-20-C under similar conditions used for YSm-20 sample of equivalent composition.

### 4.5.1. Microstructural properties of the YSm-20 and YSm-20-C-211 preform powders:

Figs. 4.10 (a) and (b) show the microstructures of the preform powders of YSm-20-C-211 and YSm-20 -211 at a magnification of 200 kX. In both the samples the size of the 211 particles are of sub micron range. It is evident from fig. 4.10 (a) that, in YSm-20-C-211 particles got sintered together; whereas in the YSm-20, presence of 50 - 80 nm sized $Sm_2O_3$ particles are seen embedded individually surrounding the Y-211 particles. The nano $sm_2O_3$ particles in the YSm-211 preform powder are marked with arrows.
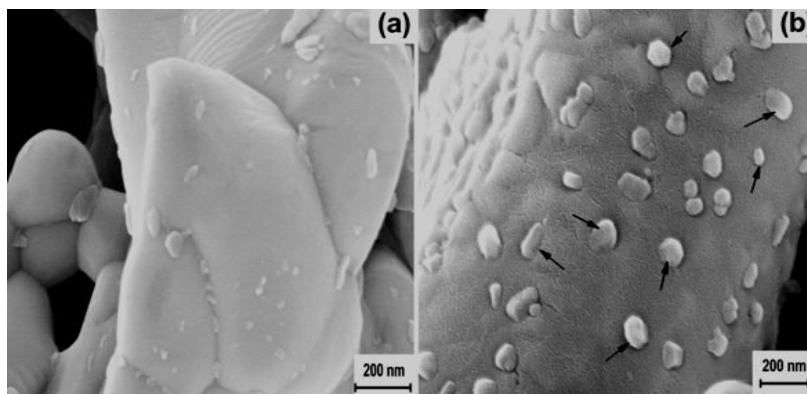


**Figure. 4.10.** FESEM image in (a) is from the chemically prepared 211 powder YSm-20-C-211; there are no $Sm_2O_3$ particles sticking to the 211 particle surface. This is unlike in (b) which shows an example (YSm-10) where $Sm_2O_3$ was added separately as nano particles to Y-211.

### 4.5.2. Structural properties of POIG processed YSm-20 and YSm-20-C samples:

The X-ray diffractograms of POIG processed YSm-20-C and YSm-20 samples are shown in fig. 4.11. The profile matching, using FULLPROF program shows that the XRD patterns of both the samples are crystallized with Pmmm space group. The prominent peak reflections can be indexed to an orthorhombic crystal structure for both the samples.

The lattice parameters (*a, b* and *c* in Å) for YSm-20-C are *a*= 3.89, *b* = 4.13 and *c* = 11.03 and the unit cell volume (v) is 178.20 $Å^3$ and for YSm-20 lattice parameters were *a*= 3.81, *b*= 3.89 and *c*=11. 65 and the unit cell volume (v) is 177.62 $Å^3$. The difference in lattice parameters of YSm-20-C compared to Y-123 [42] indicates that Sm has substituted for Y and led to the formation of YSm-123 matrix with extra YSm -211 compound. However extra peaks present suggest RE-rich solid solution formation.
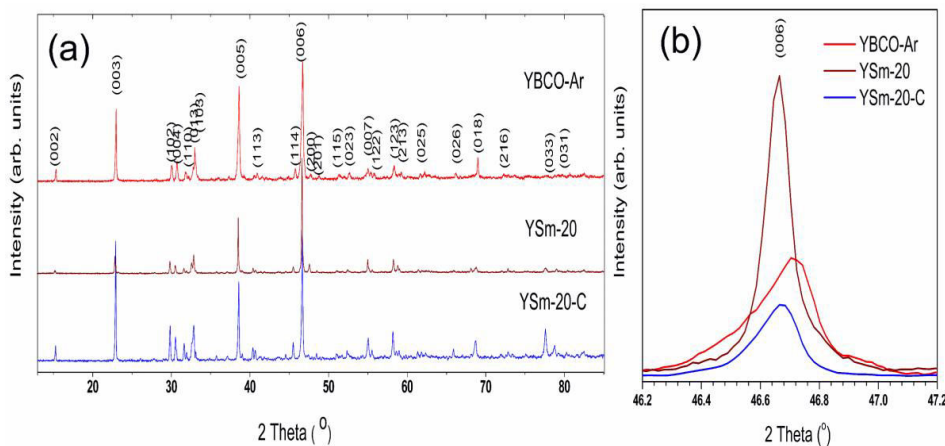


**Fig. 4.11.** (a) XRD plots of YBCO-Ar, YSm-20 and YSm-20-C samples.

### 4.5.3. Microstructural properties of YSm-20-C and YSm-20:

FESEM images of processed samples of YSm-20-C and YSm-20 are compared in fig. 4.12. (a) and (b), fig. 4.12. (c) and (d) respectively. YSm-211 particles are finer (1-4 μm) in the YSm-20-C than in YSm-20 with 2-6 μm size particles. The smaller sized YSm-211 particles are homogeneously distributed in the YSm-20-C sample compared to those in YSm-20 sample. FESEM images at lower magnification indicate that YSm-20-C sample shows less porosity compared to YSm-20 sample. In contrast to YSm-20 samples, annuli cores are not observed within the RE-211 inclusions in YSm-20-C, instead the compositional variations are smeared out throughout these particles.
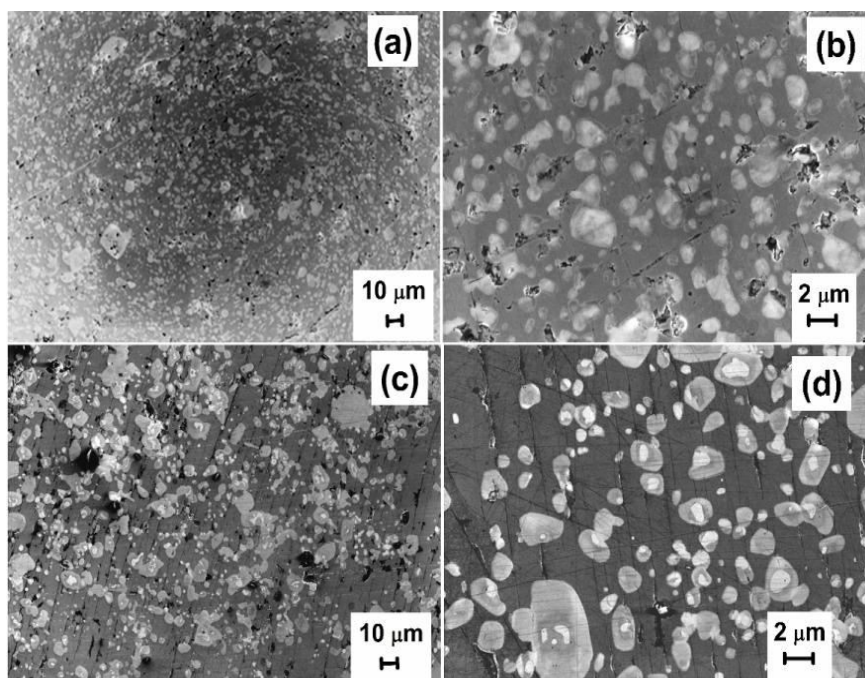


**Fig. 4.12.** (a) and (b) show FESEM images at lower and higher magnifications respectively, for YSm-20-C, the POIG processed sample prepared from powder obtained using citrate synthesis. In (c) and (d), in the lower panel, similar micrographs are shown for POIG processed YSm-20, which was prepared from powders where nano particles of $Sm_2O_3$ were separately added to Y-211.

### 4.5.4. Magnetic properties of YSm-20-C and YSm-20:

Critical superconducting transition temperature $T_c$ of both the samples YSm-20-C and YSm-20 are shown in fig. 4.13 that exhibits temperature dependence of ac susceptibility. Onset $T_c$ of both the samples is around 91 K, while the transition widths are 2.5 K and 7.5 K for YSm-20 and YSm-20-C respectively. Thus a broad diamagnetic transition is observed in YSm-20-C compared to YSm-20 sample, which indicates the presence of secondary phases of lower $T_c$ as also observed in XRD.
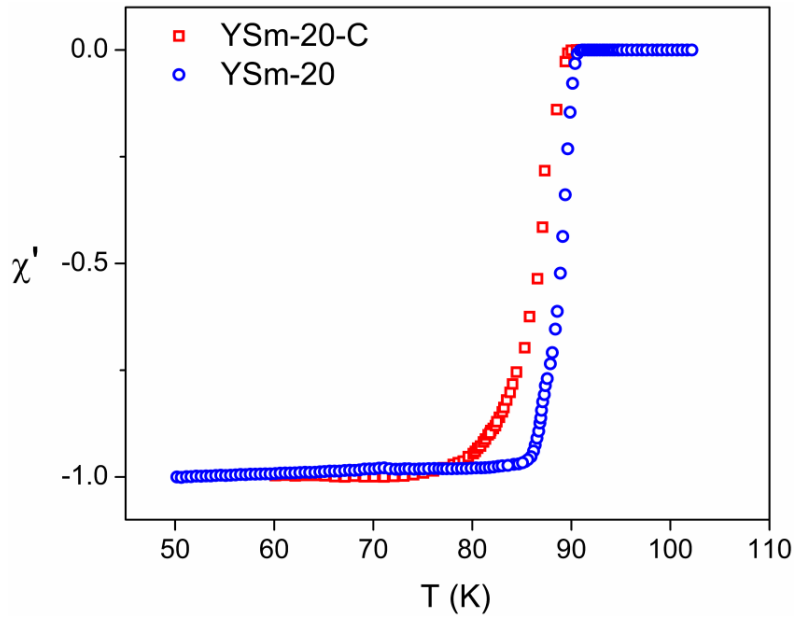


**Fig. 4.13.** Temperature dependence of real part of ac susceptibility ($\chi'$) for the samples YSm-20-C and YSm-20.

Critical current density of YSm-20-C is determined at different temperatures (25 K, 50 K, 65 K and 77 K) by recording M-H loops up to 9 T and are compared with those of YSm-20 and displayed in fig. 4.14.
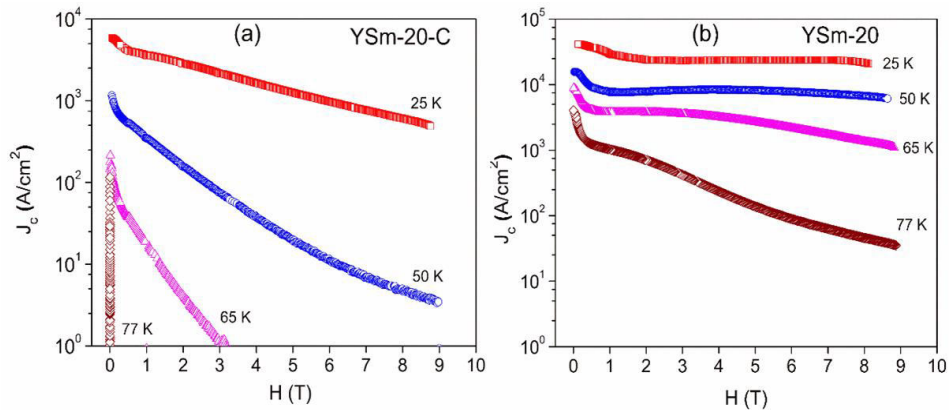
**Fig. 4.14.** Field dependence of critical current density ($J_c$) of (a) YSm-20-C and (b) YSm-20 at different temperatures.

At all temperatures $J_c(H)$ performance of YSm-20 sample is superior to that of YSm-20-C. Zero field $J_c$ at 77 K for YSm-20-C is 100 A/cm$^2$ where as for YSm-20 it is 4.2 kA/cm$^2$. $J_c(H)$ curves of YSm-20 sample at all temperatures are maintained high (flat ) up to high fields where as for YSm-20-C sample $J_c(H)$ curves show a rapid fall to zero at high temperatures (65 K and 77 K).

## 4.6. Effect of Nb$_2$O$_5$ addition on the performance of YSm-20 superconductor:

Investigations have been made to study the effect of introducing Nb into YBCO and varied results are reported [43-49]. In a study by Suresha et al. [50], temperature dependence of resistivity of YBa$_2$Cu$_{3-x}$Nb$_x$O$_{7-y}$ samples with $x = 0.3$, 0.45 and 0.6 indicated that $T_c$ varied in the range 85 - 90.3 K with composition. They reported a possible change in crystal structure with composition. Kuwabara and Kusaka [49] concluded that Cu and Nb did not co-exist in the same compound containing Y and Ba. Another study by Abdullah and Tan [43] mentioned that the added Nb formed the YBa$_2$NbO$_6$ perovskite instead of getting doped into the compound containing Cu. On the other hand, in a study by Eguchi et al. [51] it was shown that Nb substitutes for Cu in the sample with nominal

composition x = 0.01. Some groups [43, 51] reported the co-existence of two phases in Y-Ba-Cu- Nb-O compound. One is the cubic Nb perovskite $YBa_2NbO_6$, and the other $YBa_2Cu_3O_y$ phase.

Other reports indicated that at small additions of Nb content, transition temperature ($T_c$) of the Y-Ba-Cu-Nb-O compound was nearly constant [44, 49, 52] or a little higher than YBCO [45, 53]. On the other hand, a slowly increasing $T_c$ from 92 K to 95 K with an increase of Nb content is reported by others [54]. This result is [44-45] explained as an increase of oxygen index caused by small amount of Nb because of its higher affinity for oxygen than for Y, Ba and Cu. The lattice constant b remains almost unchanged while a and c increase with the increase of Nb content for $x \leq 0.10$. However, they decrease with an increase of Nb content for $x \geq 0.10$.

From the results on a series of samples of Melt processed mixed REBCO with varying amounts of Nb doping, it is reported by Murakami group that $(Nd_{0.33}Eu_{0.33}Gd_{0.33})Ba_2Cu_3O_{7-\delta}$ (NEG-123) superconductor with 35 mol.% of nano-Gd-211 and addition of 0.1 mol. % of $NbO_3$ is effective leading to the highest $J_c$ of 600 kA/cm$^2$ at 77 K in zero field [10].

Hence, we have chosen to study the effect of Nb addition on the optimum composition YSm-20 in the (Y, Sm)BCO series, through addition of 0.1 wt.% $Nb_2O_5$ along with 20 wt.% nano $Sm_2O_3$ to Y-211 powders in preform. The resultant product YSm-20-Nb was studied from structural, microstructural and magnetic properties point of view.

### 4.6.1. Temperature depenence of ac susceptibility:

The oxygen content varies considerably with synthesis conditions [55-56]. The diamagnetic transition of narrow width in the ac susceptibility measurement of the

sample is generally considered to be indicative of high-quality crystals with very good homogeneity and proper oxygenation. $T_c$ can change dramatically with the oxygen content.
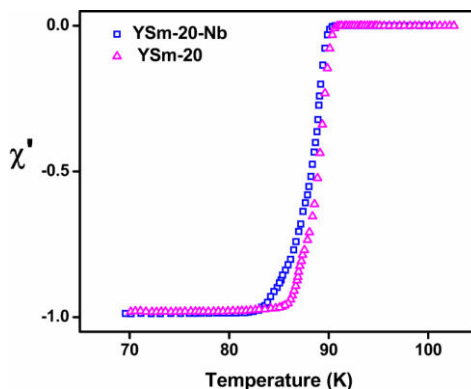


**Fig. 4.15.** Temperature dependence of real part of ac susceptibility ($\chi'$) for the samples YSm-20-Nb and YSm-20. The onset superconducting transition temperature remains the same for both the samples, but the transition width is more for the Nb- containing sample.

Superconducting transition temperatures of the samples were measured through temperature dependance of ac susceptibility which is shown in fig. 4.15. Onset $T_c$ of the YSm-20 and YSm-20-Nb samples were 90.71 K and 90.30 K respectively. A broad transition width of 5.5 K is observed for YSm-20-Nb sample where as the width of the transition for YSm-20 sample is 2.5 K.

### 4.6.2.  Structural analysis:

The X-ray diffractograms of the YSm-20 and YSm-20-Nb samples recorded using Cu K$_\alpha$ radiation (in 2θ ($^{\circ}$) ranging from 20 to 80) are shown in fig. 4.16.  In the present study it is found that Nb does not affect the orthorhombic crystal structure of YSm-20. Lattice parameters *a, b* and *c* (in Å) for YSm-20-Nb are 3.801, 3.882, 11.680 and those for YSm-20 are 3.811, 3.888 and 11.650 while the cell volumes are 172.34 Å$^3$ and 172.60 Å$^3$ respectively. A few additional peaks are seen with Nb doping, at 2θ ($^{\circ}$) of 29.79, 42.75, 53.09 and 62.09 apart from those indexed to

orthorhombic unit cell of (Y, Sm)BCO in the diffraction pattern. The extra peak positions match (indicated with ◆ symbol) with those of $YBa_2NbO_6$ compound (JCPDS file 24-1042).
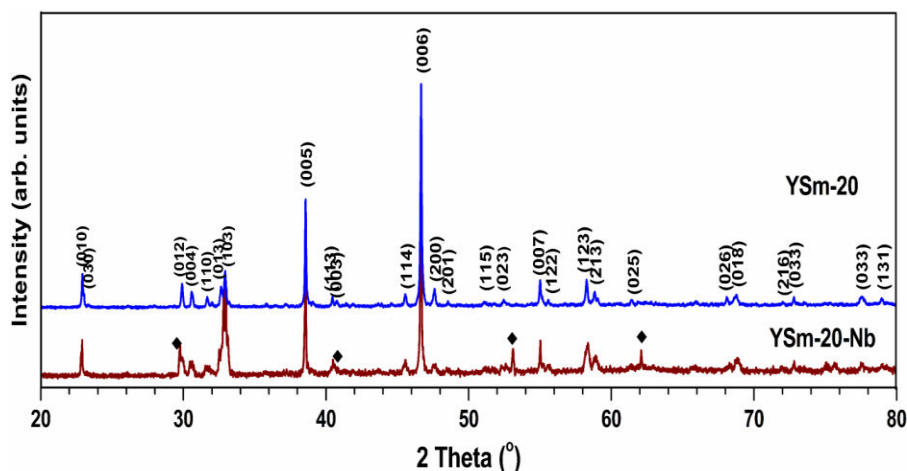


**Fig. 4.16.** X-ray diffractograms obtained from YSm-20 and YSm-20-Nb samples. The Nb- substituted sample shows the presence of an extra intermetallic phase $YBa_2NbO_6$. The diffraction lines from the phase are marked (◆).

### 4.6.3. Microstructural properties of YSm-20-Nb in comparison with those of YSm-20:

FESEM images of YSm-20-Nb and YSm-20 samples which are recorded at 2 kX using In-lens mode detector are shown in figs. 4.17 (a) and (b) respectively. A relatively homogenous distribution of second phase inclusions is evident and the RE-211 particles exhibit two regions, bright and dark, in both the processed samples. The size of the 211 particles in both the samples are more are less similar, but YSm-20 sample contains less macro porosity compared to YSm-20-Nb. Porosity in the samples is calculated considering 60000 $\mu m^2$ sampling area of the FESEM image with the help of Axiovision software. The calculated porosity for the YSm-20-Nb sample is 11.3% where as for YSm-20 it is 6.0%, although there is no change in heat treatment schedule or the atmosphere on Nb doping.
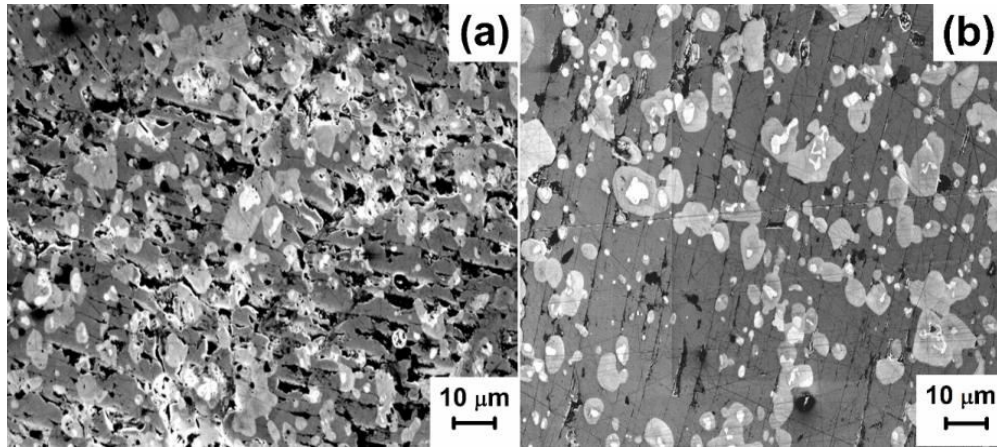
**Fig. 4.17.** FESEM images of POIG processed (a) YSm-20-Nb and (b) YSm-20. Addition of Nb to YSm-20 as given rise to more porosity in the microstructure with a minor refinement of the 211 particles.

### 4.6.4. Field dependence of critical current densities:

The magnetic $J_c$ values determined from M-H loops recorded at 25 K, 50 K, 65 K and 77 K are presented in figs. 4.18 (a), (b), (c) and (d) for both the YSm-20 and YSm-20-Nb samples. At all temperatures the value of the zero field current density ($J_c(0)$) of YSm-20-Nb is higher than for YSm-20 sample, but at higher temperatures $J_c$ falls off rapidly at high fields compared to that for YSm-20 sample. Addition of Nb enhanced the current density of YSm-20-Nb sample at zero field but does not sustain it to high fields at 65 K and 77 K.
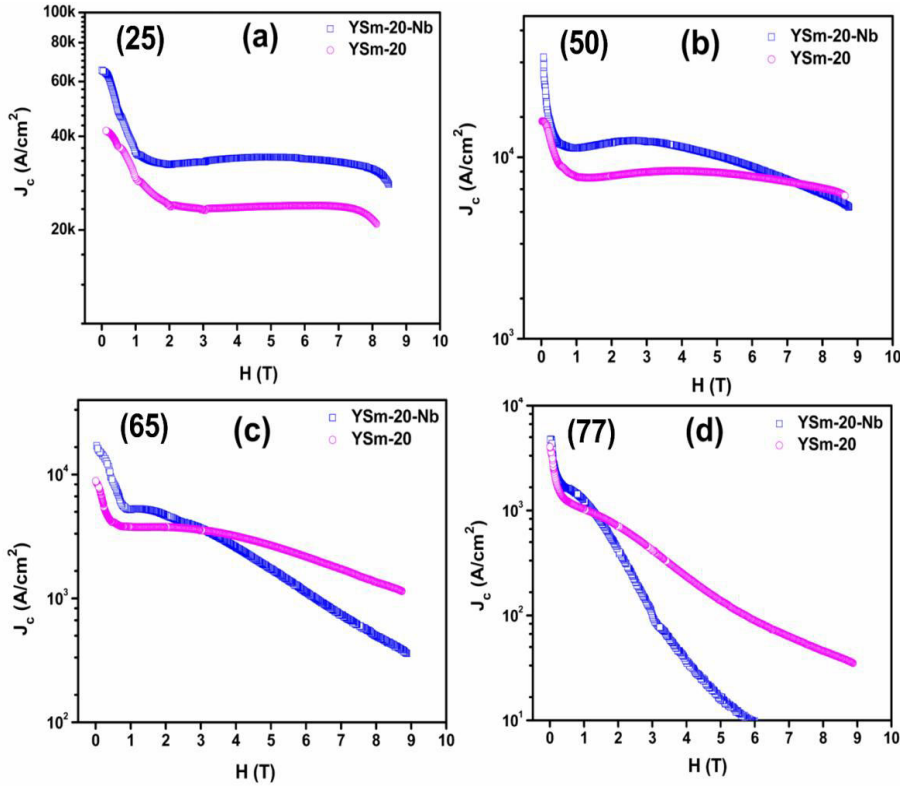
**Fig. 4.18.** Critical current densities of YSm-20-Nb and YSm-20 samples are compared as function of external field at different temperatures. $J_c(0)$ is larger for the Nb-containing samples at all temperatures. However, at higher temperatures the performance the Nb-containing samples deteriorates probably due to higher level of porosity.

### 4.6.5. Flux pinning force:

The field dependent pinning force, at different temperatures of YSm-20-Nb (in fig.19 (a)) and YSm-20 (in fig. 19 (b)) samples are shown. Flux pinning at low field may be associated with the size of RE-211 inclusions present in the RE-123 matrix and the associated interface defects. It is evident that, both the samples (shown in fig. 4.17) contain similar distribution of 211 phase particles in the sample. As a result, it is not surprising that both doped and undoped samples show comparable values of $J_c$ at zero field. It can be seen that the peak (i.e., maximum pinning force ($F_{p\ max}$)) shifts to lower fields for Nb doped sample and

occurs at 1.2 T for YSm-20-Nb, whereas $F_{p\,max}$ for YSm-20 sample is at 2.1 T at 77 K. At 65 K, $F_{p\,max}$ is 3.2 T for YSm-20-Nb and 5.1 T for YSm-20 sample.
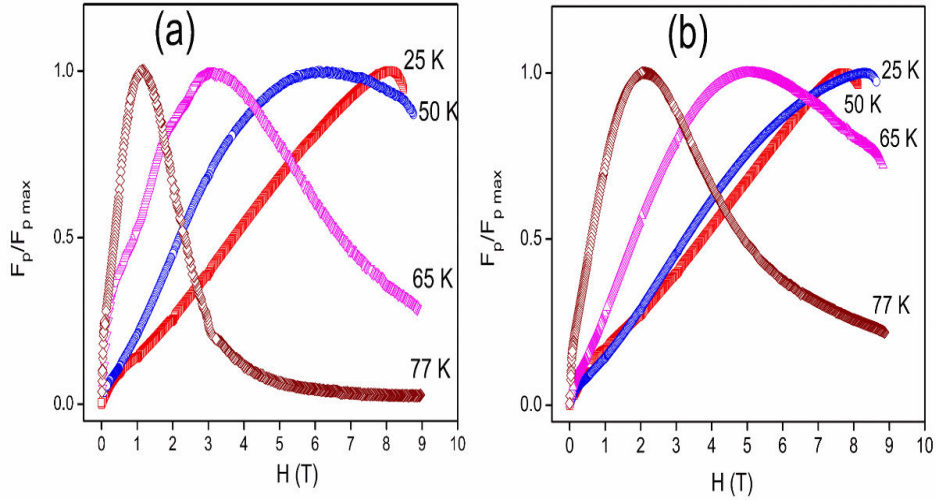


**Fig. 4.19.** The magnetic field dependence of the pinning force for the samples YSm-20-Nb and YSm-20 are shown in figs. (a) and (b) respectively. $F_p$ is normalized with respect to its maximum value at each temperature.

**Table 4.4:** Temperature dependence of $J_c(0)$ and normalized flux pinning force for YSm-20-Nb and YSm-20 samples.

|  | Sample | 77 K | 65 K | 50 K | 25 K |
|---|---|---|---|---|---|
| $J_c(H)$ (kA/cm$^2$) | YSm-20-Nb | 4.8 | 13.1 | 45.0 | 77.2 |
|  | YSm-20 | 4.1 | 8.9 | 15.8 | 41.7 |
| Peak $F_p/F_{pmax}$ | YSm-20-Nb | 1.2 | 3.2 | 6.4 | 8.2 |
|  | YSm-20 | 2.1 | 5.1 | 7.8 | 8.3 |

This demonstrates that the Nb doping has a good influence on flux pinning at low fields in these samples. Fig. 4.18 shows that though $J_c(0)$ values are comparable, the high field $J_c$ is much reduced on Nb doping at higher temperatures, the reason

for which can be attributed to the larger porosity present in YSm-20-Nb sample. The maximum $J_c(H)$ values at zero field obtained for the YSm-20-Nb and YSm-20 samples at different temperatures are tabulated in Table 4.4.

## 4.7. Discussion:

### 4.7.1. Structural properties and diamagnetic transitions:

In the end products of (Y, Sm)BCO, no unreacted liquid phases are present as evident from XRD ( fig. 4.3), which shows that the peritectic reaction was complete for all the samples. On increasing the concentration of Sm into Y-211 preform, a relative shift in the Bragg peak positions towards smaller angles has been observed indicating a change in the lattice parameters. This could be because Y ions of smaller size get replaced by larger Sm ions in the unit cells of (Y, Sm)BCO samples.

Apart from the diffraction peaks indexed to orthorhombic unit cell, un-indexed extra peaks are found in YSm-10 and YSm-30 samples indicating some amount of solid solutions to be present, which got suppressed in YSm-20 sample. As per reports in the literature [34], formation of solid solutions of $(Y, Sm)_{1+x}Ba_{2-x}Cu_3O_y$ type occurs predominantly in REBCO systems, if processed in air; which is reported to get suppressed if processed under argon atmosphere. Our results show that suppression of solid solution formation under argon was most effective only in YSm-20 sample in the present series. This conclusion is supported by the sharp diamagnetic transition observed in YSm-20 compared to the ones in YSm-10 and YSm-30 that exhibit a broad tail region (fig. 4.4).

In the YSm-20-C sample wherein Sm is chemically substituted for Y, a drastic reduction in lattice parameter c is observed. Reports in literature suggest [35] that

the complete exchange of $Y^{3+}$ by $Sm^{3+}$ in (Y, Sm)BCO samples leads to the increase of the lattice parameters. Substitution of $Ba^{2+}$ (size of 0.142 nm) with $Sm^{3+}$ (size of 0.108 nm) can cause shrinkage in c lattice parameter. The large c parameter shrinkage found in YSm-20-C sample indicates that considerable amount of $Ba^{2+}$ is substituted by $Sm^{3+}$, and that would form solid solutions of (Y, Sm)$_{1+x}$Ba$_{2-x}$Cu$_3$O$_y$ type. This argument gets support from the extra Bragg peaks seen in the XRD pattern of YSm-20-C, compared to YSm-20 shown in fig. 4.11, and from the broader diamagnetic transition with a tail region of lower $T_c$ phases as seen in fig. 4.13.

In the YSm-20-Nb sample with Nb doping, there is no substantial variation in the lattice parameters, but weak Bragg peaks are seen in XRD indicating a small amount of non-superconducting $YBa_2NbO_6$ compound to be present as second phase. There is no reduction in the onset of superconducting transition temperature due to Nb doping, as reported [44, 49, 52] in ac susceptibility measurements. The broad tail seen below the transition suggests the presence of lower $T_c$ phases which may be oxygen deficient phases (formed because of the higher affinity of Nb for oxygen than for Y, Ba and Cu [56]), rather than solid solutions of REBCO, since there are no indications of solid solution formation from XRD.

### 4.7.2. On evolution of microstructures:

A close examination of the microstructural features in the various (Y, Sm)BCO samples led to the following observations:

(i)  Spherical pores are observed throughout all the samples.
(ii)  RE-211 particles are distributed in the RE-123 matrix. In YSm-10, YSm-20 and YSm-30 samples, brighter regions (annular core formation)

surrounded by darker region are seen within the RE-211 particles indicating compositional segregation.

**(iii)** However, in YSm-20-C sample with chemical substitution of Sm for Y, the cores are smeared out within the 211 particles.

**(iv)** Additionally, considerable amount of non-spherical porosity (macro-defects) are also observed in all the samples.

**(v)** Size of RE-211 particles range in 2-6 microns on an average

It is interesting to recall and compare the microstructural features of the two POIG processed YBCO samples without any Sm, one processed under argon (YBCO-Ar) and the other processed in air (YBCO-Air), which was discussed earlier in section 3.3.2 of chapter III. There are no annuli cores present in YBCO without Sm doping in both the samples. Size of the majority of Y-211 particles in YBCO-Air sample was of the order of 0.5 - 1.5 μm with negligible porosity. But in the present samples of YBCO and (Y, Sm)BCO processed under Ar atmosphere, considerable amount of both spherical and non-spherical porosity is observed.

### 4.7.2.1. Origin of spherical porosity:

Spherical porosity is an indication of gas bubble evolution through liquid medium during its solidification. Following the reports in literature, it is essential to synthesize the REBCO samples in inert gas atmosphere. Hence all samples are processed in commercial grade Ar atmosphere to suppress the formation of solid solutions. Gas evolution either oxygen or argon was proposed in melt grown REBCO by Murakami group [58-59]. In the present samples presence of spherical porosity may be due to argon gas, entrapped at high temperatures, evolved as bubbles during solidification process while cooling through $T_p$ for ensuring the formation of (Y, Sm)BCO crystal.
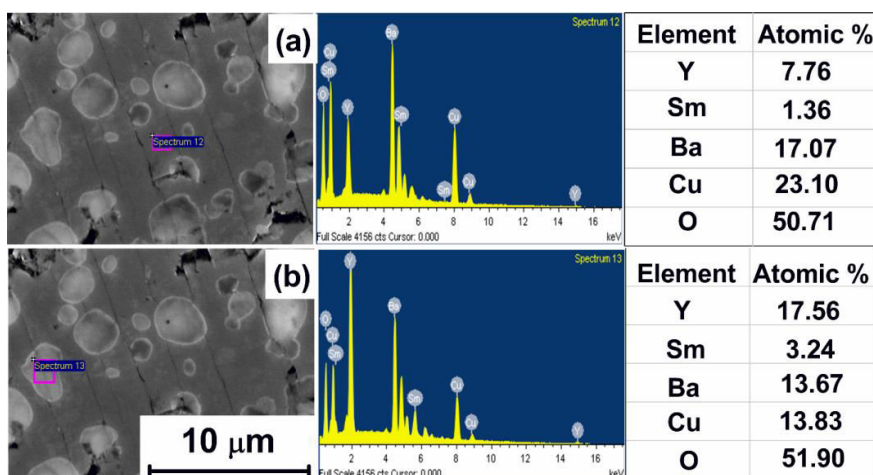
### 4.7.2.2. Formation of bright and dark regions in the precipitates and compositional fluctuations in the matrix:
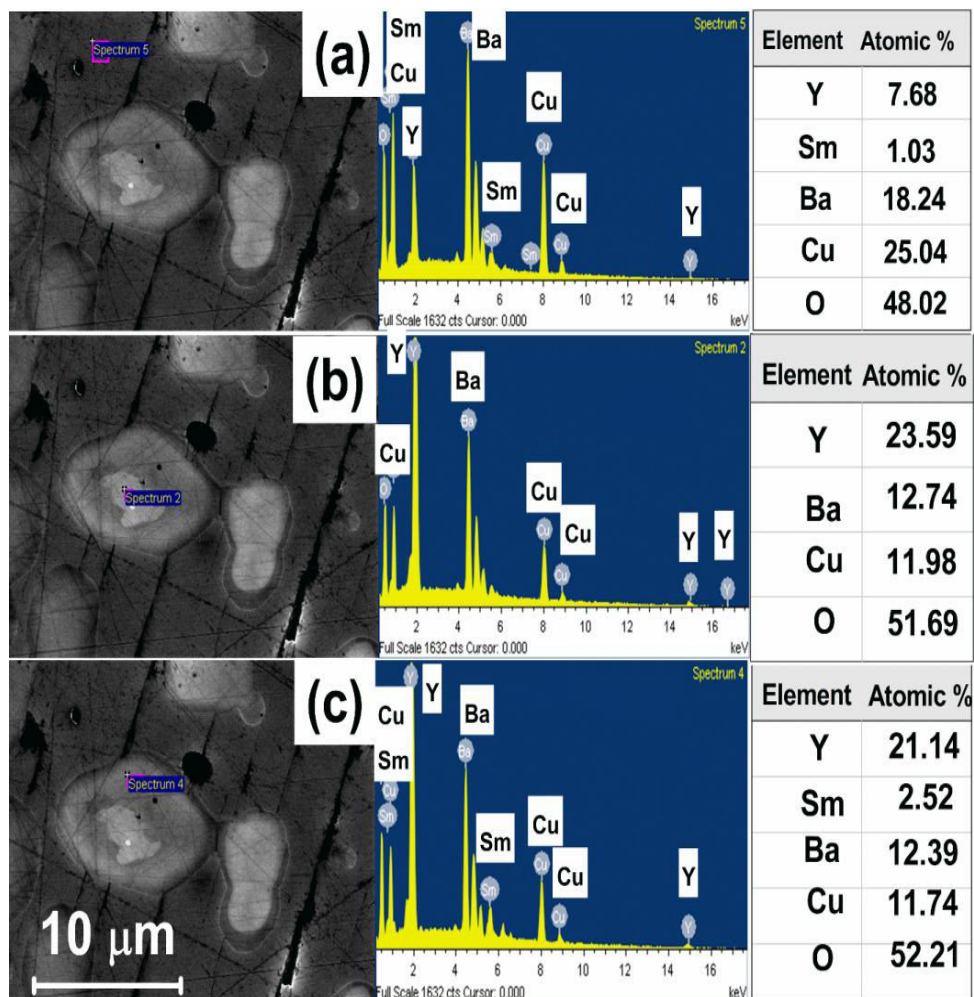


**Fig. 4.20.** Compositional analyses of POIG processed YSm-20 sample. Upper panel (a) shows the composition obtained by an area scan of the 123 matrix. The area from where the data was acquired is marked in the micrograph. The measured composition shows that the matrix consists of YSm-123. (b) the middle panel shows compositional analyses, through a point scan, of the bright region in the middle of a 211 grain. The region is found to be free of Sm and corresponds to the composition of $Y_2BaCuO_5$. (c) the lower panel is a point scan analyses of the darker outer region of a 211 grain. The composition corresponds to $(Y, Sm)_2BaCuO_5$.

In order to identify various phases observed in the matrix and in the bright and dark regions of the precipitates, compositional analysis of the synthesized samples was carried out in detail using EDS through a) area scans and b) point scan. Given below are the results of area and point scan recorded in the samples of YSm-20 chosen as an example. Mapping and line scan results are given in the Appendix.

Quantitative analyses of the elements present in the YSm-20 sample was carried out using EDS study through area scan and point scans and are shown in fig. 4.20. These measurements were done on the matrix, on the darker and brighter regions of the precipitates and are shown in fig. 4.20 (a), (b) and (c) respectively. The elemental ratios suggest the matrix phase to be YSm-123 and the darker region in the precipitates to be YSm-211. The cored bright regions are rich in Y and have no Sm and the composition is close to Y-211. This was further confirmed by line scan analysis given in appendix. The area and point scans recorded in YSm-20-C sample are given below in fig.4.21.



| Element | Atomic % |
|---------|----------|
| Y | 7.76 |
| Sm | 1.36 |
| Ba | 17.07 |
| Cu | 23.10 |
| O | 50.71 |

| Element | Atomic % |
|---------|----------|
| Y | 17.56 |
| Sm | 3.24 |
| Ba | 13.67 |
| Cu | 13.83 |
| O | 51.90 |

**Fig. 4.21.** Elemental analysis in YSm-20-C. The upper panel, we note that the matrix composition is YSm-123. A compositional analysis of the 211 grains reveals that they have Y and Sm distributed uniformly within their volumes and there is no evidence of the formation of a core of composition Y-211.

Here, the core formation is not observed but it appears to be smeared out throughout the precipitates in the matrix.

The compositional analysis on the above two samples confirmed that the three different shades within the samples correspond, within error limits, to three phases of composition YSm-123, YSm-211 and Y-211. From quantitative analysis, it is found that the dark regions in the precipitates are mainly composed of YSm-211 phase and the brighter regions looking like annuli cores are of Y-211 phase with no Sm. In the YSm-20-C sample the bright and dark regions are smeared out and contain Y and Sm throughout the YSm-211 particles, whereas in YSm-20 these dark and bright regions are distinct with no Sm in the bright cores while both Y and Sm exist in the darker regions. The matrix in both the samples contains YSm -123 phase. The matrix phase forms by peritectic reaction between the outer dark regions of YSm-211 particles with the liquid phase and hence Sm enters the matrix phase. The high solubility of the Sm and higher peritectic temperature ($T_p$) of SmBCO, compared to YBCO would cause compositional fluctuations of (RE, RE')BCO type in the matrix.

Haribabu et. al., [32] reported similar compositional segregation within the precipitates in the matrix phase of (Y, Nd)-BCO system and they proposed that the second phase particles could be solid solutions $(Y_x, Nd_{1-x})BaCuO_5$ ((Y, Nd)-211 phase) with the value of x varying from 0.7 to 0.3.

We discuss below the possible reasons for the occurrence of compositional segregation within the precipitates in the form of bright and dark regions in (Y, Sm)BCO samples. The following model also explains the occurrence of finite porosity in the final composites.

We compare the microstructures of preform powders, sintered preforms and the

final composites after POIG process to arrive at a mechanism to explain the microstructural features.
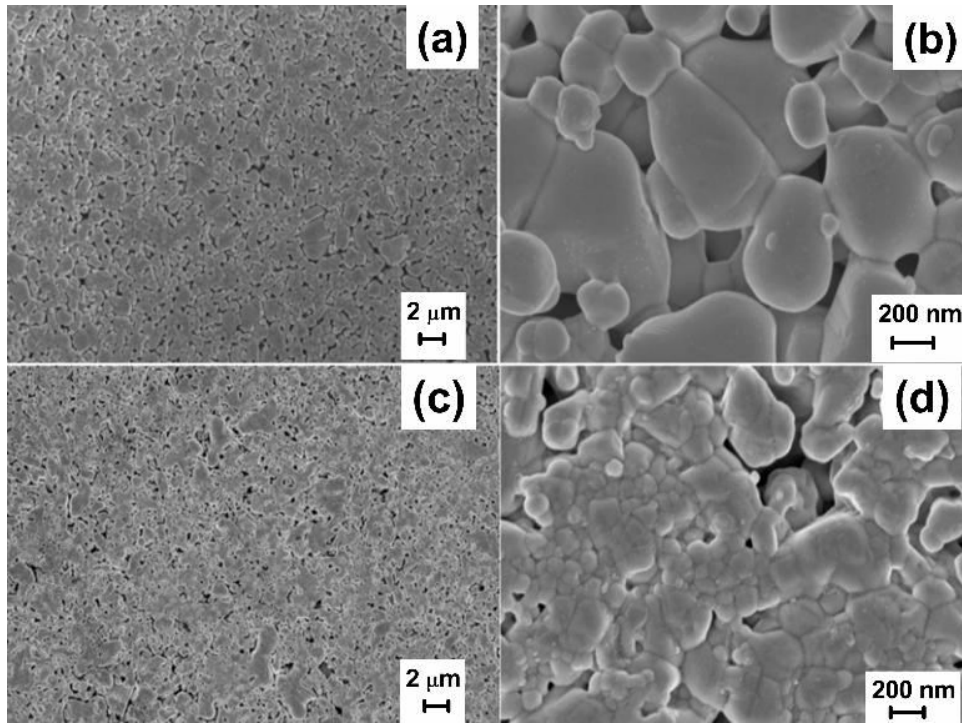


**Fig. 4.22.** FESEM images from sintered preforms used for the fabrication of POIGP YSm-20-C at lower and higher magnifications are shown in (a) and (b) respectively. Similar images from YSm-20 are shown in (c) and (d). The preforms were fabricated in a die at a pressure of 460 MPa and sintered at 950 $^\circ$C for 4h. The comparison between figs. (b) and (d) shows that in the latter sample, the 211 particles are sintered into large grains due to the higher reactivity of the $Sm_2O_3$ nano particles added to it. The observed sintering of the 211 particles are relevant from the point of view of ease of infiltration of liquid phases and the 211 grain growth in the final microstructure.

It can be seen from the FESEM images recorded in the powders of preform (fig. 4.2) and in the preforms sintered at 950 $^\circ$C for 4 hours (fig. 4.22), that the nano $Sm_2O_3$ particles of 50-80 nm size distributed homogenously on the surface of the Y-211 particles got agglomerated after sintering and their size increased to 100-200 nm. Some of the nano $Sm_2O_3$ particles slip around the Y-211 particles

(around Y-211 grain boundaries) and fill the gaps (i.e. open porosity) between the Y-211 particles in the preform. This process alters the extent of open porosity in YSm-211 preform and control the amount of liquid phases that enter into the preform.

Interaction of Sm in nano $Sm_2O_3$ with Y-211 forms YSm-211 phase particles to some extent, sometimes leaving unreacted Y-211 cores within the YSm-211 particles. The interaction at the surface of these particles fuses the particles wherever they make a contact leaving some gaps between them. During infiltration the liquid phases flow to the bottom through the gaps in the YSm-211 preforms, and react with it to form YSm-123 matrix. The Y-211 cores left back within the YSm-211 particles form bright cores of random shapes and are due to non-availability of liquid phases for further reaction.

It is interesting to compare the FESEM images of the sintered preforms of YSm-20-C-211 and YSm-20-211shown in figs. 4.22 (b) and (d) above. Larger amount of open porosity can be seen in the former preform with chemically substituted Sm (fig. 22 (b)) than in the latter preform with nano $Sm_2O_3$ addition (fig. 22 (d)). This leads to larger amount of liquid phases to enter into the former preform and thus result in reduced porosity in its final product Y-Sm-20-C with finer RE-211 particles in it (fig. 4.12(a)).
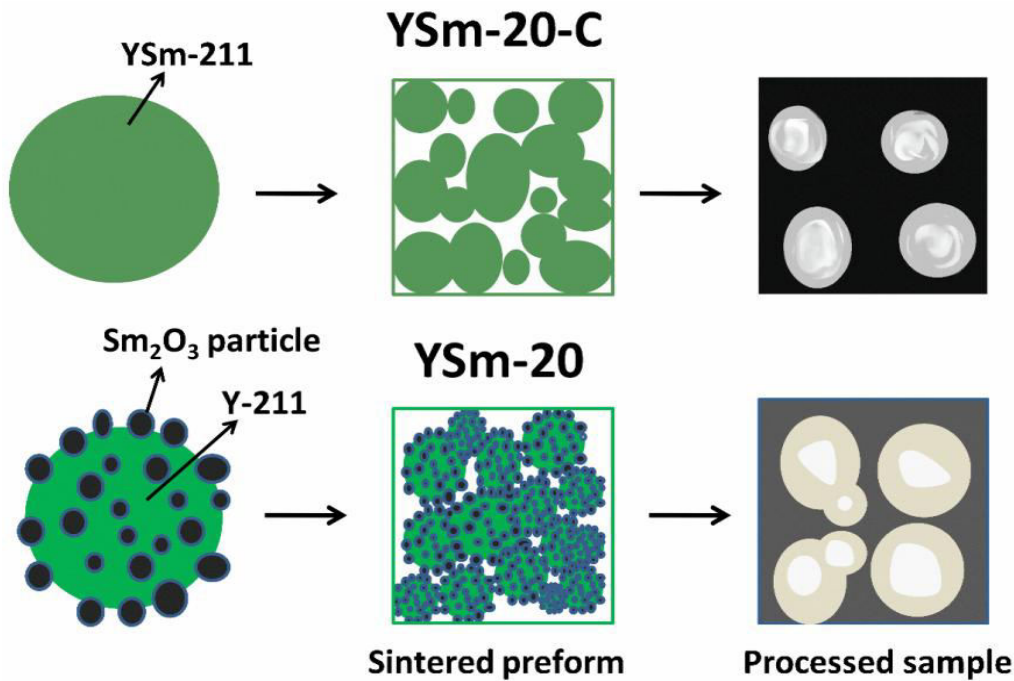
**Fig. 4.23.** Schematic figures to illustrate the mechanism of core formation within 211 precipitates in (Y, Sm)BCO samples.

Fig. 4.23 illustrates the mechanism of fusing of the YSm-211 particles in YSm-20-C preform; embedding of nano particles of $Sm_2O_3$ onto Y-211 particles and their subsequent reaction in the YSm-20 preform (during pressing and sintering at 950 $^o$C); and the smearing out or occurrence of compositional segregation within YSm-211 particles in the final microstructure. In YSm-20-C sample the distribution of Sm element in preform is homogenous; hence the microstructure of processed (Y, Sm)BCO sample contains YSm-211 particles with Y rich phase smeared out.

On the other hand, in YSm-20 as shown in fig. 4.22 the resultant preform has less porosity (gaps between Y-211 particles) that causes insufficient liquid infiltration into the preform and result in incomplete crystallization in some parts of the preform thus forming pores in the sample. Fusing of particles is not present in the

case of YSm-20-C, so the microstructure contains a number of smaller sized YSm-211 particles compared to YSm-20 as shown in FESEM images of processed samples (fig. 4.12).

The non-spherical macro-defects in the samples and the final size of 211 particles in the product thus appear to depend strongly on the quantity of liquid phases that enter the preform during infiltration process. The reasons for non-spherical porosity may thus be understood as follows. Due to limited infiltration of liquid phases into the Y-211 preform, there exists unavailability of liquid phases in some regions in the preform which limits the formation of 123 matrix leading to finite porosity. Lack of sufficient liquid phase amount also limits the refinement of 211 particles.

### 4.7.3. Compositional analysis of YSm-20-Nb sample from EDS:

The microstructure of Nb doped YSm-20-Nb sample shows several precipitates to be distributed in the matrix phase and also the presence of annuli core formation in the precipitates. Elemental analyses on different phases (on matrix and non - superconducting precipitates) have been carried out using EDS and are displayed in figs. 4.24.
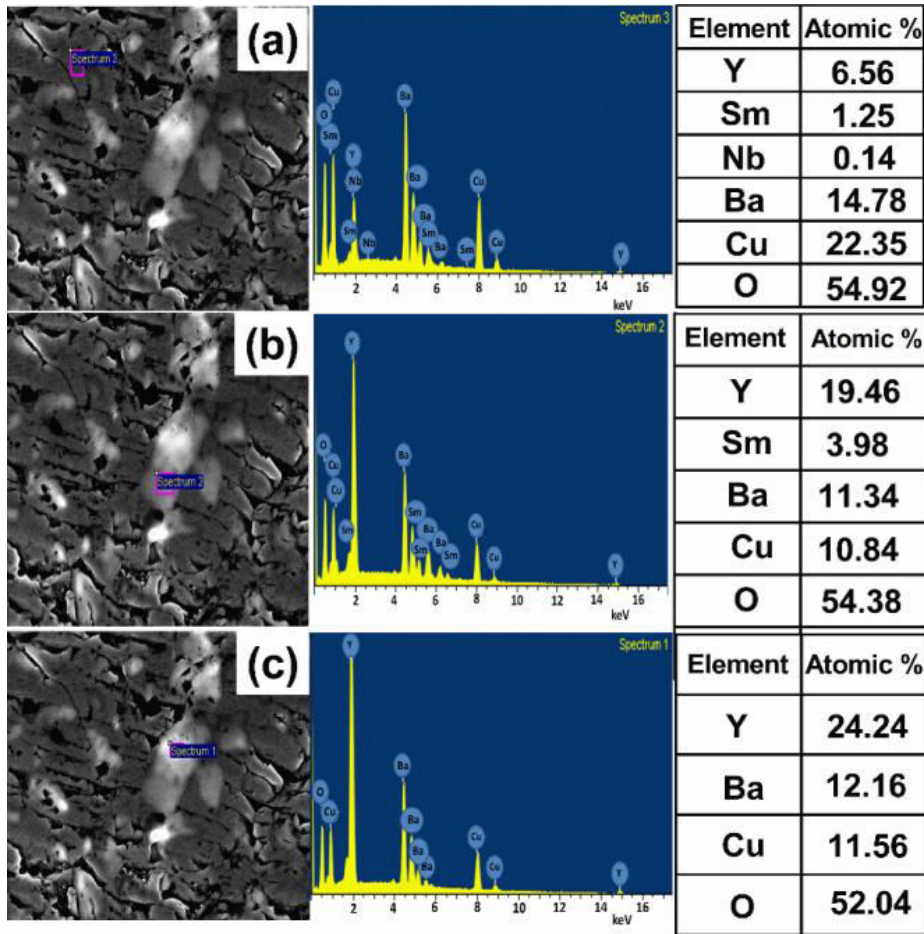
| Element | Atomic % |
|---|---|
| Y | 6.56 |
| Sm | 1.25 |
| Nb | 0.14 |
| Ba | 14.78 |
| Cu | 22.35 |
| O | 54.92 |

| Element | Atomic % |
|---|---|
| Y | 19.46 |
| Sm | 3.98 |
| Ba | 11.34 |
| Cu | 10.84 |
| O | 54.38 |

| Element | Atomic % |
|---|---|
| Y | 24.24 |
| Ba | 12.16 |
| Cu | 11.56 |
| O | 52.04 |

**Fig. 4.24.** Compositional analysis of YSm-20-Nb sample using EDS. The upper panel shows that the composition of the matrix corresponds to $(Y, Sm)Ba_2Cu_3O_{7-\delta}$, with a small amount of dissolved Nb. The middle panel shows that the composition of the darker part of the 211 precipitates correspnds to $(Y, Sm)_2BaCuO_5$. The lowest panel shows that the core region of the precipitates contains no Sm or Nb and is pure Y2BaCuO5.

Results indicate YSm-123 along with Nb to be present in the matrix, while the dark and bright regions are YSm-211 and Y-211 respectively similar to the observations in YSm-20 sample. Doped Nb does not appear to have reacted with 211 particles, and hence is not detected in the precipitates. Presence of Nb only in the matrix agrees with the traces of secondary phase of $YBa_2NbO_6$ in the matrix detected through XRD study.

### 4.7.4. Magnetic properties:

From a close examination of the doping studies reported in literature on mixed REBCO systems, we gather the following generalizations.

The variation of $T_c$ close to the tail region of the curve can be attributed to the oxygen deficient phases. In the RE-doped samples, Sm substituted for Y forms solid solutions of RE/RE[1] –ss type and gives rise to compositional fluctuations (governed by $(Y_{1-x}, Sm_x)BCO$) with minor variation in $T_c$ in the matrix phase and aids flux pinning ($\Delta T_c$ pinning) at high fields. In addition to Y ion site substitution, partial substitution of Sm into $Ba^{2+}$ sites is anticipated because of the similar ionic sizes of $RE^{3+}$ and $Ba^{2+}$ [32]. Hence one expects a distribution in $T_c$ in the (Y, Sm)BCO samples unlike in the YBCO-Ar sample with no RE element. Distribution of $T_c$ often owes its origin to the compositional fluctuations in the matrix of RE/Ba -ss phase in all the (Y, Sm)BCO samples. Small amounts of substitution of RE at Y site or Ba site cause minor variations in $T_c$ and are believed to behave like point defects and enhance the flux pinning. On the other hand, larger levels of substitution of RE at Ba site can result in considerable reduction in $T_c$. It is not clearly understood as in literature to the extent of effect of this on flux pinning and $J_c$.

The variations in $T_c$ across the transition have been observed to be anywhere from 90 K to 70 K in different samples of (Y, Sm)BCO system, as measured from ac susceptibility measurements. Such a variation can be attributed to RE/Ba substitution which results in solid solution formation of $RE_{1+x}Ba_{2-x}BCO$ in the synthesized samples. While low $T_c$ phases if present in very small amounts can aid pinning, larger amounts of low $T_c$ phases can be detrimental to the superconductor performance. We discuss below the temperature dependence of $J_c(H)$ of various samples in correlation to the solid solution formation indicated

by XRD and distribution in $T_c$ observed. $J_c$ also is sensitively dependent on size and amount of 211 particles and the porosity in the end products.

$J_c$ variations shown in fig 4.8 clearly show that even though YBCO-Ar sample shows high $J_c(0)$, it rapidly falls to zero at 5 T. Among (Y, Sm)BCO samples YSm-20 showed the best performance to fields beyond 9 T at 77 K (fig. 4.8), which can be attributed to the compositional fluctuations of Y, Sm in the unit cells of the matrix. It should be recalled here that XRD of YSm-20 shows that solid solutions of RE/Ba -ss type with lower $T_c$ are largely suppressed in this sample. The inferior performance of $J_c(H)$ of YSm-10 and YSm-30 samples, compared to YSm-20 can be attributed to the formation of large amounts of RE/Ba –ss low $T_c$ phases as also seen from XRD and $\chi_{ac}(T)$ studies. However $J_c$ at higher fields in them is far better than YBCO-Ar sample due to pinning from compositional fluctuations within the matrix which is obviously absent in YBCO-Ar.

It is interesting to note that in earlier reports [60-61] on (Y, Dy)BCO system, 20 and 80% doping of RE in RE[1] (where RE and RE[1] are different rare earth elements) has caused enhancement of superconducting properties. This is attributed to be due to the stress field associated with lattice mismatch effects to be optimal at these compositions. These are due to the differences in the sizes of neighbouring unit cells containing RE and RE[1]. Thus the stress field can be another source of pinning in addition to $\Delta T_c$ pinning.

The enhancement in $J_c$ up to high fields in YSm-20 is attributed to improved flux pinning by dispersed nano sized low $T_c$ clusters as well as stress field in the matrix, while 211/123 interface defects play a role at low fields. This is evident from the observation that in YBCO-Ar sample $F_p(H)$ peak tends to shift rapidly towards lower H at elevated temperatures, which confirms that dominant pinning

in this sample is from interfacial defects. This argument gets support from the fact that there is no solid solution formation in this sample.

Drastic reduction in $J_c(H)$ is observed for YSm-20-C sample, when compared to YSm-20. Zero-field $J_c$ at 77 K has decreased to 110 A/cm$^2$ in this sample in contrast to 4.1 kA/cm$^2$ for YSm-20.We attribute the origin of this reduction to the large fraction of solid solutions of RE/Ba –ss type formed in YSm-20-C as indicated by XRD and ac susceptibility measurements.

In Nb doped YSm-20 sample, enhanced current density is observed at low fields compared to YSm-20, especially at low temperatures. This can be due to the flux pinning caused by enhanced interfacial defect density which is evident from the finer 211 particles observed in this sample. Pinning due to secondary phases of YBa$_2$NbO$_6$, seen from XRD, may also contribute to low field pinning as suggested by *Kuwabara et al.* [49] in Nb doped YBCO system. However, at higher temperatures $J_c$ falls rapidly at high fields compared to YSm-20 sample, though compositional fluctuations of RE/RE' do exist in Nb doped YSm-20-Nb sample as well. Moreover Nb also promotes oxygen deficient phases of lower $T_c$ observed as tail in $\chi_{ac}(T)$, which can also enhance $J_c$ through $\Delta T_c$ pinning. This can be attributed mainly to the larger porosity present in the sample. In this context, rapid fall in $J_c$ at 77 K suggests that the effect of porosity seems to dominate and shadows the additional flux pinning from various sources at higher temperatures.

**References:**

1. G. Krabbes, G. Fuchs and W.F. Canders, High Temperature Superconductor Bulk Materials: Fundamentals Processing Properties Control Application Aspects (Wiley, GmbH, Weinheim) (2005).

2. A.B. Pippard, Physica C **19** (1953) 765.

3. A.A. Abrikosov, Rev. Mod. Phys. **76** (2004) 975.

4. N. Hari Babu, Kazumasa Iida, Amy Briffa, Yun-Hua Shi, Lee S. Matthews and David A. Cardwell, IEEE TRANSACTIONS ON APPLIED SUPERCONDUCTIVITY **17** (2007) 2953.

5. D.F. Lee, V. Selvamanickam and K. Salama, Physica C **202** (1992) 83.

6. U.H. Pi, Z.G. Khim and D.H. Kim, Phys. Rev. B **69** (2004) 094518.

7. R. Ramesh, S. Jin, S. Nakahara and T.H. Tiefel, Appl. Phys. Lett. **57** (1990) 1458.

8. Shih-Yun Chen, In-Gann Chen, Yang-Chung Liao, Maw-Kuen Wu, J. Mater. Res., 20 (2005) 2.

9. A. Radhika Devi, V. Seshu Bai, P.V. Patanjali, R. Pinto, N. Harish Kumar and S.K. Malik, Supercond. Sci. Technol. **13** (2000) 935.

10. M. Muralidhar, N. Sakai, M. Jirsa, M. Murakami and I. Hirabayashi, Appl. Phys. Lett. **92** (2008) 162512.

11. W. M. Yang, L. Zhou, Y. Feng, P.X. Zhang, M.Z. Wu, C.P. Zhang, J.R. Wang, Z.H. Du, F.Y. Wang, Z.M. Yu, X.Z. Wu, W. Gawalek and P. Gornert, Physica C **305** (1998) 269.

12. Caixuan Xu, Anming Hu, Naomichi Sakai, Mitsuru Izumi and Izumi Hirabayashi, Physica C **445** (2006) 357.

13. Chan-Joong Kim, Najam ul Qadir, Asif Mahmood, Y. H. Han and T. H. Sung, Physica C **463–465** (2007) 344–347.

14. N. Moutalibi, A. M'chirgui and J. Noudem, Physica C **470** (2010) 568–574.

15.  Y. Zhao, C.H. Cheng and J.S. Wang, Supercond. Sci. Technol. **18** (2005) S43–S46.

16.  N. Hari Babu, E.S. Reddy, D.A. Cardwell, A.M. Campbell, C.D. Tarrant and K.R. Schneider, Appl. Phys. Lett. **83** (2003) 23.

17.  P.M. Swarup Raju, Ph.D. Thesis (2012) "Infiltration growth processing of YBCO nano-composites: Shape forming, microstructural and magnetic studies".

18.  L. Shlyk, K. Nenkov, G. Krabbes and G. Fuchs, Physica C **423** (2005) 22-28.

19.  D. Litzkendorf, T. Habisreuther, R. Muller, S. Kracunovska, O. Surzhenko, M. Zeisberger, J. Riches and W. Gawalek, Physica C **372** (2002) 1163.

20.  G. Osabe, T. Takizawa, S.I. Yoo, N. Sakai, T. Higuchi and M. Murakami, Mater. Sci. Eng. B-Solid State **65** (1999) 11-16.

21.  Y. Xu, M.J. Kramer, K.W. Dennis, H. Wu, A. O`Connor, R.W. McCallum, S.K. Malik and W.B. Yelon, Physica C **333** (2000) 195-206.

22.  Y. Li, Y. Liu, R. Duan, X. Xiong, B. Wang, G. Cao, L. Wei, D.N. Zheng, Z.X. Zhao and J.H. Ross, Physica C **402** (2004) 179-187.

23.  M. Sano, Y. Hayakawa and M. Kumagawa, Superconduct. Sci. Technol. **9** (1996) 478-482.

24.  I. Van Driessche, B. Schoofs, E. Bruneel and S. Hoste, J. Eur. Ceram. Soc. **24** (2004) 1823-1826.

25.  N. Devendra Kumar, T. Rajasekharan, K. Muraleedharan, A. Banerjee and V. Seshubai, Supercond. Sci. Technol. **23** (2010) 105020.

26.  J. Maňka, A. Cigáň, J. Polovková, A. Koňakovský and A. Prnová, Measurement science review **11** (2011) 1.

27.  M. Murakami, S.I. Yoo, Takamitsu Higuchi, Naomichi Sakai, Jurgen Weltz, Naoki Koshizuka and S. Tanaka, Jpn. J. Appl. Physics **33** (1994) L715-L717.

28. M. Muralidharan and M. Murakami, Supercond. Sci. Technol. **13** (2000) 1315-1321.

29. T. Saitoh, K. Segawa, K. Kamada, N. Sakai, T. Segawa, S.I. Yoo and M. Murakami, Physica C **288** (1997) 141.

30. M. Oda, X Yao, Y. Yoshida and H. Ikuta, Supercond. Sci. Technol. **22** (2009) 075012.

31. Chakrapani Varanasi, Paul J. Mc Ginn, Howard A. Blackstead and David B. Pulling,
    Journal of electronic materials **24** (1995) 12.

32. N. Hari Babu, M. Kambara, E.S. Reddy, Y. Shi and D.A. Cardwell, Supercond. Sci. Technol. **18** (2005) S38–S42.

33. M. Muralidhar, M.R. Koblischka and M. Murakami, Physica C **313** (1999) 232.

34. M. Muralidhar, S. Nariki, M. Jirsa, Y. Wu and M. Murakami, Appl. Phys. Lett. **80** (2002) 1016.

35. P. Schätzle, W. Bieger, U. Wiesner, P. Verges and G. Krabbes, Supercond. Sci. Technol. **9** (1996) 869–874.

36. H.M.I Bryan and P. K. Gallagher, "Ceramic superconductors - II" (Ed. Man F. Yan) , American Ceramic Society, Ohio, 89 (1988)

37. C.P. Bean, Phys. Rev. Lett. **8** (1962) 250.

38. E.M. Gyorgy, R.B. van Dover, K.A. Jackson, L.F. Schneemeyer and J.V. Waszczak, Appl. Phys. Lett. **55** (1989) 283.

39. Shih-Yun Chen, In-Gann Chen, Yang-Chung Liao, Maw-Kuen Wu, J. Mater. Res. **20** (2005) 2.

40. D. Dew-Hughes, Philos. Mag. **30** (1974) 293.

41. M.R. Koblischka, Physica C **282** (1997) 2193.

42. Chakrapani Varanasi, J. Paul. Mc Ginn, Howard A. Blackstead and David B. Pulling, J. Electron. Mater **24** (1995) 1949.

43. M.H. Abdullah and B.T. Tan, Solid State Commune **931** (1994) 93- 96.

44. I. Grekhov, L. Delimova, I. Liniychuk, O. Semchinova and M. Baydakova, Physics C, **235-240** (1994) 1295-1296.

45. K. V. Paulose, J. Koshy and A. D. Damodaran, Japanese Journal of Applied Physics, **30** (1991) L458-L460.

46. G.K. Strukova, I.S. Smirnova, S.A. Shevchenko, A.I.K olyubakin, I.I. Zver'kova, V. Sedykh, A.A. Polyanskii, L.A. Dorosinskii and V.S. Shekhtman, Superdome Science Tech. **6** (1993) 589-592.

47. M. Bennahmias, H.B. Radousky, T.J. Goodwin and R.N. Shelton, Journal of Electronic Materials **22** (1993) 1189.

48. Y. Hikichi, T. Maruta, S. Suzuki, M. Miyamoto, S. Okada and K. Kudou, Japanese Journal of Applied Physics **31** (1992) L1232-L1235.

49. M. Kuwabara and N. Kusaka, Japanese Journal of Applied Physics **27** (1988) L1504-L1506.

50. N.G. Suresha, S. Higo, Y. Hakuraku, T. Otawa, Y. Honjo and T. Ogushi, International Journal Modern Physics B **2** (1988) 435-441.

51. K. Eguchi, K. Kuma and H. Arai, Molecular Crystals and Liquid Crystals **184** (1990) 153-157.

52. S. Higo, Y. Hakuzaku, T. Ogushi, I. Kawano and Y. Ishikawa, Molecular Physics Letters B **4** (1990) 823-830.

53. G. M. Kammlott, T. H. Tiefel and S. Jin, Applied Physics Letters **56** (1990) 2459.

54. Mucahit Yilmaz and Oguz Dogan, Materials Sciences and Application **2** (2011) 1090.

55. M. Jirsa, M.R. Koblischka, T. Higuchi, M. Muralidhar and M. Murakami, Physica C **338** (2000) 235-245.

56. H.M.I Bryanand P.K. Gallagher, "Ceramic superconductors- II" (Ed. ManF. Yan), American Ceramic Society, Ohio, 89 (1988)

57. Y. Matsumoto, T. Abe, M. Tanaka, T. Tazawa and E. sato, Mat. Res. Bull. **23** (1988) 1241.

58. A. Mahmood, B.H. Jun, Y.H. Han and C.J. Kim, Supercond. Sci. Technol. **23** (2010) 065005.

59. N. Sakai, D. Ishihara, K. Inoue and M. Murakami, Supercond. Sci. technol. **15** (2002) 698-701.

60. Yang Li, Lijie Cui, Guohui Cao, Qingzhu Ma, Chunguang Tang , Yunbo Wang , Long Wei , Y.Z. Zhang , Z.X. Zhao and Elisa Baggio-Saitovitch, Physica C **314** (1999) 55–68.

61. A Radhika Devi, V Seshu Bai, P V Patanjali, R Pinto, N Harish Kumar and S K Malik, Supercond. Sci. Technol. **13** (2000) 935.

# Chapter V

# Structural, microstructural and magnetic investigations of POIG processed (Y, NSG)BCO superconductors

Investigations on many secondary and ternary rare earth $REBa_2Cu_3O_{7-\delta}$ (REBCO) high-$T_c$ compounds, especially containing light rare earth (LRE) elements like Gd, Sm, Nd are reported in literature [1-11]. These include studies on systems like (Y, Nd)BCO, (Y, Sm)BCO, (Nd, Eu, Gd)BCO, (Y, Sm, Nd)BCO, (Sm, Eu, Gd)BCO etc. Most of these reports are on compounds processed through melt growth technique. In fourth chapter we reported results on the preparation and study of (Y, Sm)BCO superconductors synthesized by POIG process in commercial grade Ar atmosphere. In this chapter we aim at a study of the effect of introducing mixed ternary RE elements (Nd, Sm and Gd) into YBCO superconductor at Y site and assess the performance from a study of microstructural and magnetic properties. Based on the results on (Y, Sm)BCO system we note that addition of 20 wt.% $Sm_2O_3$ introduced into Y-211 preform gave the best $J_c$-H performance. Keeping this in mind, we have chosen to add 20 wt.% of $(Nd, Sm, Gd)_2BaCuO_5$ (hereafter called NSG-211) into Y-211 and then subject the pressed preform to POIG process to arrive at (Y, (Nd, Sm, Gd))$Ba_2Cu_3O_{7-\delta}$ (YNSG-123 or (Y, NSG)BCO) superconductor, hereafter referred to as YNSG sample. This has been done by addition of 20 wt.% second phase particles of NSG-211 into 80 wt.% Y-211 in the preform prior to POIG process. This is aimed at introducing lattice mismatch effects through mixed RE doping so as to enhancing the flux pinning and thus critical current densities in the resultant YNSG superconductor sample. The results are compared with those of YBCO sample without any doping, processed under same conditions.

## 5.1. Introduction:

Bulk high temperature superconductors (HTSC) promise great scope for applications such as quasi-permanent magnets by trapping magnetic fields of magnitude higher than the best conventional magnetic material. Even with the moderate electromagnetic performance of $YBa_2Cu_3O_{7-\delta}$ (Y-123 or YBCO) it was possible to trap magnetic field as high as 17 Tesla in a 12 mm thick pellet of only 26.5 mm in diameter [12-13]. $REBa_2Cu_3O_{7-\delta}$ (RE-123 or REBCO, where RE=light rare earth, Nd, Sm, Eu, Gd) compounds are reported to carry significantly higher engineering currents than Y-123 [1-3]. Even though the YBCO which is commonly used for magnetic levitation at 77 K, has a critical temperature of nearly 92 K [14], the pinning performance of Y-123 rapidly drops at high temperatures and is therefore not suitable for levitation at 90 K. In this aspect, the situation is even worse with BiSrCaCuO, TlBaCuO and other compounds with $T_c$ above 100 K because of flux creep [15-16]. These compounds cannot be used for levitation even at 77 K with liquid nitrogen cooling, due to a low-lying irreversibility line. Only the RE-123 composites exhibit a sufficiently good performance up to 90 K due to flux pinning, by controlling the microstructures through incorporation of nanoparticles and nanostripes in these materials [17-18].

It is found that the materials in which ternary RE elements are introduced into REBCO compounds exhibit the highest critical current densities among all 123-type superconductors [4-11]. The increase of the critical current density ($J_c$) is due to the additional degree of freedom by providing increased disorder on the Y-site. These components also exhibit the substitution of the $RE^{3+}$-ion on the $Y^{3+}$ and on $Ba^{2+}$ site [19]. In the regions where the RE atoms substitute for Ba within the unit cells, lower $T_c$ RE-rich solid solutions (RE/Ba -ss) of type $(RE)_{1+x}Ba_{2-x}Cu_3O_y$

form within the matrix. While low concentrations of RE/Ba −ss aid flux pinning, formation of large fraction of it degrades superconducting properties [20]. To suppress the formation of large fraction of solid solutions in the composites, RE-123 materials needed to be processed in oxygen controlled (under Ar) atmospheres [21].

On the other hand, if a second RE element (RE') substitutes partly for RE in REBCO then solid solutions (RE/RE' -ss) of type $(RE_{1+y}, RE_{1-y})Ba_2Cu_3O_y$ form in the matrix with $T_c$ values ranging from 92 to 95 K and provide additional flux pinning [22]. Such a spatial variation of superconducting properties within the sample on the size of several unit cells implies formation of nanoclusters of the size of coherence length ($\xi$) in REBCO superconductors, of the order of 3–5 nm in their *(a, b)*-plane, and can lead to increased critical current density especially at high applied magnetic fields.

Binary and ternary RE-123 compounds offer one more degree of freedom for tailor making the pinning structure, in terms of the variation of the RE ions ratio. Such materials have been studied mostly on melt-textured (MT) samples. From the magnetic studies on binary system (Y, Sm)BCO, we had seen (in Chapter 4) considerable flux pinning sustained to 9 T field to occur in YSm-20 sample which was attributed mostly to RE/RE' -ss type solid solutions with Sm at Y site. It is then interesting to study the effect of lattice mismatch defects due to mixing more RE elements at Y site on the superconducting properties of YBCO.

Murakami's group have reported highest $J_c$ in Melt processed $(Nd_{0.33}, Eu_{0.33}, Gd_{0.33})Ba_2Cu_3O_{7-\delta}$ (NEG-123) superconductor with 35 mol.% of nanometre-sized (70 nm) Gd-211 and 0.1 mol.% of nanometre-sized $NbO_3$ [23].

In this chapter, we report the effect of partially substituting Y by three RE elements in YBCO on the superconducting properties of POIG processed (Y, RE)Ba$_2$Cu$_3$O$_y$, in which RE elements are selected from the group of Nd, Sm and Gd.

## 5.2.  Experimental Details:

In order to substitute 20 wt.% of Y by mixed RE elements in the preform the following procedure is followed. Precursor powders of Y-123, Y-211 and (Nd$_{0.33}$, Sm$_{0.33}$, Gd$_{0.34}$)$_2$BaCuO$_5$ (referred to as NSG-211) were prepared by chemical route using citrate synthesis. 20 wt.% of NSG-211 was added to 80 wt.% of Y-211 powder, tumbled into intimate mixture and is pressed into preform pellet under a uniaxial pressure of 460 MPa.
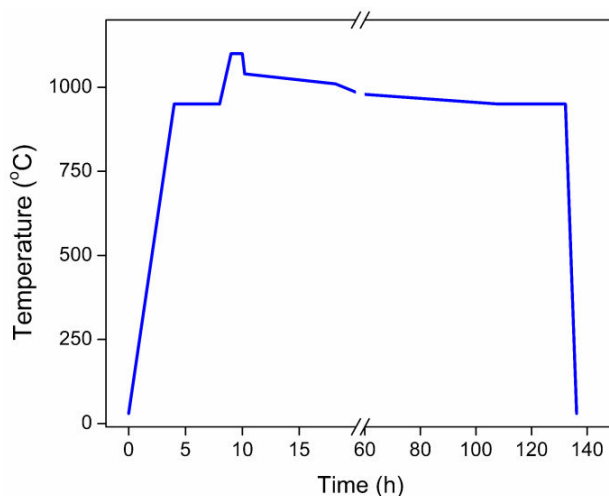


**Fig. 5.1.** Heat treatment schedule followed to synthesize the YBCO-Ar and YNSG samples.

The heat treatment profiles for POIG processing were determined according to the peritectic decomposition temperatures reported from the thermal analysis measurements on REBCO samples with different RE elements. The YNSG

preform was POIG processed using heat treatment schedule shown in fig. 5.1, in flowing commercial grade Ar atmosphere, and is same as for (Y, Sm)BCO samples discussed in chapter IV. The product obtained is referred to as YNSG. The superconductor thus obtained is characterized and the performance is compared with YBCO-Ar sample synthesized under same conditions without any doping.

## 5.3. Results:

### 5.3.1. Temperature dependence of ac susceptibility:

After processing YBCO-Ar and YNSG samples, oxygenation was done for 110 h at 460 $^o$C for allowing the samples to enable structural phase transition from non-superconducting tetragonal to superconducting orthorhombic phase. Superconducting transition temperature ($T_c$) was measured by recording ac susceptibility in the temperature range 40 K$\leq$ T $\leq$100 K at driving ac fields of rms amplitude 10 Oe and a frequency of 33 Hz, employing a PPMS-ACMS (Quantum Design, model MPMS-7).
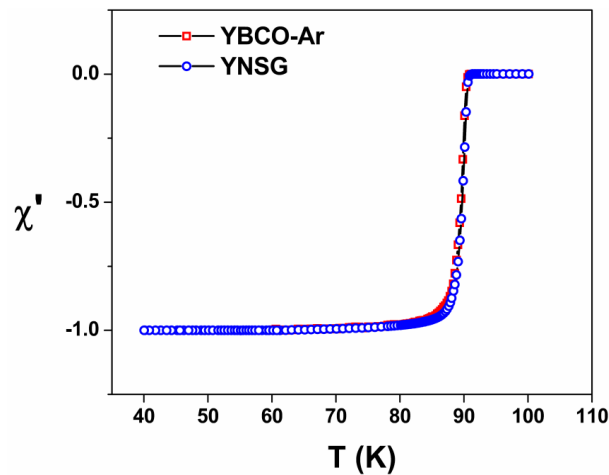


**Fig. 5.2.** Variation of normalized real part of ac susceptibility ($\chi'$) with temperature for YBCO-Ar and YNSG samples. Sharp superconducting transitions are observed.

Variation of in-phase component of ac susceptibility ($\chi_{ac}{}'$) with temperature is depicted in fig. 5.2. The onset of the critical temperature for YBCO-Ar and YNSG are 91.0 and 91.6 K respectively and the transition widths of YBCO-Ar and YNSG samples are ~ 2.5 K. It is interesting to note that there is no broad tail region in $\chi_{ac}(T)$ as observed in YSm-10 and YSm-30 samples (chaper IV section 4.4.3) and hence formation of large amounts of low $T_c$ phases has been suppressed in YNSG sample.

### 5.3.2. Structural analysis of the (Y, NSG)BCO sample:
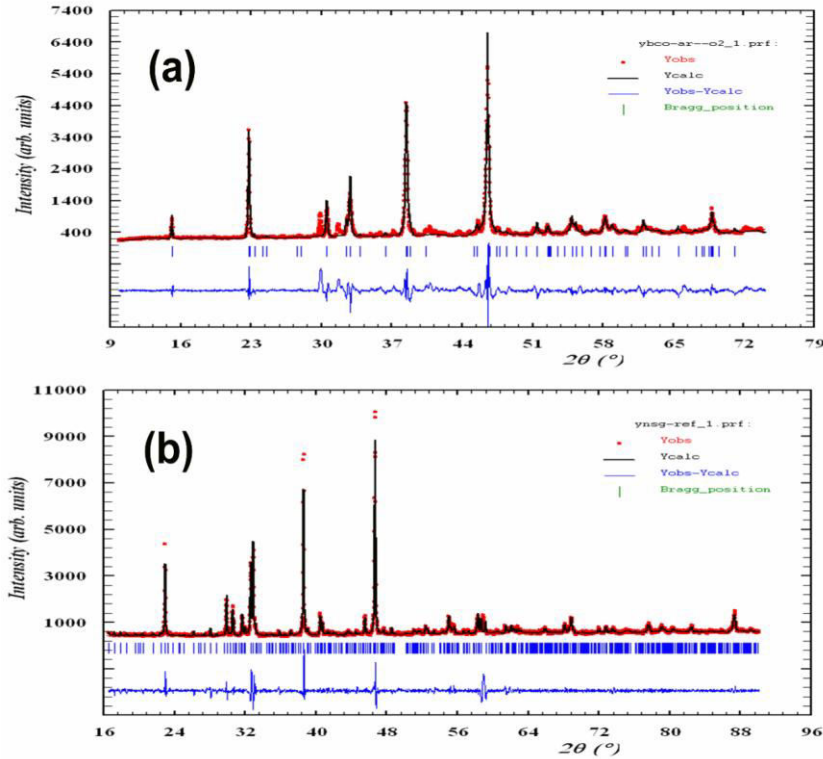


**Fig. 5.3.** X-ray diffraction patterns with Rietveld refinement for YBCO-Ar and YNSG samples were shown in (a) and (b) respectively. These samples are oxygenated and in the superconducting state.

The detailed structure and phase identification of the YBCO-Ar and YNSG compositions were done by analyzing the X-ray diffraction patterns measured by using Cu $K_\alpha$ radiation on BRUKER X-ray diffractometer. The diffraction data were collected over the diffraction angle range of $2\theta = 10 - 90°$ by step scanning with a step width of 0.02. The structural parameters of YBCO were used as a starting model for the refinement. The FULLPROF program was used to find out the space group as well as for refinement of the lattice parameters from the X-ray diffractograms and the patterns shown in fig. 5.3 (a) and (b) for YBCO-Ar and YNSG respectively. The profile matching using FULLPROF program shows that the XRD patterns can be indexed to Pmmm space group. The prominent reflections are labeled by assuming an orthorhombic structure. No traces of extra low $T_c$ phases are observed.

**Table 5.1:** Lattice parameters and the unit cell volumes of the samples.

| Sample | Lattice parameter (Å) | | | Cell volume (Å³) |
|---|---|---|---|---|
| | a | b | c | |
| YBCO-Ar | 3.810 | 3.886 | 11.697 | 172.2 |
| YNSG | 3.814 | 3.877 | 11.674 | 172.6 |

The lattice parameters and cell volumes for YBCO-Ar and YBCO are listed in Table 5.1.

The XRD patterns of YBCO-Ar and all the (Y, Sm)BCO samples discussed in chapter 4 (section 4.4.2) show that they are textured in [00l] direction. The indexed XRD pattern of YNSG is shown in fig. 5.4, along with that of YBCO-Ar.
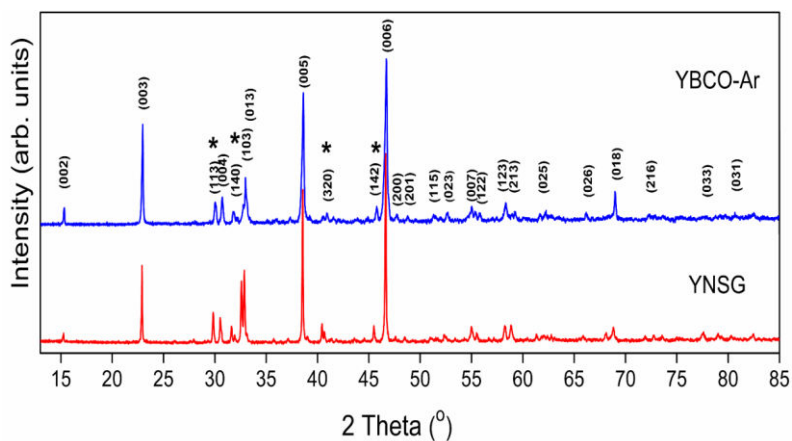
**Fig. 5.4.** X-ray diffractograms of YBCO-Ar and YNSG. * indicates the position of Bragg peaks of minor 211-phase.

### 5.3.3. Microstructural analysis:
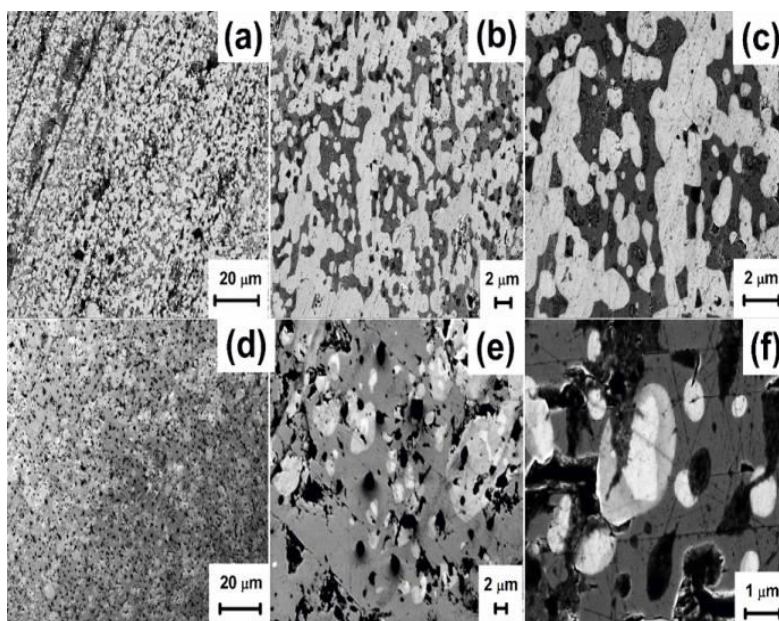


**Fig. 5.5.** FESEM micrographs from YBCO-Ar (upper panel) and YNSG (lower panel), with the magnification in the figs. increasing to the right. In both the samples spherical porosity can be seen. In the YNSG sample, one can observe that the 211 particles occur with a core of Y-211.

FESEM micrographs recorded for YBCO-Ar and YNSG samples using in-lens mode detectors are presented in figs. 5.5 (a)-(c) for YBCO-Ar and (d)-(f) for YNSG samples. It can be seen from the figure that i) nearly spherical precipitates of size submicron to 4 μm are distributed uniformly throughout the matrix phase ((a) and (d)) and ii) Spherical porosity is seen, just as in (Y, Sm)BCO samples, in both the samples ((b) and (e)). On the other hand, precipitates in the YNSG matrix contain bright core regions indicating compositional segregation as observed in the (Y, Sm)BCO samples, unlike in YBCO-Ar (discussed in chapter IV section 4.4.4).

### 5.3.4.   Compositional analysis through EDS:

Chemical compositions of different phases like the superconducting matrix and the bright and dark regions of the precipitates were established by EDS analysis. Fig. 5.6 shows the EDS results on YNSG sample.

The average composition of the matrix deduced from energy dispersive spectroscopy (EDS) analysis is found to be 123 phase with Y and RE in nearly 1:4 ratio (fig. (a) as expected. The mixing among the three RE elements is nearly equal within experimental error limits. This result indicates that compositional fluctuations exist in the matrix of the YNSG sample. The bright core regions of the precipitates are of Y-211 composition and are free from any RE element (fig. (c). On the other hand, the darker regions surrounding the cores within the precipitates do contain some amount of mixed RE elements along with Y  in the ratio of 2:1:1 for (Y,RE): Ba: Cu and thus represent YNSG-211 phase.

| Element | Atomic % |
|---------|----------|
| Y | 7.14 |
| Nd | 0.47 |
| Sm | 0.53 |
| Gd | 0.43 |
| Ba | 15.89 |
| Cu | 23.51 |
| O | 52.03 |

| Element | Atomic % |
|---------|----------|
| Y | 17.65 |
| Nd | 0.65 |
| Sm | 0.71 |
| Gd | 0.85 |
| Ba | 10.63 |
| Cu | 11.18 |
| O | 58.33 |

| Element | Atomic % |
|---------|----------|
| Y | 21.14 |
| Ba | 11.12 |
| Cu | 10.99 |
| O | 56.75 |
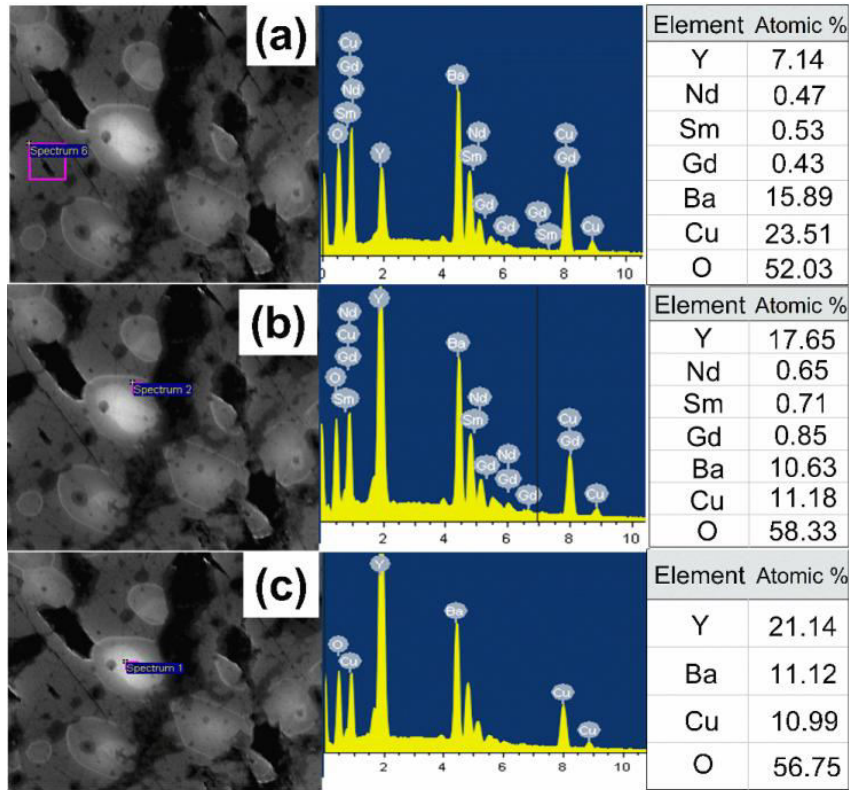
**Fig. 5.6.** Elemental analysis of YNSG sample (a) in the superconducting 123 matrix, (b) in the darker outer periphery of the 211 precipitates and (c) in the core bright region of the 211 precipitates. In the matrix as well as in the periphery of the 211 particles, there is dissolved Nd, Sm and Gd. In the core region the material is pure Y-211.

There are some reports in literature [24-27] on the observation of precipitates in differing shades in the matrix of melt grown ternary REBCO systems, which were proposed to be arising from fluctuations induced by RE/Ba substitution. However detailed analysis is not available. The size of the RE-rich clusters is observed to range from 3 to 10 nm; which often joined together and form even larger clusters of around 60 nm size [23, 28]. This may cause the high pinning at high magnetic field. Finely dispersed RE-211 particles can also contribute to the pinning enhancement in low and intermediate field region.

### 5.3.5. Critical current densities and flux pinning properties:

Flux pinning in RE system is studied by many researchers through addition of different RE elements into MG processed REBCO. Murakami et al. has proposed that nano-sized RE/Ba-solid solution clusters of lower $T_c$ act as field-induced pinning centers [29], and thus result in peak effect in the REBCO materials. Recent studies of mixing three different RE elements (NEG-123) showed that the position and height of the maximum (peak effect) in $J_c(H)$ curve observed at high fields is correlated to the chemical ratio of RE elements in the matrix phase [30-31]. Compositional fluctuations or clusters in mixed REBCO [47] arising from distinct range of the rare earth chemical ratio have strongly affected the pinning properties at high fields ($\Delta T_c$ pinning).
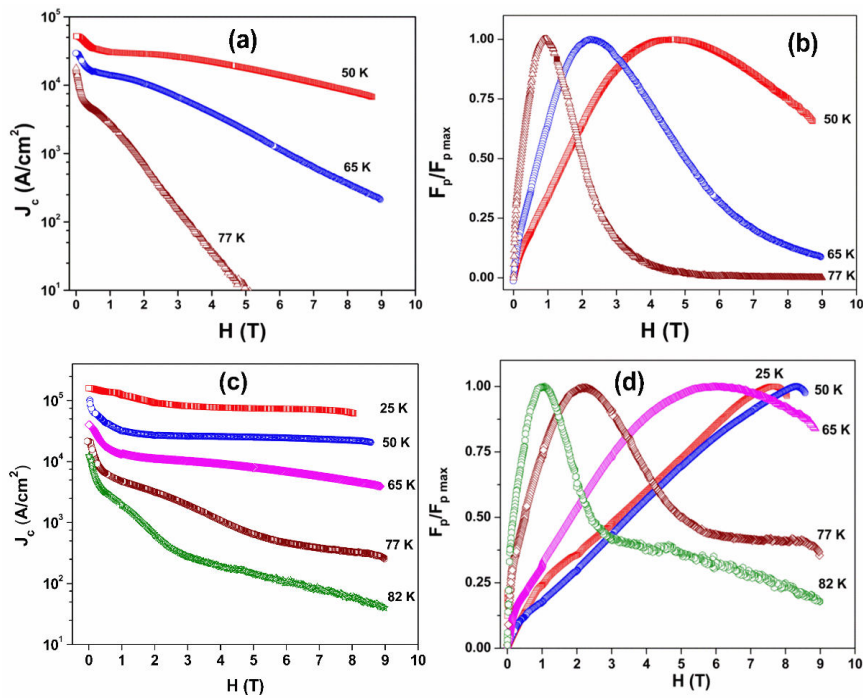


**Fig. 5.7.** Temperature dependences of $J_c$ and the field dependence of the normalized flux pinning force $F_p / F_{p\,max}$ for YBCO-Ar are shown in figs. (a) and (b) respectively. Similar plots are shown for YNSG in figs (c) and (d) respectively.

To estimate the critical current densities, magnetic hysteresis loops were recorded for which the magnetic field (H) was applied normal to the pressed surface of the sample and was varied up to 9 T. $J_c$ was estimated as a function of field, at different temperatures (50 K, 65 K and 77 K) for YBCO-Ar sample and for YNSG sample (25 K, 50 K, 65 K, 77 K and 82 K). The self field $J_c$ of YNSG sample at 77 K found to be 21.5 kA/cm$^2$ and $J_c$ curve is flat up to high fields; even at 82 K also $J_c$ curve is flat up to high fields. $J_c(0)$ of YBCO-Ar sample at 77 K is found to be 17.8 kA/cm$^2$, but falls rapidly to zero. Field dependence of the critical current density in YBCO-Ar (fig. 5.7 (a)) and YNSG (fig. 5.7 (c)) samples at different temperatures are presented. In figs. 5.7 (b) and (d), we present the variation of pinning force $F_p$, normalized by its maximum value, $F_{p\ max}$, as a function of applied field. From figs. 5.7 (b) and (d) it can be observed that the peak field position in $F_p$-H curve occurs at higher fields for YNSG sample compared to that of YBCO-Ar.

The irreversibility magnetic field ($H_{irr}$), is the field above which flux pinning becomes ineffective [32]. Shinichi Kobayashi et al. [33] defined $H_{irr}$ as the field at which the $J_c$ decreases to 100 A/cm$^2$, which for YBCO is in the range of 3-5 T at 77 K [24, 34-35]. In the present case $J_c$ reaches 100 A/cm$^2$ at 3.3 T for YBCO-Ar sample at 77 K whereas for YNSG $J_c$ >300 A/cm$^2$ was maintained up to 9 T field, which clearly indicates $H_{irr}$ to be much higher than 9 T.

## 5.4. Discussion:

From the ac susceptibility measurements on the YBCO-Ar and YNSG samples, sharp transition is observed at the critical temperature of both the samples. Absence of a broad tail region in $\chi_{ac}(T)$ and lack of extra phases in XRD suggest that the observed transition width of 2.5 K indicate oxygen deficient phases to be present in both the samples in small amounts. Structural study confirms the

majority phase to be orthorhombic RE-123 with RE-211 as minor phase and that the grains are largely oriented in [00l] direction in both YBCO-Ar and YNSG samples.

From the micro-structural analysis of the YBCO-Ar and YNSG samples it is evident that nearly spherical particles are distributed in the matrix phases. In the YBCO-Ar sample no different shades are seen in the 211 particles, whereas in YNSG sample annuli cores are observed as bright regions within the precipitates. The RE elements are present both in the matrix and in the outer dark regions of the precipitates except in the cores.

Introduction of RE in the present work is done through direct addition of 1 micron sized NSG-211 particles to Y-211 powder. This procedure differs from that of YSm-211 preforms in which nano-$Sm_2O_3$ particles get embedded onto Y-211 particles; and interaction of Sm and Y-211 in presence of liquid phases would explain the mechanism of annuli core formation in (Y, Sm)BCO samples.
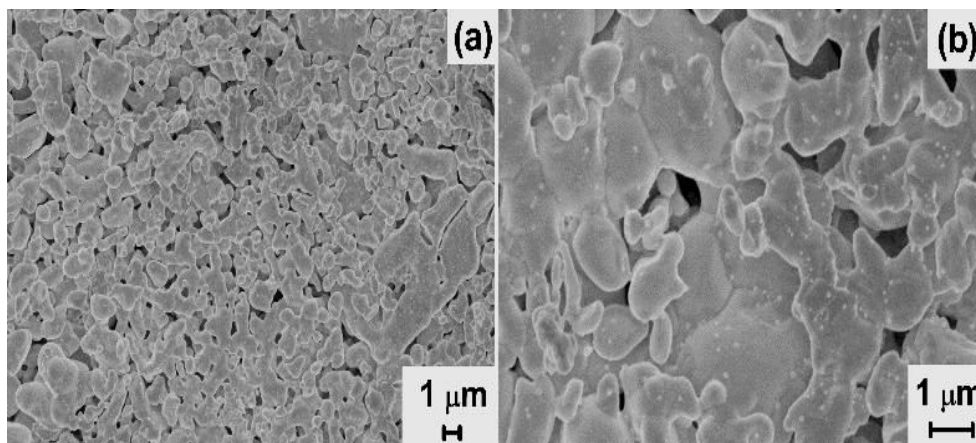


**Fig. 5.8.** FESEM images of YNSG-211 powder precursor pellet sintered at 950 $^{\circ}$C for 4 h, shown at magnifications of (a) 10 kX and (b) 25 kX. One observes that substantial grain growth takes place during the preform preparation stage.

In the present system of YNSG, the preform consists of a mixture of Y-211 and NSG 211 powders in 4:1 ratio. The reason for annuli core formation may be as follows. Fig. 5.8 shows the FESEM image recorded in the preform of YNSG sintered at 950 $^{o}$C for 4 hours, prior to infiltration of liquid phase. It can be seen that the particles have got sintered into larger grains. It is likely that Nd, Sm and Gd with faster diffusion rates [36] would promote sintering of the NSG particles with some of the Y-211 particles and in that process may enclose some Y-211 particles in the larger grains of YNSG-211. Then after liquid phase infiltration, the smaller NSG-211 and Y-211 particles may be completely consumed for the growth of RE-123. On the other hand, only the outer regions of larger YNSG-211 undergo peritectic reaction with liquid phase forming YNSG matrix phase and leaving back unreacted YNSG-211 particles containing Y-211 cores.

From the $J_c(H)$ curves in YNSG sample shown in fig. 5.7, we note that this sample exhibits the best performance at low as well as high fields at all temperatures, when compared to YBCO-Ar, and even YSm-20 samples which was the best of (Y, Sm)BCO series. This supports the argument that ternary REBCO has higher density of pinning centers compared to binary systems or pure YBCO. Sustenance of $J_c >1$ kA/cm$^2$ up to 5 T and $J_c > 300$ A/cm$^2$ at 77 K even at 9 T field can be attributed to the enhanced flux pinning due to the presence of mixed RE elements at Y site. The fact that solid solutions of RE/Ba- ss type are suppressed, as argued from XRD and $\chi_{ac}(T)$ results, suggests that the enhanced flux pinning in the YNSG sample at high fields might originate from RE-RE'-ss type solid solutions and the associated lattice mismatch effects. Oxygen deficient phases with a small distribution in $T_c$ would also contribute to flux pinning. The enhanced pinning at high fields is also evident from the normalized $F_p$ curves which show that the maximum peak field at 77 K is 1 T for YBCO-Ar and 2.25 T for YNSG sample. The higher position of the peak at 77 K in the YNSG

superconductors represents reduction in the flux creep at elevated temperatures, which is also an important aspect for applications.

It should be pointed out here that considerable $J_c(H)$ at of $> 300$ A/cm$^2$ is observed up to 9 T in spite of 6% porosity present in the YNSG sample. It is observed that all the samples processed under argon exhibit wide spread spherical porosity, suppression of which project a scope to improve the performance of these materials.
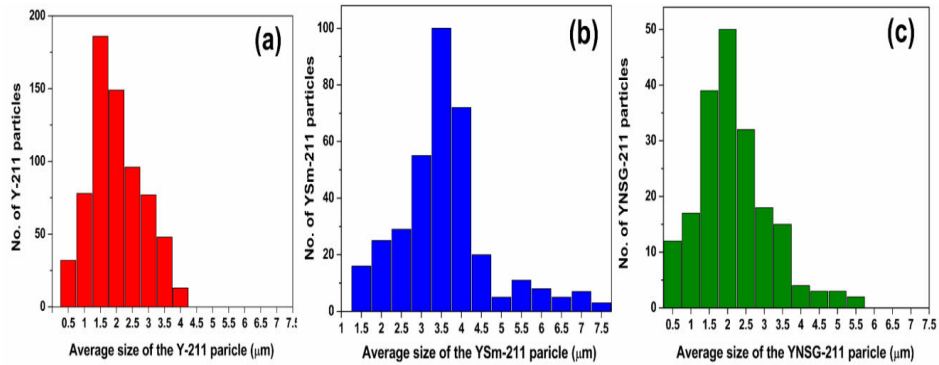


**Fig. 5.9.** Histograms of 211 sizes in (a) YBCO-Ar, (b) YSm-20 and (c) YNSG samples.

The current density values at zero field $J_c(0)$ is 21.5 kA/cm$^2$ in YNSG and is 17.8 kA/cm$^2$ in YBCO-Ar and are better than better than $J_c(0)$ of 4.2 kA/cm$^2$ in YSm-20 sample. This depends on the pinning of flux from RE-123/RE-211 interfacial defect density which in turn is controlled by the size of precipitates in the superconducting matrix. Thus larger number of finer precipitates would enhance $J_c(0)$. Fig. 5.9 shows the distribution of size of precipitates in the above samples.

## 5.5. Origin of field dependence of $J_c$ and Flux pinning:

The $J_c(0)$ calculated for the samples is also found to vary systematically with the size of the RE-211 in the final composites. These results show that the flux pinning at low fields depends on the RE-211 size and associated defects at

the RE-211/RE-123 interfaces. In YSm-20 the size of the (Y, Sm)-211 are of the order of 2-4 µm, where as for YNSG and YBCO-Ar, RE-211 phase particles were distributed over a size range from submicron to 4 µm. Therefore $J_c(0)$ of YNSG and YBCO-Ar samples are superior to that of YSm-20 sample.

The rapid fall in the magnetic field dependence of $J_c$ for melt textured YBCO with large $J_c$ values is reported to exhibit an exponential variation with magnetic field [37-39]. Since the present $J_c(H)$ curves show faster reduction at low fields, but slow decrease at high fields, we assume that there are two different mechanisms operative in describing the $J_c(H)$ behavior across the field range up to 9 T. As a result we consider two terms to fit the measured data to equation 5.1 given below.

$$\frac{J_c(H)}{J_c(0)} = A_1 \exp(-\frac{\mu_0 H}{t_1}) + A_2 \exp(-\frac{\mu_0 H}{t_2}) + y_0 \qquad \ldots\ldots\ldots(5.1)$$

Where $A_1$, $t_1$, $A_2$, $t_2$ and $y_0$ are the fit parameters.

In order to investigate the nature of flux pinning that occurs to high fields at 77 K we have normalized the $J_c(H)$ with respect to zero field $J_c$ , i.e. $(J_c(H)/J_c(0))$, which is plotted as a function of applied field in fig. 5.10 (a).

In fig. 5.10 (b) the detailed fitting of measured field dependence of normalized $J_c$ to equation 5.1 is shown, as an example, for YNSG sample. This figure shows three curves, namely fit of measured $J_c(H)$ data (i) only at lower fields to Term II, (ii) only at higher fields to Term I and (iii) in complete field range to the total equation. (5.1).
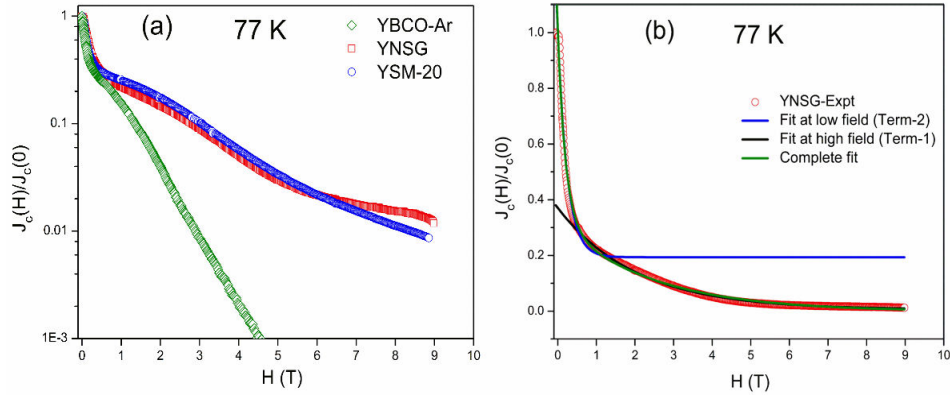
**Fig. 5.10.** (a) The normalized current density $J_c(H)/J_c(0)$ at 77 K for the samples YBCO-Ar, YNSG and YSm-20. YNSG and YSm-20 samples show similar behavior of retaining high $J_c$ up to high fields. (b) For the YNSG sample at 77 K, the normalized $J_c$ is fitted to a function in H with two exponential terms in equation 5.1.

The details of the fit parameters obtained from $J_c(H)$ curves at 77 K for the YBCO-Ar, YNSG and YSm-20 superconductors are listed in Table 5.2.

$J_c(H)$ at low fields fits well to the second term. The term II, containing the parameters $A_2$ and $t_2$, has been found to be applicable at low fields. The $J_c(0)$ calculated for the samples is also found to vary systematically with the size of the RE-211 in the final composites. These results show that the flux pinning at low fields depends on the RE-211 size and associated defects at the RE-211/RE-123 interfaces. In YSm-20 the size of the (Y, Sm)-211 are of the order of 2-4 μm, where as for YNSG and YBCO-Ar RE-211 phase particles were distributed over a range from submicron to 4 μm. Therefore $J_c(0)$ of YNSG and YBCO-Ar samples are superior than the YSm-20 sample.

The experimental $J_c(H)$ at high fields fits well to Term I, containing parameters $A_1$ and $t_1$. The parameter $t_1$ has correlation to the peak field ($H_p$) where normalized flux pinning force reaches a maximum as shown in fig. 5.10. $H_p$ was 1 T in YBCO-Ar while it was ~2.2 T in the other two samples. In YBCO samples

$A_1$ was correlated to the defect density arising from twinning [39] that resulted in an enhancement in $J_c$ up to high fields. Interestingly we did not find the presence of twins in any of the three (Y, RE)BCO samples shown in Table 5.2.

**Table. 5.2.** Fitting parameters for YBCO-Ar, YNSG and YSm-20 samples

| Sample | Fitting parameters | | | | |
|---|---|---|---|---|---|
| | $A_1$ | $t_1$ | $A_2$ | $t_2$ | $y_0$ |
| YBCO-Ar | 0.426 | 0.074 | 0.571 | 0.006 | -0.002 |
| YNSG | 0.320 | 0.192 | 0.675 | 0.016 | -0.001 |
| YSm-20 | 0.385 | 0.195 | 0.700 | 0.009 | -0.002 |

From literature [40] it is well known that the size of the defects in the superconductors plays a role in influencing $J_c$ at different fields. The presence of such defects can give rise to strong flux pinning or hike in $J_c$ at a particular field, defined as peak field. This peak field is related to the vortex lattice spacing as shown in equation 5.2.

$$H_p = \frac{\phi_0}{\sqrt{3}(a_f)^2} \ldots\ldots\ldots\ldots(5.2)$$

Where $\phi_o$ is the flux quantum, $a_f$ is the vortex lattice spacing [40]. Eq. 5.2 suggests that the flux pinning at fields less than 1 T can be caused by defects of size more than 50 nm. The interfacial defects due to RE-211/RE-123 boundaries would give rise to flux pinning at such low fields. In literature correlations were made on the flux pinning at low fields due to RE-211 content and the defects originating at the RE-211/RE-123 interfaces [40-43]. Fig. 5.11. represents the possible dependence of peak field on defect spacing at different fields as given by Eqn. 5.2. From this

figure it is clear that, smaller the defect size, larger the peak field will be. Therefore it is crucial to create fine sized defects or control the size of RE-211 particles in the RE-123 matrix to make the interface defect density large in the RE-123 matrix.
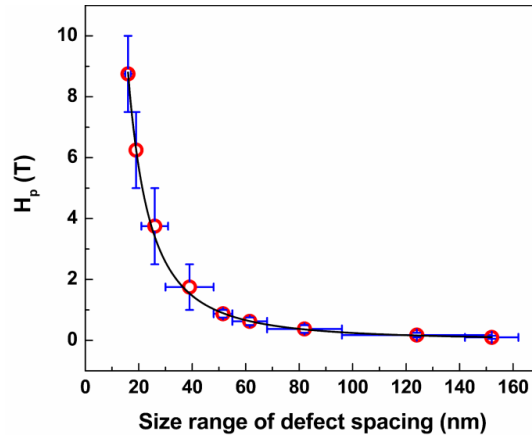


**Fig. 5.11.** Schematic diagram of the relation of peak field with the size of the defect spacing.

To account for high $J_c$ observed up to large (1-10 Tesla) fields the defect spacing should vary from $15 - 50$ nm. In present work the three (Y, RE)BCO samples being discussed showed the enhancement of $J_c$ up to high fields. Due to the addition of different RE's deviations in compositions occur. Compositional fluctuations at nanoscale occur during the peritectic transformation, which causes $T_c$ variation on a nanoscale and result in the formation of $\Delta T_c$ pinning at high magnetic fields. The extent of compositional fluctuations ($\Delta T_c$ pinning centers) is altered by the different peritectic temperatures of RE elements, their solubility in the liquid phase and their ionic radii.

The strong flux pinning observed to fields as high as 9 T is hence attributed to the presence of compositional fluctuations due to RE element (single or multiple) doping into the superconducting matrix of the samples.

**References:**

1. M. Muralidhar, N. Sakai, M. Jirsa, M. Murakami, N. Koshizuka, Supercond. Sci. Technol. **16** (2003) L46-L48.

2. M. Muralidhar, N. Sakai, M. Jirsa, N. Koshizuka, M. Murakami, Appl. Phys. Lett. **85** (2004) 3504-3506.

3. M. Muralidhar, N. Sakai, M. Jirsa, M. Murakami, N. Koshizuka, Supercond. Sci. Technol. **18** (2005) L9-L12.

4. M.R. Koblischka, M. Winter, P. Das, A. Koblischka-Veneva, M. Muralidhar, T. Wolf, N. Hari Babu, S. Turner, G. van Tendeloo and U. Hartmann, Physica C **469** (2009) 168–176.

5. M. Muralidhar, M.R. Koblischka and M. Murakami, Physica C **313** (1999) 232.

6. M. Muralidhar, H.S. Chauhan, T. Saitoh, K. Kamada, K. Segawa and M. Murakami, Supercond. Sci. Technol. **10** (1997) 663.

7. M. Muralidhar, M.R. Koblischka, T. Saitoh and M. Murakami, Supercond. Sci. Technol. **11** (1998) 1349.

8. M.R. Koblischka, M. Muralidhar and M. Murakami, Appl. Phys. Lett. **73** (1998) 2351.

9. S.Y. Chen, A. Gloter, C. Colliex, J.G. Chen and M.K. Wu, IEEE Trans. Appl. Supercond. **17** (2007) 2957.

10. D.A. Cardwell and N. Hari Babu, Physica C **445** (2006) 1.

11. S. Awaji, N. Isono, K. Watanabe, M. Muralidhar, M. Murakami, N. Koshizuka and K. Noto, Supercond. Sci. Technol. **17** (2004) S6.

12. M. Tomita and M. Murakami, Nature **421** (2003) 517-520.

13. M. Jirsa, M. Rames, P. Das, M. R. Koblischka, T. Wolf, U. Hartmann, IEEE/CSC & ESAS EUROPEAN SUPERCONDUCTIVITY NEWS FORUM, **3** (2008) 1-6.

14. S. Jin, A. Fastnacht, T.H. Tiefel and R.C. Sherwood, Phys. Rev. B **37** (1988) 5828-5830.

15. Z.Z. Sheng and A.M. Hermann, Nature **332** (1988) 138-139.

16. H. Maeda, Y. Tanaka, M. Fukufomi and A. Asano, Jpn. J. Appl. Phys. **27** (1988) L209-L210.

17. M. Muralidhar, N. Sakai, N. Chikumoto, M. Jirsa, T. Machi, Y. Wu and M. Murakami, Phys. Rev. Lett. **89** (2002) 237001.

18. M. Muralidhar, Y. Wu, N. Sakai, M. Murakami, M. Jirsa, T. Nishizaki and N. Kobayashi, Supercond. Sci. Technol. **15** (2002) 1357-1363.

19. R.W. McCallum, M.J. Kramer, K.W. Dennis, M. Park, H. Wu and R. Hofer, J. Electronic Mater. **24** (1995) 1931.

20. Chakrapani Varanasi, Paul J. Mc Ginn, Howard A. Blackstead and David B. Pulling, Journal of electronic materials **24** (1995) 12.

21. J. Maňka, A. Cigáň, J. Polovková, A. Koňakovský and A. Prnová, Measurement science review **11** (2011) 1.

22. H. Wu, K.W. Dennis, M.J. Kramer and R.W. McCallum, Appl. Supercond. **6** (1998) 87.

23. M. Muralidhar, S. Nariki, M. Jirsa, Y. Wu and M. Murakami, Appl. Phys. Lett. **80** (2002) 1016.

24. M. Muralidhar, H.S Chauhan, T. Saitoh, K. Kamada, K. Segawa and M. Murakami Supercond. Sci. Technol. **10** (1997) 663–670.

25. S. Takekawa, H. Nozaki, Y. Ishizawa and N. Iyi, Jpn. J. Appl. Phys. **26** (1987) L2076.

26. S.I. Yoo, M. Murakami, N. Sakai, T. Higuchi and S. Tanaka, Jpn. J. Appl. Phys. **33** (1994) L1000.

27. T. Egi, J.G. Wen, K.Kuroda, H. Unoki and N. Koshizuka, Appl. Phys. Lett. **67** (1995) 16.

28. M. Muralidhar and M. Murakami, Physica C **378–381** (2002) 627–630.

29. M. Murakami, S.I. Yoo, Takamitsu Higuchi, Naomichi Sakai, Jurgen Weltz, Naoki Koshizuka and S. Tanaka, Jpn. J. Appl. Physics **33** (1994) L715-L717.

30. M. Muralidhar, M. Jirsa, N. Sakai and M. Murakami, Appl. Phys. Lett. **79** (2001) 3107.

31. M. Muralidharan and M. Murakami, Supercond. Sci. Technol. **13** (2000) 1315-1321.

32. D. Dew-Hughes, Low temperature Physics **27** (2001) 9.

33. Shin-ichi Kobayashi, Tetsuyuki Kaneko, Takeshi Kato, Jun Fujikami, Ken-ichi Sato, Physica C **258** (1996) 336-340.

34. K. Iida, N. Hari Babu, Y.H. Shi, D.A. Cardwell and M. Murakami, Supercond. Sci. Technol. **19** (2006) 641.

35. D.A. Cardwell and N. Hari Babu, Physica C **445-448** (2006) 1.

36. H. Zhang , X.W Zou, Z.H Wang and Y.X Chen, Physica C **337** (2000) 307–311.

37. V. Ganesan, R. Srinivasan, R. Gopalan and T. Rajasekharan, Pramana J.Phys. **41** (1993) 61.

38. T. Yang, Z.H. Wang, H. Zhang, Y. Nie and L. Qiu, Physica C **386** (2003) 69.

39. Ph.D. Thesis entitled "Enhanced Flux Pinning to High Fields in YBCO and YBCO/Ag Superconductors through Preform Optimization in Infiltration and Growth Process" by N. Devendra Kumar, (2011), University of Hyderabad.

40. M. Nakamura, T. Hirayama, Y. Yamada, Y. Ikuhara and Y. Shiohara,  Jpn. J. Appl. Phys. **35** (1996) 3882.

41. K. Salama and D.F. Lee,Supercond. Sci. Technol.  **7** (1994) 177.

42. D.F. Lee, V. Selvamanickam and K. Salama, Physica C **202** (1992) 83.

43. C.J. Kim and G.W. Hong, Supercond. Sci. Technol. **12** (1999) R27.

# Chapter VI

## Study of key factors that control microstructures and flux pinning in (Y, LRE)-BCO superconductors

### 6.1. Introduction:

In the previous chapters (IV and V) we have studied the effect of single rare earth (Sm) and multiple rare earth (Nd, Sm and Gd) doping at Y site in YBCO. The doping was done by different methods which involved mixing of Y-211 powders with chosen amounts of

(i)  Nano $Sm_2O_3$ particles in the form of sol, in 10, 20 and 30 wt.%.

(ii)  Sm through Chemical substitution at the atomic level by 20 wt.%, and

(iii)  Fine NSG-211 particles (~ 1 μm) by 20 wt.%.

A discussion on the results obtained on the above samples was presented at the end of Chapters IV and V.  We summarize below the achievements and the problems that remain unsolved after the work done so far.

**Achievements:**

1. (Y, LRE)BCO superconductors are synthesized successfully by POIG process under commercial argon.

2. YSm-20 sample shows the highest $J_c(H)$ at 77 K, compared to YSm-10 and YSm-30 samples in (Y, Sm)BCO series.

3. $J_c(H)$ performance of YNSG samples is the best of all the samples studied, with $H_{irr}$ being > 9 T at 77 K. $J_c(0)$ is 21.5 kA/cm$^2$ at 77 K and is highest of all.

4. The introduction of mixed RE elements at Y site leading to compositional fluctuations in the superconducting matrix and the associated lattice mismatch effects have provided flux pinning at high fields up to 9 T.

5. All the samples studied here showed [00l] texture, unlike the YBCO sample processed in Air under the same conditions (chapter III).

**Problems unsolved:**

1. Spherical porosity is observed in all the samples processed under argon. Its origin and ways to eliminate are not well established.

2. Considerable non-spherical porosity is also present in the samples that limit sustenance of high $J_c$ value at high fields.

3. RE-211 precipitates in the matrix phase need be further refined and more uniformly distributed in order to achieve higher zero field $J_c$, simultaneous with flat $J_c(H)$.

4. Clearer understanding is required on the process conditions leading to large fraction of unwanted formation of solid solutions of low $T_c$.

One can observe that both the samples YSm-20 and YNSG with better $J_c(H)$ curves exhibit narrow transition  and efficient suppression of solid solutions of RE/Ba-ss type as seen from ac susceptibility and XRD data. It should also be pointed out here that considerable $J_c(H)$ of >300 A/cm$^2$ is observed up to 9 T in YNSG sample in spite of 6% porosity present in the sample. The fact that all the samples processed under argon exhibit wide spread porosity suggests that attempts to suppress the porosity through process modifications project a scope to improve the performance of these materials.

In this chapter we study the effect of different processing conditions aimed at identifying the origin of porosity, ways to suppress the porosity and refine the RE-

211 size. For this purpose we have chosen the YNSG composition as an example, since it has shown the best results after POIG process.

Six samples were synthesized using YNSG preforms and processing them under different heat treatment schedules, atmospheric conditions and pressure as described below.

## 6.2. Experimental Details:

1. The first sample is the **YNSG** sample discussed in Chapter V which was processed under argon.

2. Since all the samples processed under argon have shown wide spread spherical porosity, it is necessary to identify if argon evolution as gas bubbles is responsible for this. To confirm this hypothesis, **processing in air** under the same conditions was envisaged and the resultant sample is called **YNSG-Air**, discussed in section 6.5.

3. In order to assess during which stage of heat treatment the argon gas evolution takes place, infiltration of liquid phases into preform was rendered in air, and argon gas flow was arranged at **a later stage** during cooling through peritectic temperature during the synthesis. The sample thus prepared is referred to as **YNSG-L**. These experiments confirmed the origin of spherical porosity to be due to argon atmosphere during POIGP, as will be discussed later in section 6.6.

4. We recall here that press-sintering of once processed samples of of Bi-Sr-Ca-Cu-O superconductors led to minimization of macro-defects and their densification [1-2]. On similar lines we attempted a study of the effect of press-sintering on the POIG processed product. This was done by pressing the product again under 540 MPa pressure and reprocessing, while allowing once again the liquid infiltration from a Y-123 pellet placed

above. The resultant sample after **press-sintered** process is referred to as **YNSG-P.**

5. It is known that refinement of RE-211 particles causes an increase in the defect density at the interface of RE-211/RE-123 and leads to enhanced zero-field $J_c$. We note that the size distribution of RE-211 in YSm-20 and YNSG ranges from submicron to 4 micron. An experiment is envisaged to study the effect of reducing the duration of processing on the size range of RE-211. The details of the **new** heat treatment schedule are discussed in section 6.8 and the resultant sample is **YNSG-N.**

6. There are reports in literature suggesting that excess amount of Ba if present along with the liquid phases during melt processing of REBCO, would suppress the substitution of RE at Ba site, even when processed in air [3-5]. We have experimented mimicking the **excess Ba** condition during POIG process carried out in air medium. The resultant sample is **YNSG-Ba** and the results are discussed in section 6.10.
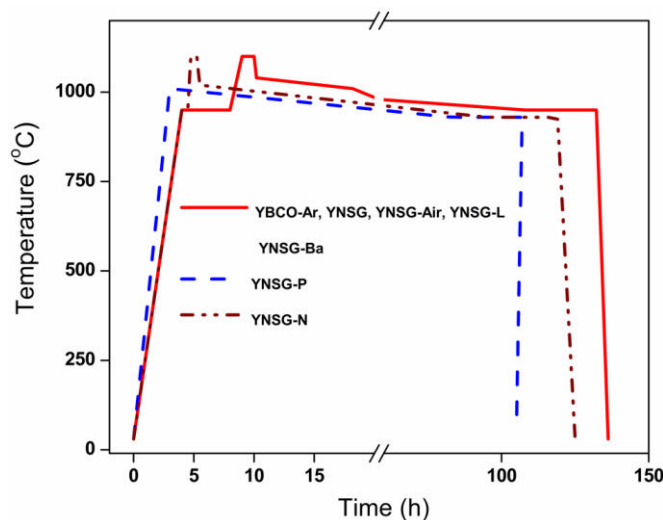


**Fig. 6.1.** Heat treatment schedules followed to synthesize the YBCO-Ar, YNSG, YNSG-Air, YNSG-L, YNSG-Ba, YNSG-P and YNSG-N samples.

The heat treatment schedules followed for synthesizing the above samples of (Y, NSG)BCO system are shown in fig. 6.1.

## 6.3. Temperature dependence of ac susceptibility:
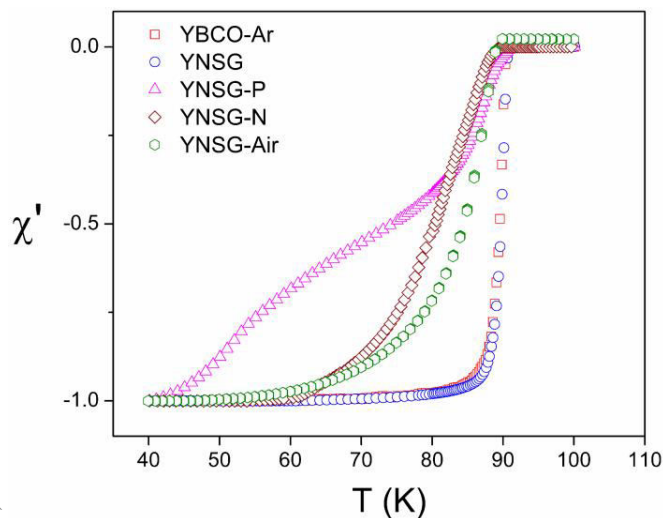


**Fig. 6.2.** Variation of normalized real part of ac susceptibility $(\chi')$ with temperature for the samples discussed in this chapter. Sharp superconducting transitions are observed for YBCO-Ar and YNSG samples, and the absence of secondary peaks, confirming the homogeneity of oxygen content compared to other three samples.

After processing the various (Y, NSG)BCO samples, oxygenation was done for 110 h at 460 $^{o}$C for the structural phase transition from non-superconducting tetragonal to superconducting orthorhombic phase to take place. Superconducting transition temperature $(T_c)$ have been determined by recording ac susceptibility $(\chi_{ac}(T))$ in the temperature range 40 K$\leq$ T $\leq$100 K at driving ac field of rms amplitude 10 Oe with a frequency of 33 Hz employing a PPMS-ACMS (Quantum Design, model MPMS-7). In-phase component of ac susceptibility $(\chi')$ with temperature for all samples is depicted in fig. 6.2. The onset of the transition for YBCO-Ar, YNSG, YNSG-P, YNSG-N and YNSG-Air occurs at 91.0, 91.6, 91.6, 90.2 and 90.0 K respectively. The transitions in YBCO-Ar and YNSG

samples are sharp with their widths $\Delta T_c$ ~2.5 K. On the other hand, YNSG-P, YNSG-N and YNSG-Air samples exhibit much broader transitions spread out to a $\Delta T_c$ ~ 50 K, 30 K and 25 K respectively; the large tail regions in these three samples represent presence of large amounts of solid solutions of lower $T_c$ values.

## 6.4. Structural analysis of the (Y, NSG)BCO samples:
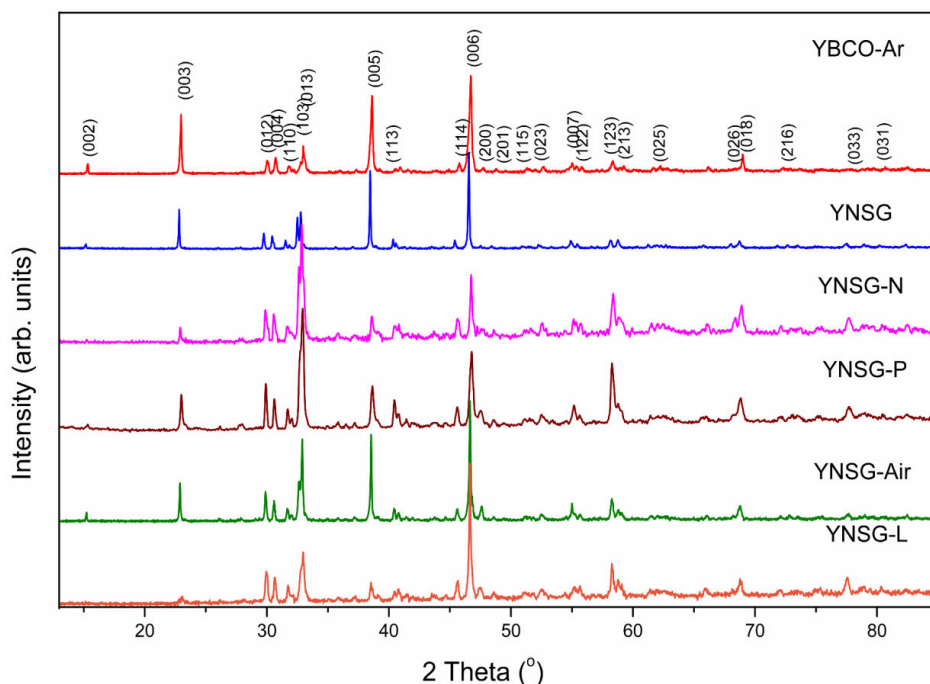


**Fig. 6.3.** X-ray diffractograms of YBCO-Ar, YNSG, YNSG-P, YNSG-N, YNSG-Air and YNSG-L.

The crystal structure of the YBCO-Ar, YNSG, YNSG-P, YNSG-N, YNSG-Air and YNSG-L composites were analyzed from the X-ray diffraction patterns (shown in fig. 6.3) recorded using Cu-K$_\alpha$ radiation on BRUKER X-ray diffractometer. The diffraction data were collected over the diffraction angles in the range $2\theta$: 10 to 90 Å by step scanning with a step width of 0.02. The structural parameters of YBCO were used as a starting model for the refinement

using The FULLPROF program. The prominent reflections show that all the XRD patterns can be indexed to an orthorhombic unit cell, from which lattice parameters are determined. The less prominent lines in YBCO-Ar and YNSG are found to represent RE-211 as minor phase. Considerable number of extra Bragg peaks observed in the other samples YNSG-P, YNSG-N, YNSG-Air and YNSG-L include not only the minor RE-211 phase but also other phases like solid solutions of RE/Ba -ss type, etc.

## 6.5. Results and discussion on YNSG-Air sample:

To examine if the origin of spherical porosity observed so far in (Y, Sm)BCO, YNSG and YBCO-Ar samples, all processed under argon, lies in the choice of atmosphere, YNSG-Air sample processed in air using the same heat treatment schedule as for YNSG sample, is studied.
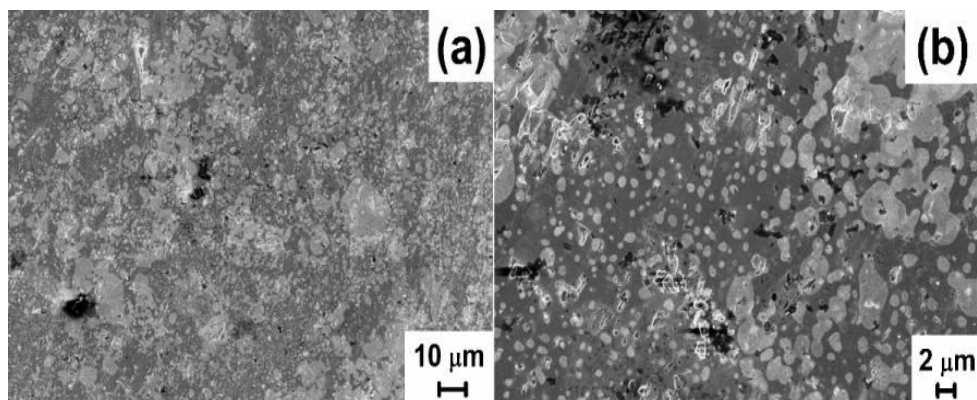


**Fig. 6.4.** FESEM images of YNSG-Air recorded at magnifications of (a) 1 kX and (b) 5 kX.

FESEM images of YNSG-Air sample are shown in fig. 6.4. Spherical porosity is evidently absent in this air processed sample. Similar to YNSG sample, dark and bright regions are observed within the precipitates which are identified to be YNSG-211 and Y-211 phases respectively from elemental analysis (given in

Appendix, section 3). The size range of the 211 particles in the YNSG-Air sample varies from submicron to 3 μm.

Field dependence of $J_c$ is calculated for YNSG-Air sample at different temperatures and displayed in fig. 6.5. Self field $J_c$ at 77 K is 7 kA/cm$^2$ and falls to zero at a field of 5.5 T. Absence of sufficient flux pinning at high fields at 77 K can be attributed to the formation of RE/Ba -ss phases in considerable amounts as seen from the tail region in $\chi_{ac}(T)$.
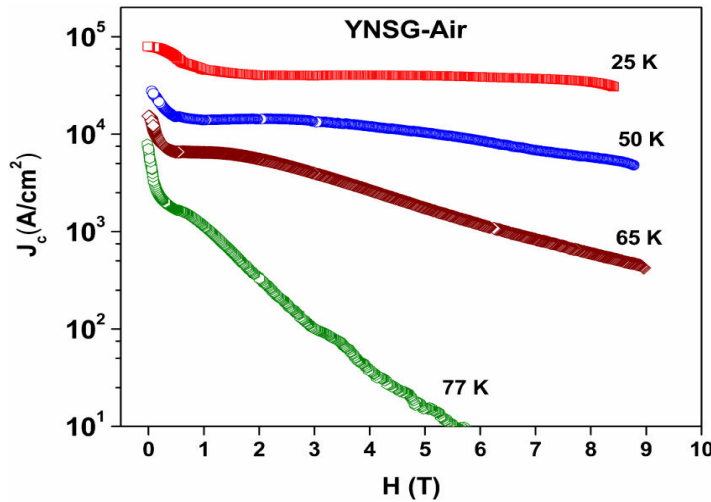


**Fig. 6.5.** Magnetic field dependence of $J_c$ of YNSG-Air sample at different temperatures.

In other words, due to processing the YNSG-Air sample in air, formation of solid solutions was not suppressed, which reflected in $J_c$ curve at 77 K.

### 6.6. Results and Discussion on YNSG-L sample:

Comparison of the nature of porosity in YNSG processed in argon and YNSG-Air processed in air confirms that the argon gas evolution takes place during solidification of the POIG process. However, processing under argon is essential to suppress the formation of solid solutions that deteriorate the superconducting properties drastically. It is likely that the argon gas gets entrapped in the liquid

phases during infiltration, which later lead to evolution of argon. In melt processed REBCO, possible evolution of oxygen and argon and the associated porosity were discussed by Murakami's group [6]. In order to see if entrapping of argon can be eliminated by carrying out infiltration in air medium and allowing argon entry at a later stage during crystallization (while cooling from 1040 $^{o}$C) to suppress solid solution formation, YNSG-L sample has been synthesized keeping same heat treatment schedule.
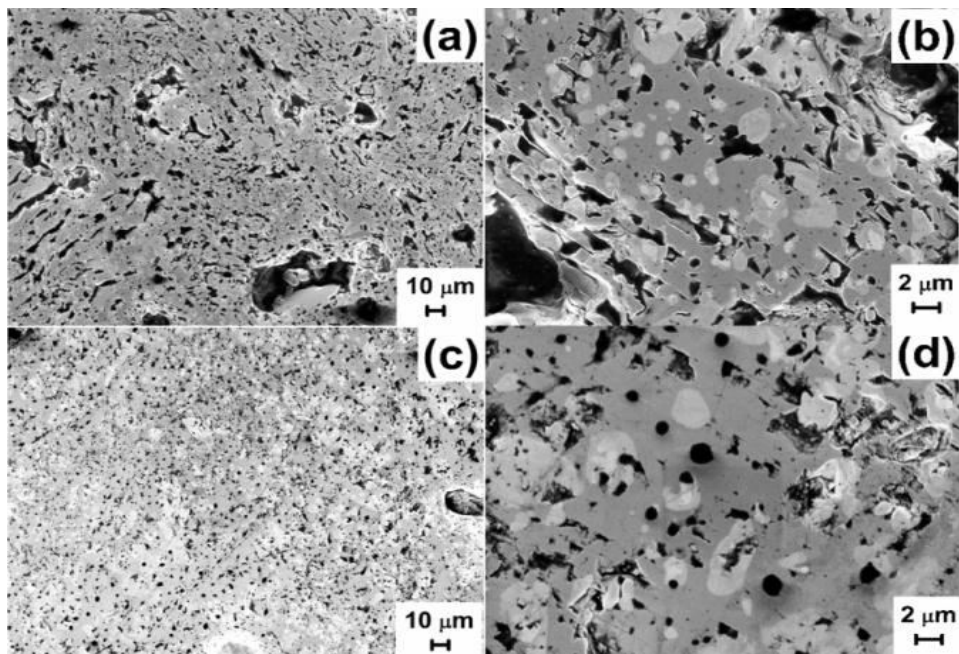


**Fig. 6.6.** FESEM images recorded at magnifications 1 kX and 5 kX from YNSG-L ((a) and (b)). (c) and (d) are FESEM images for YNSG at magnifications 1 kX and 5 kX.

FESEM micrographs recorded in YNSG-L and YNSG are compared in fig. 6.6. From these images it is clear that the spherical porosity indicating evolution of gas bubbles present in YNSG is successfully eliminated in YNSG-L sample. These results confirm the argon gas entrapment in the liquid phases infiltrated into the preform and their evolution during solidification. Infiltration in air medium

into the preform of YNSG-L sample has eliminated Ar gas entrapment and its subsequent evolution.

However there is a drastic increase in macro-defects (non-spherical porosity) in this sample. XRD also shows a number of extra peaks suggesting a large fraction of solid solutions to have formed. In summary, the spherical porosity is eliminated but microstructure of YNSG-L sample is not yet favorable for high performance.

## 6.7. Results and discussion on YNSG-P sample:

Presence of considerable (11.3%) macro-defects (non-spherical porosity) has led to deterioration of the $J_c(H)$ performance in YSm-20-Nb sample (section. 4.6.4), in spite of having enhanced density of flux pinning centres. In order to address the problem of macro-porosity, an experiment is attempted in analogy to densification reported by press-sintering process in Bi-Sr-Ca-Cu-O materials [1-2]. With an aim to eliminate the macro-porosity in the YNSG sample, after processing with same heat treatment we pressed the sample at 540 MPa and once again processed the pressed YNSG sample by heat treatment shown in fig. 6.1 for the sample YNSG-P. Sample assembly (processed YNSG sample + Y-123 pellet) was allowed to a temperature just above peritectic temperature (1010 $^o$C) for infiltrating the liquid phases (BaO + CuO) into the pressed YNSG sample and from there slowly cooled (1 $^o$C/h) through the peritectic temperature to a temperature of 930 $^o$C. Then it was maintained there for 24 hours to complete the grain growth, and was furnace cooled to room temperature.

Micrographs recorded employing FESEM at magnifications of 1 kX, 5 kX and 25 kX were shown in fig. 6.7. (a)-(c) respectively. Different shades are found in RE-211 phase particles as observed in YNSG sample which are YNSG-211 phase particles (dark region) and Y-211 phase particles (bright region) in the matrix, as

determined from elemental analysis shown in Appendix (section 2). The distribution of the RE-211 particles in the matrix is homogenous and the size of the RE-211 phase particles was of the order of 1-4 µm. From the FESEM image at low magnification (in fig. 6.7. (a)) the platelet widths are observed clearly to be small compared to YNSG sample and the unreacted liquid phases can be observed to be left back in the platelet gaps and macro-pores.
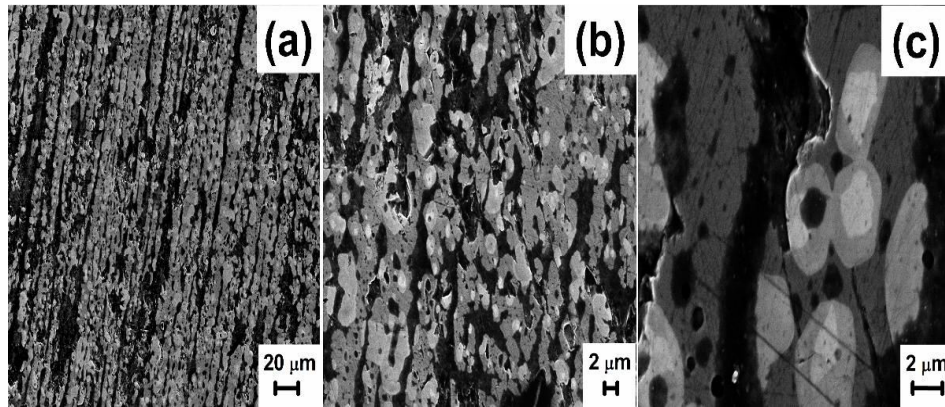


**Fig. 6.7.** Micrographs at different magnifications from YNSG-P material. It shows different phases present in the material and the solidified liquid in platelet gaps.

Current density ($J_c$) of the YNSG-P superconducting sample at different temperatures (25, 50, 65 and 77 K) up to 9 T field was calculated from M-H loops and displayed in fig. 6.8. The $J_c$ value is 0.7 kA/cm$^2$ at zero field and decreases to 100 A/cm$^2$ at 0.8 T at 77 K, while at temperatures 65 K, 50 K and 25 K $J_c(0)$ is found to be 1.5 kA/cm$^2$, 3.8 kA/cm$^2$ and 13.5 kA/cm$^2$ respectively.

The $J_c(H)$ variation in YNSG-P sample is inferior to all other samples studied. This can be explained by the presence of large amount of non-superconducting liquid phases (Ba-Cu-O) seen in microstructures, and the very large amount of solid solutions observed from the wide tail in $\chi_{ac}(T)$ measurements.
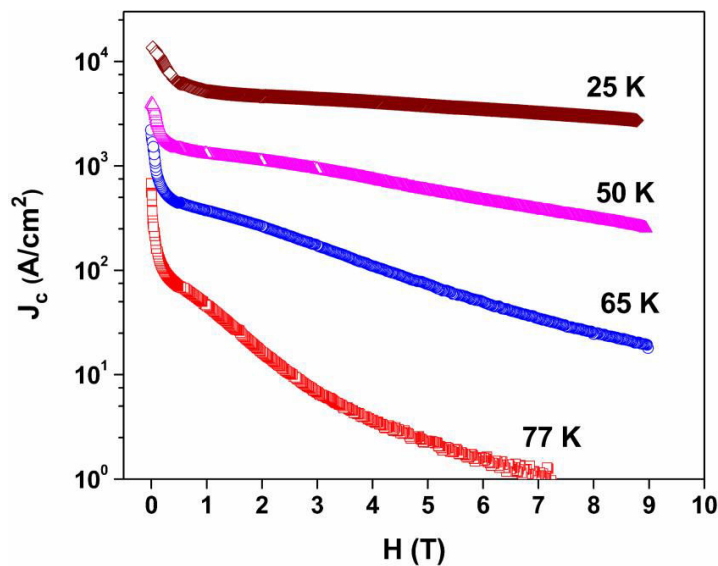
**Fig. 6.8.** *J$_c$* vs applied magnetic field for YNSG-P sample at various temperatures.

## 6.8. Results and discussion on YNSG-N sample:

Allowing high temperatures for longer time during the preform sintering and at grain growth stage can cause abrupt growth of RE-211 inclusions in the REBCO samples.  The microstructures of (Y, Sm)BCO, YBCO-Ar, and the samples derived from YNSG discussed above show larger sized RE-211 particles in the range : submicron to 6 μm to be present in the matrix phase.

To verify if shorter duration of heat treatments would lead to finer RE-211 particles, the following studies are carried out. We hypothesize that the RE-211 grains are likely to grow during (i) the sintering stage (4 hours at 950 $^o$C) of preform prior to infiltration and (ii) the prolonged infiltration stage (1 hour at 1100 $^o$C) and (iii) slow cooling through peritectic temperature ( 100 hours from 1040 $^o$C to 930 $^o$C) for textured grain growth.
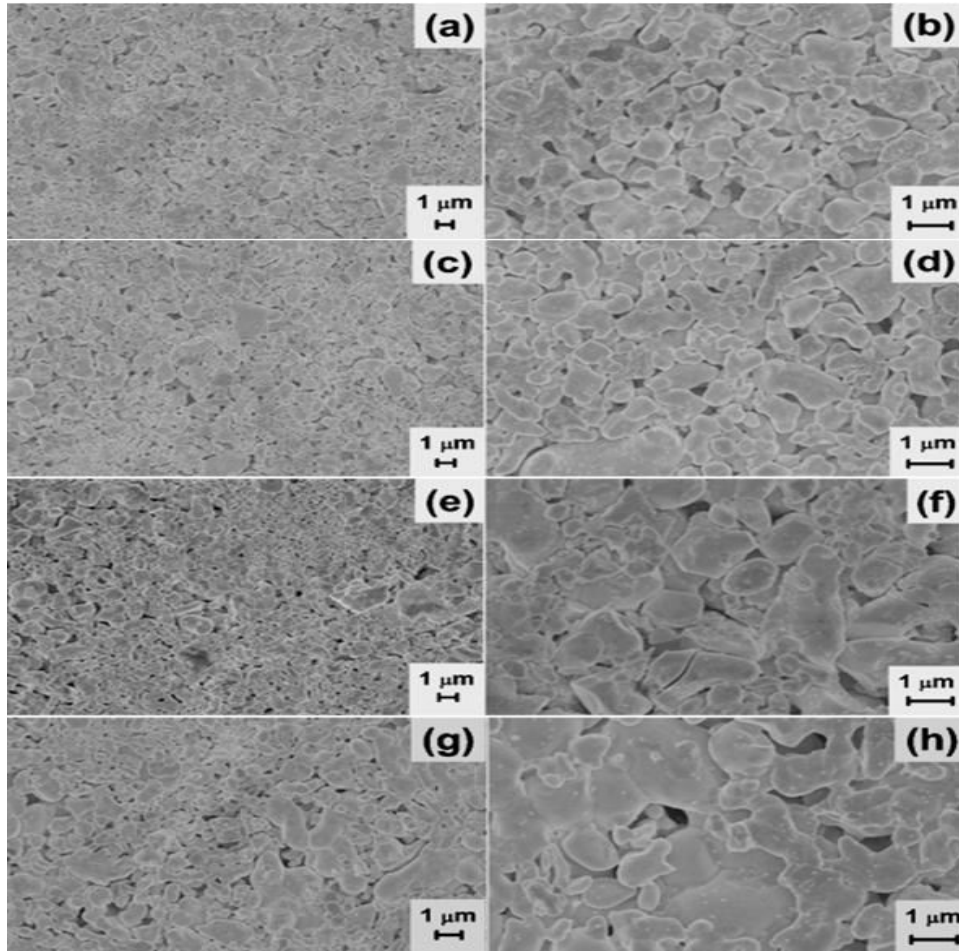
**Fig. 6.9.** FESEM images of YNSG-211 preforms sintered at 15, 30, 60 and 240 minutes, with the duration of sintering increasing in the figures from top to bottom. The panels on the left are at a magnification of 10 kX and those at the right are at a magnification of 25 kX.

The present sample is synthesized by a **new schedule** by reducing the sintering time, decreasing the dwell time at 1100 $^o$C and increasing the rate of cooling.

a) Initially small pellets of YNSG preform were subjected to different sintering durations of 15, 30, 60 and 240 minutes at 950 $^o$C, and the resultant microstructures were observed, which are shown in fig. 6.9. An examination of the images shows that sintering for longer durations of 240

minutes (fig. 6.9 (g and h)) results in large particles of RE-211 and less open porosity (gaps between the RE-211 particles) compared to all other preforms, while too less a sintering duration of 15 minutes (fig. 6.9 (a and b)) results in a preform containing enough porosity, but not having enough strength to support liquid phase infiltration. The preform sintered for 30 minutes (fig. 6.9 (c and d)) has optimum RE-211 size, sufficient open porosity and enough strength.

b) Dwell (at 1100 $^o$C) time was decreased to 30 minutes, and

c) Cooling was done with a faster ramp rate of 1 $^o$C/h all the way to 930 $^o$C, unlike YNSG sample.

The heat treatment schedule used for YNSG-N sample is shown in fig. 6.1.

FESEM images of YNSG-N sample, recorded using in-lens detector at a magnification of 1 kX, 5 kX and 10 kX are shown in figs. 6.10 (a), (b) and (c) respectively. As observed in YNSG sample, different shades of non-superconducting inclusions of YNSG-211 (dark color) and Y-211 (bright color) were found in the matrix of YNSG-N sample.

Large numbers of RE-211 (YNSG-211 and Y-211) phase particles are found, as expected, in sub micron range which may be because of shorter heat treatment at fast cooling rate, relative to YNSG and YBCO-Ar samples. The content of RE-211 phase particles in the YNSG matrix is found to be 46%.
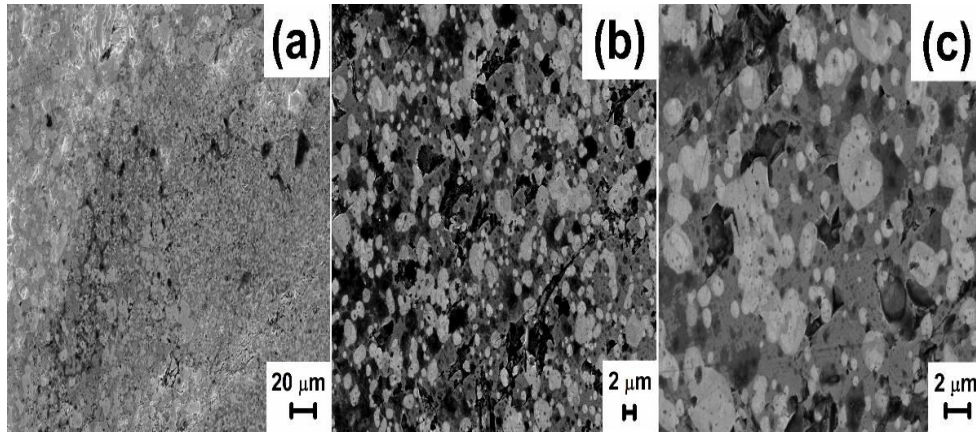
**Fig. 6.10.** FESEM images of YNSG-N sample recorded at magnifications of 1kX, 5 kX and 10 kX ((a), (b) and (c) respectively).

Critical current density at different temperatures was calculated by sweeping magnetic field up to 9 T and the representative plots are shown in fig. 6.11.
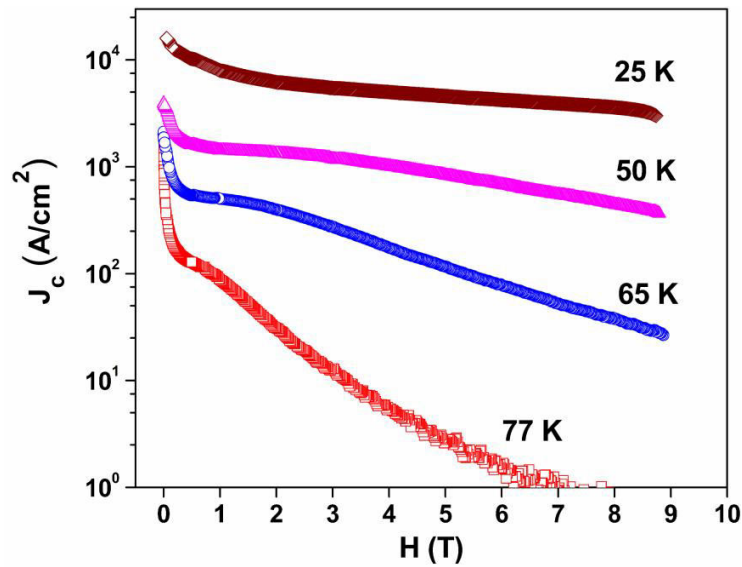


**Fig. 6.11.** $J_c$ is plotted against applied magnetic field for the YNSG-N sample at temperatures.

The calculated $J_c(0)$ at 77 K is 1.5 kA/cm$^2$ while it is 2.1 kA/cm$^2$, 3.9 kA/cm$^2$ and 16 kA/cm$^2$ at 65 K, 50 K and 25 K respectively. $J_c$ reduces to 100 A/cm$^2$ at 0.8 T

and its performance is only marginally better than YNSG-P sample, and in spite of finer RE-211 particles being present. However, considerable extent of solid solution formation is seen from $\chi_{ac}(T)$. It can be seen from micrographs that the distribution of RE-211 is quite inhomogeneous and spherical porosity due to argon still exists. The reductions in infiltration time and faster cooling rates have thus not improved the performance.

## 6.9. Discussion on structure and ac susceptibility of the various YNSG samples:

From ac susceptibility results (i) a sharp transition in the $\chi$ vs T curve that indicates the absence of low $T_c$ phases is observed in the case of YBCO-Ar and YNSG samples (ii) a tail in the curve is reflecting the oxygen deficient phases present in the YBCO-Ar and YNSG sample (iii) the distribution of $T_c$ over a broad range in ac susceptibility measurement for YNSG-P, YNSG-N and YNSG-Air samples represents the presence of large fractions of solid solutions due to the substitution of $RE^{3+}$ ions with $Ba^{2+}$ and the other non superconducting phases.

**Table 6.1.** Lattice parameters and unit cell volumes of the YBCO-Ar, YNSG, YNSG-P and YNSG-N samples.

| Sample | Lattice parameter (Å) | | | Cell volume (Å³) |
|---|---|---|---|---|
| | a | b | c | |
| YBCO-Ar | 3.810 | 3.886 | 11.697 | 172.2 |
| YNSG | 3.814 | 3.877 | 11.674 | 172.6 |
| YNSG-P | 3.823 | 3.882 | 11.681 | 173.4 |
| YNSG-N | 3.812 | 3.856 | 11.651 | 171.3 |

It is also observed that the intensities of (00l) diffraction peaks are enhanced in YBCO-Ar YNSG, YNSG-Air and YNSG-L, indicating the presence of c-texture or [00l] texture in the samples where as in the other two samples (YNSG-P and YNSG-N) [103] texture is observed. The lattice parameters and the cell volume are listed in Table 6.2.

As discussed in chapter 4 (section 4.4) all the (Y, Sm)BCO samples also showed texture in [00l] direction, as YBCO-Ar and YNSG. We recall from chapter III that YBCO sample processed in air showed [103] texture. An examination of the data shows that the atmosphere (argon or air) has no role to play in texturing of the samples.

Instead we find a correlation that all the samples processed using prolonged heat treatment of 100 hours while cooling through peritectic, choosing two types of cooling rates (1 and 0.5 $^{o}$C/h) showed [00l] texture. YNSG-P and YNSG-N for which shorter heat treatments are given with cooling rate of 1 $^{o}$C/h showed textured in [103] direction. From these results it is evident that the texturing in [00l] direction depends on the heat treatment schedules.

## 6.10. Results and discussion on YNSG-Ba sample:

We summarize below the results on the different (Y, NSG)BCO based samples discussed above in sections 6.1 to 6.8 synthesized with process modifications. Table 6.2 provides a comparison of main differences in process details and the outcome of the efforts made.

**Table 6.2.** Comparison of various (Y, NSG)BCO samples dealt with in this chapter.

| Sample | Heat treatment | Atmosphere | $\Delta T_c$(K) | $H_{irr}$ (T) at 77 K | Remarks |
|--------|---------------|------------|------|-----------|---------|
| YBCO-Ar | 100 h (1 & 0.5 °C/h) | Ar (99 %) | 2.5 | 3.3 | No RE additions, 6.8 % porosity present |
| YNSG | 100 h (1 & 0.5 °C/h) | Ar (99 %) | 2.5 | >9 | Best $J_c$(H) but 6 % porosity present |
| YNSG-Air | 100 h (1 & 0.5 °C/h) | Air | 25 | Air | No spherical porosity Large fraction of solid solutions |
| YNSG-L | 100 h (1 & 0.5 °C/h) | Ar (99 %) during cooling | -- | -- | Pores due to Ar was suppressed Large macro-porosity |
| YNSG-P | 80 h (1 °C/h) | Ar (99 %) | 50 | 0.8 | Pores filled with liquid phases Large fraction of solid solutions |
| YNSG-N | 90 h (1 °C/h) | Ar (99 %) | 30 | 1 | Smaller sized 211 but inhomogeneous Large fraction of solid solutions |

The main points can be summarized as below:

1. The compositional segregation within the RE-211 precipitates was observed in the matrix phase of all the above samples. The bright core regions are of Y-211 surrounded by darker region of YNSG-211.

2. The YNSG sample, POIG processed under argon, shows the best $J_c$(H) curve. However, this sample exhibits 6% porosity and also spherical porosity due to argon evolution.

3. The origin of spherical porosity is identified to be due to argon entrapment during infiltration and re-evolution during solidification through $T_p$, from the results on YNSG-Air and YNSG-L samples.

4. However faster cooling rates in YNSG-N yielded finer RE-211 particles in the RE-123 matrix, but they are inhogeneously distributed.

5. Press-sintering in YNSG-P, processing in air in YNSG-Air and shorter preform sintering followed by faster cooling rates in YNSG-N are found to result in a large fraction of solid solutions of RE/Ba-ss type and deteriorate the superconducting properties.

Based on these observations, we have chosen to synthesize YNSG-Ba sample which was processed in air after providing additional amount of Ba in the preforms. The motivation for this was from the reports in literature [3-5] that solid solution formation during processing REBCO in air can be suppressed, if the ratio between Ba and Cu in the liquid phase ($Ba_3Cu_5O_8$) is maintained to be 4:5 rather than 3:5. Hence we added an extra amount of BaO to the YNSG-211 preform, to maintain the ratio of Ba to Cu at 4:5. The heat treatment schedule is maintained same as for YNSG sample, except that the processing was done in air for YNSG-Ba sample, while it was in argon for YNSG sample.
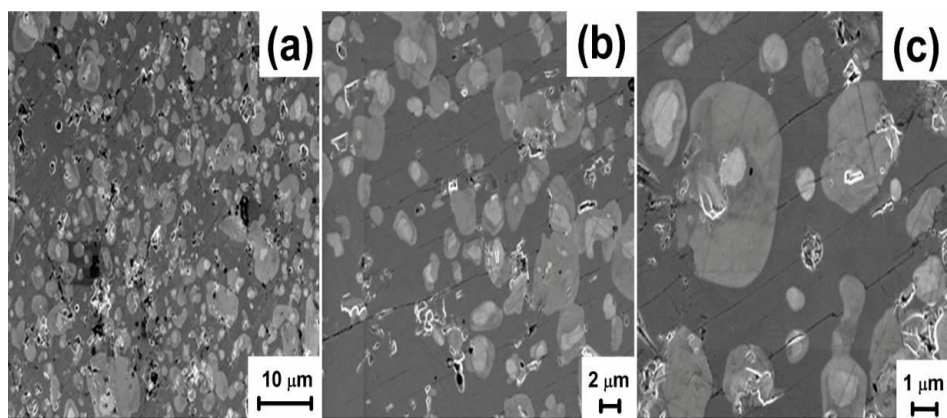


**Fig. 6.12.** FESEM images of YNSG-Ba sample recorded at different magnifications (a) 2 kX, (b) 5 kX and (c) 10 kX.

The FESEM images recorded using in-lens detector for YNSG-Ba sample are shown (fig. 6.12) below at different magnifications. The sizes of the RE-211 particles in the YNSG-Ba are of the order of 2-5 μm. The numbers of submicron – 1 μm size particles are minimal. The sizes of RE-211 particles thus are somewhat bigger than in YNSG sample. This suggests a reduction in the interfacial defect density in YNSG-Ba sample. Spherical porosity is eliminated in the present sample as in the air processed YNSG-Air sample. Even the other types of defects / macroporosity are remarkably reduced to ~ 1%.

The RE-211 particles distributed homogeneously in the matrix phase and they also exhibit bright and dark regions, as observed in all the YNSG –based samples as well as (Y, Sm)BCO samples.

Interesting result in the present sample is the presence of twinning which has not been observed in any of the other RE-doped samples studied in this thesis. The size range of twin widths present in the sample is of the order of 25-200 nm. The wide spread twinning observed in YNSG-Ba sample is shown in fig. 6.13.
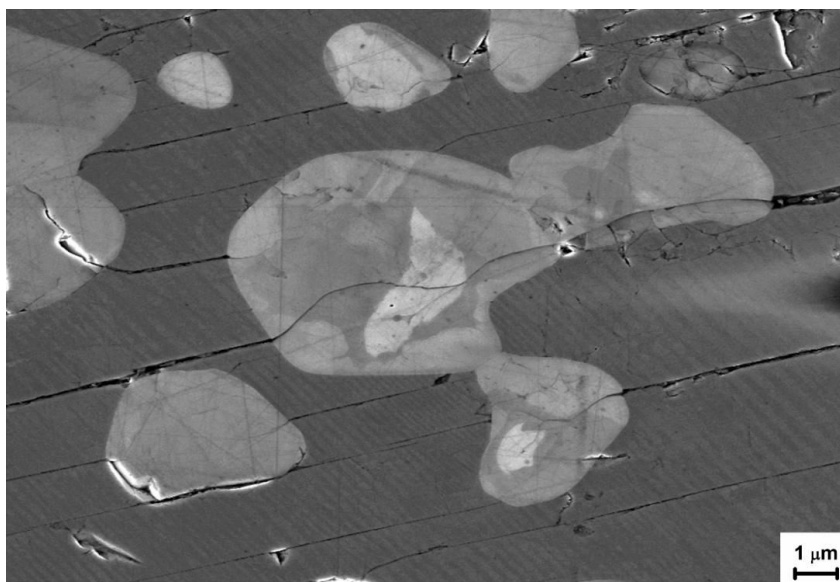


**Fig. 6.13.** FESEM image of YNSG-Ba recorded at a magnification of 15 kX. Presence of widespread twinning can be seen.

It is worth mentioning here that in POIG processed YBCO with no doping, prominent twinning was observed [7]. From detailed EBSD studies, it was shown that defects of varied sizes in a broad range are created associate with twinning, and that they provide flux pinning in a wide range of magnetic fields. The result of this was observation of flat $J_c(H)$ to high fields in undoped YBCO. Twinning

occurs in YBCO superconductors during oxygenation process from tetragonal to orthorhombic phase [8].

Field dependence of $J_c$ at different temperatures determined from M-H loops for YNSG-Ba sample are shown in fig. 6.14 (a). The $J_c(H)$ curves can be seen to be flat up to 9 T field at all temperatures above 77 K. This gives evidence that efficient flux pinning is present in this sample at all fields up to 9 T.
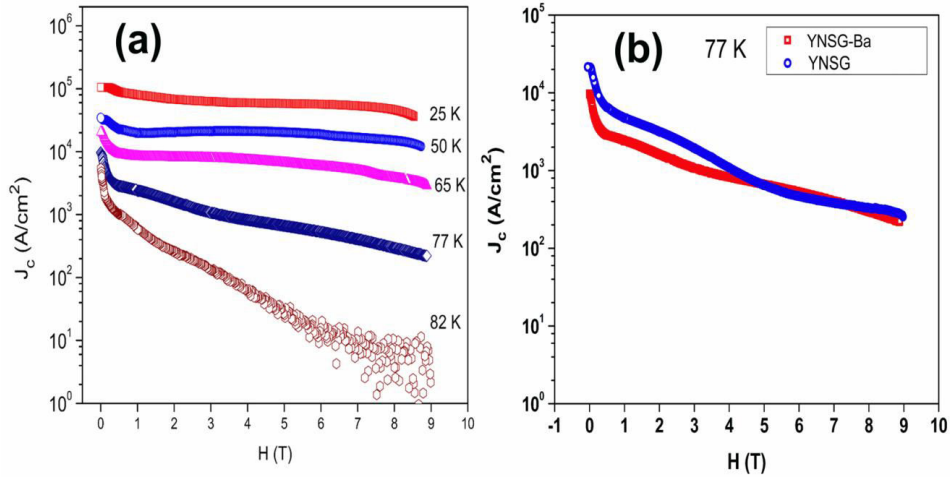


**Fig. 6.14.** (a) Field dependence of $J_c$ for YNSG-Ba sample at different temperatures. In (b), the $J_c$ vs H curves for YNSG-Ba and YNSG are compared at 77 K.

The $J_c(H)$ curves at 77 k determined for YNSG-Ba and YNSG samples are compared in fig. 6.14 (b). It can be seen that $J_c(0)$ of YNSG-Ba sample is 11 kA/cm$^2$ and is less than 21.5 kA/cm$^2$ of YNSG. The flux pinning at low fields is known to depend on the RE-211/RE-123 interfacial defect density, which in turn is decided by the size of precipitates. The larger RE-211 particles, compared to those in YNSG, account for the reduction in $J_c(0)$.

It is interesting to note that even though the $J_c(0)$ is lower by a factor of two, the $J_c$ values at fields higher than 5 T are equal to or better than those for YNSG sample. We attribute the enhanced flux pinning observed in YNSG-Ba sample at

high fields to the presence of wide range of defects associated with twinning, in addition to the compositional fluctuations and the associated lattice mismatch effects which are also present in YNSG sample.

**References:**

1. N. Harish Kumar and V. Seshu Bai, Phys. Rev. B **53** (1996) 15281.

2. Vladimir Beilin, Alexander Goldgirsh, Emanuel Yashchin, Michael Roth and Michael Schieber, IEEE TRANSACTIONS ON APPLIED SUPERCONDUCTIVITY **9** (1999) 2.

3. Y. Shi, N. Hari Babu, K. Iida and D. A. Cardwell IEEE TRANSACTIONS ON APPLIED SUPERCONDUCTIVITY **17** (2007) 2.

4. J.Q. Dai, Z.X. Zhao and J.W. Xiong, Supercond. Sci. Technol. **16** (2003) 815–819.

5. A. Hu, N. Sakai, H. Zhou, M. Matsui and M. Murakami, Supercond. Sci. Technol. **16** (2003) 33–38.

6. N. Sakai, D. Ishihara, K. Inoue and M. Murakami, Supercond. Sci. technol. **15** (2002) 698-701.

7. Ph.D. Thesis entitled "Enhanced Flux Pinning to High Fields in YBCO and YBCO/Ag Superconductors through Preform Optimization in Infiltration and Growth Process" by N. Devendra Kumar, (2011), University of Hyderabad.

8. C. Barry, Journal of Electron Microscopy Technique **8** (1988) 325–337.

# Chapter VII

# Summary and Conclusions

The present thesis work is focussed on introducing multiple rare earths (RE) at Y site to form $(Y,RE)Ba_2Cu_3O_{7-\delta}$ composite superconductors through Preform Optimized Infiltration Growth (POIG) process. The structure, microstructure and superconducting properties have been measured on different composites synthesized and various observations are correlated.

Infiltration Growth process allows fabrication of bulk $REBa_2Cu_3O_{7-\delta}$ (REBCO) composites in near net shape with improved microstructural properties in comparison with the melt growth process [1-8]. Even though the IG process is superior to the melt growth process, there are reports on the spatial inhomgeneity in the distribution of $RE_2BaCuO_5$ (RE-211) in the final composites which resulted in a large variation in the superconducting properties at different locations in the sample [10]. Paying attention to problems associated with IG process, *Devendra et al.* [9] developed Preform Optimized Infiltration Growth process (POIGP) which yielded a homogeneous and dense distribution of fine $Y_2BaCuO_5$ (Y-211) particles in $REBa_2Cu_3O_{7-\delta}$ (YBCO or Y-123) superconductor. This process has suppressed the rapid fall in the Jc values, often reported in MG processed samples, at higher fields. In the case of conventional melt grown superconductors [11], further hike in $J_c$ values were reported by introducing nano-sized inclusions and mixed rare earth elements into the superconducting matrix phase.

The defects generated at the interface of non-superconducting RE-211 particles with RE-123 matrix, and those associated with nano-particle inclusions, dislocations, twins, and stacking faults have been proven to act as efficient flux

pinning centres. Much efforts have been made to increase the amounts of the small-sized (submicron -1 micron) non-superconducting phase and thereby the interfacial defect density in the superconductors, through addition of Pt, $CeO_2$, $BaCeO_3$ that refine the size of RE-211 [12-15]. Such refinement led to enhanced $J_c$ mainly in low-field regions. The coherence length of the REBCO superconductors is on nanoscale; and hence defects of nano-size associated with compositional fluctuations due to mixed RE elements in the matrix should be beneficial for pinning up to high fields. However, reports in literature on $J_c$ in mixed REBCO show enhanced pinning in intermediate field range of 4-5 T, reported as peak effect in melt grown samples. Extensive range of nano-twinning with larger number of crossing twins, and the associated high defect densities in a broad size range are identified to be the source of flux pinning responsible for the enhancement in $J_c$ at fields as high as 9 T [13-15]. Superior $J_c(H)$ performance can possibly be achieved by combining the advantages of additional flux pinning due to nano-sized defects associated with mixed rare earth elements in the superconducting matrix phase with the sustenance of considerable $J_c$ to high fields from POIG process. With this as major objective, this thesis presents the results of detailed investigations carried out on POIG processed superconductors with Sm doped for Y and mixed RE elements namely Nd, Sm and Gd doped for Y in YBCO and discuss the factors that influence the microstructures and thereby the superconducting properties of these materials.

In chapter III, we examined the possibility of lowering the infiltration temperature ($T_i$) from 1100 $^o$C used in POIGP to 1040 $^o$C, so that texturing the samples using seeding can be attempted. For this, the effect of infiltration temperature (1100 $^o$C and 1040 $^o$C) on the microstructural and superconducting properties was studied taking YBCO as an example. It is found that infiltration

at higher temperature yielded highly dense composites with minimal macro-defects. Microstructural properties on gross scale show almost similar distribution of Y-211 phase particles in Y-123 matrix. Sample Y-1 processed at infiltration temperature of 1100 $^o$C showed enhanced hardness along with high $J_c$ up to high fields, compared to Y-2 processed at 1040 $^o$C, though $J_c(0)$ value is same for both. Enhancement in both hardness and $J_c$ in sample Y-1 is attributed to the presence of high density of nanometric defects associated with twinning in the matrix, starting at the twin boundaries as seen from TEM images [16]. The sample Y-2 exhibits rapid fall in high field $J_c$ and lower hardness and there were no traces of twinning. From these observations $T_i$ of 1100 $^o$C was maintained for all the samples studied in this work, since high $J_c$ up to high fields along with enhanced hardness is crucial for practical applications.

Reports from literature show that it is essential to process the REBCO compounds, with exception of Y-123, in reduced oxygen atmospheres to prevent the formation of $RE_{1-x}Ba_{2+x}Cu_3O_y$ solid solutions (RE/Ba–ss type) with lower $T_c$ [17-18]. In REBCO systems, where RE represents the light rare-earth elements (LRE) like La, Nd, Sm, Eu, etc., it is observed that the $LRE^{3+}$ ions can occupy the $Ba^{2+}$ sites because their ionic radii are close to each other. Increasing replacement of $Ba^{2+}$ sites is found to result in a deterioration of superconducting properties, and substantial reduction of critical temperature especially at high substitution levels [19-24]. Synthesis in commercial argon (with 1% oxygen) or usage of excess Ba during processing is reported to effectively suppress the substitution of RE at Ba site. It not only suppresses the formation of solid solutions of the LRE $_{1+x}Ba_{2-x}Cu_3O_y$ type but permits local compositional fluctuations of $(RE_{1-x}, RE'_x)BCO$ type (i.e. RE/RE' –ss) in the processed samples which leads to enhanced flux pinning [25].

In chapter IV, the results on the effect of doping single RE element Sm at Y site in YBCO are presented. The addition of Sm was done in two different ways. In first part different amounts of (10, 20 and 30 wt.%) nano $Sm_2O_3$ (50-80 nm) particles prepared in sol form were added to the Y-211 preform using a novel process called Nano dispersive sol casting method [26]. Using this method, nano particles of $Sm_2O_3$ could be distributed individually, and without agglomeration, on the surface of the Y-211 particles. The preforms thus prepared were subjected to POIG process to form YSm-10, YSm-20 and YSm-30 samples. FESEM images of the final products had precipitates with compositional segregation (Y-211 as bright cores with YSm-211 in the darker outer regions), distributed in the matrix. YSm-20 showed better performance than YSm-10 and YSm-30 samples with finite $J_c$ even at 9T field, suggesting 20 wt.% doping to be optimum. Similar observation of optimum doping concentrations were reported to show best Jc in thin films of (Y, Dy)BCO system due to match between defect density and vortex density [27].

In second part of chapter IV, Sm was dispersed chemically by synthesizing the $(Y_{1.6}, Sm_{0.4})BaCuO_5$ preform powders in citrate route, which was POIG processed to form YSm-20-C sample. Interestingly, the microstructures of this sample showed smearing of brighter and darker regions within the YSm-211 particles in the 123 matrix, unlike in YSm-20 sample of equivalent composition where Sm doping was from nano $Sm_2O_3$. The two different types of microstructural features (cored and smeared bright regions in the 211 phase particles) in (Y, Sm)BCO samples is explained through a possible mechanism. The superconducting property of the YSm-20-C sample was inferior to YSm-20 sample, processed through external addition of nano $Sm_2O_3$. We attribute the origin of this reduction in $J_c$ to the large fraction of solid solutions of RE/Ba –ss type formed in YSm-20-C as indicated by XRD and ac susceptibility measurements.

On similar lines to the report on melt processed (Nd, Eu, Gd)-123 with 35 mol.% of Gd-211, that states 0.1 mol.% of nanometer-sized $NbO_3$ has shown enhanced flux pinning [11], in the present work 0.1% of $Nb_2O_5$ was added as nano sized sol to YSm-211 preform and its effect on $J_c$ was studied. It is found that $J_c(0)$ is enhanced at all temperatures, possibly due to additional pinning from fine distribution of Nb in the YSm-123 matrix. However an increase in porosity to 16% overshadowed the positive effect of additional pinning due to lattice mismatch effects associated with the presence of Nb, Sm and Y in the matrix causing $J_c$ to fall rapidly by 6 T at 77 K. Increase in porosity could be due to reduced liquid phase infiltration through gaps in the preform, which is possibly due to Nb promoting greater sintering of YSm-211 grains in the preform.

However, there were other difficulties observed during IG processing using the YSm-211 preforms. Deposition of nano $Sm_2O_3$ particles on the surface caused sintering of the YSm-211 particles and reduced the open porosity in the preform. This limited the entry of liquid phases during IG process leading to considerable porosity and larger 211 particles in the end product.

Studies in literature on ternary mixed rare earth superconductors [28-31], report strong flux pinning due to stress fields arising from the presence of different RE elements present in the matrix. Possible reasons for enhanced pinning may be related to the following factors: firstly, RE sites are substituted by Nd, Eu and Gd elements, due to which the lattice mismatch arises among the neighbouring unit cells containing Nd, Eu, and Gd.

The present results on the effect of ternary RE elements (Nd, Sm, Gd − called NSG) doped by 20 wt.% at Y site in YBCO are presented in Chapter V. For this purpose, 20 wt.% of NSG-211 powder of ~1μm size was mixed with 80% of Y-211 powder ~ 1 μm size to form YNSG-211 preform powders. The preforms were

POIG processed to form YNSG superconductor. FESEM images show annuli cores within YNSG-211 precipitates in the matrix. The $J_c(0)$ was 22 kA/cm$^2$ and remained better than 300 A/cm$^2$ even at 9 T field. This sample showed the highest $J_c$ among all the samples studied in this thesis. Similar $J_c(H)$ curve was observed for the YBCO sample [16] that showed wide spread twinning, after being POIG processed in air. The YNSG sample on the other hand shows no twinning, but gives high $J_c$ sustained to high fields and we attribute the strong flux pinning at high fields to lattice mismatch defects due to the presence of ternary RE elements.

From the structural, microstructural and magnetic properties of the superconductors of (Y, Sm)BCO and (Y,NSG )BCO systems discussed in chapters III to V, we consolidate the following observations. YBCO with no RE doping was also made under same conditions for comparison.

(i)    All the above samples were synthesized using POIG process under commercial argon atmosphere, which contains 1% oxygen

(ii)   Spherical pores were observed throughout all the samples

(iii)  RE-211 particles are distributed in the RE-123 matrix. In YSm-10, YSm-20, YSm-30 as well as YNSG samples, brighter regions (annular core formation) surrounded by darker region are seen within the RE-211 particles indicating compositional segregation.

(iv)   However, in YSm-20-C sample with chemical substitution of Sm for Y, the cores are smeared out within the 211 particles.

(v)    Additionally, considerable amount of non-spherical porosity (macro-defects) are also observed in all the samples.

(vi)   Size of RE-211 particles range in 2-6 microns on an average, and is larger than POIG processed YBCO in air.

**Problems yet unsolved:**

1. Spherical porosity is observed in all the samples processed under argon. Its origin and ways to eliminate are not well established.

2. Considerable non-spherical porosity is also present in the samples that limits sustenance of high $J_c$ value at high fields as in YSm-20-Nb.

3. RE-211 precipitates in the matrix phase need be further refined and more uniformly distributed in order to achieve higher zero field $J_c$, simultaneous with flat $J_c(H)$.

4. Clearer understanding is required on the process conditions leading to large fraction of unwanted formation of solid solutions of low $T_c$.

The fact that all the samples processed under argon exhibit wide spread porosity suggests that attempts to suppress the porosity through process modifications project a scope to improve the performance of these materials.

In sixth chapter the effect of different processing conditions was studied aimed at identifying the origin of porosity, ways to suppress the porosity and refine the RE-211 size. For this purpose YNSG composition was chosen as an example, since it has shown the best $J_c(H)$ after POIG process. Six samples were synthesized using YNSG preforms and processing them under different heat treatment schedules, atmospheric conditions and pressure.

Various (Y, NSG)BCO samples, thus prepared were YNSG processed in argon, YNSG-Air (processed in air), YNSG-L ( argon entry at later stage during solidification), YNSG-P (press-sintered), and YNSG-N( new schedule of shorter durations for sintering and solidification through $T_p$) and YNSG-Ba (with excess Ba in preform to suppress solid solutions even when processed in air.

The results on the above (Y, NSG)BCO can be summarized as

1. The transitions in YBCO-Ar and YNSG samples are sharp with their widths $\Delta T_c$ ~2.5 K. On the other hand, YNSG-P, YNSG-N and YNSG-Air samples exhibit much broader transitions spread out to a $\Delta T_c$ ~ 50 K, 30 K and 25 K respectively; the large tail regions in these three samples represent presence of large amounts of solid solutions (RE/Ba -ss type) and deteriorate the superconducting properties.

2. The compositional segregation within the RE-211 precipitates was observed in the matrix phase of all the above samples. Elemental analysis from EDS shows that the bright core regions are of Y-211 surrounded by darker region of YNSG-211.

3. The YNSG sample, POIG processed under argon, shows the best $J_c(H)$ curve. However, this sample exhibits 6% porosity and also spherical porosity due to argon evolution.

4. The origin of spherical porosity is identified to be due to argon entrapment during infiltration and re-evolution during solidification through $T_p$, from the results on YNSG-Air and YNSG-L samples.

5. However faster cooling rates in YNSG-N yielded finer RE-211 particles in the RE-123 matrix, but they are inhogeneously distributed in the sample. It also shows spherical porosity and considerable macro-defects and exhibits inferior $J_c(H)$.

**Results on YNSG-Ba sample:**

Based on these observations, we have chosen to synthesize the sixth sample YNSG-Ba which was processed in air after providing additional amount of Ba in the preforms. The motivation for this was from the reports in literature [19-24] that solid solution formation during processing REBCO in air can be suppressed, if the ratio between Ba and Cu in the liquid phase ($Ba_3Cu_5O_8$) is maintained to be

4:5 rather than 3:5. The heat treatment schedule was maintained same as that for YNSG sample, except that the processing was done in air for YNSG-Ba sample, while it was in argon for YNSG sample.

The FESEM images in YNSG and YNSG-Ba are compared in fig. 7.1. The figure shows that sizes of the RE-211 particles in the YNSG-Ba are of the order of 2-5 μm and thus are somewhat bigger than in YNSG sample. This suggests a reduction in the interfacial defect density in YNSG-Ba sample. The RE-211 particles are distributed homogeneously in the matrix phase and they also exhibit bright and dark regions, as observed in all the YNSG –based samples as well as (Y, Sm)BCO samples.
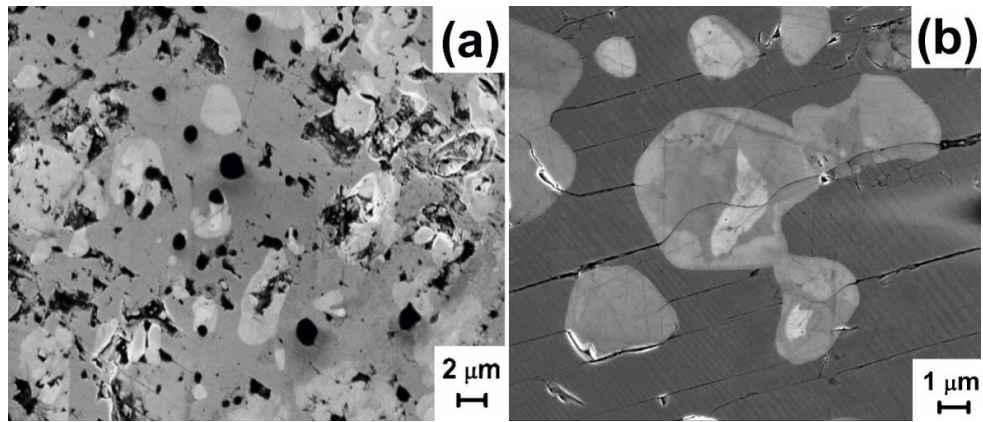


**Fig. 7.1.** FESEM images for (a) YNSG and (b) YNSG-Ba samples. Absence of spherical porosity and widespread twinning can be seen in YNSG-Ba sample.

Spherical porosity is eliminated in the present sample, as in the air processed YNSG-Air sample. Even the macro defects / non-spherical porosity is remarkably reduced to ~ 1%.

Interestingly twinning was observed with twin widths of 25-200 nm. The wide spread twinning observed in YNSG-Ba sample is shown in fig. 7.1 (b). Observation of flat $J_c(H)$ to high fields in undoped YBCO [16] was shown to be

due to the presence of defects of varied sizes, associated with twinning, and that they provide flux pinning in a wide range of magnetic fields.

Field dependence of $J_c$ at different temperatures determined from M-H loops for YNSG-Ba sample (fig. 6. 14) can be seen to be flat up to 9 T field at all temperatures above 77 K. This gives evidence that efficient flux pinning is present in this sample at all fields up to 9 T.
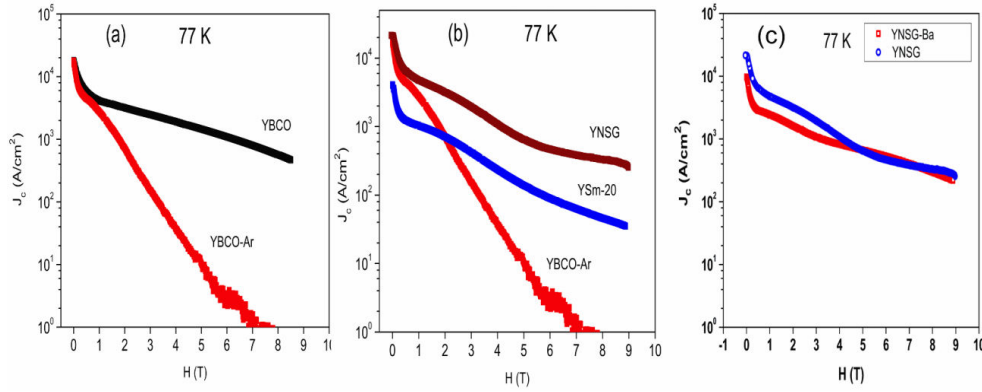


**Fig. 7.2.** Field dependence of $J_c$ at 77 K are compared for (a) POIG processed YBCO sample in air (YBCO) with YBCO-Ar, (b) YBCO-Ar, YSm-20 and YNSG samples and (c) YNSG sample $J_c$ with YNSG-Ba.

Fig. 7.2 (a) compares the $J_c(H)$ curves obtained at 77 K for undoped YBCO superconductors POIG processed in air (YBCO) and in argon (YBCO-Ar). It can be seen that both samples have comparable values of $J_c(0)$, but high field performance is quite different, though RE doping and the associated pinning are absent in both. The fall in $J_c$ at high fields in argon processed sample is due to ~6% porosity and RE/Ba-ss formation, unlike Air processed YBCO which additionally has enhanced pinning from twinning-associated defects.

Fig. 7.2 (b) shows the $J_c(H)$ variation at 77 K for YBCO-Ar, YSm-20, YNSG samples. The fact that $J_c(H)$ of YNSG sample and YNSG –Ba are superior to that for YSm-20 confirms that the flux pinning from lattice mismatch effects is

enhanced at high fields by doping multiple RE (NSG) elements instead of a single RE (Sm).

Fig. 7.3 (c) compares the $J_c(H)$ curves for YNSG and YNSG-Ba at 77 K. $J_c(0)$ of YNSG-Ba sample is 11 kA/cm$^2$ and is less than 22 kA/cm$^2$ of YNSG and is due to the flux pinning caused at low fields by the RE-211/RE-123 interfacial defect density. This in turn is decided by the size of precipitates; thus the larger RE-211 particles, compared to those in YNSG, account for the reduction in $J_c(0)$.

It is interesting to note that even though the $J_c(0)$ is lower by a factor of two, the $J_c$ values at fields higher than 5 T are equal to or better than those for YNSG sample. We attribute the enhanced flux pinning observed in YNSG-Ba sample at high fields to the presence of wide range of defects associated with twinning, in addition to the compositional fluctuations and the associated lattice mismatch effects which are also present in YNSG sample.

**Major outcome of this work:**

1. (Y, LRE)BCO superconductors are synthesized successfully by POIG process under commercial argon.

2. However spherical porosity was observed, the origin of which is identified to be due to argon entrapment during infiltration and re-evolution during solidification through $T_p$, from the results on YNSG-Air and YNSG-L samples

3. Texture was observed [00l] or [103] was observed from XRD, though no seed was used. An examination of texture in various samples shows that the atmosphere (argon or air) has no role to play in texturing of the samples, instead we find a correlation that all the samples processed using prolonged heat treatment of 100 hours while cooling through peritectic,

showed [00l] texture while those (YNSG-P and YNSG-N) shorter heat treatments are textured in [103] direction.

4. Study of the mechanical properties of the processed YBCO show correlation of hardness and the field dependence of current density to be affected similarly by the network of nanometric defects present in the YBCO composites.

5. FESEM images demonstrate the successful introduction of individual $Sm_2O_3$ nanoparticles on the Y-211 particle surfaces, without agglomeration even at the high concentrations involved during the fabrication of YSm-211 preforms.

6. One can observe that both the good samples YSm-20 and YNSG with better $Jc(H)$ curves exhibit narrow transition and efficient suppression of solid solutions of RE/Ba-ss type as seen from ac susceptibility and XRD data.

7. The introduction of mixed RE elements at Y site leading to compositional fluctuations in the superconducting matrix and the associated lattice mismatch effects have provided flux pinning at high fields up to 9 T, in all POIG processed samples, in which porosity and solid solution formation are controlled.

8. YSm-20 sample shows the highest $J_c(H)$ at 77 K, compared to YSm-10 and YSm-30 samples in (Y, Sm)BCO series.

9. $J_c(H)$ performance of YNSG is the best of all the samples studied, with $H_{irr}$ being > 9 T at 77 K. $J_c(0)$ is 21.5 kA/cm$^2$ at 77 K and is highest of all.

10. Considerable $J_c(H)$ of >300 A/cm$^2$ is observed up to 9 T in YNSG sample in spite of 6% porosity present in the sample.

11. Excess Ba in preform enabled successful formation of YNSG in air, which not only eliminated the spherical porosity but also minimized the macroporosity to 1%. $J_c(H)$ performance of YNSG-Ba is marginally better

than YNSG processed in argon at high fields and this is attributed to the pinning from defects associated with twinning.

Future direction of work would be to refine the size of RE-211 and introduce nano-inclusions in mixed RE doped YBCO to enhance the $J_c(0)$ further and maintain it high at high fields through POIG process.

**References:**

1.   E. Sudhakar Reddy and T. Rajasekharan, J. Mater. Res. **13** (1998) 2472.

2.   E.   Sudhakar Reddy and T.   Rajasekharan, Supercond.   Sci.   Technol. **11** (1998) 523.

3.    N.V.N. Viswanath, T. Rajasekharan, N. Harish Kumar, L. Menon and S.K. Malik, Supercond. Sci. Technol. **11** (1988) 420.

4.    R.  Cloots, T.  Koutzarova, J.P.  Mathieu and M.  Ausloos, Supercond.  Sci. Technol. **18** (2005) R9.

5.   S.   Meslin, K.   Iida, N.   Hari Babu, D.A.   Cardwell and J.G.   Noudem, Supercond.
Sci. Technol.  **19** (2006) 711.

6.   K.   Iida, N.   Hari Babu, T.D.   Withnell, Y.   Shi, S.   Haindl, H.W. Weber and D.A. Cardwell, Physica C **445–448** (2006) 277.

7.   S.Y.   Chen, Y.S.   Hsiao, C.L.   Chen, D.C.   Yan, I.G.   Chen and M.K. Wu, Mater.                                                       Sci. Eng. B **151** (2008) 31.

8.   S. Meslin and J.G. Noudem, Supercond. Sci. Technol.  **17** (2004) 1324.

9.   K.   Lida, N.   Hari Babu, Y.   Shi and D.A.   Cardwell, Supercond.   Sci. Technol. **18** (2005) 1421.

10. N. Devendra Kumar, Ph.D. Thesis (2011) "Enhanced flux pinning to high fields in YBCO and YBCO/Ag superconductors through Preform Optimization in Infiltration and Growth Process".

11. M. Muralidhar, S. Nariki, M. Jirsa, Y. Wu and M. Murakami, Appl. Phys. Lett. **80** (2002) 1016.

12. D. Volochova´n, P. Diko, V. Antal, M. Raduˇsovska and S. PiovarcˇI, Journal of Crystal     Growth **356** (2012) 75.

13. N. Ogdwa, I. Hirdbayashi and S. Tanaka, Physica C **177** (1991) 101.

14. N. Ogawa, M. Yoshida, I. Hirabayashi and S. Tanaka, Supercond. Sci. Technol. **5** (1992) S89.

15. Michael J. Cima, Met-ton C. Flemings, Anacleto M. Figueredo, Masahiko Nakade, Hideo Ishii, Harold D. Brady and John S. Haggerty, J. Appl. Phys. **71** (1992) 1868.

16. N. Devendra Kumar, T. Rajasekharan, Ravi C. Gundakaram and Vummethala Seshubai, IEEE TRANSACTIONS ON APPLIED SUPERCONDUCTIVITY **21** (2011) 6.

17. J.M.S. Skakle, Materials Science and Engineering **R23** (1998) 1.

18.  M. Murakami, N. Sakai, T Higuchi and S. I. Yoo, Supercond. Sci. Technol. **9** (1996) 1015.

19. G. Osabe, T. Takizawa, S.I. Yoo, N. Sakai, T. Higuchi, M. Murakami, Mater. Sci. Eng. B-Solid State **65** (1999) 11-16.

20. Y. Xu, M.J. Kramer, K.W. Dennis, H. Wu, A. O`Connor, R.W. McCallum, S.K. Malik, W.B. Yelon, Physica C **333** (2000) 195-206.

21. Y. Li, Y. Liu, R. Duan, X. Xiong, B. Wang, G. Cao, L. Wei, D.N. Zheng, Z.X. Zhao, J.H. Ross, Physica C **402** (2004) 179-187.

22. M. Sano, Y. Hayakawa and M. Kumagawa, Superconduct. Sci. Technol. **9** (1996) 478-482.

23. I. Van Driessche, B. Schoofs, E. Bruneel, S. Hoste, J. Eur. Ceram. Soc. **24** (2004) 1823-1826.

24. V.A. Drozd, I.L Baginski, S.A. Nedilko and V.S. Meľnikov, J. Alloys Compounds **384** (2004) 44-50.

25. J. Maňka, A. Cigáň, J. Polovková, A. Koňakovský and A. Prnová, Measurement science review **11** (2011) 1.

26. P.M. Swarup Raju, Ph.D. Thesis (2012) "Infiltration growth processing of YBCO nano-composites: Shape forming, microstructural and magnetic studies".

27. A Radhika Devi, V Seshu Bai, P V Patanjali, R Pinto, N Harish Kumar and S K Malik, Supercond. Sci. Technol. **13** (2000) 935.

28. M. Muralidhar, M.R. Koblischka and M. Murakami, Physica C **313** (1999) 232.

29. M. Muralidhar, H.S. Chauhan, T. Saitoh, K. Kamada, K. Segawa and M. Murakami, Supercond. Sci. Technol. **10** (1997) 663.

30. M. Muralidhar, M.R. Koblischka, T. Saitoh and M. Murakami, Supercond. Sci. Technol. **11** (1998) 1349.

31. C. Cai, B. Holzapfel and J. Hänisch, Physical Review B. **69** (2004) 104531.

# Figure captions

**Fig. 1.1.**    Typical H vs T phase diagrams for type-I and type-II superconductors. There is only one critical field ($H_c$) in a Type-I superconductor and there are two critical fields ($Hc_1$ and $Hc_2$) for a type-II superconductor.

**Fig. 1. 2**    Typical phase diagram of a superconductor.

**Fig. 1.3.**    Increase in critical temperatures of superconductors over the years.

**Fig. 1.4.**    The crystal **s**tructure of an $ABO_3$ perovskite type with the origin centered at (a) the B-site ion and (b) the A-site ion.

**Fig. 1.5.**    Evolution of the crystal structure of $YBa_2Cu_3O_{7-x}$ from the triple-perovskite unit $Y_3Cu_3O_9$.

**Fig. 1.6.**    SEM image of sintered YBCO.

**Fig. 1.7.**    Pseudo-binary phase diagram of the Y-Ba-Cu-O system, where the $YBa_2Cu_3O_{7-\delta}$ (solid lines) phase exists. The phase diagram with $NdBa_2Cu_3O_{7-\delta}$ is shown in dashed lines; $123 = REBa_2Cu_3O_{7-\delta;}$ $211 = RE_2BaCuO_5$; $200 = RE_2O_3$; $010 = BaO$; L= Liquid phases.

**Fig. 1.8.**    SEM image of YBCO processed by melt growth process. Nearly spherical Y-211 particles can be seen in Y-123 matrix.

**Fig. 1.9.**    A comparison between Melt Growth and Infiltration Growth processes for REBCO materials.

**Fig. 1.10.**    TEM images of MG processed NSGBCO samples with the addition of (a) 10 mol.% Gd-211 and (b) 30 mol.% of Gd-211, from Murakami et al.

**Fig. 1.11.**    TEM dark-field images from NSEBCO superconductors with 10 and 30 mol.% of Gd-211 additions. The white and black contrast in the micrographs has been attribute to compositional fluctuations occurring due to RE/Ba substitution.

**Fig. 2.1.**    A schematic diagram of the furnace used.

infiltrated at 1100 $^o$C. The arrows point to the final POIG processed samples.

distributed individually and without agglomeration on the Y-211 surface in (a). In (b) and (c) such particles are too numerous to individually resolved.

**Fig. 4.3.**   XRD patterns obtained from YBCO-Ar, YSm-10, YSm-20 and YSm-30 samples are shown. The patterns were obtained using Cu $K_\alpha$ radiation. The Bragg peak positions corresponding to the 211 minority phases are indicated by (*).

**Fig. 4.4.**   Temperature dependence of the real part of ac susceptibility ($\chi'$) for YBCO-Ar, YSm-10, YSm-20 and YSm-30 samples.

**Fig. 4.5.**   FESEM image from YBCO-Ar, and the corresponding Y-211 particle size histogram, are shown in (a) and (b) respectively.

**Fig. 4.6.**   FESEM images obtained from the samples YSm-10 YSm-20 and YSm-30 using In-lens detector are shown in (a), (b) and (c) respectively. In all the images, the presence of YSm-211 particles can be seen in the YSm-123 matrix. The corresponding 211 particle size histograms are shown in figs. (d), (e) and (f) respectively.

**Fig. 4.7.**   FESEM images obtained from the samples YSm-10 YSm-20 and YSm-30 (at 5 kX) are shown in (a), (b) and (c) respectively. In all images YSm-211 particles can be seen in YSm-123 matrix. The micrographs obtained at higher magnifications than those in fig. 4.6 are intended to clearly show the Y-211 core region (bright) in the YSm-211 particles.

**Fig. 4.8**.   The field dependence of $J_c$ at temperatures 25 K, 50 K, 65 K and 77 K (for YBCO-Ar, YSm-10, YSm-20 and YSm-30 POIG processed samples) are shown in figs. (a), (b), (c) and (d) respectively. YBCO-Ar shows maximum $J_c$ at zero field ($J_c(0)$) in comparison with other samples at all temperatures. Among all (Y, Sm)BCO samples, YSm-20 showed the best performance and it supported significantly larger $J_c$ up to high magnetic fields at all temperatures.

**Fig. 4.9.**   The field dependence of the normalized flux pinning force $F_p / F_{p\,max}$ for the samples YBCO-Ar, YSm-10, YSm-20 and YSm-30 at temperatures 25 K, 50 K, 65 K and 77 K are shown in figs. (a), (b), (c) and d). The curve for sample YSm-20 peaks at the maximum field of 2.1 T at 77 K.

**Fig. 4.11.**   (a) XRD plots of YBCO-Ar, YSm-20 and YSm-20-C samples.

**Fig. 4.12.**  (a) and (b) show FESEM images at lower and higher magnifications respectively, for YSm-20-C, the POIG processed sample prepared from powder obtained using citrate synthesis. In (c) and (d), in the lower panel, similar micrographs are shown for POIG processed YSm-20, which was prepared from powders where nano particles of $Sm_2O_3$ were separately added to Y-211.

**Fig. 4.13.**  Temperature dependence of real part of ac susceptibility ($\chi'$) for the samples YSm-20-C and YSm-20

**Fig. 4. 14.**  Field dependence of critical current density ($J_c$) of (a) YSm-20-C and (b) YSm-20 at different temperatures.

**Fig. 4.15.**  Temperature dependence of real part of ac susceptibility ($\chi'$) for the samples YSm-20-Nb and YSm-20. The onset superconducting transition temperature remains the same for both the samples, but the transition width is more for the Nb- containing sample.

**Fig. 4.16.**  X-ray diffractograms obtained from YSm-20 and YSm-20-Nb samples. The Nb- substituted sample shows the presence of an extra intermetallic phase $YBa_2NbO_6$. The diffraction lines from the phase are marked ( ◆).

**Fig. 4.17.**  FESEM images of POIG processed (a) YSm-20-Nb and (b) YSm-20. Addition of Nb to YSm-20 as given rise to more porosity in the microstructure with a minor refinement of the 211 particles.

**Fig. 4.18.**  Critical current densities of YSm-20-Nb and YSm-20 samples are compared as function of external field at different temperatures. $J_c(0)$ is larger for the Nb-containing samples at all temperatures. However, at higher temperatures the performance the Nb- containing samples deteriorates probably due to higher level of porosity.

**Fig. 4.19.**  The magnetic field dependence of the pinning force for the samples YSm-20-Nb and YSm-20 are shown in figs. (a) and (b) respectively. $F_p$ is normalized with respect to its maximum value at each temperature.

**Fig. 4.20.**  Compositional analyses of POIG processed YSm-20 sample. Upper panel (a) shows the composition obtained by an area scan of the 123 matrix. The area from where the data was acquired is marked in the micrograph. The

measured composition shows that the matrix consists of YSm-123. (b) the middle panel shows compositional analyses, through a point scan, of the bright region in the middle of a 211 grain. The region is found to be free of Sm and corresponds to the composition of $Y_2BaCuO_5$. (c) the lower panel is a point scan analyses of the darker outer region of a 211 grain. The composition corresponds to $(Y, Sm)_2BaCuO_5$.

**Fig. 4.21.** Elemental analysis in YSm-20-C. The upper panel, we note that the matrix composition is YSm-123. A compositional analysis of the 211 grains reveals that they have Y and Sm distributed uniformly within their volumes and there is no evidence of the formation of a core of composition Y-211.

**Fig. 4.22.** FESEM images from sintered preforms used for the fabrication of POIGP YSm-20-C at lower and higher magnifications are shown in (a) and (b) respectively. Similar images from YSm-20 are shown in (c) and (d). The preforms were fabricated in a die at a pressure of 460 MPa and sintered at 950 $^{\circ}$C for 4h. The comparison between figs. (b) and (d) shows that in the latter sample, the 211 particles are sintered into large grains.

**Fig. 4.23.** Schematic figures to illustrate the mechanism of core formation within 211 precipitates in (Y, Sm)BCO samples.

**Fig. 4.24.** Compositional analysis of YSm-20-Nb sample using EDS. The upper panel shows that the composition of the matrix corresponds to $(Y, Sm)Ba_2Cu_3O_{7-\delta}$, with a small amount of dissolved Nb. The middle panel shows that the composition of the darker part of the 211 precipitates correspnds to (Y, Sm)$_2BaCuO_5$. The lowest panel shows that the core region of the precipitates contains no Sm or Nb and is pure $Y_2BaCuO_5$.

**Fig. 5.1.** Heat treatment schedule followed to synthesize theYBCO-Ar and YNSG samples.

**Fig. 5.2.** Variation of normalized real part of ac susceptibility ($\chi'$) with temperature for YBCO-Ar and YNSG samples. Sharp superconducting transitions are observed.

**Fig. 5.3.** X-ray diffraction patterns with Rietveld refinement for YBCO-Ar and YNSG samples were shown in (a) and (b) respectively. These samples are oxygenated and in the superconducting state.

# Tables Captions

**Table 1.1:**    Superconducting transition temperature ranges of different types of superconductors, where m=1 and 2 and n=1, 2, 3…

**Table. 3.1.**    Microstructural and magnetic properties of the samples Y-1 and Y-2.

**Table. 3.2.**    Mechanical properties of Y-1 and Y-2 measured on the Y-123 and Y-211 phases in both the samples.

**Table 3.3.**    Comparison of mechanical properties with those reported in the literature.

**Table 4.1.**    Lattice parameters and cell volumes of YBCO-Ar, YSm-10, YSm-20 and YSm-30 samples.

**Table 4.2:**    $T_c$ onset and transition widths ($\Delta T_c$) obtained from ac susceptibility measurements for YBCO-Ar, YSm-10, YSm-20 and YSm-30 samples. YSm-211 phase content (Vol. %), YSm-211 particle size-range, and porosity in the matrix estimated from microstructural studies, are also shown.

**Table 4.3:**    Current density at zero field ($J_c(0)$) for the YBCO-Ar, YSm-10, YSm-20 and YSm-30 samples at 25 K, 50 K, 65 K and 77 K.

**Table 4.4:**    Temperature dependence of $J_c(0)$ and normalized flux pinning force for YSm-20-Nb and YSm-20 samples.

**Table 5.1:**    Lattice parameters and the unit cell volumes of the samples.

**Table. 5.2.**    Fitting parameters for YBCO-Ar, YNSG and YSm-20 samples

**Table 6.1:**    Lattice parameters and unit cell volumes of the YBCO-Ar, YNSG, YNSG-P and YNSG-N samples.

**Table 6.2.**    Comparison of various (Y, NSG)BCO samples dealt with in this chapter.

# APPENDIX

## 1. Elemental analysis of YSm-20:

In order to identify various phases observed in the matrix and in the bright and dark regions of the precipitates, compositional analysis of the synthesized samples was carried out in detail using EDX through a) mapping, b) area scans and c) point scan. Given below are the results on one of the samples YSm-20, chosen as an example.

### (i) Mapping:
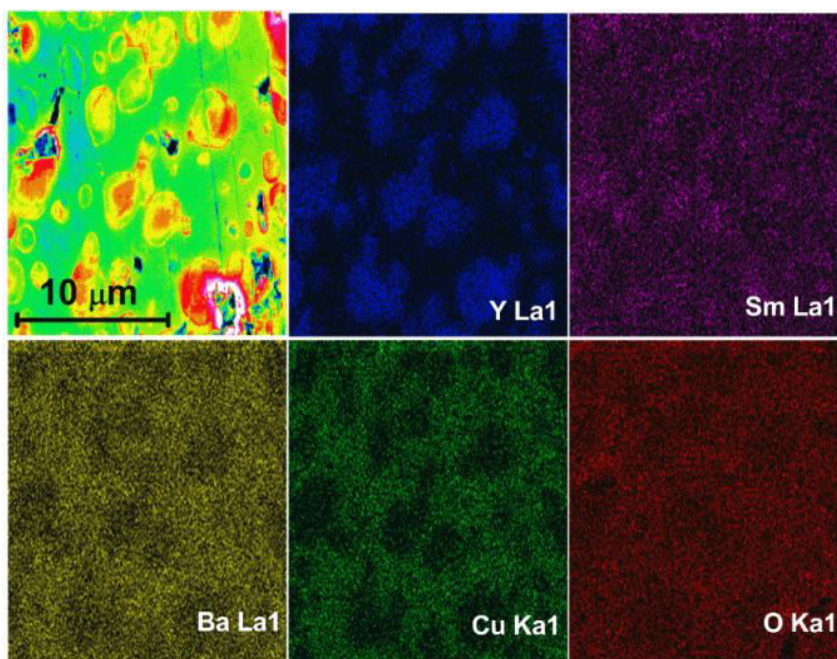


**Fig. A.1.** Mapping data for sample YSm-20. In (Y, Sm)-211 particles RE elements (Y and Sm) present more than in matrix. In RE-211 phase in centre regions of the particles more Y concentration can be found.

Mapping investigations identify the local distribution of individual elements by measuring the corresponding characteristic X- radiation ($K_{\alpha 1}$, $L_{\alpha 1}$ , etc.) of the elements, one at a time. Such data on YSm-20 is shown in fig. 4.10 (b-f) for elemental scan of Y, Sm, Ba, Cu and O. Fig. 4.10 (a) is a superposition of all the scans. An examination of the mapping indicates that Y and Sm elements are present all over the mapping frame that contains the matrix phase and the precipitates.

It can also be observed that the amounts of RE (Y and Sm) elements are more in the precipitates than in the matrix, while Ba and Cu elements are in lesser amounts in the precipitates as in RE-211, compared to RE-123 matrix. Y is found to be rich in the cores of precipitates.

For more precise estimate of the amounts of the elements present in different regions, area scans are recorded as discussed below.

**(ii)** **Line Scan :** The elemental scans done along a line chosen across the precipitate within the matrix are shown below.

Line scan images of YSm-10, YSm-20 and YSm-30 samples are shown in fig. 4.12 (a), (b) and (c) respectively. Line was drawn in the matrix phase via dark and bright regions of the 211 particles. In all samples it is observed that the dark shade of the 211 particle consists of both the Y and Sm elements, whereas the core part of the 211 phase contains only Y. These results confirm that the compositions of the dark regions of the 211 particles are (Y, Sm)-211 and the brighter regions of the 211 particles are Y-211.
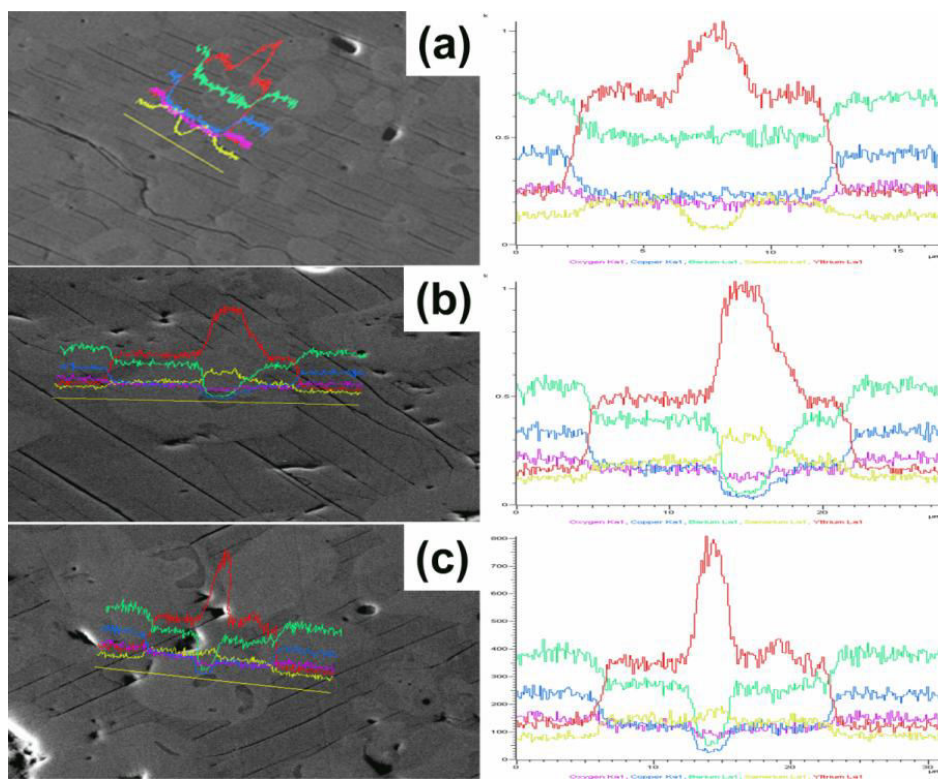
**Fig. A.2.** Line scan images of YSm-10, YSm-20 and YSm-30 are shown in (a), (b) and (c) respectively. Red line for Y, Yellow line for Sm, Blue line for Cu, Green color for Ba and Orange color line for Oxygen.

## 2.   Compositional analysis of YNSG-P through EDS:

Elemental analysis of the YNSG-P sample was carried out by employing EDS and pictured in fig. 6.5.  In this sample also three different shades were found as same as observed in YNSG sample (fig. 5.5.) which are 123 matrix and YNSG-211 and Y-211 phases. Measurements were done on matrix, YNSG-211 and Y-211 phase particles and shown in figs. A.3. (a)-(c) respectively.
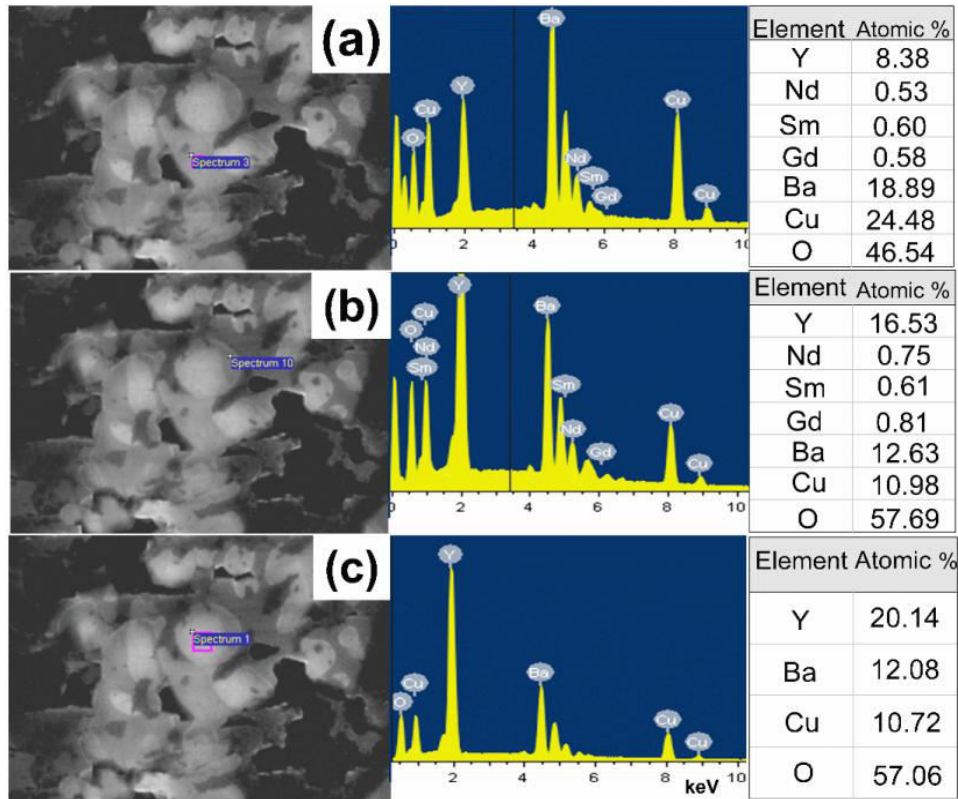
**Fig. A.3.** Composition analysis of the YNSG-P sample (a) on matrix, (b) on YNSG-211 and (c) on Y-211 phase.

To confirm this excess Ba and Cu in the sample, composition analysis was carried out on the black region which is believed to be pore filled with liquid phases. From the measurements as shown in the fig. A.4., it is found that the presence of Ba and Cu is higher which is confirming the solidification of liquid phases in pore.

| Element | Atomic% |
|---------|---------|
| Y | 7.74 |
| Nd | 0.37 |
| Sm | 0.21 |
| Gd | 0.10 |
| Ba | 19.54 |
| Cu | 17.43 |
| O | 54.61 |
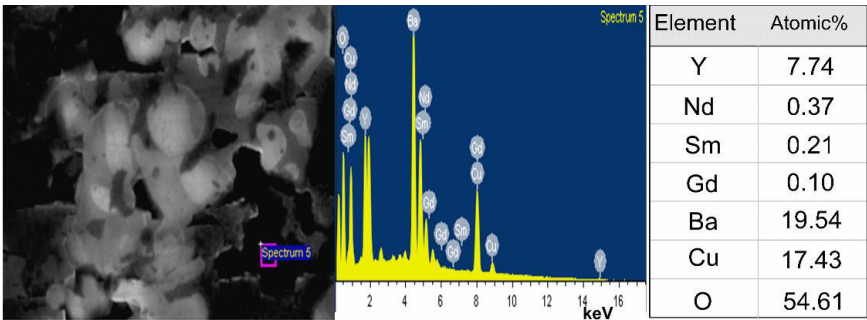
**Fig. A.4.** Compositional analysis on pore filled with liquid phase.

### 3.   EDS results of YNSG-Air:



(a)

| Element | Atomic % |
|---------|----------|
| Y | 7.07 |
| Nd | 0.36 |
| Sm | 0.36 |
| Gd | 0.43 |
| Ba | 16.19 |
| Cu | 21.82 |
| O | 53.77 |

(b)

| Element | Atomic % |
|---------|----------|
| Y | 18.18 |
| Nd | 0.91 |
| Sm | 1.08 |
| Gd | 1.18 |
| Ba | 11.46 |
| Cu | 11.04 |
| O | 56.15 |

(c)

| Element | Atomic % |
|---------|----------|
| Y | 20.96 |
| Ba | 11.62 |
| Cu | 10.82 |
| O | 56.60 |
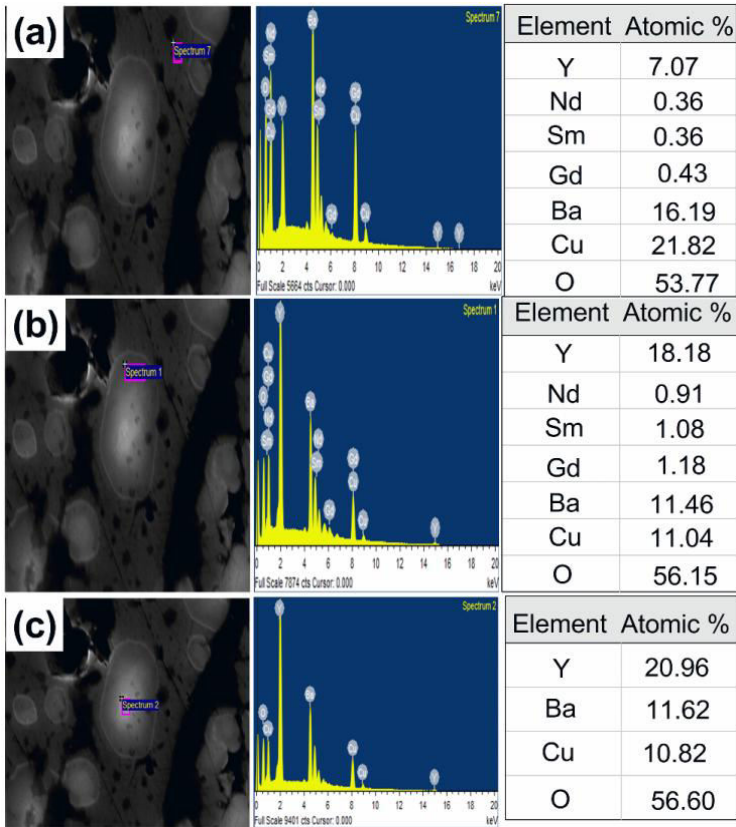
**Fig. A.4.** EDS measurement on (a) 123 matrix, (b) dark region of the precipitate and (c) bright region of the precipitate.

# S. Pavan Kumar Naik

*Phone: +91-8886162262*
*E-mail: pavan0555@gmail.com*

## Contact Details

**Work**                                    **Home**

Research scholar                            S. Pavan Kumar Naik
School of Physics                           S/o. S.Bojja Naik
University of Hyderabad                      Narasanayani kunta (V)
Hyderabad – 500046                          Anantapur (Rural)-515004
Telangana, India                            Andhra Pradesh, India
Phone: +91-40-23134365, 23010241            Mobile: +918886162262

## Academics

- Pursuing Doctor of Philosophy (**Ph.D**.), thesis submitted in School of Physics, University of Hyderabad under the supervision of Prof. V. Seshubai.

    *   Specialization    :  High Temperature Superconductivity
    *   Title of the thesis :  "**Effect of RE-doping at Nanoscale on   the Microstructures and Flux Pinning in Infiltration Growth Processed (Y, LRE)BCO Superconductors**"

- Master of Science (**M.Sc**.) from Sri Venkateswara University, Tirupathi in Physics stream, during the academic year 2007-09 with **75.10 %**

    *   Specialization : Applied Spectroscopy

- Bachelor of Science (**B.Sc**.) from Arts college, Anantapur, 2004 – 2007 with **70.10** %.

- **Intermediate** from Board of Intermediate Education, Andhra Pradesh, 2004 with **65.0 %**.

- **Class X (SSC)** from Board of Secondary Education, Andhra Pradesh, 2002 with **71.0 %**.

## Additional Qualifications:

- Secured **80.66** percentile in Graduate Aptitude Test in Engineering (GATE), 2010 National Level Examination (PH1410719).

- Qualified in CSIR First Paper held in 2010 December.

- Qualified for Rajiv Gandhi National Fellowship for the academic year 2010.

- Qualified in APSET held in 2012 (H.T. No. 111601092)

- Worked as Teaching Assistant for 3 years (6 semesters) in School of Physics, University of Hyderabad, Hyderabad for M.Sc- Physics, I. M.Sc-Physics courses.

## Publications and Presentations:

1. **Effect of infiltration temperature on the properties of infiltration growth processed YBCO superconductor**
   **S. Pavan Kumar Naik,** N. Devendra Kumar, P. Missak Swarup Raju, T. Rajasekharan, and V. Seshubai, Physica C: 487, 72-76(2013)

2. **The Effect of $CeO_2$ nanoparticles doping on refinement of Y-211 particles in POIG processed YBCO composites**
   P. Missak Swarup Raju, **S. Pavan Kumar Naik,** N. Devendra Kumar, T. Rajasekharan and V. Seshubai, International Journal of Modern Physics: Conference Series Vol. 22 page 497–500 (2013)

3. **Effect of Ag addition on the microstructures and superconducting properties of bulk YBCO fabricated by Directionally Solidified Preform Optimized Infiltration Growth Process**

N. Devendra Kumar, P. Missak Swarup Raju, **S. Pavan Kumar Naik**, T. Rajasekharan and V. Seshubai.  Physica C 496 (2014) 18–22

4. **Effect of Preform Compaction Pressure on the Final Microstructures and Superconducting Properties of YBa$_2$Cu$_3$O$_{7-\delta}$ Superconductors Fabricated by Directionally Solidified Preform Optimized Infiltration Growth Process**
   N Devendra Kumar, P Missak Swarup Raju, **S Pavan, Kumar Naik**, T Rajasekharan, V Seshubai, Journal of Low Temperature Physics (Impact Factor: 1.19). 10/2013; DOI 10.1007/s10909-013-0955-x

5. **Growth Mechanism in Infiltration Growth Processed YBCO Composites through Quench Studies**
   **S. Pavan Kumar Naik**, P. Missak Swarup Raju, T. Rajasekharan and V. Seshubai, J Supercond Nov Magn. (2014) 27:1211–1215. DOI 10.1007/s10948-013-2448-1.

6. **Origin of Stable Critical Current Densities at High Applied Magnetic Fields in Ceria Doped YBCO Superconductors**
   P. Missak Swarup Raju, **S. Pavan Kumar Naik,** N. Devendra Kumar,  T. Rajasekharan, V. Seshubai. International Journal of Chem Tech Research, Vol.6, No.3, pp 1699-1701, May-June 2014.

7. **Introduction of Nano Ceria into Infiltration Growth Processed YBCO Superconducting Composites**
   P. Missak Swarup Raju, N. Devendra Kumar, **S. Pavan Kumar Naik**, T. Rajasekharan and V. Seshubai, J J Supercond Nov Magn (2014) 27:2277–2282 DOI 10.1007/s10948-014-2592-2

8. **Structural and microstructural properties of Infiltration Growth processed (Y, Sm)BCO superconductors**
   **S. Pavan Kumar Naik**, P. Missak Swarup Raju and V. Seshubai, (Manuscript under preparation).

9. **Microstructural and magnetic properties of  nano Sm$_2$O$_3$ doped POIG processed YBCO superconductors**
   **S. Pavan Kumar Naik,** P. Missak Swarup Raju, T. Rajasekharan, and V. Seshubai, (Manuscript under preparation).

# List of presentations in International/National conferences:

1. **Magneto caloric and shape memory effects in nickel-rich $Ni_{53.5}Mn_{26.0}Ga_{20.5}$ alloy**
   M. Ramudu, A. Satish Kumar, **S. Pavan Kumar Naik** and V. Seshubai

   Andhra Pradesh Science Academy (APSA) is organized a Science Congress (APSC-2011) at Gitam University, Vishakhapatnam during 14-16, November 2011

2. **Integration of Directional Solidification with Preform Optimized Infiltration Growth Process: A novel method for fabricating near net shaped high Jc $YBa_2Cu_3O_{7-\delta}$ superconductors in short time durations**
   N. Devendra Kumar, P. Missak Swarup Raju, **S. Pavan Kumar Naik** and V. Seshubai.

   Andhra Pradesh Science Academy (APSA) is organized a Science Congress (APSC-2011) at Gitam University, Vishakhapatnam during 14-16, November 2011

3. **Fabrication of $GdBa_2Cu_3O_{7-\delta}$ (GdBCO) superconductor in air through Preform Optimized Infiltration Growth Process (POIGP)**
   **S. Pavan Kumar Naik**, P. Missak Swarup Raju, N. Devendra Kumar, T. Rajasekharan and V. Seshubai.

   St. Thomas College, Pala, Kerala is organized International Conference on Materials Science and Technology (ICMST-2012) during 10 - 14 June 2012.

4. **On introduction of nano-ceria into Y-211 preforms for flux pinning in YBCO superconductors**
   P. Missak Swarup Raju, N. Devendra Kumar, **S. Pavan Kumar Naik**, V. Seshubai and T. Rajasekharan.

   St. Thomas College, Pala, Kerala is organized International Conference on Materials Science and Technology (ICMST-2012) during 10 - 14 June 2012.

5. **Refinement of Y-211 Particles in YBCO Superconducting Matrix through Modified Preform Optimized Infiltration Growth Process**

**S. Pavan Kumar Naik,** P. Missak Swarup Raju, N. Devendra Kumar, T. Rajasekharan and V. Seshubai

Govt. Engineering College Bikaner and Ceramic Electrical Research & Development Centre, Bikaner organized an International Conference on Ceramics (ICC-2012) at Bikaner, Rajasthan during 12-13 December 2012.

6. **Nano sized defects for flux pinning at high fields in REBCO superconductors**
   V. Seshubai, **S. Pavan Kumar Naik** and P. Missak Swarup Raju

## Workshops / Training courses participated:

1. Participated in Awareness workshop of UGC-DAE Consortium for Scientific Research (October 28-30, 2013) organized by UGC-DAE for Scientific Research, Mumbai Centre & School of Engineering Sciences & Technology, University of Hyderabad held at University of Hyderabad.

2. Participated in Frontiers in Physics (FIP-2013, September 20-22) organized by School of Physics, University of Hyderabad, Hyderabad, India.

3. Workshop on Machine Drawing and machining organized by University of Hyderabad during November 22-29, 2012.

4. Participated and volunteered in Andhra Pradesh Science Academy (APSA) is organized a Science Congress (APSC-2013) at University of Hyderabad, Hyderabad during 14-16, November 2013.

5. Participated in Frontiers in Physics (FIP-2014, 17-18, October 2014) organized by School of Physics, University of Hyderabad, Hyderabad, India.

6. Participated and volunteered in "25th National Symposium on Cryonics" School of Physics, University of Hyderabad during 8-10, December 2014, Hyderabad, India.

## Research Interests

- Applied superconductivity

- Functional Ceramics and Composite Materials

- Coated Conductors, Superconducting Wires and Tapes

- Materials modeling and Simulations through DFT

- Structural Investigations (XRD, RAMAN etc.,)

## Skills

- $Sm_2O_3$ nano particles preparation doped YBCO superconductors were fabricated through Preform Optimized Infiltration growth process for my Ph.D. work**.**

- Hands on experience on various material processing techniques (both solid state and chemical routes) such as Powder Metallurgy processing

- Preparation of nano particles through chemical sol-gel route

- Versed with various characterize techniques like:

  - Microstructural analysis (on micrographs obtained both from optical and electron microscopes)

  - Four probe resistivity, ac susceptibility, magnetization, magnetic levitation etc.

  - Crystal structure determination and refinement of lattice parameters using Fullprof, Topaz etc., software's.

  - Familiar with compression strength, indentation, density measurement, measurement.

  - Magnetization measurements on PPMS based VSM (Quantum design mane) and VSM (lakeshore make).

- Materials modeling and simulations using first principle calculations using different packages.

## Hands on experience with

* Physical Property Measurement System 'PPMS' (Quantum Design-make) with various attachments like Vibrating Sample Magnetometer (with Oven), ac susceptibility measurement, Resistivity, thermal transport measurement etc.

* Microscopes like
  * Field Emission Scanning Electron Microscope FE-SEM (Zeiss make, Ultra 55) (I have operated it for more than 1 year)

  * Metallurgical Optical Microscope with Polarizer attachment (Zeiss make, Axiovert)

* Low Speed Diamond Saw, ISOMET 1000 and an Auto-polisher of Buehler make. Developed expertise in preparing samples for observation under SEM / TEM.

* Furnaces operating to $1200^{o}$C/$1700^{o}$C controlled by programmable temperature controller and thyristor (Eurotherm-make/WEST-make)

* Heat treatment of samples in different atmospheres (Ar, $H_2$, etc,.).

* Versed with sample preparation techniques for fabricating high temperature bulk (RE)BCO superconductors, ceramic composites.

* Shaping machines like lathe, miller, hydraulic press, dicer etc.

* Nanoindentation (TI 900 Tribo-Indenter, Hysitron made) measurement to carryout Hardness and young's modulus of the materials.

## Computational skills

* Origin, MS office (Word, excel, power-point etc.).
* Microstructural analysis using Axio-vision / Image analysis software.

* Having familiarity with scientific software like JCPDS data cards, binary phase diagrams.
* Familiarity with LABVIEW.
* Rietveld refinement using FULLPROF and TOPAS programs.
* Materials modeling using Quantum Espresso, LAMMPS, VESTA, packages.

## Personal

❖ Father's Name : Sri. S. Bojja Naik
❖ Mother's Name : Smt. S. Lakshmakka
❖ Date of Birth : May 02, 1987
❖ Marital Status : Married
❖ Nationality : Indian
❖ Gender : Male
❖ Passport : Yes (valid up to 2020)

## Reference

❖ Dr. V. Seshubai, School of Physics, University of Hyderabad, Hyderabad, India. E-mail: seshubai@gmail.com

❖ Prof. M. C. Valsa Kumar, Outstanding Scientist (Retd.), Head of the Materials Physics division, IGCAR, Kalpakkam.
Email: mc.valsakumar@gmail.com

❖ Prof. M Ghanashyam Krishna, School of Physics, University of Hyderabad, Hyderabad, India. E-mail: mgksp@uohyd.ernet.in, ghanshuk@yahoo.com

❖ Prof. V. Sundara Raja, Solar Energy Lab (Retd.), Dept. of Physics, Sri Venkateswara University, Tirupati-517502, Andhra Pradesh - INDIA.
Email: sundararajav@rediffmail.com

## Declaration

I declare that the information provided is true to the best of my knowledge.


**S. Pavan Kumar Naik**

**Date**: August 10, 2015
**Place**: Hyderabad

# Effect of Re-Doping in the Preforms At Nanoscale on the Micro Structures and Flux Pinning in Infiltration Growth Processed

**25**% 
SIMILARITY INDEX

**4**% 
INTERNET SOURCES

**21**% 
PUBLICATIONS

**6**% 
STUDENT PAPERS

PRIMARY SOURCES

**1** Pavan Kumar Naik, S., N. Devendra Kumar, P. Missak Swarup Raju, T. Rajasekharan, and V. Seshubai. "Effect of infiltration temperature on the properties of infiltration growth processed YBCO superconductor", Physica C Superconductivity, 2013.
Publication

**4**%